Author:
Yuan, Guanjie

Title:
Investigation of the mechanical behaviour of nuclear-grade SiC fibre reinforced SiC matrix composite and Cr-coated zircaloy-4 cladding materials under extreme conditions

Investigation of the mechanical behaviour of nuclear-grade SiC fibre reinforced SiC matrix composite and Cr-coated zircaloy-4 cladding materials under extreme conditions

By

Guanjie Yuan

School of Physics
Faculty of Science
University of Bristol

A dissertation submitted to the University of Bristol with the requirements for award of the degree of Doctor of Philosophy in the Faculty of Science.

DECEMBER 2023

Word count: 63585

I declare that the work in this dissertation was carried out in accordance with the requirements of the University's *Regulations and Code of Practice for Research Degree Programmes* and that it has not been submitted for any other academic award. Except where indicated by specific reference in the text, the work is the candidate's own work. Work done in collaboration with, or with the assistance of, others, is indicated as such. Any views expressed in the dissertation are those of the author.

SIGNED: ……Guanjie Yuan……..... DATE: 21/12/2023

Abstract

SiC fibre-reinforced SiC matrix composite (SiC_f-SiC_m) and Cr-coated zircaloy materials are widely recognized as promising candidate cladding materials for the nuclear accident tolerant fuels (ATF). For their future industrial application, it is critical to understand their mechanical behaviour and failure processes under extreme conditions. Therefore, this project mainly focuses on the deformation and fracture processes of two types of SiC_f-SiC_m claddings (one with single-layer outer/inner SiC coatings; one with multi-layer SiC coating), and four types of Cr-coated zircaloy-4 claddings (three types of Cr coatings manufactured by cold-sprayed (CS) method with different manufacturing parameters, one Cr coating manufactured by physical vapour deposition (PVD) method). Real-time synchrotron micro X-ray computed tomography (μXCT) is employed in current project to monitor the crack formation and propagation via C-ring compression tests of these materials at ambient and high temperatures.

Both types of SiC_f-SiC_m claddings were tested at room temperature (RT) and 1200°C. Both materials processed temperature-dependent variations in failure processes. For both types of materials tested at both temperatures, cracks initiated in the outer SiC coating, and various cracks' toughening mechanisms occurred simultaneously rather than in a sequence. These are significantly diverging from the widely assumed toughening theory in such SiC_f-SiC_m materials tested via uniaxial tension loading. Before the μXCT experiments, local property and residual stress of individual components in the materials were respectively estimated by nanoindentation and Raman spectroscopy. Lastly, the correlation between microstructures, local properties, residual stresses and macro-scale performance of these materials are studied.

Four types of Cr-coated zircaloy-4 claddings were tested at both RT and 345°C. Post-failure coating cracks' patterns was analyzed via scanning electron microscope (SEM) imaging under higher resolution. Prior to the real-time testing, local properties of Cr coatings and underlying zircaloy-4 substrate were measured by nanoindentation method, and the microstructures of Cr grain in these Cr coatings were analyzed by electron backscatter diffraction (EBSD) method. It was found that, the different manufacturing processes of CS and PVD methods consequently lead to different Cr grains' microstructures in the coating, which subsequently affect local properties of these materials, as well as their mechanical behaviour. Additionally, the different manufacturing parameters of CS process could also result in different mechanical behaviour and coating crack patterns. Finally, the relationship between microstructure, local properties and high temperature mechanical behaviour of these Cr-coated zircaloy-4 materials are investigated.

Acknowledgements

First of all, I would like to express greatest gratitude to my supervisor, Dr. Dong Liu for offering me this PhD opportunity. She provided continued guidance, patience and support throughout this project and the COVID-19 pandemic. She taught me how to think and work as an independent scientist. She is the best supervisor I have ever met.

I would also like to thank Dr. Joachim-Paul Forna-Kreutzer for his training and guidance with X-ray tomography and image segmentation software, and his dedicated help during the numerous and tiring synchrotron experiments; Mr. Daniel Cogbill and Mr. Alex Comyn for their help in synchrotron experiments. Dr. Alexander Leide for his help in training me polishing machines, nanoindenter and Raman spectroscopy; Dr. Qiance Zhang for his help in FIB-SEM tomography; and Mr. Bearcroft Chris (UK Atomic Energy Authority) for his help in the EBSD.

I am also very thankful for the expertise and insightful advice provided by Prof. Mahmoud Mostafavi (University of Bristol), Dr. Luiz Kawashita (University of Bristol) and Prof. Rob Ritchie (University of California, Berkeley). I would like to offer thanks to Dr. Edward J. Lahoda (Westinghouse Electric Company LLC) for providing numerous testing materials for the project and more importantly, for his advice and guidance of this PhD project.

The financial assistance from the Engineering and Physical Sciences Research Council (EPSRC) which made this project possible is also greatly appreciated.

I would also like to thank all the teachers I met in my life, especially Prof. Qiang Feng and Prof. Wangyue Yang in USTB. Without them, I can not become who I am today. I would like to thank my roommates Mr. Kaho Chiu and Mrs. Haiqi Huang, who are the best roommates I have ever met in UK.

Finally, I dedicate this thesis to my family. I wish to sincerely thank my parents Prof. Chao Yuan and Mrs. Xun Guan, my grandparents Mr. Duowen Guan and Mrs. Yuqin Sun, and my aunt Mrs. Ju Guan for their continuous love, unconditional trust, endless patience and encouragements. Especially, my grandparents Mr. Duowen Guan and Mrs. Yuqin Sun are 85 years old, and we have a video chat everyday since I first went to UK in 2019; I wish them to be happy and healthy, and could attend my wedding in the future. Additionally, great thanks to my elder sister Mrs. Haoyu Zhang, who continuous help and encourage me since I am an undergraduate student.

Contents

List of abbreviations

Abbreviation	Meaning
1D	One-dimensional
2D	Two-dimensional
3D	Three-dimensional
3D-LMC	3D laser melt-coating
AE	Acoustic emissions
ALS	Advanced Light Source
Ar	Argon
AOO	Anticipated operational occurrences
ASTM	American Society for Testing and Materials
ATF	Accident tolerant fuel
BCC	Body centred cubic
BF-TEM	Bright-field transmission electron microscopy
BSE	Back-scattered mode
BWR	Boiling water reactor
CCD	Charge-coupled device
CMCs	Ceramic-matrix composites
CS	Cold spraying
CVD	Chemical vapour deposition
CVI	Chemical vapor infiltration
D	Disorder mode
DBA	Design-basis accident
DE	Deposition efficiency
DIC	Digital image correlation
DLS	Diamond Light Source
EBSD	EBSD Electron backscatter diffraction
FE	Finite element modelling
FEA	Finite element analysis
FFT	Fast fourier transform
FIB-DIC	Focused ion beam-digital image correlation
FIB-SEM	Focused ion beam scanning electron microscopy
FOV	Field of view
FWHM	Full-Width-at-Half-Maximum
G	Graphitic mode

GA	General Atomic
HCP	Hexagonal close packed
HIP	Hot isostatic pressing
IPFs	Inverse pole figures
LA-DVC	Local digital volume correlation
LO	Longitudinal optical phonon mode
LOCA	Loss of coolant accident
LSI	Liquid silicon infiltration
LWRs	Light water reactors
MI	Melt-infiltration
MTS	Methyltrichlorosilane
NITE	Nano-infiltrated transient eutectic phase process
NO	Normal operating
OPT ZIRLO	ZIRLO Optimized ZIRLO
PCS	Polycarbosilane
P-FIB	Plasma focused ion beam
PIP	Polymer infiltration pyrolysis
PR	Power ramps
PVD	Physical vapor deposition
PWR	Pressurized water reactor
PyC	Pyrolytic carbon
RBMK	Reaktory Bolshoy Moshchnosti Kanalniy Reactor
RIA	Reactivity insertion accident
SBO	Station blackout
SE2	Secondary electrons mode
SEM	Scanning electron microscopy
SiC	Silicon carbide
SiC_f-SiC_m	SiC fibre reinforced SiC matrix composites
SNR	Signal-to-noise ratio
SOD	Stand-off-distance
TEM	Transmission electron microscopy
TO	Transverse optical phonon
TRISO	Tristructural-isotropic
UKAEA	United Kingdom Atomic Energy Authority
UO_2	Uranium oxide

UTS	Ultimate tensile stress
VVER	Vodo-Vodyanoi Energetichesky Reactor
XCT	X-ray computed microtomography
zircaloy	Zirconium-based alloys
μXCT	Micro X-ray computed micro-tomography

List of figures

List of tables

1. Introduction

Due to its excellent corrosion resistance, excellent mechanical performances and low neutron absorption cross-sections, the zirconium-based alloys (zircaloy) have been widely used as fuel cladding materials in light water nuclear reactors (LWRs) for decades. However, under extreme accident conditions (*e.g.*, design-basis accident (DBA) and loss of coolant accident (LOCA) conditions), the propensity of zircaloy to swiftly oxidize in high-temperature steam and consequently emit combustible hydrogen gas poses a potential risk for severe incidents akin to the 2011 Fukushima disaster [1]. Consequently, the concept of accident tolerant fuel (ATF) cladding has emerged with the objective of enhancing the safety efficacy of nuclear fuels in extreme events such as DBA and LOCA [2]–[5].

Based on the ATF concept, two main solutions has been raised for the cladding materials. The near-term solution involves the application of an oxidation-resistant coating on the outer surface of current zircaloy claddings. Among the array of coating materials available, Cr was widely chosen for its remarkable attributes, including excellent corrosion and oxidation resistance, high melting point and strength, and chemical compatibility with zircaloy [5]–[7]. Two methods are widely used for the application of Cr coatings on the zircaloy, including: cold spraying (CS) and physical vapor deposition (PVD) [1]. However, the different manufacturing processes of these two methods result in different microstructures and properties of the Cr coatings, which subsequently affect the mechanical behaviour and failure processes of the entire cladding system [1]. Additionally, for the same manufacturing method, the changes in manufacturing parameters could also affect the mechanical behaviour of the coating and the Cr-coated cladding system [8]. Therefore, for the future industrial application of these Cr-coated materials, it is crucial to conduct mechanical testing under both normal and abnormal service conditions. Such testing is essential for establishing a relationship between the microstructures and the mechanical performance of these material systems, thereby improving the design of these material.

The long-term solution is to totally replace the current zircaloy material by other materials [9]–[13]. Silicon carbide (SiC) fibre reinforced silicon carbide matrix composites (SiC_f-SiC_m) has been considered as a promising candidate cladding material due to its superior irradiation and oxidation resistance, good strength and toughness at elevated temperatures [14]. Such SiC_f-SiC_m materials have also been considered to serve as channel boxes. For such complex material system, their damage evolution and failure processes significantly rely on the existence and

variability of local microstructures as well as imperfections and defects. Therefore, for future applications, it is essential to conduct mechanical experiments on these materials under both normal and extreme service conditions. These experiments are crucial for understanding the materials' microstructural evolution and mechanical behaviour under various conditions, and thereby optimize the their design. Moreover, it is critical to employ novel techniques for capturing three-dimensional microstructural evolution in such materials in real-time [14].

The materials investigated in current PhD project involve various types of SiC_f-SiC_m claddings and Cr-coated zircaloy-4 claddings. A unique set-up was adopted which allows real-time X-ray microtomography imaging of the materials under mechanical testing at high temperatures. The microstructures, local properties and residual stresses of as-received materials were also characterized. Finally, the current project explored the establishment of a comprehensive link between the microstructures, local properties, residual stresses, and the mechanical properties and progressive failure processes in various types of SiC_f-SiC_m claddings and Cr-coated zircaloy-4 claddings at both ambient and high temperatures.

The current thesis consists of 9 Chapters. In Chapter 2, the manufacturing processes, microstructures, local properties, mechanical properties and failure processes at elevated temperatures of various types of SiC_f-SiC_m and Cr-coated zircaloy materials are reviewed. In Chapter 3, detailed information of tested materials, sample preparation procedures, experimental set-ups, and brief principles of the techniques involved in current PhD project are presented. Chapters 4 to 8 and result Chapters. In Chapter 4 and Chapter 5, the microstructures, local properties, residual stress distributions of two types of SiC_f-SiC_m cladding materials (one with single-layer outer/inner SiC coatings (Chapter 4); and one with multi-layers outer SiC coating (Chapter 5) are investigated by several techniques, with the aim of illuminating their mechanical behaviours and failure processes at room temperature (RT) and 1200°C. In Chapter 6, the microstructures and local properties of two types of Cr-coated zircaloy-4 cladding materials (with the Cr coatings manufactured by CS and PVD methods, respectively), to understand their potential influences on the mechanical behaviour, failure processes and coating crack patterns of materials at RT and 345°C. In Chapter 8, two types of Cr-coated zircaloy-4 cladding materials (the Cr coatings were produced by CS method with different manufacturing parameters) are studied; the relationship between microstructures, local properties, residual stresses in the coatings, and mechanical performance, failure processes and coating crack patterns at RT and 345°C are investigated. Finally, the general conclusions of current work are presented in Chapter 8 and future work is discussed in Chapter 9.

2. Literature review

2.1. Light water nuclear power reactor and zirconium alloy cladding

2.1.1. Light water reactor

Light water reactor (LWR) is the most common type of thermal-neutron reactor which uses normal water as its coolant and neutron moderator [15]. Among the 451 civilian nuclear power reactors in operation in the world, 372 of them are LWRs [16], [17]. In the LWR, the released thermal energy from the nuclear fission reaction of uranium oxide (UO_2) in the fuel rods is absorbed by the surrounding water (which cycles through the core) to produce steam. And the steam is subsequently employed to spin the turbine to generate electrical power [2], [17], [18]. There are two main types of LWRs, which including the boiling water reactor (BWR) and pressurized water reactor (PWR), as presented in Fig. 2.1.

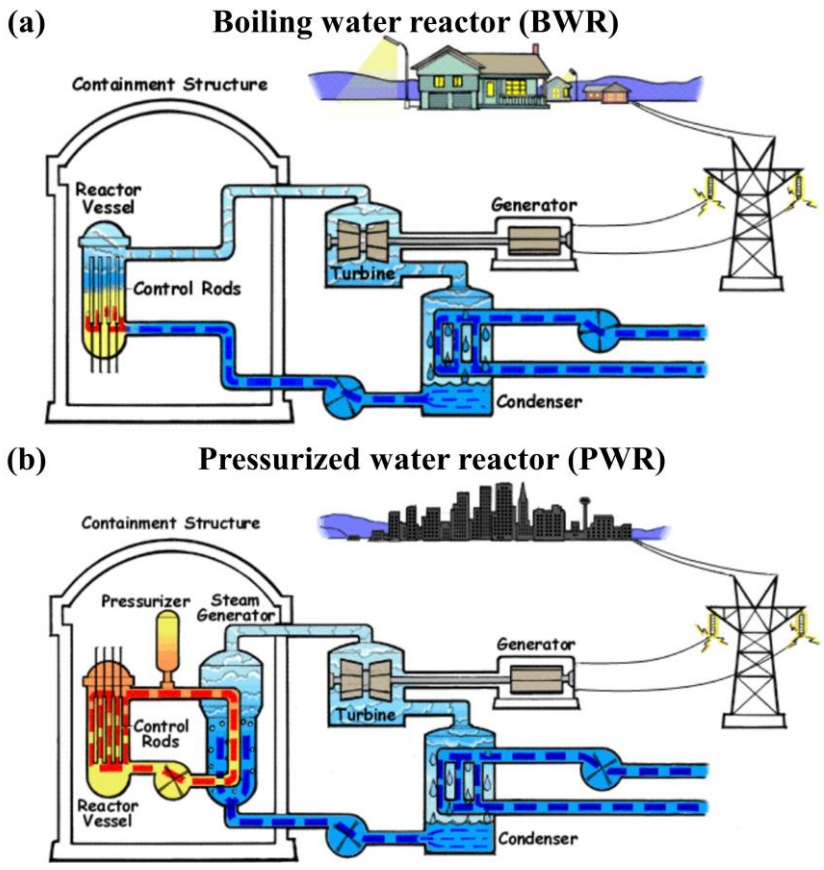

Figure 2-1. Schematics of (a) boiling water reactor (BWR) and (b) pressurized water reactor (PWR). Figure is reproduced from ref [19].

In BWR, the water is boiled in the vessel in that, the generated steam directly spins the turbine for generating electricity. The water within the circuit is ~275°C ~288°C at the inlet and outlet, respectively; with the pressure maintains at ~7.6 MPa in the circuit [17], [20]. As for the PWR,

unlike BWR, the water is maintained at a higher pressure (~16 MPa at 290°C to 330°C) in the primary circuit to prevent it from boiling. And the steam is generated in the secondary circuit (~285°C, with a pressure of ~7 MPa) to produce the power [20].

The core of the LWR is the fuel assemblies, and the schematic of a typical fuel assembly of PWR is presented in Fig. 2.2. The fuel assembly is about 4 m to 5 m in height, 20 cm in width and 0.5 t in weight. The top and bottom nozzles can provide mechanical support to the fuel rods and control rods in the PWR [21]. The typical structure of one fuel rod is presented in Fig. 2.2, where fuel pellets are assembled in the fuel tube. A gap (typically 200 to 400 μm) is designed between the fuel pellets and the inner surface of the cladding tube to facilitate the insertion of the pellets into the cladding [22], as well as compensate for the deformation fuel pellets during operation (*e.g.*, temperature- and irradiation- induced swelling) [23]. In general, the fuel cladding tube is of a length of ~4 m , ~9 mm of outer diameter and ~0.6 mm of wall-thickness [24]. To maintain the continuity of the nuclear chain reaction and facilitate the transfer of heat, the material of the cladding tube should possess several specific properties: high thermal conductivity, good resistance to corrosion, excellent irradiation resistance and low neutron absorption [25].

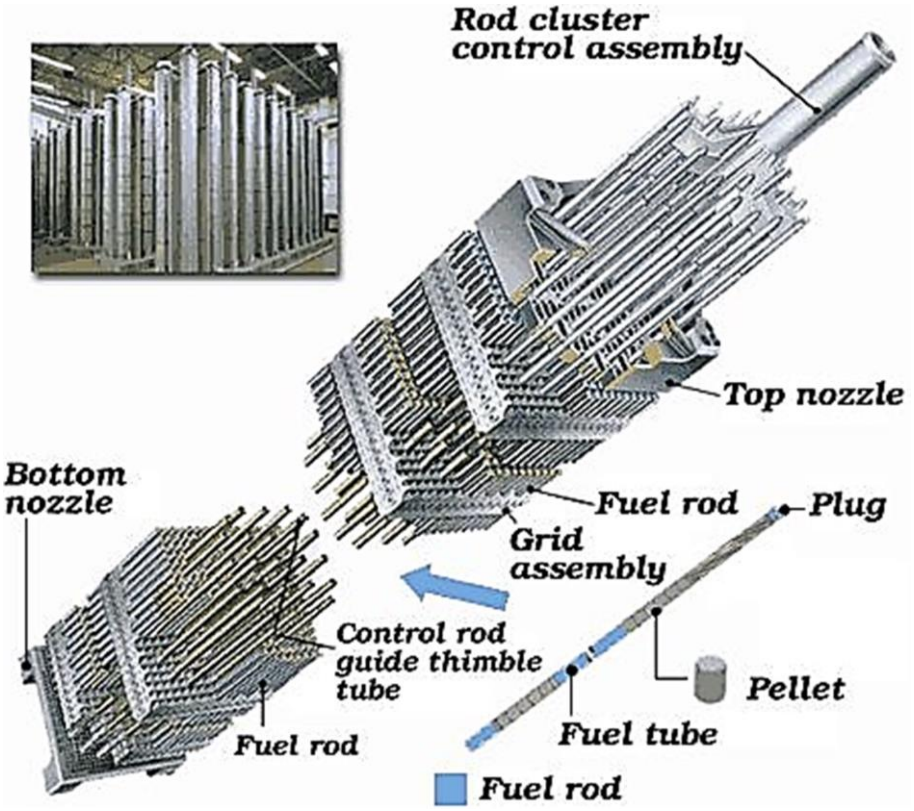

Figure 2-2. Schematics of typical fuel assembly and fuel rod in PWR. Figure is reproduced from ref [21].

2.1.2. Application Zirconium alloy cladding in LWRs

Due to its low neutron absorption, good corrosion resistance, excellent mechanical properties and high melting point (1852°C), zirconium-based alloys (zircaloy) have been utilized as fuel cladding materials in LWRs for decades [18], [20], [26]–[36].

The Zr element was first discovered by Kalproth in 1789, and the method of large-scale industrial production of Zr from Zr-containing ores was established by Kroll in 1944 [37]. Typically, Zr has a hexagonal close packed (HCP) structure (α-Zr) [17] at the temperature below 862°C, and changes to body centred cubic (BCC) structure (β-Zr) in the temperature range of 862°C to its melting point (1852°C). The development of Zr alloys as cladding material for the nuclear application started in the 1950s under the naval propulsion program in USA [38]. To overcome the detrimental effects of nitrogen (N) on the corrosion-resistance (especially under high temperature steam) of Zr, zircaloy-1 alloy was developed with 2.5% of the Sn [39]. To further enhance the corrosion-resistance, Fe, Cr and Ni was further added into zircaloy-1 and zircaloy-2 (Zr-1.5%Sn-0.2%Fe-0.1%Cr-0.05%Ni) was developed [39]; and the zircaloy-2 is still utilized in BWRs at present. However, the application of Ni could facilitate the formation of hydride in the zircaloy-2 at high temperatures and pressures, and limits its application in the PWRs, which have higher temperature and pressure than BWRs [39]. Consequently, for reducing the occurrence of hydride and further increasing the corrosion-resistance of zircaloy, zircaloy-4 was developed for PWRs with the removal of Ni, and the increasing of contents of Fe from 0.12% to 0.2% [39]. The zircaloy-2 and zircaloy-4 alloys have respectively became the standard cladding materials for BWRs and PWRs since 1970s [40], [41]. Additionally, to enhance the corrosion-resistance and manufacturability of zircaloy-2, three prototype zircaloys were designed, named zircaloy-3A, zircaloy-3B and zircaloy-3C. However, the strength of these three types of zircaloys was only 75% of the zircaloy-2 and they were not utilized in the nuclear reactors. In addition to the Zr-Sn alloy system developed by USA, the former Union of Soviet Socialist Republics developed the Zr-Nb alloy system [42], [43], with the successful application of three alloys (named E110, E125 and E635) in the Vodo-vodyanoi energetichesky reactors (VVER) and Reaktor bolshoy moshchnosti kanalniy reactors (RBMK). The chemical compositions of these zircaloy materials were summarized in Table 2.1.

Table 2-1. Chemical compositions (weights%) of various types of zircaloy materials. The data are compiled from ref [41].

Alloy	Sn	Fe	Cr	Nb	Other elements	Application
Zircaloy-1	2.5	-	-	-	-	Not suitable
Zircaloy-2	1.5	0.12	0.1	-	0.12 O, 0.05 Ni	BWR
Zircaloy-3A	0.25	0.25	-	-	-	Not suitable
Zircaloy-3B	0.5	0.4	-	-	-	Not suitable
Zircaloy-3C	0.5	0.2	-	-	0.2 Ni	Not suitable
Zircaloy-4	1.5	0.2	0.1	-	0.09 to 0.13 O	PWR
E110	-	-	-	0.95 to 1.05	≤0.10 O	PWR/RBMK/VVER
E110M	-	0.07 to 0.05	-	0.90 to 1.10	0.10 to 0.15 O	PWR/RBMK/VVER
E125	-	-	-	2.20 to 2.60	2.20 to 2.60 O	PWR/RBMK/VVER
E635	1.10 to 1.30	0.3 to 0.4	-	0.95 to 1.05	0.05 to 0.12 O	PWR/RBMK/VVER
ZIRLO	1.02	0.1	-	1.01	0.09 to 0.15 O	PWR
M5	-	0.05	0.015	1	0.09 to 0.13 O	PWR
AXIOM-X1	0.3	0.05	-	0.7 to 1	0.12 Cu, 0.2 V	PWR
AXIOM-X2	-	0.06	-	1	-	-
AXIOM-X4	-	0.06	0.25	1	0.08 Cu	-
AXIOM-X5	0.3	0.35	0.25	0.7	0.05 Ni	-
AXIOM-X5A	0.45	0.35	0.25	0.3	-	-

Since 1980s, to attain a elevated burnup, coolant temperature and the refueling interval of the PWRs were increased, and the ZIRLO (chemical composition: Zr-1.0%Sn-1.0%Nb-0.1%Fe) was subsequently designed by Sabol *et al*. in 1987 [44]. Compared with zircaloy-4, the ZIRLO possesses enhanced corrosion resistance, dimensional stability, creep resistance, and have been utilized as cladding material in almost all the reactors designed by Westinghouse in USA since 1990s [45]. Recently, an optimized ZIRLO (OPT ZIRLO) has been developed by Westinghouse [46], [47]. The enhanced corrosion resistance and creep resistance of OPT ZIRLO is achieved by the reduction amount of Sn from 1% to the range of 0.6% to 0.8%, in parallel to the optimizations in fabrication parameters and final annealing temperatures [46], [47]. Another optimized zircaloy material, named M5 (chemical composition: Zr-1.0%Nb-0.6%O), was developed since 1980s [48]. Compared with zircaloy-4, the absence of Sn and the

refined heat treatment parameters of the M5 alloy lead to its better creep resistance and relativity lower hydrogen pickups [49]. Until 2011, more than 4.5 million of M5 fuel claddings have been utilized in around 94 commercial PWRs [50]. AXIOM Zircaloy was also designed for high-duty PWRs since 2011 [51]. The chemical compositions of various types of zircaloy materials are listed in Table 2.1, and one schematic of the development history of cladding materials for LWRs is presented in Fig. 2.3.

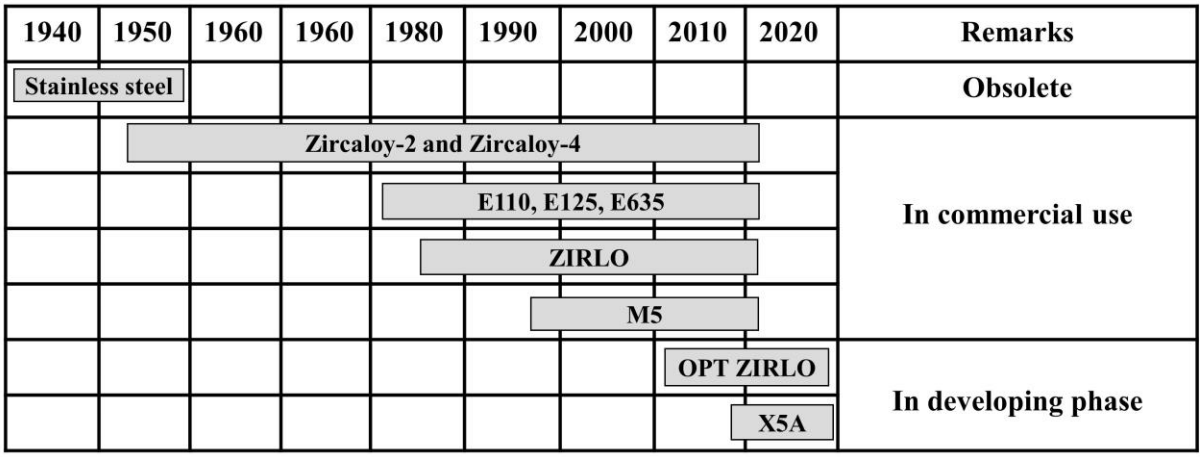

Figure 2-3. Schematic of history of the development of cladding materials in LWRs. Figure is reproduced from ref [52].

2.2. Overview of accident tolerant fuel claddings for LWRs

The concept of accident tolerant fuels (ATFs) has been proposed after the Fukushima-Daiichi accident happened in 2011 [18], [22], [29], [53], [54]. During such accident, the cooling water could not circulate within reactors, which led to the significant increase of temperatures in the reactors' core: rapidly raised to around 700°C - 900°C, far beyond the normal operating temperature: around 345°C [22], [55]. This type of accident is a typical station blackouts (SBO). Under such circumstances, the zircaloy claddings was exposed and reacted with the high temperature steam following Eq. 2.1.

$$Zr(s) + 2H_2O(l, v) \leftrightarrow ZrO_2(s) + 2H_2(g), \quad (2.1)$$

The release of combustible hydrogen (H_2) gas has caused serious explosions during the accident, resulting in the seriously damage of the steam turbine factories and surrounding facilities [56]. The heat generated during the reaction (Eq. 2.1) could also increase the temperature of the zircaloy cladding materials, which further facilitates the oxidation of zircaloy. Furthermore, due to their oxidation, zircaloy cladding materials experience a significant degradation of their strength and structural integrity. This results in a release of fuel pellets and fission products into surrounding water. The substantial hydrogen production in the

core leads to an increase in reactor's pressure, and the leakage and explosions of hydrogen led to serious damage of the reactor containment building, and eventually led to the escape of radioactive substances into the environment [57]. Therefore, the primary objective of the ATFs is to enhance the safety and performance of nuclear fuels and cladding materials when subjected to the normal operating conditions, anticipated operational occurrences (AOOs) conditions (*e.g.*, loss of offsite power and turbine trip) and serious off-normal operating conditions (*e.g.*, LOCA and RIA) [2]–[5]. Based on the ATFs' concept, the desirable properties of both the fuel pullet and fuel cladding for LWRs under normal operating (NO) condition, as well as under some typical serious off-normal conditions (including: LOCA, power ramps (PR), reactivity insertion accident (RIA), and SBO) are summarized in Table 2.2. The upward and downward arrows in Table 2.2 respectively represent for the increasing or decreasing magnitudes of a specific properties, and a dash signifies insensitivity to the properties [29]. It can be found, although specific higher or lower properties are required for the fuel cladding and pellet under different operating conditions, the oxidation resistance is consistently desirable in the fuel cladding.

Table 2-2. Desirable properties of fuel claddings and fuel pellets in LWRs under both normal operation (NO) conditions and some typical serious off-normal operating conditions: power ramps (PR), loss-of-coolant accident (LOCA), reactivity insertion accident (RIA), and station blackout (SBO). Upward and downward arrows respectively indicate that the increasing and decreasing magnitudes are desirable for a specific property, while a dash indicates insensitivity of a specific property. The data are compiled from ref [29].

	Fuel cladding					Fuel Pellet				
	NO	PR	LOCA	RIA	SBO	NO	PR	LOCA	RIA	SBO
Thermal conductivity	↑	↑	↑	–	–	↑	↑	↑	–	–
Heat capacity	–	–	↑	–	↑	–	–	↑	↓	↑
Oxidation rate	↓	↓	↓	↓	↓	–	–	↓	–	↓
Coefficient of thermal expansion	–	–	–	–	–	–	↓	–	↓	–
Creep rate	↑	↑	↓	–	↓	↑	↑	–	–	–
Strength	↑	↑	↑	↑	↑	–	↓	–	↓	–
Critical heat flux	↑	↑	–	↑	–	–	–	–	–	–

Strategies based on ATF concepts can be classified into three primary domains: improvements of the fuel pellets, enhancements of the cladding materials, and enhancements of non-fuel components (control rods and channel box) [58]. As for the cladding materials, the main objective is to delay or avoid the oxidation of current zircaloy materials under serious conditions, *e.g.*, design basis accident (DBA) and LOCA [2]–[5]. To achieve such objective, both the short-term and long-term solutions are under investigation [59], [60], and one schematic of these solutions is presented in Fig. 2.4. The short-term solution is the application of a protective thin coating on the surface of zircaloy claddings [61]. The coating materials should possess the potential abilities under normal and off-normal operation conditions: enhancing the cladding's heat transfer [62], maintaining good adhesion to the zircaloy substrate, enhancing the oxidation resistance of the cladding, and exhibiting good chemical stability with the zircaloy. Materials capable of the high-temperature resistance to steam oxidation include Cr_2O_3, Al_2O_3, and/or SiO_2. As such, the protective coating must encompass at least one element from the following set: Cr, Al, or Si [29]. Recently, investigations of the application of various types of coatings on zircaloy claddings have been carried out; these coating materials include: pure Cr [3]–[6], [63], CrAl [64], CrN [65], SiC [66], FeCrAl [67], TiAlN [68], AlCrN [69], $ZrSi_2$ [70] and MAX phases: $M_{n+1}AX_n$, n in the range of 1-4, M represents a transition metal, *e.g.*, Sc, Ti, Cr; A represents elements in the A-group, mainly IIIA and IVA, or groups 13 and 14; and X represents either C or N [71]. Among these potential materials for the coating, Cr is commonly selected due to its commendable corrosion and oxidation resistance, elevated melting point (1907°C), robust mechanical strength and the good chemical compatibility with zircaloy [5]–[7].

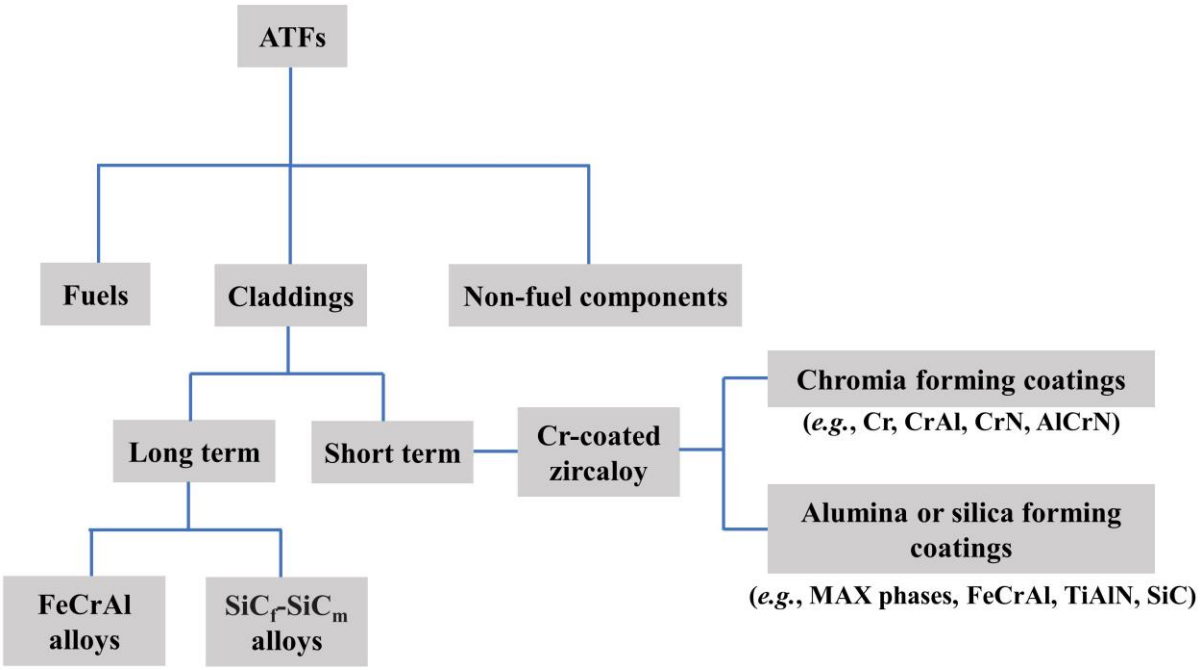

Figure 2-4. Schematics of the development of ATF cladding materials in LWRs. Figure is reproduced from ref [60].

The long-term solution involves the complete substitution of present zircaloy claddings with alternative materials, and the SiC fibre-reinforced SiC matrix composites (SiC_f-SiC_m) has been considered as a promising candidates [14] because of its exceptional tolerance to irradiation, elevated strength, remarkable toughness, and resistance to oxidation at elevated temperatures [9]–[13]. Additionally, FeCrAl alloys are also been considered as ATF claddings owing to its good strength, excellent creep-resistance and oxidation resistance under normal operating conditions [72]. However, the main challenges of FeCrAl alloy are its higher neutronic penalty and potential for increased tritium release [73].

As the nuclear-grade Cr-coated zircaloy and SiC_f-SiC_m cladding materials represent the subject of this thesis, the subsequent portion of the literature review section will be dedicated exclusively to describe the current comprehension of these two types of materials. For the Cr-coated zircaloy materials, thorough considerations will be devoted to the manufacturing methods of Cr coatings, microstructures and local properties of different types of Cr-coated zircaloy claddings, mechanical properties of the entire coated claddings, and coating crack patterns under mechanical loading. As for the SiC_f-SiC_m materials, considerations will focus on the microstructures, properties and processing methods of individual components within the composites and the mechanical performances of the entire composites. Such comprehensive literature review will facilitate identification of the research gaps in current literatures, this

further facilitates the selection of suitable experimental and characterization methodologies, the discussion of which will follow.

2.3. Cr-coated zircaloy cladding materials

Various deposition techniques have been employed for the application of Cr coating onto the Zircaloy substrate and these techniques can be categorized into three principal types: cold spraying (CS) method [4], [6], [67], [74]–[78], physical vapour deposition (PVD) method [79]–[85], and three-dimensional laser melt-coating (3D-LMC) method [86]–[88]. Among these methods, CS and PVD are currently widely utilized, their preparation processes and the characteristics of the prepared Cr coatings will be detailed discussed in the following sections.

2.3.1. CS Cr-coated zircaloy cladding materials

2.3.1.1. Intro to CS method

CS technique is a powder deposition method which evolves from conventional thermal spraying process [25]. One schematic of the CS process is presented in Fig. 2.5. During CS manufacturing process, powder particles are accelerated to attain high velocities at a relatively low temperature (0-800°C) [89], which is different to the thermal spraying method as particles are melted above their melting points. In the CS preparation process, coating materials' powder particles are firstly mixed with a preheated inert gas (either N_2 or He) under pressurized conditions within a spray gun. Subsequently, composite particle-gas streams are accelerated to high speed and impacted upon the surface of the substrate material at supersonic velocities (200 to 1200 m/s) by the gas jet (Fig. 2.5). The mechanism of solid deposition of the coating is actualized through high-strain-rate plastic deformation and the associated adiabatic shear processes that occur among the particles, and more importantly, between the particles and the surface of the substrate (Fig. 2.5). These eventually result in the mechanical interlocking and metallurgical bonding between the powder particles and the surface of the underlying substrate to form the coating [78].

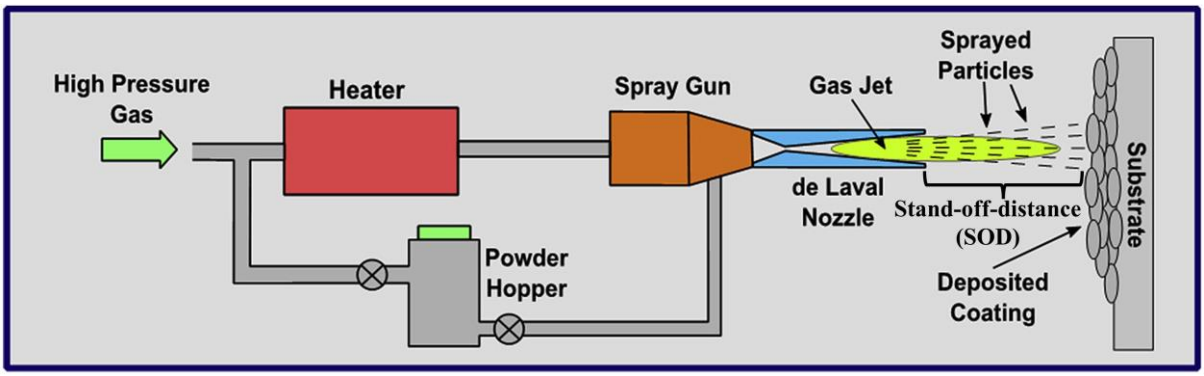

Figure 2-5. Schematics of the typical CS manufacturing process. Figure is reproduced from ref [4].

Such low deposition temperature leads to the advantages of CS method, as little to no oxidation, decomposition, evaporation and phase transformations of the powder particles happen during the deposition process [90]. Moreover, this prevents the extensive generation of oxide inclusions and phase separation within the coatings [90]. Additionally, the high deposition rate (more than 10 μm/min) of the CS technique enable its potential for the large-scale manufacturing, particularly for the production of full-sized coating on the surface of cladding tube [90]. However, the current CS technique also possesses several disadvantages, *e.g.*, the high deposition rate enhances the challenges of control of the coatings' quality; and the plastic deformation of underlying substrate during manufacturing process may affect its strength [4].

During the CS process, several main manufacturing parameters could affect the quality of the coating, as listed below. (i) The type of the high pressure gases: N_2 and He are two commonly used gases, and a higher velocity of the powder particles can be achieved when using He (as He is lighter than N_2); however, the higher cost of He (compared with N_2) limits its industrial application [8]. (ii) The feed rate of the powder particles (quantity of particles dispensed into the spray nozzle per unit time): a higher feed rate results in a lower velocity of the particles when impacting with the substrate, which could subsequently increase the residual stresses in the coating and in the coating/substrate interface due to shot peening effect [91]. (iii) Parameters of spray nozzle, which include the transverse speed of the nozzle and the distance between the nozzle and the substrate (stand-off-distance, SOD) [92]; generally, a higher transverse speed of the nozzle results in a higher velocity of the particles, and subsequently lead to the lower harness and lower residual stresses within the coating [93], [94]; as for the SOD, the velocity of the particles and the deposition efficiency (DE) firstly increase with the increasing of SOD, and then gradually reduce after reaching a critical value of SOD [95]. Parameters of powder particles (including size, composition, geometry and temperature of the particles): the lower sizes of the particles could enhance their critical adhesion velocity; and a

higher temperature of the particles reduce the critical adhesion velocity of the particles [96]. In summary, the influences of CS manufacturing parameters on the properties of the coating are summarized in Table 2.3.

Table 2-3. The influences of manufacturing parameters on the different properties of the coating during the CS process. Upward and downward arrows respectively indicate that the increasing and decreasing magnitudes with the increasing values of the parameters, while a dash indicates insensitivity of a specific property. The data are compiled from ref [97].

Parameters	Degree	Deposite strength	Adhension	Depositie efficiency	Porosity	Residual stress
Gas pressure	↑	↑	↑	↑	↓	↑
Gas temperature	↑	↑	↑	↑	↓	↑
Gas molecular weight	↑	↓	↓	↓	↑	↓
Particle velocity*	↑	↑	↑	↑	↑	↓
Powder feed rate	↑	↓	↓	↓	↑	↑
Stand-off-distance	↑	-	-	-	-	-

* Although an increase of the particle velocity enhances the adhesion deposit efficiency, new findings find that they could also decrease at very high velocity [98], [99].

2.3.1.2. Microstructures and local properties of CS Cr-coated zircaloy

The typical cross-sectional morphology of the one CS Cr-coated ZIRLO cladding materials are presented by scanning electron microscopy (SEM) images in Figs. 2.6a and 2.6b [100]. It can be found the coating/substrate interface is tortuous (Fig. 2.6a), which is attributed to the mechanical interlocking of the Cr and substrate at the interface during the CS manufacturing process [101], [102]. Some pores are observed in the coating, Fig. 2.6b; and splatted Cr grains can be commonly observed in the CS coating. The bright-field transmission electron microscopy (BF-TEM) images collected at the coating/substrate interface illustrates that, deformed and elongated Cr grains distribute in the coating close to the interface (Fig. 2.6c), with smaller grain sizes distribute in the Zircaloy substrate close to such interface, Fig. 2.6d [100]. It is suggested that these are most likely attributed to the plastic deformation occurring in the coating and underlying zircaloy substrate near the coating/substrate interface during manufacturing process of CS method [100]. Additionally, during the manufacturing process of cold spraying, the interdiffusion of Zr and Cr elements occur within a distance of around 40 nm to 200 nm, and subsequently resulting in the formation of a region with intermixed bonding region close to the interface [100]

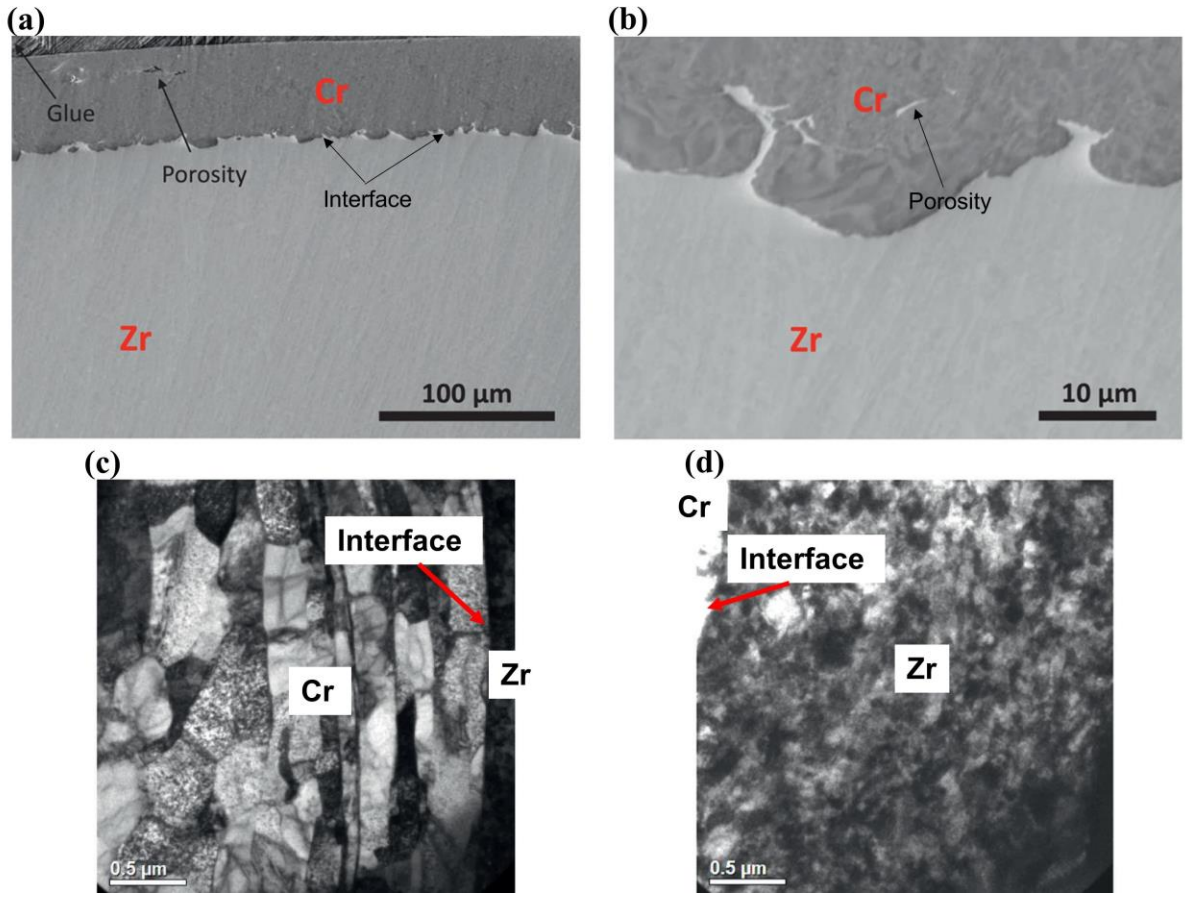

Figure 2-6. (a) and (b) are respectively low and high SEM images of cross-section of CS Cr-coated optimized ZIRLO cladding materials in as-received condition. (c) and (d) are BF-TEM images collected at the interface of CS Cr-coated optimized ZIRLO cladding materials with (c) in the coating side and (d) in the substrate side. Figure is reproduced from ref [100].

The plastic deformation incurred during cold spraying process may significantly influence local properties of both the coating and substrate at the interface region [1]. Thus, for a comprehensive understanding of the mechanical behaviour and overall structural integrity of CS Cr-coated Zircaloy claddings, it becomes essential to investigate the impact of the CS process on the underlying Zircaloy substrate [1]. However, limited literature exists focusing on this specific research domain. Recently (2021), Fazi *et al.* [100] conducted nanoindentation tests in the coating and substrate areas close to the coating/substrate interface of one CS Cr-coated optimized ZIRLO^{TM} material, with their results presented in Fig. 2.7. Although no exact elastic modulus and hardness were reported by them [100], the measured hardness values from the area in the middle of their coating was found ~27.8% higher than that measured in locations adjacent to the interface (in the coating but with a distance of 3 µm or less to the interface); and the measured hardness of underlying ZIRLO^{TM} substrate close to interface area (with a distance less than 5 µm to the interface) was ~40% higher than substrate away from the interface

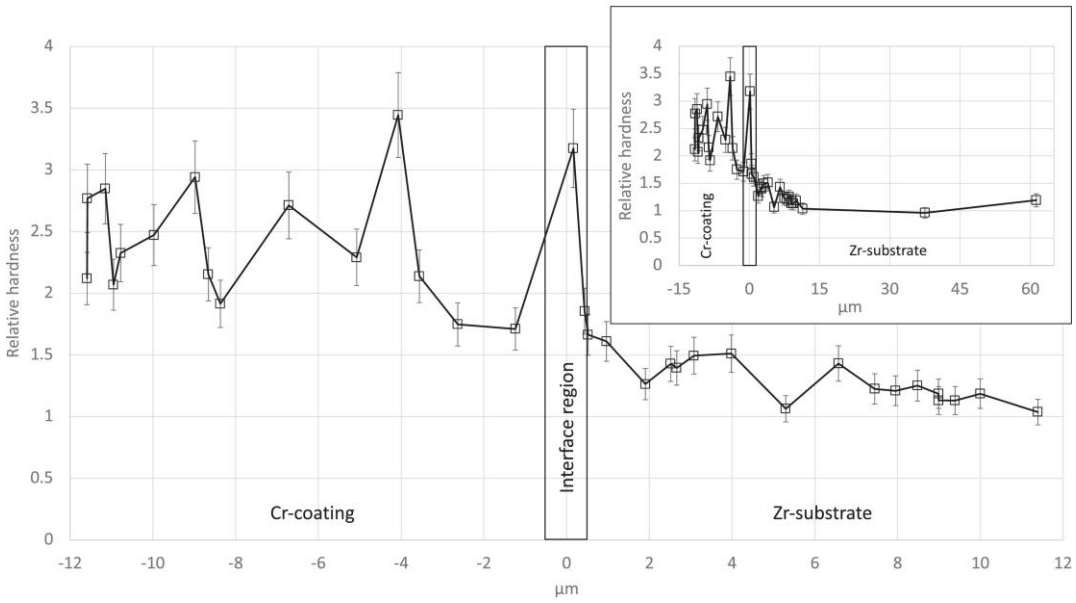

Figure 2-7. Nanoindentation measurements performed on the coating/substrate interface area in the polished cross-sections of a CS Cr-coated optimized ZIRLO^{TM} cladding material. Figure is reproduced from ref [100].

2.3.1.3. Mechanical behaviour and coating crack patterns of CS Cr-coated zircaloy

Before discussing the mechanical behaviour of the CS Cr-coated cladding materials, the directions and corresponding stresses in a cladding tube is presented in Fig. 2.8a.

Table 2.4 displays hoop strength (maximum hoop stress of the material under uniaxial loading in the hoop direction) of CS Cr-coated Zircaloy cladding materials with testing at RT and 315°C from open literatures. Shah *et al*. [103] investigated the mechanical properties of both CS Cr-coated (with a coating thickness of around 50 µm) and uncoated (selected as reference) OPT ZIRLO cladding tube materials at RT under tensile tests. Similar ultimate tensile stress (UTS) values were reported for the coated (~701 MPa) and uncoated materials (~715 MPa), and they suggested the application of CS Cr coating showed minor influences on the mechanical properties of the underlying ZIRLO substrate [103].

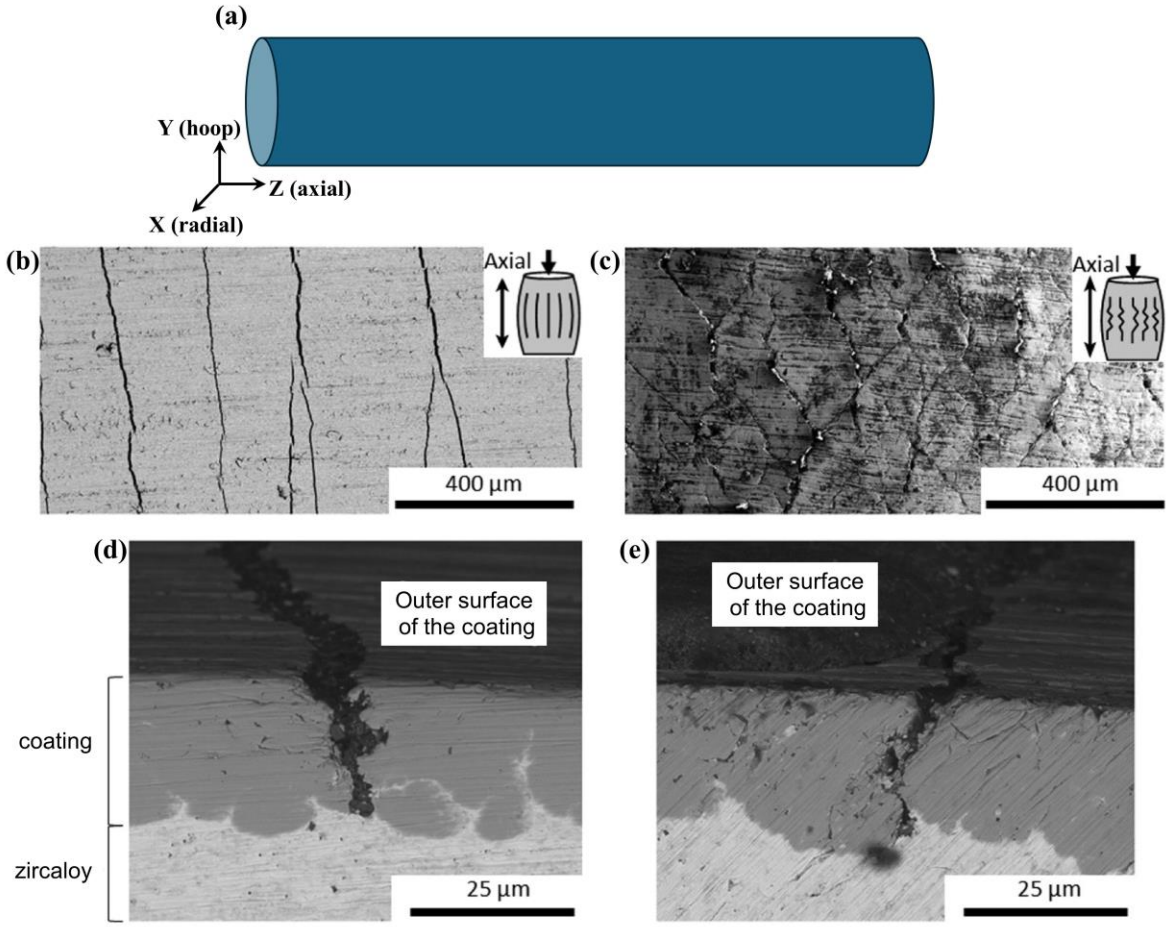

Figure 2-8. (a) shows the definition of directions and corresponding stresses in a cladding tube material. (b) and (c) are representative micrographs of coating surface fracture patterns acquired after (b) room temperature and (c) 315°C expanding plug testing of CS Cr-coated Zircaloy cladding materials. (d) and (e) are representative cross-sectional micrographs showing through-thickness cracks of samples tested at 315°C. Figure is reproduced from ref [103].

Table 2-4. Maximum hoop stresses of different types of CS Cr-coated zircaloy materials (detailed information of tested materials are included, extracting from corresponding literature in cited references); tested by plug-expansion and tensile tests at RT and 315°C.

Information of the tested materials	Testing method	Testing temperature (°C)	Maximum hoop stress (MPa)
Cladding tube samples with a length of 12.7 mm; and the rubber plug insert having a length of 6.35 mm; with a coating thickness of 35 to 45 µm and zircaloy-4 substrate. Ref. [104].	Plug-expansion	RT	700-800
Cladding tube materials with a coating thickness of ~50 µm, and OPT ZIRLO substrate. Ref. [103].	Tensile	RT	~701
Cladding tube samples with an inner diameter of ~9.6 mm; with a coating thickness of ~24 µm and zircaloy-4 substrate. Ref. [105].	Plug-expansion	RT	~1000
		315°C	~500

Roache *et al.* [105] recently (2022) conducted real-time plug-expansion tests at both RT and 315°C on their CS Cr-coated Zircaloy claddings with ~24 μm of the thickness of the coating. A reduction of the hoop strength was reported with the increasing of temperature: ~1000 MPa at RT and reduced by 50% (~500 MPa) at 315°C. They also conducted acoustic emissions (AE) and digital image correlation (DIC) methods to monitor the hoop strain at where coating cracks initiated, and such hoop strains were reported to be ~0.40% at room temperature and ~0.34% at 315°C. From their SEM imaging on the post-tested specimens, different coating crack patterns were reported at RT and 315°C, Fig. 2.8 [103]. At RT, coating cracks were mostly oriented at angles of ~85° to the axial direction, Fig. 2.8b; However, coating cracks were found more tortuous (oriented at angles of ~65° to ~75° to the axial direction) and finer in width Fig. 2.8c [105]. Based on their finite element analysis (FEA) calculation, tensile residual strains were estimated in axial (0.026%) and circumferential (0.031%) directions between the coating and the underlying substrate [103], respectively. This could generate a shear stress conducive to off-axis coating cracks and generate a multidimensional stress state within the CS Cr coating, and subsequently attributed to the formation of tortuous finer cracks in the Cr coating at 315°C [105]. Additionally, once cracks formed in the CS coating, they tended to deflect along the splatted grain boundaries and link up with the pores within the coating, and consequently formed tortuous crack pathways (in addition to a cleavage crack path) [105], [106], with representative examples presented in Figs. 2.8d and 2.8e.

In summary, the vast majority studies of coating crack behaviours rely on the *post-mortem* analyses, and they could not provide a comprehensive mechanical view of the initiation and progressive development of these cracks. Additionally, as discussed in Section 2.3.1.1, residual stresses could be introduced into Cr coatings during the CS manufacturing process and consequently influence the mechanical performance of the cladding system. However, very limited studies focus on the investigation of residual stress in the CS Cr coating.

2.3.2. PVD Cr-coated zircaloy cladding materials

2.3.2.1. Introduce to PVD method

PVD technique is commonly utilized to deposit thin films onto the substrate material and have widely been used in various industrial applications, *e.g.*, aerospace and chemical engineering [107]. During the PVD process, the surface of the target coating material is firstly vaporized into gaseous particles (including ionized particles, atoms or molecules) through a high energy source. Subsequently, the deposition of thin film coating onto the substrate is accomplished by

permitting these particles to move freely or by subjecting them to acceleration within an electric field [25]. The PVD methods can be divided into three types based on the excitation mechanisms for producing the coatings, which include sputtering-plating, evaporation-plating and ion-plating [25]. During the sputtering-plating process, the coating materials (target materials) serve as electrodes. The sputtered particles are produced through the bombardment of the target surface by high-energy plasma particles, accelerated by an electric field generated in argon gas. As for the evaporation-plating process, the target materials are firstly heated within a molten pool, and subsequently evaporated at elevated temperatures and eventually formed particles. The ion-plating process is a combination of evaporation-plating and sputtering-plating methods, which involves both evaporation and ionization of target materials in a low-pressure discharge [25]. The schematics of the sputtering-plating and evaporation-plating process are presented in Figs. 2.9a and 2.9b, respectively [108].

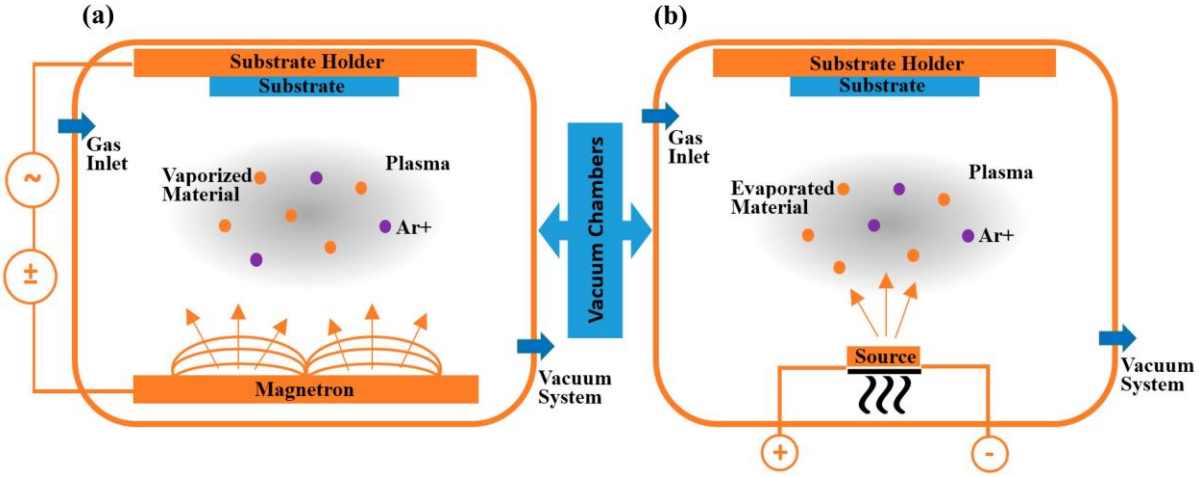

Figure 2-9. Schematics of the two typical PVD manufacturing processes: (a) sputtering-plating, and (b) evaporation-plating. Figure is reproduced from ref [108].

The PVD method possesses the two notable advantages: (i) the relatively low deposition temperature (less than 500°C, even can be achieved at room temperature), and (ii) the coating quality can be controlled through adjusting the flexible and controllable manufacturing parameters [109]. However, some certain limitations are associated with the PVD method: the line-of-sight deposition nature of the PVD process limits the deposition of coatings on complex 3D materials; additionally, the low deposition rate (typically 1 to 3 μm coating's thickness per hour) increases the cost of PVD method, especially when depositing thick coatings [107], [110], [111]. During the PVD process, the deposition rate and adhesion of the coating are significantly affected by the manufacturing parameters (*e.g.*, flow, pressure and temperature of

the gas, bias current and the geometry of the substrate) [108]; which subsequently affect the properties of the coating (*e.g.*, hardness, elastic modulus, thickness and microstructures).

2.3.2.2. Microstructures and local properties of PVD Cr-coated zircaloy

Typical cross-sectional morphology of the PVD Cr-coated zircaloy-4 cladding is presented by scanning electron microscopy (SEM) images in Fig. 2.10a [79]. Compared with the Cr coating produced by CS method, coating/substrate interface produced by PVD method is smooth as no mechanical interlocking between Cr and substrate occurred at the interface are during the PVD process. Electron backscattering diffraction (EBSD) map of PVD Cr coating indicates, Cr grains are mostly in the shape of columns, and smaller grains can be observed clustering close to interface region , Fig. 2.10b. Additionally, no obvious pores are observed within the PVD Cr coating, Fig. 2.10b. The Fig. 2.10c displays the TEM image collected at the PVD Cr/substrate interface. Compared with the materials produced by CS process, no discernible plastic deformation was evident (*e.g.*, elongation) of zircaloy substrate at the interface after the PVD process [1].

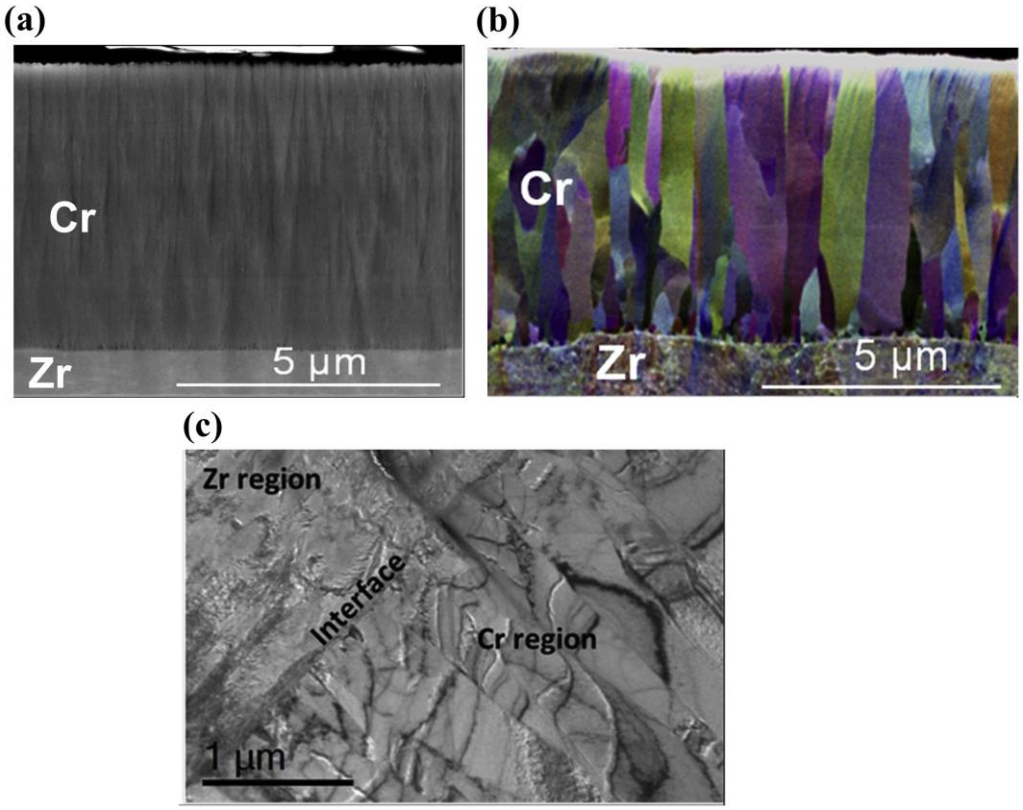

Figure 2-10. (a) SEM image of cross-section of PVD Cr-coated zircaloy-4 cladding material in as-received condition; (b) EBSD mapping on the coating shows columnar structured Cr grains with no obvious porosity; (c) TEM image collected at the coating/substrate interface. Figure is reproduced from ref [79].

The PVD process is reported showing little to no influence on local properties of the substrate, as modulus and hardness are widely reported to be of zircaloy close to the interface area (*e.g.*, ~2.7 GPa and ~113.4 GPa) and away from the interface (*e.g.*, ~2.6 GPa and ~109.2 GPa) [1]. As for the Cr coating close to the interface area (with 3 μm or less distance away from the interface), higher hardness values (in the range of 10% to 20% [1]) are commonly reported when compared with the middle of the coating; which could be mainly caused by the finer grains close to the interface area [79].

2.3.2.3. Mechanical behaviour and coating crack patterns of PVD Cr-coated zircaloy

The hoop strengths of PVD Cr-coated zircaloy cladding materials tested at increasing temperatures (up to 500°C) from open literature are summarized in Table 2.5.

Table 2-5. Maximum hoop stresses of different types of PVD Cr-coated zircaloy materials (detailed information of tested materials are included, extracting from corresponding literature in cited references); tested tensile and uniaxial tension tests at temperature up to 500°C.

Information of the tested materials	Testing method	Testing temperature (°C)	Maximum hoop stress (MPa)
1.2 mm in thickness, 4 mm in width and 17 mm long sheet specimen; zircaly-4 substrate; with 10 to 15 μm (in thickness) coating on both surfaces. Ref. [79]	Tensile	RT	~700
1.2 mm in thickness, 4 mm in width and 17 mm long sheet specimen; recrystallized zircaly-4 substrate; with 10 to 15 μm (in thickness) coating on both surfaces. Ref. [79]	Tensile	RT	~680
1.2 mm in thickness, 14 mm in width and 60 mm long sheet specimen; M5 substrate; with ~16 μm (in thickness) coating on both surfaces. Ref. [112]	Tensile	RT	~400
Cladding tube samples with ~4.18 mm of inner radius, ~4.75 mm of outer radius, 0.57 mm of wall thickness; 50 mm in gauge length; with 15 to 18 μm (in thickness) Cr coating on the outer surface, zircaloy-4 substrate. Ref. [112]	Uniaxial tension	RT	~1322
0.6 mm in thickness, 3 mm in width and 20 mm long sheet specimen; zircaloy substrate; with ~13 μm (in thickness) coating on both surfaces, zircaloy-4 substrate. Ref. [53]	Tensile	RT	~440
		250°C	~300
		300°C	~260
		350°C	~240
		400°C	~220
		450°C	~200
		470°C	~185
		500°C	~160

Brachet *et al*. [79] investigated the tensile properties of PVD Cr-coated (10 to 15 μm in coating thickness) zircaloy sheet samples at RT, with a un-coated materials as reference. Similar maximum hoop strength values were reported for Cr-coated (~680 MPa) and un-coated materials (~700 MPa), indicated the application of PVD Cr coating showed little influence on the tensile properties of the un-coated reference materials [79]. However, according to Kim *et al*. [113], application of Cr coating produced by PVD method, as well as subsequently initiation and propagation of coating cracks under loading showed notable influences on the mechanical performances of the cladding system. They performed room temperature ring-compression experiments performed on two kinds of PVD Cr-coated zircaloy samples with two Cr coating thicknesses (respectively about 8.3 μm and about 18.8 μm) and the un-coated reference materials, with representative curves are displayed in Fig. 2.11a. Note that, the application of even a relatively thin PVD Cr coating (~8.3 μm) yielded a discernible impact on the curve. Evident reductions in load can be observed when the displacement was over 6 mm, with the values of load drop increasing in proportion to the thickness of the PVD Cr coating [79]. It is suggested that cracks in the Cr coating served as pre-existing flaws and facilitated stress-concentration. These coating cracks subsequently propagated into the underlying substrate and consequently led to the failure of the entire cladding system. This failure manifests as the load drops happened in the load-displacement curve when compared to reference materials (uncoated materials) [79].

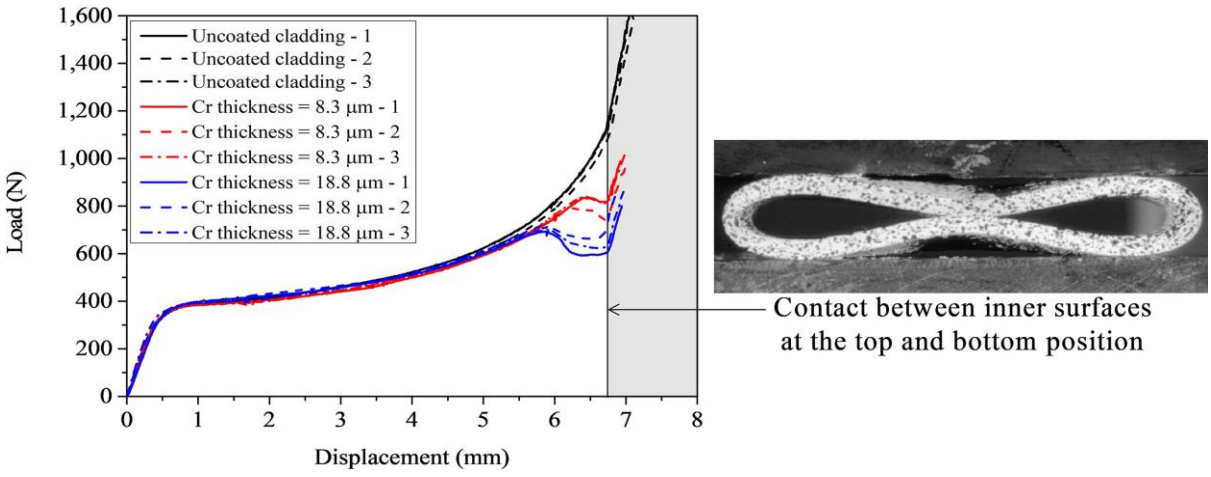

Figure 2-11. Load-displacement curves obtained from ring-compression tests of the un-coated and PVD Cr-coated zircaloy cladding materials at RT. Figure is reproduced from ref [79].

To monitor the initiation and progressive growth of coating cracks at elevated temperatures, some mechanical tests combined with real-time SEM imaging were carried out. For instance, Jiang *et al.* [53] recently (2021) carried out real-time tensile tests on PVD Cr-coated zircaloy claddings (around 13 μm of Cr coating thickness) sheet samples from room temperature to

500°C. The investigation revealed a substantial decreasing of the tensile strength, decreasing of about 60% as the temperature increased from RT to 500°C. Specifically, the tensile strength was approximately 430 MPa at RT and reduced to approximately 160 MPa at 500°C. The real-time SEM images indicated a decline in the density of saturated cracks as the temperature increased. At RT, the crack density was approximately 15 cracks per mm (the distance between cracks in the Cr coating was estimated to be ~66 μm); whereas at 450°C, the density was approximately 3 cracks per mm (the distance between cracks in the Cr coating was ~330 μm) [53].

Additionally, due to the different microstructures of PVD and CS coatings, the PVD coating crack behaviours were commonly reported to be different with that of CS coating [1]. For instance, compared with the tortuous crack pathways in the CS coating, cracks in PVD coating was reported to propagate preferably along the boundaries between the Cr grains, which resulted in a cleavage crack behaviours [14]. A representative example of cleavage behaviour of PVD coating cracks is presented in Fig. 2.12.

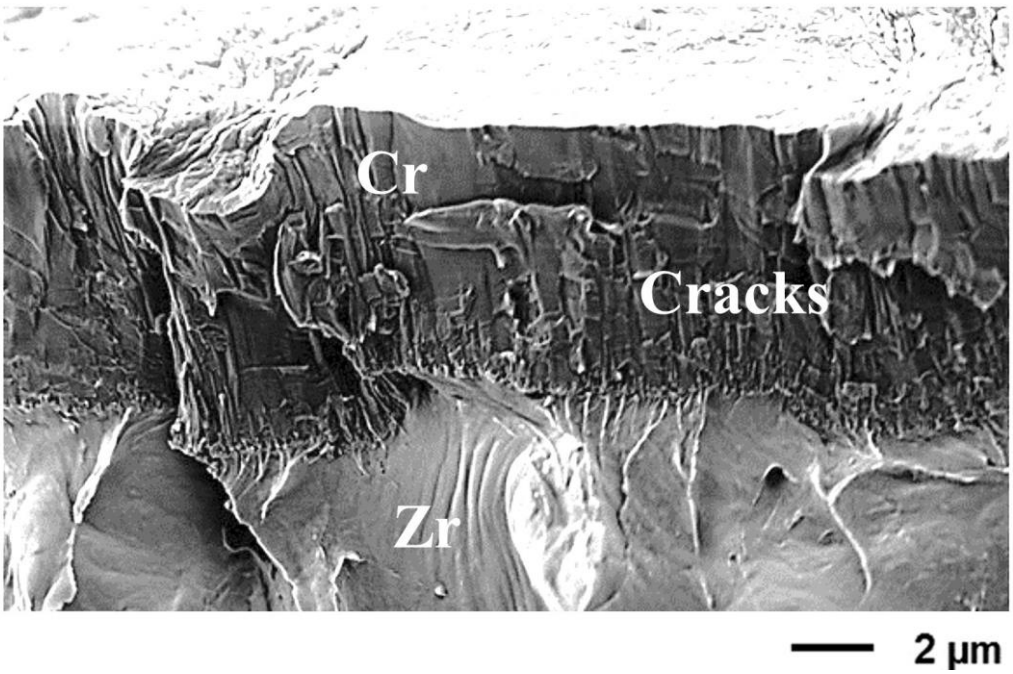

Figure 2-12. SEM images of the post-tested PVD Cr-coated zircaloy materials under RT tensile tests showing cleavage coating crack behaviour. Figure is reproduced from ref [79].

In summary, investigations of coating crack behaviours of PVD Cr-coated zircaloy cladding materials predominantly rely on the *post-mortem* analysis. Consequently, these could not offer a thorough mechanical view of the initiation and the cracks' growth in Cr coatings. And SEM images in the recent studies only present information on the cross-sections on the edge of the

tested samples, as well as on the surface of Cr coatings, without any information of the cracks in the coating.

2.4. Nuclear-grade SiC_f-SiC_m cladding materials

Generally, SiC possesses the following advantages, including high melting point (2730°C), low neutron absorption cross-section (0.08 barns), excellent irradiation tolerance and low thermal expansion (3.2-5.1 ppm/K) [114]–[116]. Additionally, at the typical operating temperature of LWRs (285°C to 350°C), it is reported that the β-SiC (in symmetric cubic structure) can maintain good elastic modulus and hardness (390 GPa and 21 GPa, respectively), low thermal expansion coefficient (4.12 ppm/K), high shear modulus (160 GPa) and good yield strength (400 MPa) after neutron irradiation in 1 dpa [117], [118]. These indicates SiC materials can potentially be utilized in nuclear applications, especially for fuel claddings in LWRs.

Nuclear-grade SiC fibre-reinforced SiC matrix composites (SiC_f-SiC_m) commonly consists of SiC fibres, SiC matrix, and interphase between the fibre and matrix [14]. For such SiC_f/SiC_m materials underloading, cracks are mostly propagated in the matrix; instead of broken the fibre, cracks tended to deflect along the weak interface of fibre/matrix, and commonly resulting in fibre pull-out [24]. These provide pseudo ductility of SiC_f/SiC_m materials and enhanced their fracture toughness [119]. The development of SiC_f-SiC_m for nuclear application can be traced back to the 1970s, when SiC fibres with high tensile strength and high elastic modulus were developed from polycarbosilane (PCS) by Yajima *et al.* [120]–[122]. In 1980s and 1990s, early research mainly focused on the optimization of the chemical components and enhancement of the irradiation-resistance of the SiC fibres [123]. In 2000s, significant progress was made in the development of SiC_f-SiC_m composites with enhanced mechanical properties and radiation resistance. For instance, Snead *et al.* [124] conducted four-points bending tests on their plain SiC_f-SiC_m (Hi-Nicalon™ fibre, matrix produced by chemical vapor infiltration (CVI) method, with porous SiC interphase). No significant reduction of the ultimate fracture stress (462 MPa) was reported for the tested materials after irradiation at 385°C of ~1.1 dpa when compared with the unirradiated ones (507 ± 75 MPa). Subsequently, the maintenance of mechanical properties of similar SiC_f-SiC_m materials were reported to extend to temperature up to 900°C [125] and irradiation dose up to 12 dpa [126]. After the 2011 Fukushima accident, SiC_f-SiC_m has been widely considered as a promising candidate ATF cladding material to replace the current Zircaloy cladding system in LWRs [14].

At LOCA conditions (with temperature up to 1000°C), compared with current zircaloy, it is reported that SiC_f-SiC_m materials can still maintain excellent corrosion resistance and oxidation

resistance, excellent chemical stability and low neutron absorption (25% lower than zircaloy) in both air and steam ambientes in a temperature up to 1600°C [18], [24]. For instance, after being exposed to steam at 1200°C for 4 hrs (without irradiation), the Zircaloy-4 was found to be completely oxidised and lost its structural integrity [127], Fig. 2.13a; however, no significant oxidation of SiC_f-SiC_m materials was found after exposure to steam at 1200°C up to 110 hrs [127], Fig. 2.13a. Furthermore, early studies reported SiC_f-SiC_m materials (reinforced with different types of fibres) can maintain more than 60% of the room temperature tensile strength at elevated temperatures (in air) up to 1400°C, Fig. 2.13b [41]. In contrast, the zircaloy materials experience a significant reduction of strength even below 500°C, Fig. 2.13b [41]. These observations again indicate the future industrial application of SiC_f-SiC_m materials as ATF claddings in LWRs. Indeed, several research studies have been conducted on the SiC_f-SiC_m materials and yielded promising results [119], [128]–[132].

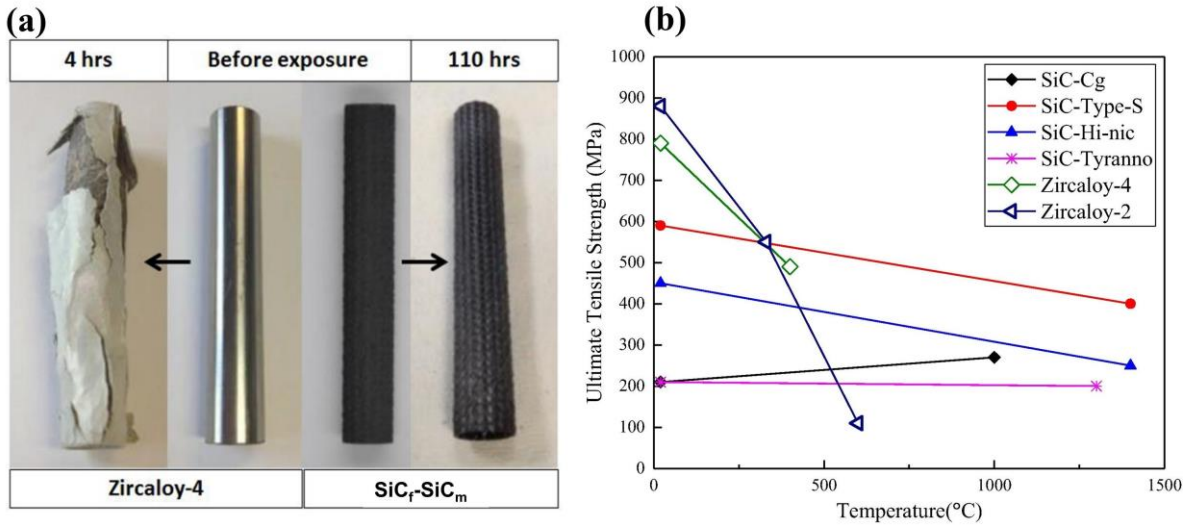

Figure 2-13. (a) Comparison of zircaloy-4 and SiC_f-SiC_m claddings after exposed to steam at 1200°C for 4 hrs and 110 hrs, respectively [127]; (b) ultimate tensile strength (maximum tensile stress that material can withstand before fracture) of several types of zircaloy materials and SiC_f-SiC_m materials as a function of testing temperatures [41]. Figure is reproduced from ref [133].

Before discussing the physical and mechanical properties of various types of SiC_f-SiC_m materials, it is important to introduce the individual components in SiC_f-SiC_m materials as they affect the properties of the entire composite materials [14]. Brief introduction of types and properties of fibres (Section 2.4.1), matrix (Section 2.4.3), interphase (Section 2.4.4), architecture of fibres (Section 2.4.2), as well as their influences on the entire composite materials are presented in the following sections.

2.4.1. Types and properties of SiC fibres

The continuous SiC fibres investigated by Yajima *et al.* [120]–[122] in 1975 is considered to be the first generation SiC fibre, and currently various types of third generation SiC fibres have been investigated and achieved commercialization [134]. For the nuclear-grade SiC fibres, the most commonly manufacturing method is precursor polymer pyrolysis, where PCS is used as precursor [121]. The development of the fabrication process of three generations of SiC fibres are summarized in Fig. 2.14, with the detailed properties and chemical compositions of them tabulated in Table 2.6. It can be observed that, with the development of the fibres, the tendency is to fabricate near-stoichiometric (atomic Si:C ratio ≈1:1) SiC fibres, as well as reduce the content of oxygen. Such improvements consequently enhance the oxidation resistance, irradiation resistance, corrosion resistance and the mechanical properties of the fibres [134]. Among these fibres, only the third generation of SiC fibres (*e.g.*, Hi-Nicalon Type-S, Tyranno SA and Sylramic-iBN) can be classified into nuclear-grade fibres, due to their high purity and crystallinity.

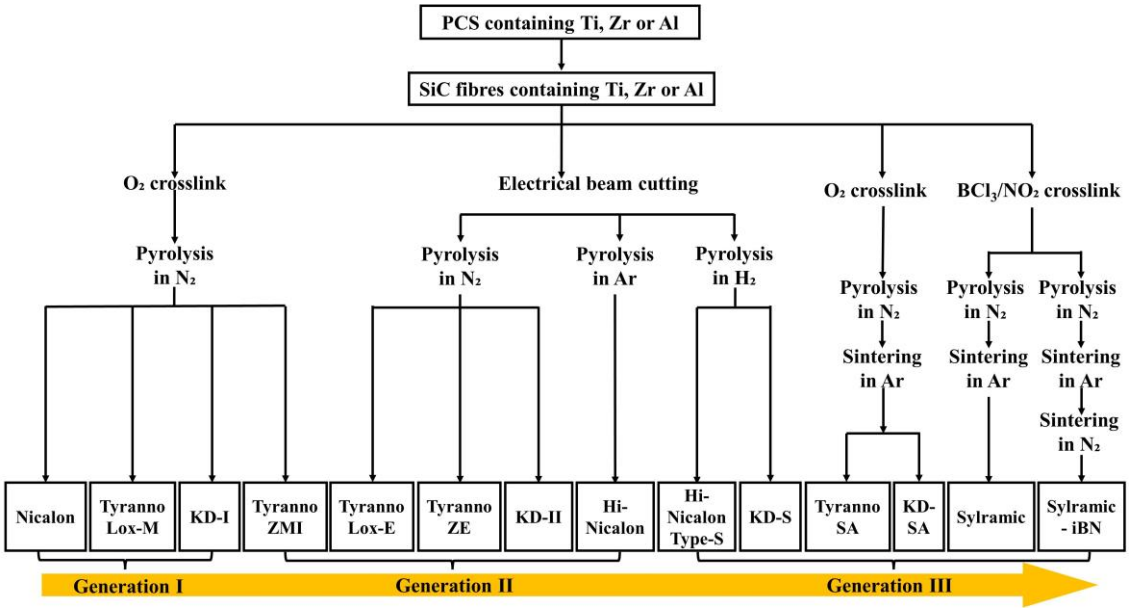

Figure 2-14. Development of the fabrication processes of three generations of commercial SiC fibres. Figure is reproduced from ref [133].

Table 2-6. Properties and chemical compositions of three generations of commercial SiC fibres.

Generation	Name	Diameter (μm)	Elements	Grain size (nm)	C/Si ratio	Tensile strength (GPa)	Elastic modulus (GPa)
1st Ref. [135]	Nicalon	14	Si, C, O	2-3	1.33	3	200-220
	Tyranno Lox-M	11	Si, C, O, Ti	1-2	1.38	3.3	185
	KD-I	11-14	Si, C, O	10	1.29	> 2.5	> 170
2nd Ref. [135]	Hi-Nicalon	14	Si, C, O	5-10	1.38	2.8	270
	Tyranno Lox-E	11	Si, C, O, Ti	-	1.59	2.9	199
	Tyranno ZMI	11	Si, C, O, Zr	2	1.41	3.4	200
	Tyranno ZE	11	Si, C, O, Zr	-	1.54	3.5	233
	KD-II	10-12	Si, C, O	8	1.35	> 2.7	267-293
3rd Ref. [134]	Hi-Nicalon Type-S	12	Si, C, O	12	1.02	2.6	420
	Tyranno SA	7.5-11	Si, C, O, Al	7.5-11	1.1	2.8	375
	Sylramic	10	Si, C, O, B, N, Ti	10	1.01	3.2	~400
	Sylramic-iBN	10	Si, C, O, B, N, Ti	10	1.01	3.1	~400
	Super Sylramic-iBN	10	Si, C, O, B, N, Ti	10	1.01	3	~400
	KD-S	11	Si, C, O	11	1.1	2.7	310
	KD-SA	10.5	Si, C, O, Al	10.5	1.05	2.5	380

Among these third generation SiC fibres, Tyranno SA3 (Ube Industries Ltd, Japan) and Hi-Nicalon™ Type S fibres (NGS Advanced Fibers Co., Ltd, Japan) [136]–[138] are commonly used in manufacturing the SiC_f-SiC_m materials. Both types of fibres consist primarily of near-stoichiometric and nano-polycrystalline β-SiC, they additionally encompass minute quantities of residual oxygen and carbon, existing in the form of SiO2 and SiOC, both on surface of the SiC fibre and throughout SiC fibre [139], [140]. The Hi-Nicalon™ Type S fibres have excellent oxidation-resistance, and they can still maintain a tensile strength of 1.8 GPa (70% of the room temperature tensile strength) after exposed to dry air for 10 hrs at 1200°C [141]. However, as the sintered temperature of Hi-Nicalon™ Type S fibres is 1500°C, after being exposed above such temperature, the SiC grains could grow rapidly and eventually lead to the loss of structural integrity of the fibre, Fig. 2.15 [134]. As for the Tyranno SA3 fibres, with the additionally Al content, as well as a higher sintered temperature (over 1800°C), they can maintain a tensile strength of 2.2 GPa (80% of the tensile strength at RT) after heated in argon for 1 h at 2000°C (Fig. 2.15 [134]), and maintain the room temperature strength after exposed to dry air for 100 hrs at 1000°C [142]–[144]. All these fibres were exposed to steam, without irradiation.

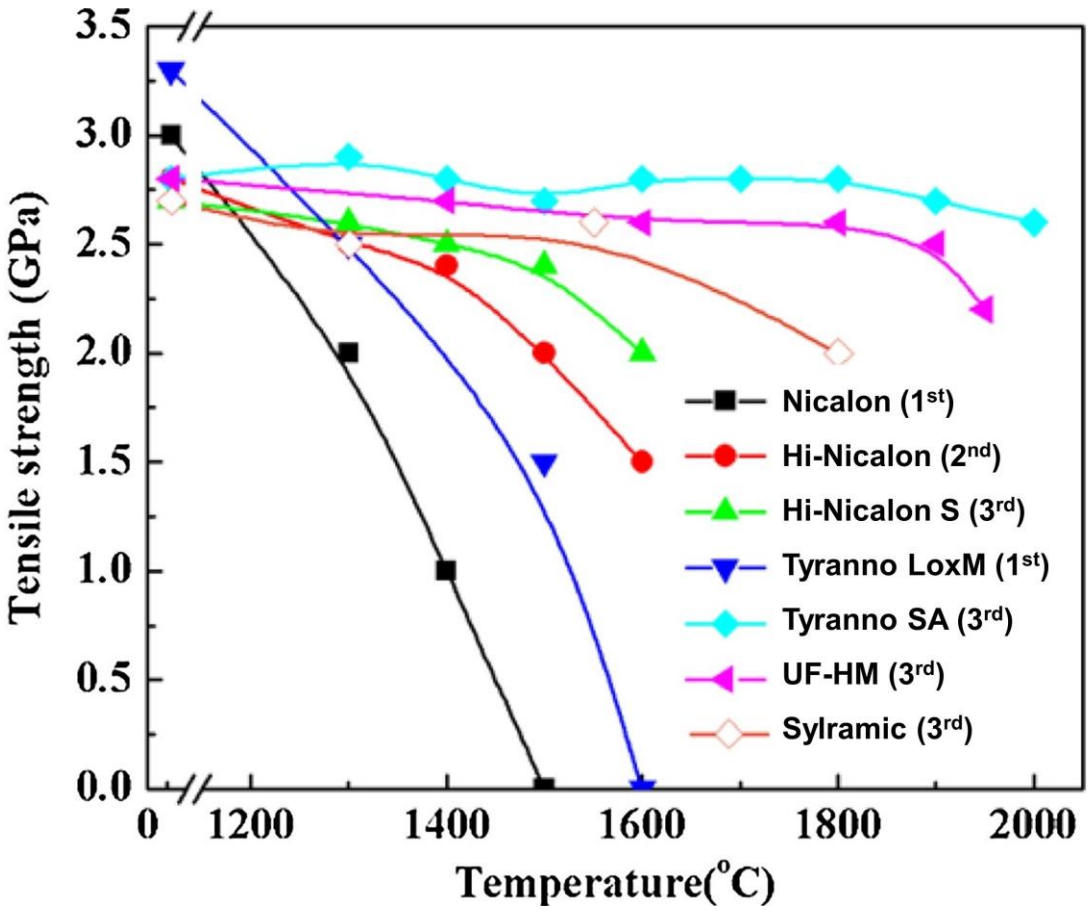

Figure 2-15. Heat-resistance of the three generations SiC fibres (after heat-treatment in argon for 1 h) [142]–[144]. Figure is reproduced from ref [134].

2.4.2. Architecture of SiC fibres

The overall SiC_f-SiC_m materials' properties (*e.g.*, tensile strength and conductivity in multiple directions [133]) are widely reported to be determined by the architecture of SiC fibres, including the fibre braiding angles, fibre braiding patterns and the volume fraction of fibres in the composites [145]. Therefore, to optimize the properties of SiC_f-SiC_m materials for future industrial application, many research studies have been conducted on the design of fibres' architecture [146], [147].

To strengthen the nuclear-grade SiC_f-SiC_m materials in both the transverse (x direction) and longitudinal (y direction) directions (as defined in Fig. 2.16), there are four common types of fibre architectures: (i) one-dimensional (1D) filament winding, Fig. 2.16a; two-dimensional (2D) braiding which typically takes the form of woven fabrics, Fig. 2.16b; 2.5D braiding patterns with cross weaving through the woven fabrics and three-dimensional (3D) orthogonal braiding, Fig. 2.16c. Among these architectures, the 2D and 3D braiding patterns have gained popularity due to their remarkable conformability and damage resistance [148]. Additionally, the 3D braiding patterns are produced by intertwining or orthogonally interlacing yarns to form an integrated structure; such approach provides through-thickness reinforcement while simultaneously offering adaptability to an extensive array of complex geometry. Generally, it is reported that the flexural and tensile strengths of SiC_f-SiC_m materials follow the trend: 3D>2.5D>2D [148], [149].

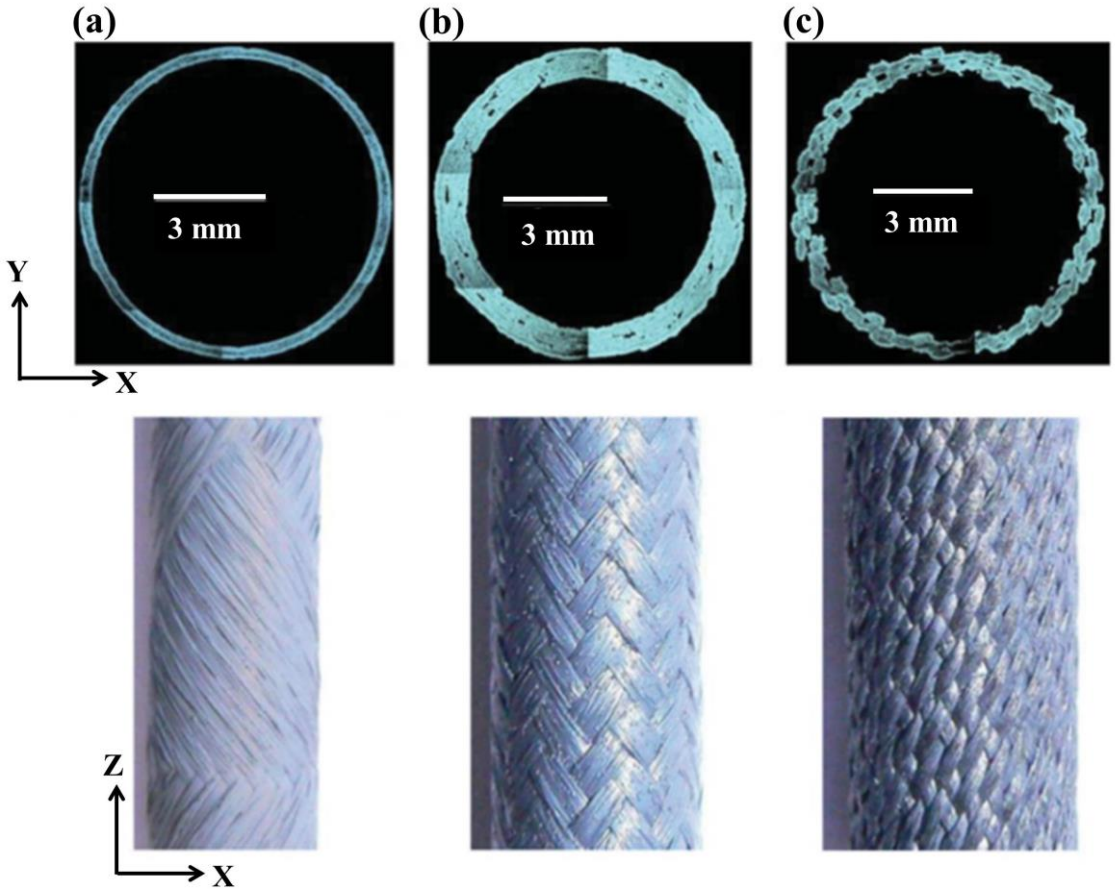

Figure 2-16. Examples of the architecture of fibres of nuclear-grade SiC_f-SiC_m cladding materials: (a) filament winding, (b) 2D braiding, and (c) 3D braiding. Figure is reproduced from ref [148].

The above fibre braiding patterns are widely reported to show significant influences on the fibre volume fraction, and size and distribution of pores of the SiC_f-SiC_m materials, and consequently show influence on mechanical and thermal properties of cladding system. It is suggested that for the SiC_f-SiC_m tube materials in a filament winding of fibres, if the fiber bundles are more parallel to the tube's axis, under loading to failure a higher tensile strength can be achieved with a reduction of strain at RT, Fig. 2.17a [148]. Additionally, for the 2D-plain weave SiC_f-SiC_m materials, a [0°/90°] braiding pattern of fibre bundles could enhance the materials' tensile strength at elevated temperatures up to 1300°C, Fig. 2.17b [146].

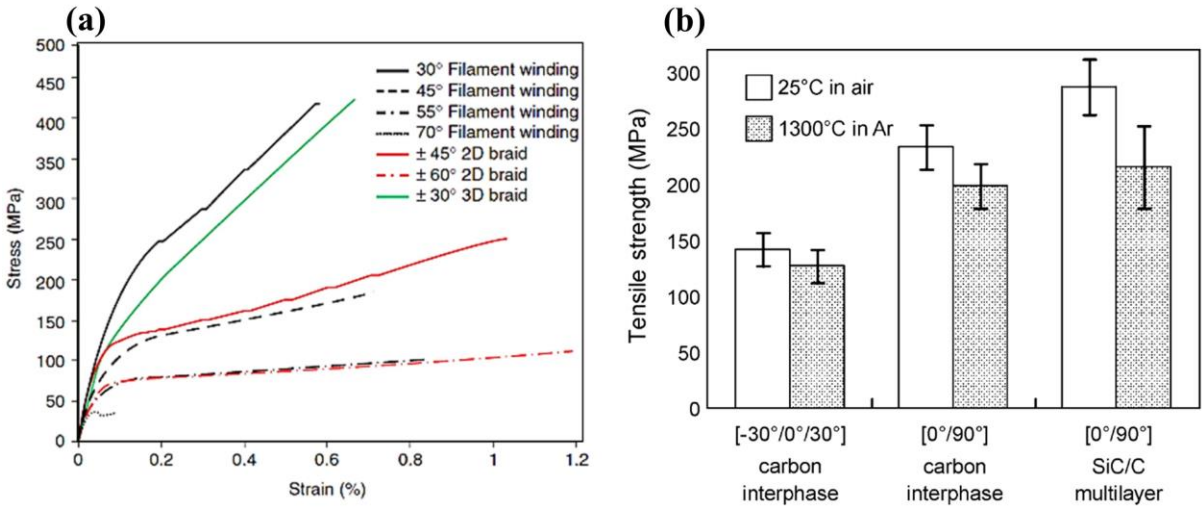

Figure 2-17. Influence of fibre architectures on the tensile strength of SiC_f-SiC_m materials: (a) for filament winding and 2D braiding of fibre bundles at RT [148], and (b) for 2D braiding of fibre bundles at RT in air and 1300°C in argon atmosphere [146]. Figure is reproduced from ref [133].

2.4.3. Interphase

Prior to the densification process of the matrix, an interphase is deposited on the surface of the SiC fibres [133]. Once cracks formed in the matrix, the interphase between matrix/fibre is expected to deflect the tips of matrix cracks through debonding and interfacial sliding without breaking the fibres; and the subsequently occurrence of fibre pull-out consequently enhance the strength and toughness of the entire SiC_f-SiC_m materials [131]. The interphase materials should possess the following abilities: irradiation-resistance, adequate bonding strength and interfacial sliding strength [117]. Among the various types of interphase (*e.g.*, pyrolytic carbon (PyC), SiC, PyC/SiC multi-layers, boron nitride (BN) and BN/SiC multi-layers), PyC interphase is widely used in nuclear-grade SiC_f-SiC_m materials [117]. The manufacturing process of PyC interphase and its influences on the entire SiC_f-SiC_m materials are discussed below.

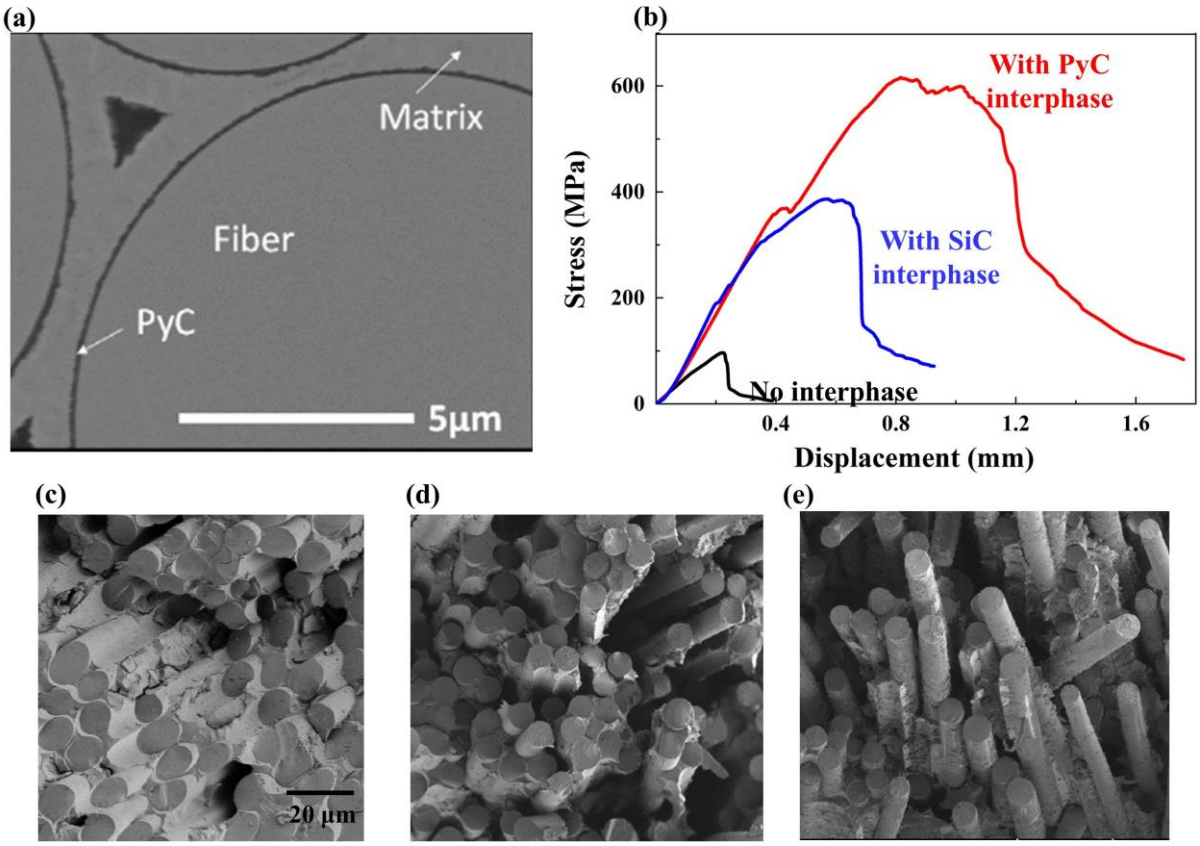

Figure 2-18. (a) SEM image of the typical microstructure of polished cross-section of SiC_f-SiC_m material showing PyC interphase, fibre and matrix [13]; (b) typical RT flexural stress-displacement curves of several SiC_f-SiC_m materials, including: the one with PyC interphase, the one with SiC interphase and the one with no interphase [150]. (c) to (e) are fracture surfaces of the above SiC_f-SiC_m materials, with (c) for the material without interphase, (d) for the material with SiC interphase and (e) for the material with PyC interphase. Figure is reproduced from refs [13], [150].

PyC interphases are commonly deposited by CVI (chemical vapour infiltration) method from the hydrocarbon precursors, including: methane (CH_4), propylene (C_3H_6), and ethylene (C_2H_4); at the temperature range of 900°C to 1200°C [151]. Generally, PyC can be regarded as a composite assembly comprising numerous discrete graphitic subdomains, which exhibit distinct orientations or textures in relation to the fibres [152]. One typical microstructure of the PyC interphase between fibre/matrix is presented in Fig. 2.18a. It has been widely reported that the application of PyC interphase can significantly affect the mechanical properties of SiC_f-SiC_m materials [150]. For instance, Hou *et al.* [150] conducted room temperature three-points bending tests on various types of SiC_f-SiC_m materials (including the one with PyC interphase, the one with SiC interphase and the one with no interphase). It can be found, the application of PyC interphase significantly enhances the flexural strength of the overall SiC_f-SiC_m materials (around 600 MPa) when compared with the materials with SiC interphase (around 400 MPa) and materials with no interphase (around 100 MPa), Fig. 2.18b. Without interphase, SiC_f-SiC_m materials mostly exhibit a brittle failure mode, representing by the large load drop when

reaching peak load (Fig. 2.18b). And no fibre pull-out was observed, Fig. 2.18c. In contrast, the materials with SiC interface and PyC interphase have enhanced resistance to sudden brittle failure, Fig. 2.18b. Fibre pull-out was commonly observed for these two types of materials (Figs. 2.18d and 2.18e), which facilitate crack energy dissipation, and thereby enhance the material's ductility.

Moreover, it has been widely reported that the thickness of PyC interphase could affect the mechanical properties of SiC_f-SiC_m materials, and the thicknesses of the PyC interphase are reported to be in the range of 25 to 1000 nm [114], [117], [138], [153]–[155]. It is suggested by Katoh *et al.* [154] that the application of PyC interphases (in a thickness in the range of 50 nm to 300 nm) did not show significant influences on the tensile strength of their SiC_f-SiC_m materials (Tyranno-SA fibre with [0°/90°] braiding angles to the tube axis, reinforced with CVI matrix) at RT [154]. However, Katoh *et al.* [138] also pointed out that if the thickness of PyC interphase exceeding 300 nm, it could result in the insufficient load transfer between matrix and fibre, and consequently reduces the tensile strength of the entire SiC_f-SiC_m materials. Additionally, if the PyC interphase is too thin (*e.g.*, below 50 nm in thickness), it will result in a relatively low interfacial shear strength and stiffness; which could subsequently cause excessive frictional stress at the fibre/matrix interface and finally results in the brittle failure of the entire SiC_f-SiC_m materials [138], [154].

2.4.4. SiC matrix

Several methods have been developed to produce SiC matrix and densify the SiC_f-SiC_m materials, including: CVI, nano-infiltrated transient eutectic phase process (NITE), polymer infiltration pyrolysis (PIP) and melt-infiltration (MI), and liquid silicon infiltration (LSI) [133]. Among these methods, CVI and NITE methods have been proved to provide high-crystallinity, high-purity and good oxidation resistance SiC matrix, and thus have been widely used in the manufacturing of SiC_f-SiC_m materials [117]. The manufacturing processes of these two methods and the SiC matrix produced by them are discussed below.

2.4.4.1. CVI SiC matrix

Currently, CVI process is reported to be the most reliable method for manufacturing high-purity and crystalline SiC matrix of the SiC_f-SiC_m materials [138]. Additionally, the processing temperature of CVI method is relatively low (around 1000°C), which do not show significant influences on the braiding fibres [156]. The investigation of CVI process is currently mature and such process can be divided into 7 steps, as presented in Fig. 2.19 [157]. Methyltrichlorosilane (MTS) is widely selected as the precursor, as it has stoichiometric atomic

ratio (Si:C=1:1), which subsequently facilitate the formation of stoichiometric SiC matrix [133]. During the CVI process, MTS precursors firstly diffuse to the boundary layer and into the pores within the fabric preform, and subsequently being absorbed onto the pores at the inner surface. Then, these precursors react with the H_2 on the surface and form SiC, with the by-products (hydrogen chloride, HCl) being desorbed from the surface. Finally, these by-products diffuse throughout the pore and subsequently through the boundary layer, Fig. 2.19. Note that, the diffusion of MTS and the transportation of resultant by-product (HCl) are regulated through mass-transfer, as marked in yellow in Fig. 2.19; and the surface absorption and subsequent chemical reactions area regulated by kinetics, marked in purple in Fig. 2.19.

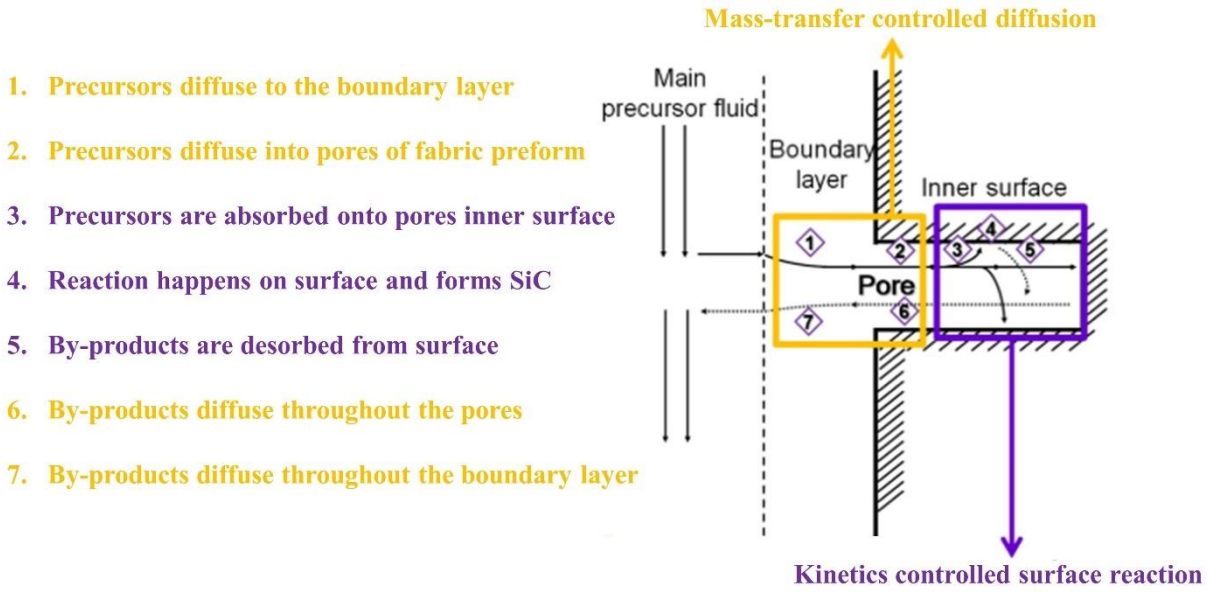

Figure 2-19. Schematic of the 7-steps CVI process when producing the SiC matrix of the SiC_f-SiC_m materials. Figure is reproduced from ref [157].

One main limitation of the CVI-densified SiC_f-SiC_m materials is the high level of porosity. Two types of the pores can be found in the SiC_f-SiC_m material, including: macropores locates at fibre bundles' crossovers, as marked Fig. 2.20; micropores locates in the SiC fibre bundles, Fig. 2.20.

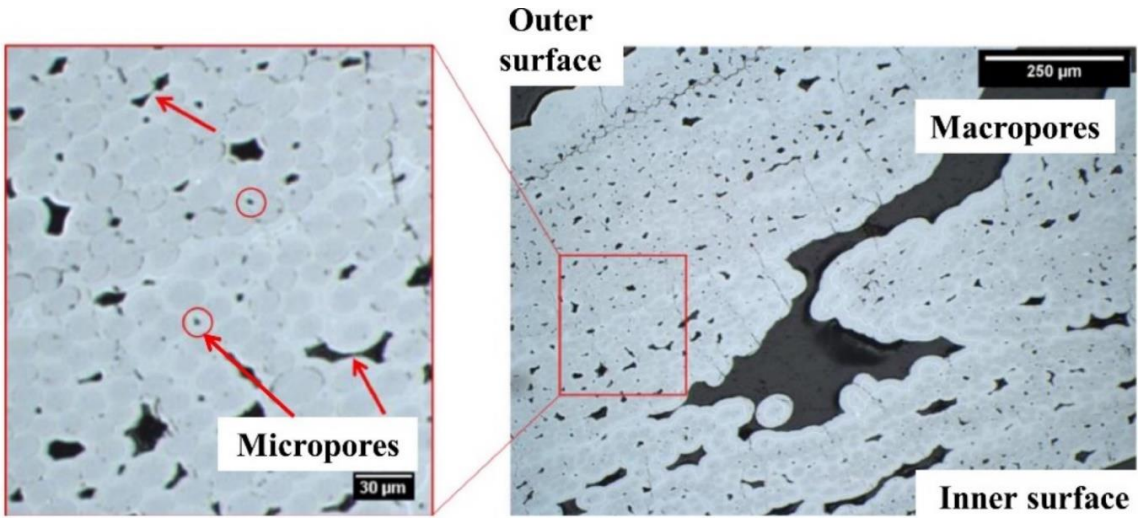

Figure 2-20. High-resolution optical image of the polished cross-sections of one type of SiC_f-SiC_m cladding material with CVI SiC matrix, showing macropores and micropores. Figure is reproduced from ref [158].

These pores could potentially serve as the pathways for fission gases and reduce the hermeticity of the cladding materials [14], [119]. Additionally, stress could concentrate on the sharp boundaries of macropores when the SiC_f-SiC_m material is under loading, which consequently lead to crack initiation at these areas [14]. One solution for reduction of the porosity level in the SiC_f-SiC_m material is to reduce the deposition rate during the CVI process [159], but it also results in a higher fabrication time. Generally, the porosity in SiC_f-SiC_m material is reported in the range of 5% to 13.8% [119], [132], [160]–[162], and it is still challenging to achieve a low porosity level of <5% for the CVI-densified SiC_f-SiC_m materials. The detailed information of these CVI-densified SiC_f-SiC_m materials and corresponding porosity levels is summarized in Section 2.4.5. Additionally, residual stresses could be introduced into the SiC fibres during the CVI densification processes. For instance, Nance *et al.*[163] measured the residual stresses of the SiC phase in Hi-Nicalon Type-S SiC fibres prior to and post the CVI densification process, and the compressive residual stresses were reported to change from -0.70 GPa to -1.08 GPa.

2.4.4.2. NITE SiC matrix

The NITE method is commonly utilized in manufacturing almost fully dense SiC_f-SiC_m materials [164]. The NITE method was developed from the liquid phase sintering (LPS) method with employing nano-sized SiC powders and a small amount of oxide additives [165]. The general outline of NITE process is presented in Fig. 2.21. Firstly, a slurry of nano-sized SiC powders, along with oxide slurring additives such as aluminium oxide (Al_2O_3) and yttrium oxide (Y_2O_3), is infiltrated into SiC fibers to produce intermediary. Subsequently, these intermediary prepreg sheets are sectioned, coiled, stacked, and subjected to compression to

achieve varied configurations. Finally, following hot isostatic pressing (HIP) at temperatures ranging from 1800°C to 2000°C, SiC_f-SiC_m materials of diverse geometries (*e.g.*, tube, rod and board) can be achieved [166], Fig. 2.21.

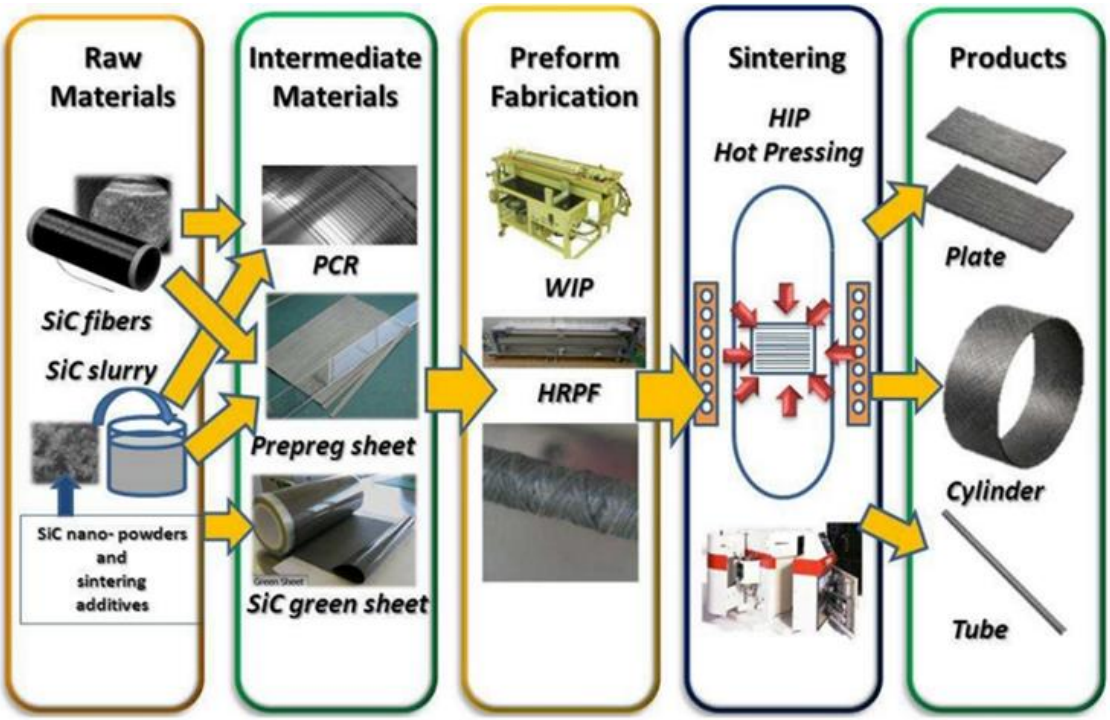

Figure 2-21. Schematic of the NITE process for the producing the SiC matrix of the SiC_f-SiC_m materials. PCR is pre-composite ribbon, WIP is worm isostatic press, HRPF is hot roller press forming and HIP is hot isostatic pressing. Figure is reproduced from ref [166].

Due to the hot-pressing sintering during the NITE process, the NITE-densified SiC_f-SiC_m materials are commonly reported to have a relatively low porosity level (below 5%), and consequently have good leak-tightness (hermeticity) [164]; with one representative example of the microstructure of NITE-densified SiC_f-SiC_m materials presented in Fig. 2.22a.

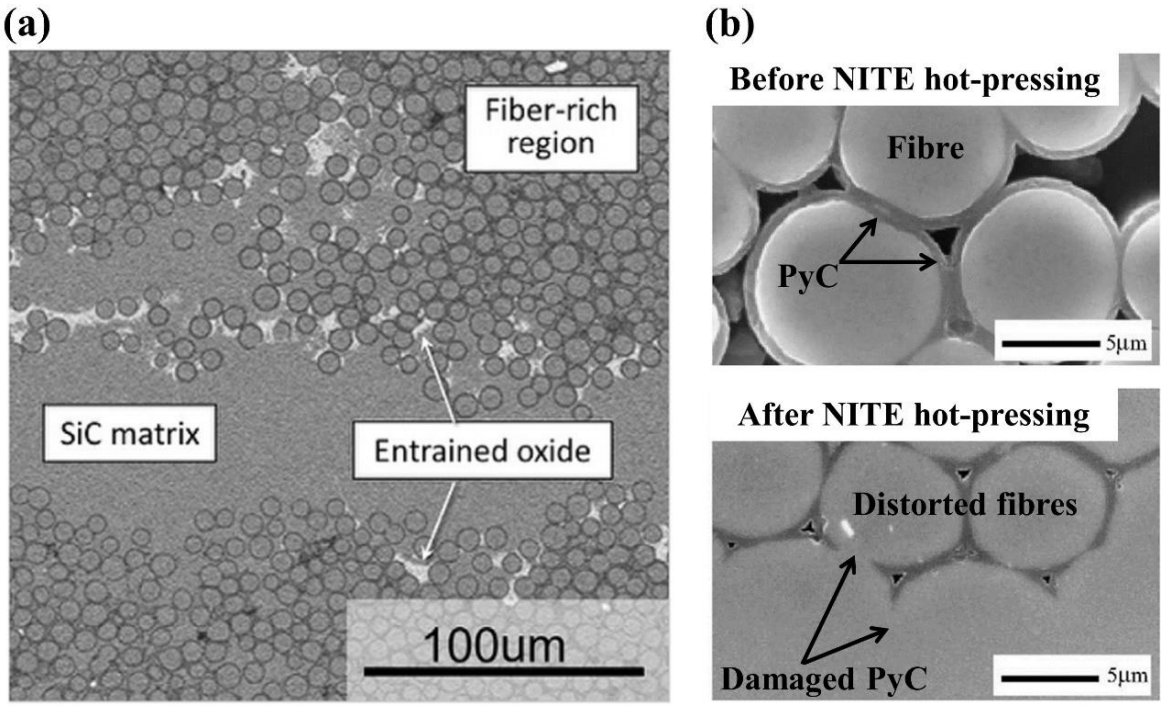

Figure 2-22. (a) SEM image shows the microstructure of polished cross-sections of one NITE-densified SiC_f-SiC_m materials, with low level of porosity but high level of the entrained oxides; and (b) SEM images of the SiC_f-SiC_m materials before and after the hot-pressing of NITE process, where distorted SiC fibres and destroyed PyC interphase can be observed. Figure is reproduced from refs [164], [167].

However, there are still two critical drawbacks of the NITE method, including oxide slurring additives and the HIP process [133]. The oxide slurring additives are commonly reported distribute along the boundaries of SiC fibres (one representative example presented in Fig. 2.22a) and consequently resulting in a deterioration in thermal conductivity of the entire SiC_f-SiC_m materials [145]. Note that, the Al_2O_3 additive is reported to give rise to the formation of the very long-lived, radiologically-hazardous isotope ^{26}Al, which consequently diminishes the irradiation stability of materials in nuclear reactors [168]. Additionally, the amorphization of these oxide slurring additives has been experimentally established as a principal factor contributing to the substantial irradiation-induced swelling. For instance, as reported by Koyanagi *et al.* [169], for both NITE SiC (contain 9wt.% additives) and CVD SiC materials under 5 dpa Si^{2+} ion irradiation at 280°C, the swelling of NITE SiC was found to be twice of the CVD SiC material. During the HIP process, materials are under high temperature and high pressure conditions, the oxide slurring additives can react with the PyC interphase between fibre/matrix, and damage it [164], [167], see Fig. 2.22b. Such phenomenon could subsequently restrict the pull-out of fibre (which is facilitated by the PyC interphase to prevent the breakage of SiC fibres) and consequently diminish the strength of the overall SiC_f-SiC_m materials. Additionally, under the same testing conditions and fibre braiding patterns, the tensile strength of NITE-densified SiC_f-SiC_m materials has been reported to be lower than the CVI-densified

SiC_f-SiC_m materials, which could be attributed to the damage of fibres (*e.g*, distorted fibres after NITE process, Fig. 2.22b) introduced by the HIP process [170]. The information of one NITE-densified SiC_f-SiC_m materials and corresponding porosity level is summarized in Section 2.4.5.

2.4.5. Physical properties of CVI-densified SiC_f-SiC_m cladding materials

The class of CVI-densified SiC_f-SiC_m materials represents the subject of this PhD project; therefore a detailed summary of some physical properties (including fibre architectures, fibre type, fibre volume fraction, porosity level and geometry) of various types of CVI-densified SiC_f-SiC_m cladding tube materials is tabulated in Table 2.7. Generally, these materials have a fibre volume fractions in the range of 20% to 51% [119], [128], [161], [162], [171], and the tensile strength of SiC_f-SiC_m materials increases with the increasing of fibre volume fractions [172]. For instance, Kim *et al.*[162] conducted room temperature *ex-situ* plug-expansion tests on their SiC_f-SiC_m (with both outer and inner monolithic coatings, and reinforced with Hi-Nicalon type-S fibres or Tyranno SA3 fibres) with various fibre volume fractions. It was found that, for both types of fibres, the hoop strength of the SiC_f-SiC_m tubes tends to increase with the volume fraction of reinforced fibres, Fig. 2.23. However, further increase of fibre volume fraction could increase the potential of contacting and damaging of the adjacent fibres, and consequently diminish the strength of the entire SiC_f-SiC_m materials, as suggested by Shimoda *et al.* [172]. Additionally, the lower fibre volume fraction could not enhance the strength of the SiC_f-SiC_m materials and composite materials could still possess a brittle-fracture behaviour.

Table 2-7. Summary of some physical properties (including porosity, fibre volume fraction and geometry) of various nuclear-grade SiC_f-SiC_m cladding materials from open literature with the matrix produced by CVI and NITE methods, respectively, brief information of these SiC_f-SiC_m materials is also included.

Composite information	Matrix	Type of fibre	Porosity (%)	Fibre volumn fraction (%)	Outer diameter (mm)	Wall thickness (mm)
Three layers of fibre in a ±45° of braiding angle to the tube axis, 100 nm PyC interphase, without any inner or outer SiC coating. Ref. [161]	CVI	Hi-Nicalon type-S	10.4 to 11.1	-	9.6	1.75
2D patterns with ±30° of braiding angle between reinforcement direction and the tube axis, PyC interphase, without any inner or outer SiC coating. Ref. [128]	CVI	Hi-Nicalon type-S	-	35	9.6	1.7
Axially biased fibre architecture, with PyC interphase	CVI	Hi-Nicalon type-S	~12	30-35	10.63	1.4
Duplex fibre architecture, 1.3:1 of the fibre tow in the hoop to axial direction (hoop biased), 150 nm PyC interphase, with inner Hexoloy SiC. Ref. [119]	CVI	Hi-Nicalon type-S	~20	-	8.8 to 9.6	1.3 to 1.5
Duplex fibre architecture, 1.3:1 of the fibre tow in the hoop to axial direction (hoop biased), 150 nm PyC interphase, without any inner or outer SiC coating. Ref. [119]	CVI	Hi-Nicalon type-S	~20	-	8.8 to 9.6	1.2 to 1.4
Duplex fibre architecture, 1.3:1 of the fibre tow in the hoop to axial direction (hoop biased), 150 nm PyC interphase, with inner Hexoloy SiC coating. Ref. [119]	CVI	Hi-Nicalon type-S	~20	-	8.8 to 9.6	1.3 to 1.5
Duplex fibre architecture, 1:1.5 of the fibre tow in the hoop to axial direction (axially biased), 150 nm PyC interphase, without any inner or outer SiC coating. Ref. [119]	CVI	Hi-Nicalon type-S	~20	-	8.8 to 9.6	1.2 to 1.4

Table 2.7 continued						
Duplex fibre architecture, 1:1.5 of the fibre tow in the hoop to axial direction (axially biased), 150 nm PyC interphase, with outer Hexoloy SiC coating. Ref. [119]	CVI	Hi-Nicalon type-S	~20	-	8.8 to 9.6	1.9 to 2.1
Duplex fibre architecture, without inner or outer SiC coating. Ref. [171]	CVI	-	8.7 to 12.7	35	10	1.8
±55° of fibre braiding angle to the tube axis, PyC interphase, without any inner or outer SiC coating. Ref. [160]	CVI	Hi-Nicalon type-S	13.8 ± 2.8	51	~9.5	~0.78
±45° of fibre braiding angle to the tube axis, 200 nm PyC interphase, with both monolithic outer (~100 μm in thickness) and inner (300 μm to 500 μm in thickness) SiC coatings. Ref. [162]	CVI	Hi-Nicalon type-S or Tyranno SA3	10 to 17	20 to 25	9.6 to 10.1	1.1 to 1.6
±55° of fibre braiding angle to the tube axis, 200 nm PyC interphase, with both monolithic outer (~100 μm in thickness) and inner (300 μm to 500 μm in thickness) SiC coatings. Ref. [162]	CVI	Hi-Nicalon type-S or Tyranno SA3	10 to 17	20 to 25	9.6 to 10.1	1.1 to 1.6
±65° of fibre braiding angle to the tube axis, 200 nm PyC interphase, with both monolithic outer (~100 μm in thickness) and inner (300 μm to 500 μm in thickness) SiC coatings. Ref. [162]	CVI	Hi-Nicalon type-S or Tyranno SA3	10 to 17	20 to 25	9.6 to 10.1	1.1 to 1.6
Plane-woven structure, ±30° of fibre braiding angle to the tube axis, PyC interphase (70 nm to 170 nm in thickness), without any inner or outer SiC coating [173]	CVI	Tyranno SA	15 to 24	30 to 37	7.6	1.7

Table 2.7 continued						
Plane-woven structure, ±90° of fibre braiding angle to the tube axis, PyC interphase (42 nm to 226 nm in thickness), without any inner or outer SiC coating [173]	CVI	Tyranno SA	18 to 23	35	7.6	1.7
±60° of fibre braiding angle to the tube axis, with PyC interphase [174]	NITE	-	-	-	10	1

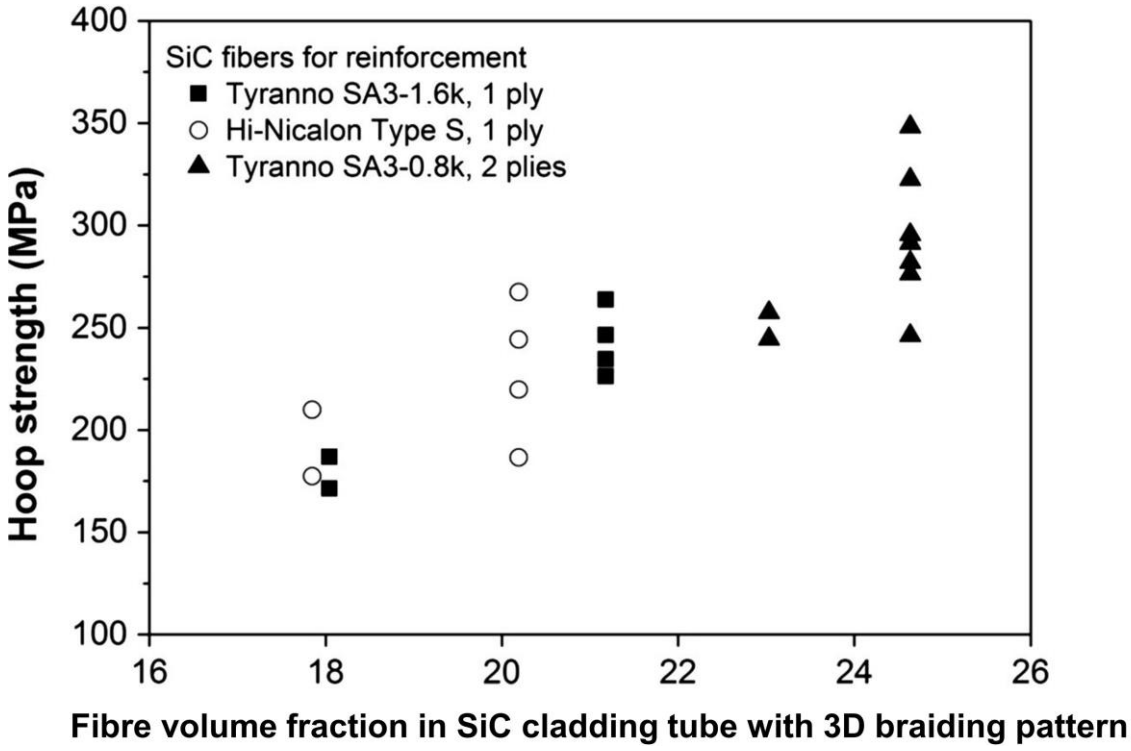

Figure 2-23. Variation of the measured hoop strength of the 3D braiding SiC_f-SiC_m cladding tubes with the volume fraction of SiC fibres. Figure is reproduced from ref [162].

To serve as ATF claddings, some requirements of the geometries for the design of SiC_f/SiC_m tube materials should be considered. Firstly, to compensate for the deformation of UO_2 cylindrical fuel pellets during operation (*e.g.*, temperature- and irradiation- induced swelling [23]), a gap (typically 200 to 400 μm) was designed between the fuel pellets and the inner surface of the cladding [22]. Therefore the inner diameter of SiC_f/SiC_m claddings should be slightly higher than the fuel pellets' diameter (typically 7-10 mm [175]). Then, the thermally conductivity of SiC_f/SiC_m materials are relatively low: 18 W/m-K to 28 W/m-K at RT, and 16 W/m-K to 22 W/m-K at 1200°C [176], which could lead to high temperature gradients, and thermal stress through materials' wall-thickness, and increases its failure probabilities [119]. Therefore, the SiC_f/SiC_m claddings' wall-thickness shouldn't be too thick (less than 2 mm). Based on these requirements, the SiC_f/SiC_m claddings were widely reported with an outer diameter of 8 to 11 mm, with the wall-thickness of 0.78 mm to 2.1 mm [119], [128], [161], [162], [171].

The porosity of CVI-densified SiC_f-SiC_m cladding materials has widely been reported in the range of 8–24% [119], [128], [161], [162], [171]. Such porosity level is significantly higher than the NITE-densified SiC_f-SiC_m cladding materials, mostly <5 [174]. As discussed in Section 2.4.4.1, these pores could diminish SiC_f-SiC_m claddings' hermeticity. SiC coating layers (commonly produced by chemical vapour deposition (CVD) method) were applied to

either or both outer and inner surfaces of the SiC_f/SiC_m claddings, and served as impermeable fission gas barriers [14], [119], [130], [132]. Among the recent studies, there is a trend to increase the thickness of outer CVD SiC coating of SiC_f/SiC_m cladding materials [14], [119], [130]–[132]: from ~50 μm reported by Jacobsen *et al* [131] in 2014 to ~200 μm reported by Yuan *et al*. [14] in 2023. As far as the authors are aware, the thickness of outer CVD SiC coatings were mostly below 200 μm in the openly-published references [14], [119], [130]–[132], with only one early-published work (2015) reported a ~600 μm thickness (~30% of the total wall-thickness of the composite, ~2.1 mm) of one SiC_f/SiC_m cladding materials by Deck *et al* [119]. To be noted that, such early design beyond the requirements of the claddings' geometry mentioned above.

2.4.6. Tensile properties of CVI-densified SiC_f-SiC_m cladding materials

Recently, to understand the mechanical properties (mostly tensile properties) and fracture of SiC_f/SiC_m claddings, several testing configurations have been employed, including uniaxial tension and compression, plug-expansion, open-end burst, closed-end burst and C-ring compression experiments. The schematics of these testing configurations are presented in Fig. 2.24. For uniaxial tension/compression test, where samples undergo tensile/compressive forces along a single axis to assess their ultimate tensile/compressive strength and fracture behaviour [129]. For plug-expansion, internal pressurization is induced to the specimen by applying an axial load to an elastic plug inserted in the specimen [131]. For C-ring compression, cladding is firstly cut into C-ring shape, and compressive stress then applied to the sample. The open-end and close-end burst testing entails subjecting a test specimen to progressively increasing internal pressure until it reaches the point of bursting or fracturing. However, during the burst testing, a mixed-mode stress (including hoop and axial stress) state is commonly introduced to the cladding sample. And the combination of material anisotropy and the mixed-mode stress conditions in such test can complicate the interpretation of the results [131]. Compared with plug-expansion test, C-ring compression has various advantages, *e.g.*, simplicity in equipment setup and easy for high temperature testing, which services as a pertinent and expedient method for evaluating the mechanical integrity of cladding materials[14], [131], [132]. Furthermore, the C-ring compression configuration aligns more closely with service conditions experienced by these cladding materials during their industrial application, where they are subjected to internal pressure [1].

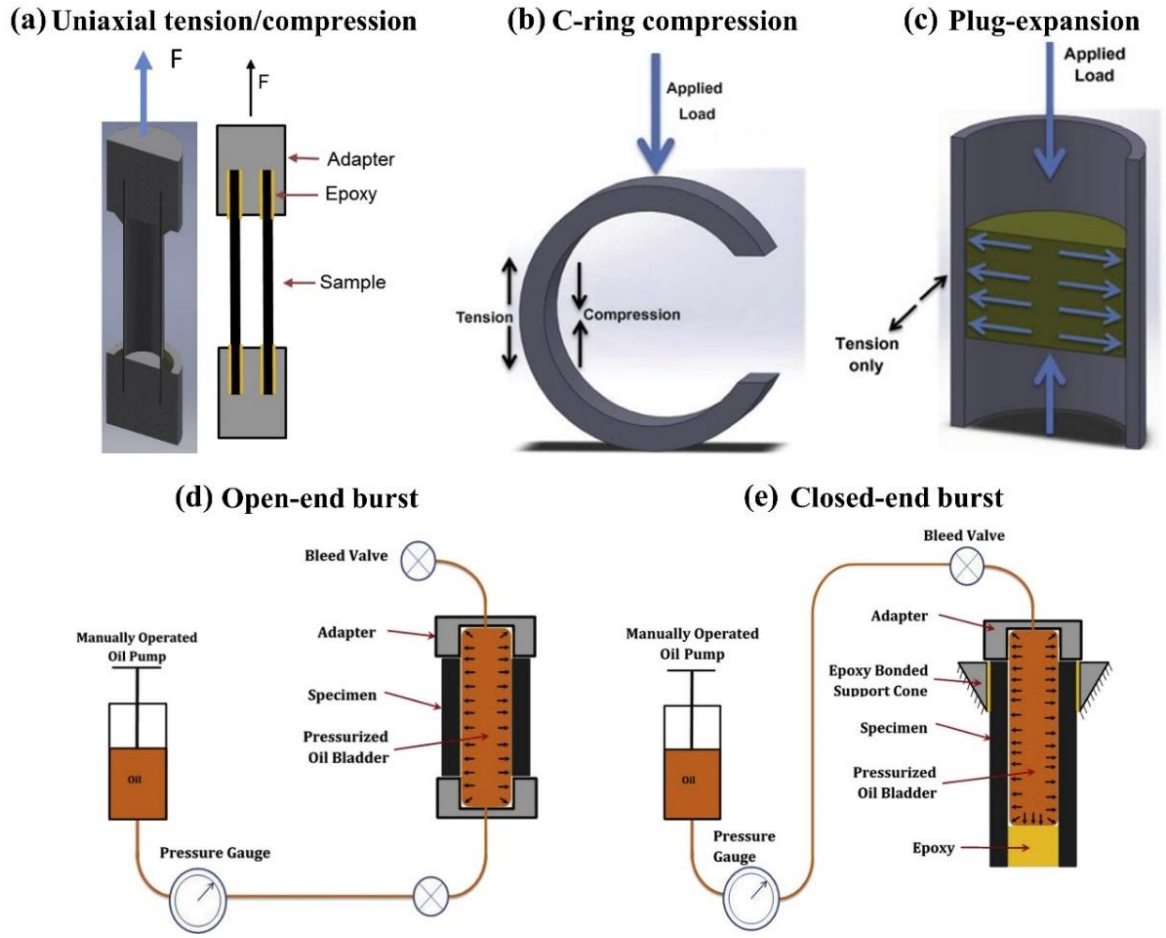

Figure 2-24. Schematics of testing configurations of measuring the hoop strength of the SiC_f-SiC_m cladding materials: (a) for uniaxial tensile/compression test; (b) for C-ring compression test; (c) for plug-expansion test; (d) for open-end burst test and (e) for close-end burst test. Figure is reproduced from refs [129], [131].

Most of the investigations of hoop strength of SiC_f/SiC_m cladding materials are performed at RT. Jacobsen *et al*. [131] investigated the room temperature strengths of two types of SiC_f/SiC_m cladding materials (named LWR SiC_f/SiC_m and EM^2 SiC_f/SiC_m, both reinforced with Tyranno SA3 fibres and have outer SiC coating (less than 50 μm in thickness), and a fibre volume fraction of 30% to 35%) via plug-expansion and C-ring compression tests. Comparable mechanical strengths were reported for both testing configurations: 413 ± 55 (C-ring) and 418 ± 33 (plug-expansion) for LWR SiC_f/SiC_m and 381 ± 50 (C-ring) and 406 ± 38 (plug-expansion) for EM^2 SiC_f/SiC_m, respectively. The *post-mortem* crack analyses indicated that for both types of materials under loading, cracks deflected in the fibre bundles; and the pull-out and broken of fibres were also observed [131]. Deck *et al*. [119] investigated room temperature mechanical behaviour (via C-ring compression) of various types of SiC_f/SiC_m claddings (reinforced with Hi-Nicalon type-S fibres), including: composites with 1.3:1 of the fibre tow in the hoop to axial direction (referred to hoop biased, as the fibre bundles are mainly braided

in the hoop direction, which is the Y direction in Fig. 2.16), with or without outer Hexoloy SiC coating; composites with 1:1.5 of the fibre tow in the hoop to axial direction (referred to axially biased, as the fibre bundles are mainly braided in the axial direction, which is the Z direction in Fig. 2.16), with or without inner Hexoloy SiC coating. It was reported that, for the hoop biased composites, the application of outer Hexoloy SiC coating resulted in a slight reduction (around 6%) of the hoop strength: ~331 MPa for the uncoated composites and ~311 MPa for the composites with outer coating. As for the axially biased materials, the application of inner Hexoloy SiC coating also led to a decreasing (around 20%) of the hoop strength: ~209 MPa for the uncoated composites and ~174 MPa for the composites with inner coating [119]. Moreover, the applications of either outer or inner SiC coating enhanced the hermeticity of the composites. Additionally, fibre braiding architectures were reported showing significantly impact on the strength of uncoated SiC_f/SiC_m cladding materials, the hoop biased materials possessed a higher hoop strength (~49%) than the axially biased materials: ~311 MPa and ~209 MPa, respectively [119].

Subsequently, acoustic emission (AE) and digital image correlation (DIC) methods were adopted in the mechanical testing, to respectively measure the elastic limit and surface strains of SiC_f/SiC_m claddings under loading. Rohmer *et al*. [128] performed room temperature axial and hoop tensile tests on their SiC_f/SiC_m claddings (reinforced with Hi-Nicalon type-S fibres, ±30° of fibre braiding angle between the reinforcement direction and axis of the tube, without either outer or inner SiC coating), and markable anisotropy in the mechanical properties was reported. In hoop direction, hoop stresses at elastic limit and the ultimate strength (~35 MPa and ~64 MPa, respectively) were found to be significantly lower than that in the axial direction (~80 MPa and ~460 MPa, respectively); however, the failure strain in the hoop direction (Y direction in Fig. 2.16) was 1.50%. This was much higher than that in the axial direction (Z direction in Fig. 2.16), 0.70%, and the strains at the elastic limit were measured similar at both directions: 0.3%. They attributed such anisotropy to the geometry of the fibrous preform, and it was suggested the strength in hoop direction could be enhanced by increasing the fibre braiding angles. Furthermore, the *post-mortem* SEM images reviewed similar crack patterns as reported by Jacobsen *et al*. [131], where cracks propagated in the fibre bundles and deflected along the PyC interphases between fibre and matrix [128]. However, opposite results were reported by Shapovalov *et al*. [129]. They studied the room temperature strength of one axially biased SiC_f/SiC_m claddings (reinforced with Hi-Nicalon type-S fibres, 1:1.4 of the fibre tow in the hoop to axial direction, without either outer or inner SiC coating) via various testing

configurations, including: elastomeric insert, open-end and closed-end burst tests for measuring hoop strength; and uniaxial tensile tests and closed-end burst tests for measuring the strength in axial direction. And DIC method was applied for estimating the failure strains at the surface of the materials. In the hoop direction, the strengths and failure strains measured by closed-end burst tests (135 MPa and 0.04%, respectively) were found higher than that measured by uniaxial tensile tests (respectively 245 MPa and 0.64%). In axial direction, closed-end burst tests showed the highest strength and strain (respectively 370 MPa and 0.73 %) among all testing configurations, while elastomeric insert tests yielded lowest values (respectively 135 MPa and 0.04 %) among all testing configurations. It is noteworthy, the hoop strengths exceed the axial strengths, despite the preferential fibre reinforcement along the axial direction. These observations from Shapovalov *et al*. [129] imply that factors beyond the architecture of the fibres, such as the distribution of pores, could also contribute to the anisotropic behaviours of SiC_f/SiC_m cladding materials. However, these studies were based on the *post-mortem* analyses and characterizations of the surface of SiC_f/SiC_m materials, which still could not provide sufficient characterizations of the microstructural evolution of the SiC_f/SiC_m materials under mechanical loading [14].

To overcome such limitations, mechanical tests have been carried out, in the combination with real-time micro X-ray computed micro-tomography (μXCT) imaging, which enable the 3D characterizations of the damage evolution in the SiC_f/SiC_m materials. Although more scarce, these investigations have offered substantially deeper insights into the damage evolution and failure mechanisms in the SiC_f/SiC_m materials [132], [158], [177], [178]. For instance, Saucedo-Mora *et al.* [132] performed room temperature C-ring compression experiments on theis SiC_f/SiC_m claddings (±45° of fibre braiding angle between the reinforcement direction and the tube axis) with outer monolithic SiC coating. The *in-situ* μXCT images directly revealed the initiation of cracks in SiC coating on the outer surface, as well as the broken of fibres after sample reaching peak load (around 123 N). More recently, Croom *et al*. [178] performed RT plug-expansion tests combined with real-time XCT images at room temperature on one SiC_f/SiC_m cladding without either inner or outer SiC coating. It was observed that the cracks exhibited a propensity to initiate primarily at fibre tows' intersections, and subsequently propagated in the axial direction and connected with the fibre tow overlap sites. Additionally, their DVC calculation revealed the significantly variation of the hoop strains across the entire thickness of the composite under loading; with the highest strains reported to be around 0.35% at 95% of the peak load, as consequently resulted in the initiation of cracks in the SiC matrix

[178]. Table 2.8 displays the room temperature hoop strengths and failure strains of various types of SiC_f/SiC_m cladding materials, a detailed information of these materials is also presented.

Table 2-8. Summary of the maximum hoop stresses and composite failure hoop strains (measured by either DIC or strain gauge methods) of different kinds of SiC_f-SiC_m composite materials (information of tested samples are included, extracting from corresponding literatures by author), tested by various testing methods (including C-ring compression, plug-expansion, open-end burst, closed-end burst, tensile and compressive tests) at room temperature.

Composite name	Composite information	Testing method	Maximum hoop stress (MPa)	Failure hoop strain
LWR SiC_f-SiC_m with outer coating. Ref. [131]	Tyranno SA3 fibre, <50 um outer SiC coating produced by CVD, with ~2.73 mm of r_i, ~5.23 mm of r_o, 2.5 mm wall thickness of composites tubes and ~2.5 mm width of C-ring samples	C-ring compression	413 ± 55	-
		Plug-expansion	418 ± 33	0.46% by strain gauge
EM^2 SiC_f-SiC_m with outer SiC coating. Ref. [131]	Tyranno SA3 fibre, <50 um outer SiC coating produced by CVD, with ~8.44 mm of r_i, ~10.94 mm of r_o,2.5 mm wall thickness of composites tubes and ~2.5 mm width of C-ring samples	C-ring compression	381 ± 50	-
		Plug-expansion	406 ± 38	0.57% by strain gauge
SiC_f-SiC_m without inner or outer SiC coating. Ref. [119]	Hi-Nicalon type-S fibre, 1.3:1 of the fibre tow in the hoop to axial direction (hoop biased), inner Hexoloy SiC coating, 1.3-1.5 mm wall thickness of composites tubes and 2-3 mm width of C-ring samples	C-ring compression	331 ± 74	-
SiC_f-SiC_m without inner or outer SiC coating. Ref. [119]	Hi-Nicalon type-S fibre, 1:1.5 of the fibre tow in the hoop to axial direction (axially biased), 1.3-1.5 mm wall thickness of composites tubes and 2-3 mm width of C-ring samples	C-ring compression	209 ± 24	-
SiC_f-SiC_m with inner SiC coating. Ref. [119]	Hi-Nicalon type-S fibre, 1:1.5 of the fibre tow in the hoop to axial direction (axially biased), inner Hexoloy SiC coating, 1.3-1.5 mm wall thickness of composites tubes and 2-3 mm width of C-ring samples	C-ring compression	174 ± 28	-
		Plug-expansion	152 ± 8	-

Table 2.8 continued

SiC_f-SiC_m with outer SiC coating. Ref. [119]	Hi-Nicalon type-S fibre, 1.3:1 of the fibre tow in the hoop to axial direction (hoop biased), outer Hexoloy SiC coating, 1.9-2.1 mm wall thickness of composites tubes and 2-3 mm width of C-ring samples	C-ring compression	311 ± 59	-
		Plug-expansion	271 ± 2	-
SiC_f-SiC_m without outer SiC coating. Ref. [129]	Hi-Nicalon type-S fibre, 1:1.4 of the fibre tow in the hoop to axial direction, with ~4.00 mm of r_i, 5.10 mm of r_o, 1.10 mm wall thickness and 25 mm in length of composites tubes	Plug-expansion	336 ± 14	0.82% by DIC
SiC_f-SiC_m without outer SiC coating. Ref. [129]	Hi-Nicalon type-S fibre, 1:1.4 of the fibre tow in the hoop to axial direction, with ~4.00 mm of r_i, 5.10 mm of r_o, 1.10 mm wall thickness and 30 mm in length of composites tubes	Open-end burst	281 ± 21	0.76% by DIC
SiC_f-SiC_m without outer SiC coating. Ref. [129]	Hi-Nicalon type-S fibre, 1:1.4 of the fibre tow in the hoop to axial direction, with ~4.00 mm of r_i, 5.10 mm of r_o, 1.10 mm wall thickness and 64 mm in length of composites tubes	Closed-end burst	271 ± 12	0.73% by DIC
SiC_f-SiC_m without outer SiC coating. Ref. [128]	Hi-Nicalon type-S fibre, ±30° of fibre braiding angle between reinforcement direction and the tube axis, with CVI SiC matrix	Tensile	64	1.52% by strain gauge
2D-woven SiC_f-SiC_m without outer SiC coating. Ref. [173]	Tyranno™ SA fibre, with ±30° of fibre braiding angle, with PyC interface between fibre and matrix	Tensile	~140	-
2D-woven SiC_f-SiC_m without outer SiC coating. Ref. [12]	Tyranno SA3 fibre, with ±90° of fibre braiding angle, with PyC interface between fibre and CVI matrix	Tensile	~220	-

Generally, there are very few mechanical experiments on the SiC_f/SiC_m cladding tubes conducted at high temperatures, and a detailed summary of the hoop strengths and failure strains are tabulated in Table 2.9. For instance, Nozawa *et al*. [9] conducted *ex-situ* uniaxial tension and compression tests on their SiC_f/SiC_m materials (Tyranno-SA3 fibres, ~35% of fibre volume fraction and ~13% of porosity, without either inner or outer SiC coating) at elevated temperatures up to 1000°C in vacuum. No significant degradation of the strength was reported for both tension and compression tests up to 1000°C: for tension, ~244 MPa at RT, ~230 MPa at 600°C, ~240 MPa at 800°C and ~226 MPa at 1000°C; for compression, ~336 MPa at RT, ~370 MPa at 800°C and ~393 MPa at 1000°C. More recently (2019), Shapovalov *et al*. [130] conducted *ex-situ* C-ring compression experiments on two types of SiC_f/SiC_m claddings (Hi-Nicalon Type S fibres, with 33% to 37% of the fibre volume fraction) in air up to 1100°C, including: (i) the materials without outer SiC; (ii) the materials with outer SiC coating (~100 μm of the coating thickness). It was reported that, for the uncoated materials tested in air, peak loads (no exact strength values were reported) reduced by ~40% from RT to 1100°C: ~16 N at RT, ~12 N at 700°C and ~10 N at 1100°C. As for the materials with coating, no reduction of the peak loads was found at elevated temperatures: ~16 N at both RT and 1100°C. These indicated the application of outer SiC coating could enhance the oxidation-resistance of the overall SiC_f/SiC_m materials [130]. Note that, the high temperature mechanical tests on SiC_f/SiC_m materials are mostly *ex-situ* experiments and based on the *post-mortem* analyses, which could not provide 3D microstructural evolutions of the materials under loading.

Table 2-9. Summary of the maximum hoop stresses and composite failure hoop strains (measured by strain gauge) of different kinds of SiC_f-SiC_m composite materials (information of tested samples are included, extracting from corresponding literatures by authors) by various testing methods including C-ring compression, tensile and compressive tests at high temperatures (in the range of 600°C to 1500°C) in various atmospheres including inert gas, vacuum and air. To be noted that, in one high temperature C-ring compression test works on one SiC_f-SiC_m cladding tube materials [130], they did not report the maximum hoop stresses but peak loads were reported, as presented in this table.

Composite name	Composite information	Testing method	Testing temperature (°C)	Maximum hoop stress (MPa)	Failure hoop strain
2D-woven SiC_f-SiC_m without outer SiC coating. Ref. [9]	Tyranno-SA3 fiber, with CVI SiC matrix and PyC interphase, 3 mm of the gauge length	Tensile	600 (vacuum)	230 ± 36	0.71%
			800 (vacuum)	240 ± 27	0.14%
			1000 (vacuum)	226 ± 23	0.14%
		Compressive	600 (vacuum)	370 ± 32	0.24%
			1000 (vacuum)	393 ± 91	0.39%
2D-woven SiC_f-SiC_m without outer SiC coating. Ref. [9]	Tyranno-SA3 fiber, with CVI SiC matrix and PyC interphase, 1.5 mm of the gauge length	Compressive	600 (vacuum)	282 ± 57	0.20%
			1000 (vacuum)	280 ± 31	0.20%
2D-woven SiC_f-SiC_m without outer SiC coating. Ref. [173]	Tyranno™ SA fibre, with ±90° of fibre braiding angle, with PyC interface (70 nm to 170 nm in thickness), 30% to 37% of fibre volume fraction, and 15% to 24% of porosity	Tensile	1200 (Ar)	~195	-
	Tyranno™ SA fibre, with ±30° of fibre braiding angle, with PyC interface (42 nm to 226 nm in thickness), ~35% of fibre volume fraction, and 18% to 23% of porosity	Tensile	1200 (Ar)	~115	-

Table 2.9 continued

2D-woven SiC_f-SiC_m without outer SiC coating. Ref. [12]	Tyranno SA3 fibre, with ±90° of fibre braiding angle, with PyC interface between fibre and CVI matrix	Tensile	1300 (Ar)	~165	-
			1500 (Ar)	~155	-
SiC_f-SiC_m without outer SiC coating. Ref. [130]	Hi-Nicalon type-S fibre, with PyC interphase (a thickness <500 nm), 33% to 37% of fibre volume fraction, ~4.0 to ~4.1 mm of r_i, ~4.8 to ~4.9 mm of r_o, 0.8 mm wall thickness of composites tubes and ~2.1 mm width of C-ring samples	C-ring compression	700 (Air)	A peak load at ~13 N	-
			1100 (Air)	A peak load at ~11 N	-
			1040 (Ar)	A peak load at ~8 N	-
			1360 (Ar)	A peak load at ~11 N	-
			1760 (Ar)	A peak load at ~10 N	-
			1900 (Ar)	A peak load at ~9 N	-
SiC_f-SiC_m with outer SiC coating. Ref. [130]	Hi-Nicalon type-S fibre, with PyC interphase (a thickness <500 nm), 33% to 37% of fibre volume fraction, ~4.0 to ~4.1 mm of r_i, ~4.8 to ~4.9 mm of r_o, 0.8 mm wall thickness of composites tubes and ~2.1 mm width of C-ring samples; with outer SiC coating of ~100 μm in thickness	C-ring compression	500 (Air)	A peak load at ~16 N	-
			950 (Air)	A peak load at ~15 N	-
			1100 (Air)	A peak load at ~16 N	-

2.5. Summary

2.5.1. CS and PVD Cr-coated zircaloy cladding material

The various manufacturing processes of CS and PVD manufacturing methods result in varied local microstructures and properties of Cr coatings and the coating/substrate interfaces. These differences could consequently affect the coating crack behaviours, and the mechanical properties and failure processes of the entire Cr-coated zircaloy materials. However, there is still a lack of the investigation of the differences of interfacial properties (*e.g.*, interfacial toughness), and their influences on the behaviours of both CS and PVD Cr-coated zircaloy claddings.

Furthermore, the investigations of coating crack behaviours are mostly based on *post-mortem* analyses. Although few recent works combined mechanical testing with *in-situ* SEM imaging to capture the initiation and propagation of coating cracks, the 2D SEM images could only provide information of either cracks in the Cr coating at the cross-sections at the edge of the sample or at the surface of coating, without any information for pathways of cracks in Cr coating. There remains a deficiency in 3D image characterization methods to monitor progressive failure processes and damage evolution of these materials under loading at increasing temperatures relevant to operational conditions. Additionally, these *in-situ* mechanical tests all used sheet samples, which could not thoroughly represent the behaviours of Cr-coated zircaloy claddings under real operation conditions.

For the CS Cr-coated zircaloy claddings, differences in the manufacturing parameters (*e.g.*, type of the high pressure gases) could result in different microstructures (*e.g.*, porosity), local properties and residual stress distributions in the coating, and consequently lead to differences in the coating crack behaviours and mechanical properties of the entire material systems. Moreover, it has been reported the residual stresses in the CS coating could lead to the generation of a multi-dimensional stress-state in Cr coating at elevated temperatures and lead to temperature-dependent coating crack bahaviours [105]. Therefore, for a more comprehension of the mechanical behaviours of the CS Cr-coated materials, it is of critical importance to conduct investigations of the residual stresses' distribution in Cr coating.

In summary, several key questions are raised in this context:

i. How do the microstructures of CS and PVD Cr-coated zircaloy claddings attribute to their differences of coating crack behaviours and mechanical properties?

ii. For CS and PVD Cr-coated zircaloy claddings under loading, will their coating crack behaviours and mechanical properties be temperature-dependent?

iii. How do the interfacial properties affect the mechanical properties of both the CS and PVD Cr-coated zircaloy claddings?

iv. For the CS Cr-coated zircaloy cladding materials, how do the variation of residual stresses and microstructures of the coating affect the mechanical properties of the entire material systems?

2.5.2. CVI-densified SiC_f-SiC_m cladding materials

The documented failure processes of SiC_f-SiC_m materials under loading at RT are conventionally considered to happen in three steps [129], [131], [179]: (i) the applied load is shared by the fibres and matrix, with minimal formation of the cracks in the materials; (ii) upon reaching the proportionality limit, cracks initiate in the matrix and propagate along the PyC interphase between fibre/matrix; (iii) as the matrix experiences substantial fracture, the load is primarily transferred to the fibres, leads to fibre pull-out and breakage. However, these observations are mostly based on *post-mortem* analyses, and there is still lack of real-time experiments (especially at high temperatures), which provide real-time observations of crack initiation and progressive propagation in the SiC_f-SiC_m materials under loading.

Moreover, the applications of CVD SiC coatings at either or both outer and inner surfaces of the materials have drawn researchers' interests recently. As reported by Saucedo-Mora *et al.* [132] for their coated SiC_f-SiC_m materials under C-ring compression load at RT, the cracks first initiated in the outer SiC coating instead of occurred in the matrix. Therefore, for different types of SiC_f-SiC_m materials under different testing configurations, the real failure mores could be different from the conventional failure modes. And it could be inappropriate to presume the same failure processes in one certain testing configuration or in one type of material will apply to all others. These again indicated that, it is critical to apply *in-situ* 3D characterization methods to acquire the microstructural information of the SiC_f-SiC_m materials under loading, especially at high temperatures representative of normal and abnormal service conditions; which enables a comprehensive understanding of the complex behaviour of the composite materials. And it is critical to investigate the influence of local microstructure on the fracture processes of the complexed SiC_f-SiC_m materials. Although some mechanical tests combined with *in-situ* XCT imaging were conducted, but to date, there is still no such real-time high temperature experiments with XCT imaging on these SiC_f-SiC_m materials in the open literature.

Additionally, residual stresses are generated in individual components of the SiC_f-SiC_m materials during the manufacturing processes. It is suggested that, the initiation of cracks, as well as being exposed to increasing temperatures has the potential to alter the distribution of residual stress in the SiC_f-SiC_m materials [14], [180]; and these modifications could potentially affect the failure strain and mechanical behaviour of the entire cladding materials. Therefore, it is important to perform a comprehensive examination of the distribution of residual stresses in these cladding materials. This analysis is essential not only for the interpretation of their deformation and fracture characteristics but also for the comparative assessment of different materials produced by diverse manufacturing procedures.

Consequently, several research inquiries arise within this context:

i. Do failure modes exhibit consistency across distinct temperatures within various SiC_f-SiC_m material systems?
ii. What impact do diverse microstructural characteristics, such as pores, fiber architectures, and outer SiC coatings, exert on fracture mechanisms?
iii. What are the scale and patterns of residual stresses within different SiC_f-SiC_m material systems?
iv. How do residual stresses influence the failure strain of SiC_f-SiC_m material systems at increasing temperatures?

Addressing the questions presented above, a potential solution for exploring the relationship between microstructures and failure modes involves the combination of high-temperature mechanical testing with real-time 3D images, utilizing synchrotron X-ray computed microtomography (XCT). 3D strain quantification in SiC_f-SiC_m materials can be subsequently accomplished through the application of optical tracking via digital volume correlation (DVC). Therefore, a brief literature review of the XCT and DVC techniques will be presented in the following sections.

2.6. X-ray Computed Tomography and digital volume correlation

2.6.1. Introduce to XCT

XCT is a 3D nondestructive imaging technique employed for visualizing the internal microstructure of an object [181]–[190]. Its origins can be traced back to its initial development for medical applications during the 1950s. Subsequent advancements have significantly enhanced the accuracy of contrast and spatial resolution in XCT images by Grodizns [191] in 1983 and Flannery *et al.* [192] in 1987. Consequently, XCT has garnered growing interest

across diverse research domains, encompassing materials science, biology, and geosciences [193]–[198].

The fundamental principle of XCT is grounded in the attenuation of X-ray intensity as it traverses a homogeneous target, adhering to Beer-Lambert's Law (Eq. 2.2):

$$I_x = I_0 e^{-\mu x}, \tag{2.2}$$

where I_x is the X-ray beam intensity after passing through the target, I_0 is the intensity of the beam upon entering the target material, μ is the linear attenuation coefficient and x is the distance of the beam travelled through the target material [199]–[201]. In the case of monochromatic X-ray beam traverse a heterogeneous object consisting of multiple materials, the calculation for the transmitted beam intensity is as follows (Eq. 2.3):

$$I(L) = I_0 e^{-\int_0^L \mu(x)dx}, \tag{2.3}$$

where Eq. 2.1 is modified by means of a line integral taken over a path L, and the linear attenuation coefficient (μ) exhibits the variation at each point along the path [183].

A typical XCT setup comprises three primary elements: an X-ray source, an X-ray intensity detection system, and a rotational apparatus to support the objects being imaged, as illustrated in Fig. 2.25. The main imaging procedure involves the following two steps (Fig. 2.25):

(i) The acquisition of an adequate number of radiographic projections of the specimen. During this process, either the specimen or the X-ray source are rotated over 180º or 360º, with projections are acquired at different rotational intervals. In these projections, the grayscale values signify the attenuation of X-ray intensity along linear trajectories as the X-ray beam traverses the object [187], [188], [202].

(ii) The reconstruction of the 3D of X-ray attenuation, which is accomplished through the application a computed algorithm to produce equidistant cross-sectional slices of the target material [181]–[190]. The most commonly utilized algorithm is the filtered back projection. The reconstructed slices correspond to grayscale images, with variations in contrast originating from the distinct X-ray attenuation properties of various phases in the target material. Consequently, after the reconstruction of XCT slices, it becomes feasible to differentiate and quantitatively assess different phases by discerning their characteristic grayscale values.

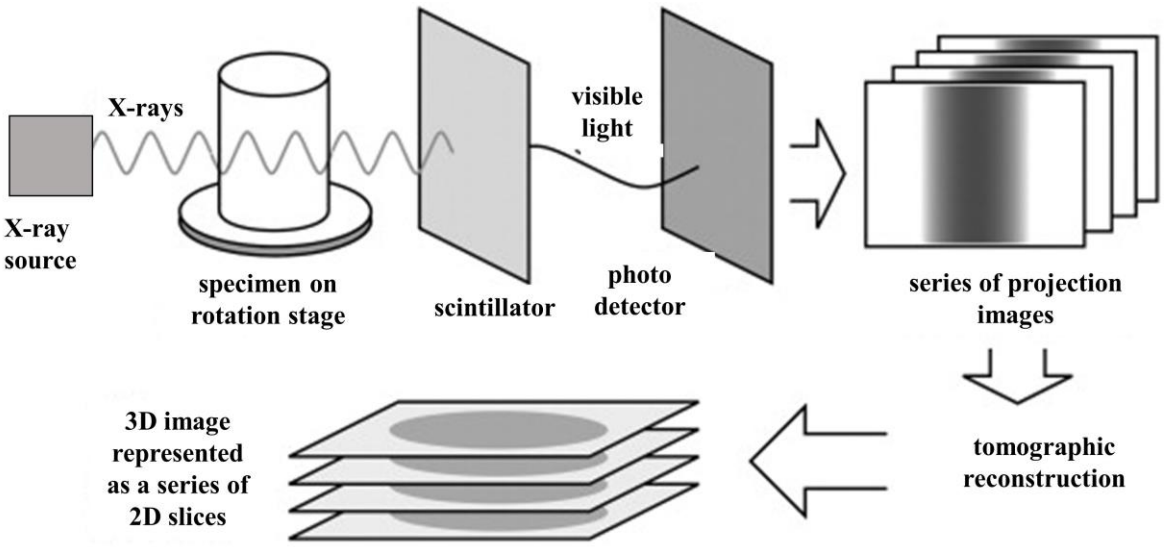

Figure 2-25. Schematic of a general workflow of laboratory based XCT scan. Figure is reproduced from ref [182].

2.6.2. Lab XCT and synchrotron XCT

Based on the differences of the X-ray sources, XCT setups can be categorized into two primary classifications: lab XCT and synchrotron XCT [181]. Schematics of these two types of setups are presented in Fig. 2.26.

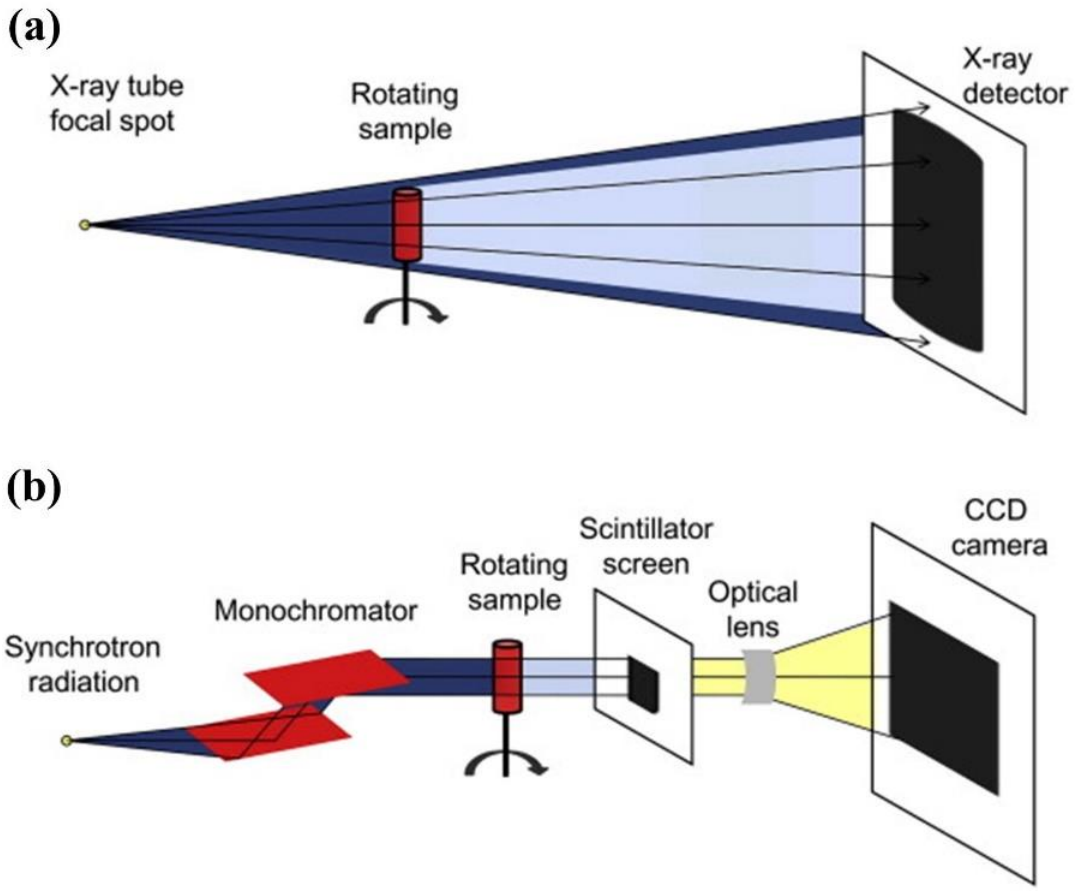

Figure 2-26. Schematics of typical setups of (a) lab-based XCT and (b) synchrotron XCT. Figure is reproduced from ref [181].

The most common lab XCT setup is the standard cone-beam XCT [203], where the conical X-ray beam permits the geometrical magnification by enabling the placement of the target material at any desired position within the distance between the X-ray source and the XCT detector [204], Fig. 2.26a. Three main parameters of the X-ray source affect the quality of XCT images: (i) focal spot size of the X-ray source, a smaller spot size results in a higher resolution of the XCT images [205]. (ii) Energy of the X-ray (represents the penetrative ability of X-ray), the elevated energy levels generally result in a heightened penetrative ability. (iii) X-ray intensity (X-ray flux), a higher intensity commonly results in a decreasing of the signal-to-noise ratio (SNR) of the images in a certain exposure time; however, a higher X-ray flux results in a bigger focal spot size, which consequently decreases the resolution of XCT images. Additionally, the distance of sample-to detector should be taken into consideration for obtaining a proper image resolution: a smaller distance leads to a lower resolution, but yields a higher field of view (FOV) [206], [207].

In contrast to the point X-ray source of lab XCT setup, synchrotron XCT commonly uses parallel X-ray beams with higher X-ray flux (Fig. 2.26b), which significantly reduces the

acquisition time (to mins and secs), as well as considerably improves the SNR of the images [208]–[213]. These parallel X-ray beams of monochromatic and narrow wavelength bands are commonly generated during the acceleration of high-energy electrons in the large synchrotron facilities (*e.g.*, Advanced Light Source (ALS) in the U.S. and Diamond Light Source (DLS) in the U.K.) [185], [187], [188], [192], [200]. As the synchrotron XCT uses parallel X-ray beams, so the magnification of target material remains constant on the detector. Consequently, the spatial resolution of synchrotron XCT is only dictated by the scintillator, optical lens (for magnification) and charge-coupled device (CCD) camera [214]–[217]. In an XCT scan, when its voxel size is several micrometres or less, it is therefore commonly referred to as micro X-ray computed microtomography (μXCT).

Several types of artifacts have been commonly reported in the reconstrued μXCT images, and are briefly discussed in the following context [183], [218]–[220]:

i. Ring artifacts: these artifacts manifest as a consequence of variations in the sensitivities exhibited by contiguous detector elements, and are commonly observed in the form of concentric circles, with their center positioned at the rotational axis;
ii. Beam hardening: when a polychromatic X-ray beam traverses an object, it is observed that lower-energy X-rays experience greater attenuation compared to their higher-energy ones. This phenomenon results in an overall elevation in the mean X-ray energy, referred to as beam hardening. This could be corrected by employing a suitable filter to suppress excessively low-energy photons from the X-ray beam;
iii. Center of rotation error: center of rotation could be inaccurately determined (due to the sample rotation), it can give rise to the appearance of double edges or, in the case of minor discrepancies, result in the blurring of edges. Consequently, it becomes imperative to detect the center of rotation after each scan, in order to facilitate the precise application of alignment compensation during the subsequent reconstruction process;
iv. Motion artefacts: as the resolution of μXCT is in several micrometres or less, it is highly susceptible to the occurrence of motion blur, which emanates from either or both the intrinsic (*e.g.*, breathing) or extrinsic processes (*e.g.*, movement of the loading stage).

Note that, for the materials involved in this PhD project, the Cr coatings of the Cr-coated Zircaloy cladding materials are very thin (~20 μm in thickness) when compared with the underlying substrate (~1 mm in thickness); and the crack networks are complex in the SiC_f-

SiC_m materials. Therefore, it is imperative to conscientiously account for the artifacts above, as they could potentially impact the detection and quantification of damage in these materials.

Both the lab XCT and synchrotron XCT have been utilized in the microstructural characterization and damage evolution of various types of nuclear materials, including: SiC_f-SiC_m materials [14], [158], [177], [178], [221], [222], nuclear graphite [223], [224], MAX phase materials [225]–[227], Cr-coated Zircaloy cladding materials [1], and tristructural-isotropic (TRISO) fuel particles [180], [228]. They are also widely utilized in the characterization of damage evolution in other types of materials, *e.g.*, aerospace ceramic-matrix composites (CMCs) [229], battery materials [230], fossils [231] and Ti-Al alloys [232].

2.6.3. Digital volume correlation

Digital Volume Correlation (DVC) is a technique rooted in digital image correlation (DIC) method. DIC works on the fundamental principle of calculating displacement fields by tracking and comparing successive recorded images of a deforming material's surface. This matching process, known as correlation, is achieved by discretizing each image into a number of subsets, or interrogation windows, that are identical in size and shape [233]–[235].

The schematic of DIC method is presented in Fig. 2.27. The displacement between point $P\ (x, y)$ in reference image and point $P'\ (x', y')$ in target image (after deformation) can be defined by Eq. 2.4 and Eq. 2.5:

$$x' = x_0 + \Delta x + \mu + \frac{\partial \mu}{\partial x}\Delta x + \frac{\partial \mu}{\partial y}\Delta y \tag{2.4}$$

$$y' = y_0 + \Delta y + v + \frac{\partial v}{\partial x}\Delta x + \frac{\partial v}{\partial y}\Delta y \tag{2.5}$$

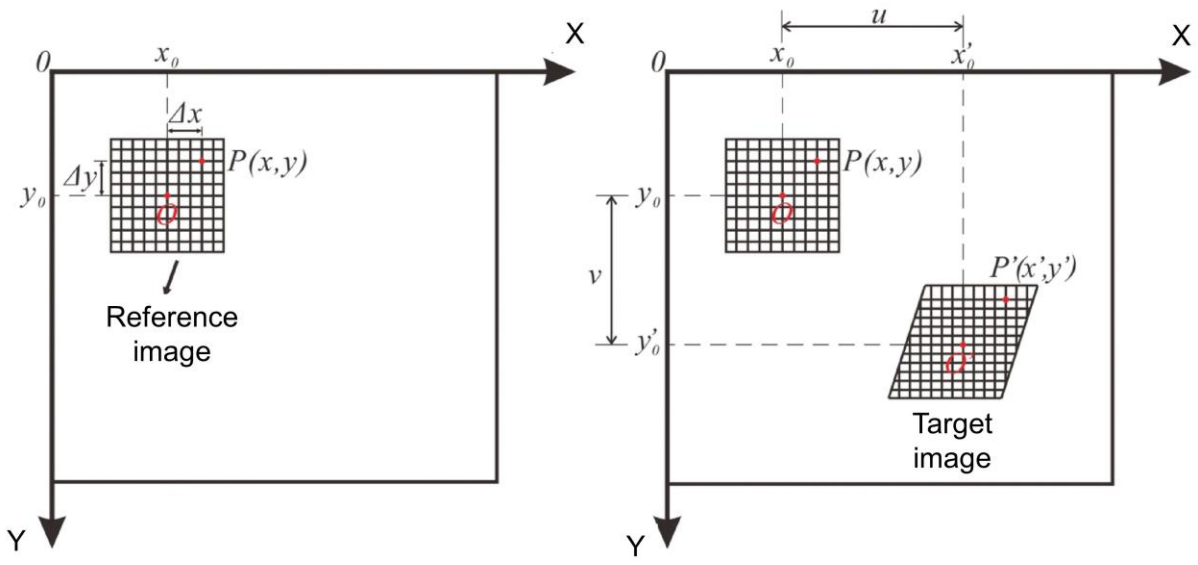

Figure 2-27. Simplified schematic shows the DIC process. Point *P (x, y)* is from the reference image, and it becomes point $P'(x', y')$ after deformation, and point $O\ (x_0, y_0)$ is the centre point of the reference image. Figure is reproduced from ref [236].

DVC extends the principles of 2D-DIC into 3D space. It calculates the strain field within a material's volume using a correlation strategy fundamentally analogous to that employed in the initial implementation of DIC [233]–[235].

Generally, the DVC process involves three primary steps: (i) the delineation of a region of interest containing designated measurement locations; (ii) the determination of displacements at each of these specified locations through correlating the reference and deformed datasets; and (iii) the subsequent computation of strain values at each measurement point by estimating the deformation gradients within their immediate vicinity [235]. And a schematic of DVC process is presented in Fig. 2.28.

In current PhD project, full field DVC analysis is conducted for the investigation of local strain distributions of the SiC_f-SiC_m cladding materials via XdigitalVolumeCorrelation Module in Avizo Lite software (version 2019.4); with the results will be presented in Section 4.5. Specially, the local DVC approach is utilized, and a brief review of such approach is presented in the following content. The local DVC approach consists of: (i) both the reference and deformed datasets are divided into smaller sub-volumes; and (ii) these sub-volumes are subsequently subjected to individual correlation analysis, primarily guided by cross-correlation criteria [229]. The Fast Fourier Transform (FFT) is commonly employed to significantly reduce the computational time required for correlation calculations. This method enhances the accuracy of displacement measurements and increases the reliability of DVC measurements due to its robustness against noise. [229]. For a FFT procedure, the reference and deformed

datasets are first converted from spatial data into the frequency domain. Then, cross-correlation between the reference and deformed interrogation windows is efficiently performed by multiplying the FFT of the reference window with the complex conjugate of the FFT of the deformed window. After this, the inverse FFT of the cross-correlated data is applied to return the data to the spatial domain, providing the correlation map. Finally, the displacement vector is determined by identifying the peak in the correlation map, which corresponds to the optimal match between the reference and deformed sub-volumes. In such implementations, only a mean 3D displacement vector at the centre of each sub-volume is retained. Consequently, a subsequent interpolation process becomes necessary to ascertain a continuous displacement field. This interpolation step is carried out independently from the original registered images and the DVC computation [237].

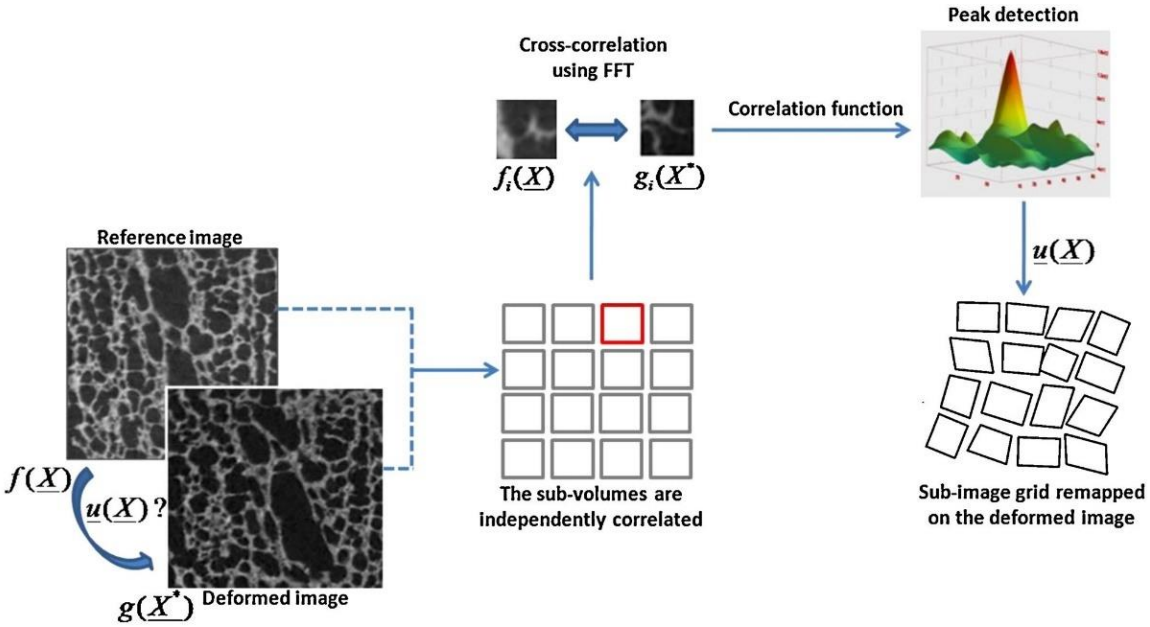

Figure 2-28. Schematic shows the typical local DVC process, as sub-volumes are independently correlated, and an additional independent interpolation step is required for the generation of continuous displacement field. Figure is reproduced from ref [238].

The quality of local DVC approach can be accessed via the normalized cross-correlation coefficient (C_{LA-DVC}), which is defined following Eq. 2.6:

$$C_{LA-DVC}=\frac{\sum f(X)g(X^*)}{\sqrt{\sum f(X)^2 \sum g(X^*)^2}}, \tag{2.6}$$

where *X* and *X** refer to coordinates (in voxels) of the same material point in the reference and the deformed image, respectively. *f(X)* and *g(X*)* are the scalar grey levels in the reference and deformed datasets, respectively. For the values of C_{LA-DVC}, 1 represents for the perfect correlation, whereas 0 represents for the complete mismatch [229], [238]. Furthermore, the

employment of ‘multi-pass’ methods in local DVC approach has been reported to improve the precision and accuracy of the measurement [229], [239]. A multi-pass approach employs a predictor-corrector methodology, in which the displacement computed during the predictor step serves as the initial value for the corrector step; and the corrector step utilizes smaller sub-volumes compared to those employed in the predictor phase [240].

The DVC method combined with high resolution XCT images have been employed by many researchers to investigation the damage evolution and estimation local strains of various nuclear materials, *e.g.*, SiC_f-SiC_m materials [14], [158], [177] and nuclear graphite [241].

3. Materials and experimental procedures

The materials and experimental procedures from current Chapter have been published in Materials & Design during the PhD project. The current Chapter contains minor additions and modifications compared to the published article by Yuan *et al.* [14]. Guanjie Yuan: Investigation, Formal analysis, Data curation, Writing – original draft, Writing – review & editing; J. Paul Forna-Kreutzer: Experiments; Peng Xu: Resources; Sean Gonderman: Resources, Review & editing; Christian Deck: Resources, Review & editing; Luke Olson: Resources, Review & editing; Edward Lahoda: Resources, Review & editing; Robert O. Ritchie: Resources, Funding acquisition, Supervision, Writing – review & editing; Dong Liu: Conceptualization, Resources, Methodology, Funding acquisition, Supervision, Writing – review & editing. The current Chapter also contains minor additions and modifications compared to the published article by Yuan *et al.* [1]. Guanjie Yuan: Investigation, Formal analysis, Data curation, Writing – original draft, Writing – review & editing; J. Paul Forna-Kreutzer: Experiments; Jon Ell: Experiments; Harold Barnard: Resources, Review & editing; Benjamin R. Maier: Resources, Review & editing; Edward Lahoda: Resources, Review & editing; Jorie Walters: Resources, Review & editing; Robert O. Ritchie: Resources, Funding acquisition, Supervision, Writing – review & editing; Dong Liu: Conceptualization, Resources, Methodology, Funding acquisition, Supervision, Writing – review & editing.

3.1. Introduction

In the current Chapter, the materials investigated in this PhD project are described, as well as the sample preparation procedures and experimental setups. A brief introduction of the investigated materials is presented in Section 3.2. The detailed experimental procedures and setups, as well as the specimen preparation processes of different experiments are described in Section 3.3. And Section 3.4 gives the conclusion of current Chapter.

3.2. Materials

The materials investigated in this research project include two classes of SiC_f-SiC_m cladding materials: (i) with single layer of CVD SiC coatings at both outer and inner surfaces of the cladding (Chapter 4), and (ii) with multiple-layers CVD SiC coating at the outer surface of the cladding (Chapter 5). It also includes four classes of Cr-coated zircaloy-4 cladding tube materials, which have same type of substrate: zircaloy-4, but with different manufacturing processes of the Cr coatings (Chapters 6 and 7). The detailed information for each type of material is listed in the individual sections below.

3.2.1. SiC_f-SiC_m cladding materials

The materials investigated in this part of the project comprised two SiC_f-SiC_m cladding materials produced by General Atomics (GA). The construction of the SiC_f-SiC_m materials consisted of Hi-Nicalon™ Type S fibres (~12 μm in diameter), SiC matrices, PyC coating at the fibre/matrix interface and SiC coatings at either or both the outer and inner surfaces (will be referred to as 'outer SiC coating' and 'inner SiC coating' in the text). The manufacturing process of SiC_f-SiC_m cladding materials comprises the following steps: (i) Hi-Nicalon™ Type S fibres were first braided around a cylindrical mandrel [163]; (ii) PyC coating layers were then deposited surrounding the fibres by CVD method [242], [243]; (iii) after that, SiC matrices were deposited by CVI method to densify the tube structure; (iv) finally, either or both the inner and outer SiC coatings were deposited by CVD method. For these two SiC_f-SiC_m material systems, one (Chapter 4) has both outer and inner single layer SiC coatings, and the fibre braiding angle is ±60° of braiding angles between the reinforcement direction and the tube axis. whereas another system (Chapter 5), has multiple-layers outer SiC coating, and the fibre braiding angle is ±45° of braiding angles between the reinforcement direction and the tube axis. These two material systems were characterized under C-ring compression tests via real-time high-temperature μXCT, with results presented in Chapter 4 and Chapter 5, respectively. Digital volume correlation (DVC) method was applied to the material (both outer and inner single layer SiC coatings) to calculate the failure hoop strain of the outer SiC coating, with results presented in Chapter 4. The typical geometry of the C-ring specimen is given in Fig. 3.1, r_o is the outer radius, r_i is the inner radius, t is the wall-thickness and b is the width of the C-ring sample. The exact C-ring sample dimensions for these two materials were measured by μXCT imaging and are listed in Table 3.1.

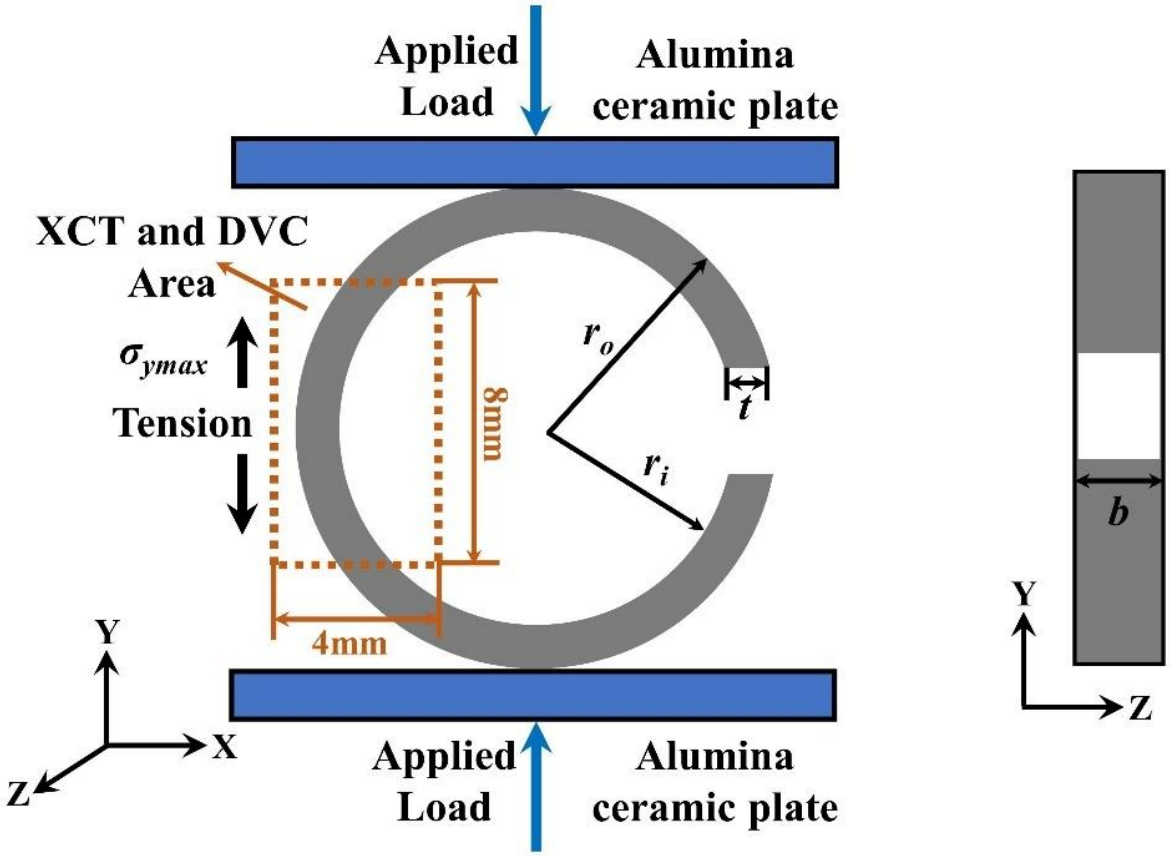

Figure 3-1. Schematic of the configuration of C-ring compression tests of the SiC_f-SiC_m cladding tube materials and Cr-coated zircaloy-4 cladding tube materials, including the coordinate system and dimensions of C-ring specimens. r_o is the outer radius, r_i is the inner radius, t is the wall-thickness and b is the width of the C-ring sample. The μXCT images (marked by dashed rectangular) were scanned at the region of the C-ring sample with maximum tensile stress/strain.

Table 3-1. C-ring specimen dimensions of SiC_f-SiC_m cladding tube materials measured by μXCT imaging.

Material	**Outer radius (r_o, mm)**	**Inner radius (r_i, mm)**	**Wall-thickness (t, mm)**
With both outer and inner single layer SiC coatings	4.64 ± 0.16	3.74 ± 0.16	0.90 ± 0.017
With multiple-layers outer SiC coating	4.78 ± 0.19	3.74 ± 0.13	1.04 ± 0.021

Prior to the *in-situ* mechanical testing, nanoindentation and Raman spectroscopy were applied to respectively measure the local properties and residual stress distribution of individual components of both types of the as-received materials. The microstructures of the polished cross-sections of both types of as-received materials were captured by scanning electron microscopy (SEM) imaging. These techniques and sample preparation methods are detailed described in subsequent sections, and the results are presented in Chapter 4 and Chapter 5, respectively.

3.2.2. Cr-coated zircaloy-4 cladding materials

The materials investigated in this part of the project contained four types of Cr-coated zircaloy-4 cladding tube materials provided by Westinghouse Electric Company LLC. They can be classified into two groups: group one contains two types of Cr-coated zircaloy-4 materials with the Cr coating produced by CS and PVD methods (Chapter 6), respectively, and will be referred to as CS Cr-coated materials and PVD Cr-coated materials in the following text; group two contains two types of Cr-coated zircaloy-4 materials with the Cr coating produced by CS method but with different manufacturing parameters (*e.g.*, carrier gases are helium and nitrogen, respectively), and will be referred to as HCS Cr-coated materials and NCS Cr-coated materials in the following text. Note that, these four types of materials have the same type of substrate: zircaloy-4 material. And no more fabrication details can be provided by Westinghouse Electric Company LLC. These four types of material systems were characterized under C-ring compression tests via real-time high-temperature μXCT imaging; the typical geometry of the C-ring sample can be found in Fig. 3.1, with the exact specimen dimensions for these materials measured by μXCT imaging and are listed in Table 3.2.

Table 3-2. C-ring specimen dimensions of Cr-coated zircaloy-4 cladding materials measured by μXCT imaging.

Material	**Outer radius (r_o, mm)**	**Inner radius (r_i, mm)**	**Wall-thickness (t, mm)**
CS Cr-coated	4.59 ± 0.014	3.94 ± 0.052	0.65 ± 0.035
PVD Cr-coated	4.58 ± 0.018	3.94 ± 0.076	0.64 ± 0.034
HCS Cr-coated	4.59 ± 0.026	3.95 ± 0.045	0.64 ± 0.052
NCS Cr-coated	4.59 ± 0.087	3.96 ± 0.077	0.63 ± 0.034

Prior to the high temperature mechanical testing, nanoindentation and electron backscatter diffraction (EBSD) mapping were conducted on the polished cross-sections of all types of the as-received Cr-coated zircaloy-4 cladding materials to measure the local properties and Cr grain distributions inside the coating, respectively. After the high temperature mechanical testing, post failure crack patterns of all types of materials were examined by SEM imaging. Specially, the coating crack pathways in the coating of post-tested HCS and NCS Cr-coated materials were examined by plasma focused ion beam (P-FIB) milling combined with SEM imaging (FIB-SEM tomography), with the results are presented in Chapter 7. The residual stresses distribution inside the Cr coatings of as-received HCS and NCS Cr-coated materials were investigated via ring-core focussed ion beam milling combined with digital image correlation analysis (FIB-DIC), and the results are summarized in Chapter 7. These techniques

are detailed described in the subsequent sections, as well as the detailed sample preparation methods of different techniques.

3.3. Experimental methods

3.3.1. Mechanical testing with real-time X-ray computed microtomography

3.3.1.1. Sample preparation procedures

For the preparation of C-ring samples for the *in situ* high-temperature C-ring compression tests, a CUTLAM®1.1 manual cutting machine was used. A slow speed diamond saw was used to extract specimens from the cladding tube to a C-ring geometry, which operated at 230 rpm. Specially, for the SiC_f-SiC_m cladding materials, the width of the C-ring samples is 4 to 5 mm; and for the Cr-coated Zircaloy cladding materials, the width of the C-ring samples is 2 to 3 mm. Representative examples for these C-ring samples, as well as the cladding tubes are presented in Fig. 3.2. All the C-ring samples were cleaned by water and ethanol, and air-dried more than three days before the *in-situ* mechanical experiments.

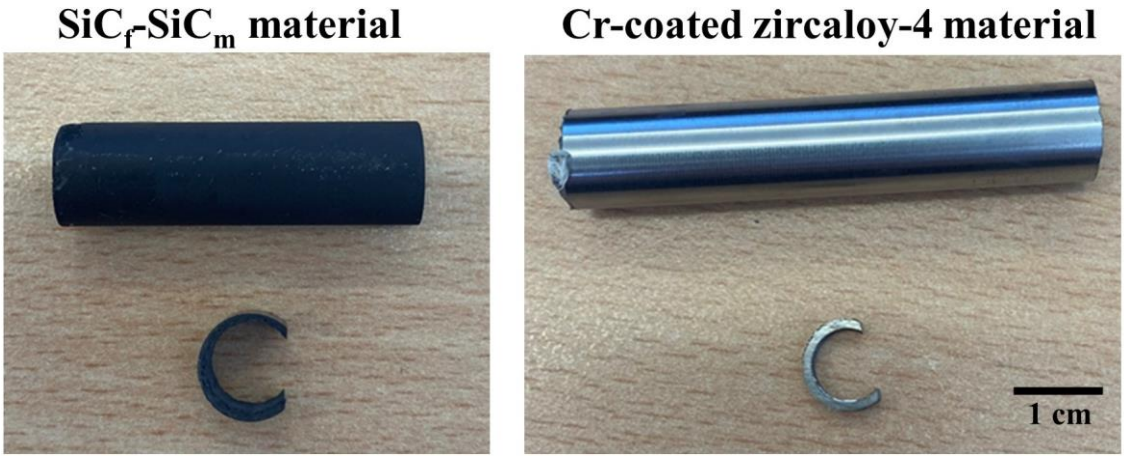

Figure 3-2. Representative examples show the cladding tube materials and the C-ring samples.

3.3.1.2. *In-situ* C-ring compression tests

In-situ high-temperature C-ring compression tests combined with simultaneous synchrotron μXCT imaging were performed at beamline 8.3.2 of the Advanced Light Source at the Lawrence Berkeley National Laboratory, U.S. During the tests, a unique high-temperature testing device was used, which enables mechanical testing at elevated temperatures up to 1600°C [223], [244], [245], facilitating the investigation of SiC_f-SiC_m materials and Cr-coated zircaloy-4 cladding materials under and beyond service-relevant conditions. A brief overview of the device is provided here and more detailed information of this can be found in refs [223], [244], [245]. The central part of the device is an aluminium chamber in a diameter of ~150 mm. Six ellipsoidal 150 W Halogen lamps were installed inside the chamber, generate a

uniform hot zone region of ~0.5 cm^3 at the chamber's centre to provide heating. During the experiment, all the samples were placed in the hot zone and aligned with a 300 μm thick aluminium window, enabling the transmission of the incoming X-ray beam with low absorption from the source to the detector. The testing temperatures were measured via a thermocouple attached to the outer surface of the C-ring specimens and were controlled by a programmable power supply. The compressive load was applied to the C-ring samples by the alumina ceramic plates, see Fig. 3.1, and the maximum hoop stress (σ_{ymax}, Eq. 3.1) was calculated according to ASTM Standard C1323-16 [246] from the relationship:

$$\sigma_{ymax} = \frac{P_U R}{btr_o}\left[\frac{r_o - r_a}{r_a - R}\right], \tag{3.1}$$

where P_U is the maximum applied load (peak load), b is the width of specimen. The average radius r_a and the term R are respectively defined by Eqs. 3.2 and 3.3.

$$r_a = \left(\frac{r_o + r_i}{2}\right), \tag{3.2}$$

$$R = \frac{r_0 - r_i}{ln\frac{r_o}{r_i}}, \tag{3.3}$$

It is noticeable that, according to the ASTM C1323-16, the recommended limit for the width of C-ring sample (b) is no more than twice of the sample's wall-thickness (t) to prevent the variation of circumferential stresses through the entire sample's width [246]. However, this constraint has been reported to be relaxed by Embree *et al.* [247] from their finite element analysis (FEA) on various b/t ratio combinations of C-ring samples under compression load, with detailed data points are tabulated in Table A.1 in the Appendices. In the current study, the b/t ratios of the C-ring samples are ~4.9 for the SiC_f-SiC_m materials with single layer outer/inner SiC coatings; ~3.8 for the SiC_f-SiC_m materials with multi-layers outer SiC coating; ~3.4 to ~3.8 for the CS and PVD Cr-coated materials, and ~3.5 to ~3.8 for the HCS and NCS Cr-coated materials. Based on ref. [247], on the sample's outmost surface, hoop stress is still as least an order of magnitude higher than the axial stress (stress in the Z direction in Fig. 3.1).

During the experiments, all the C-ring samples were monotonically loaded to failure in an argon (Ar) atmosphere. Different testing temperatures were employed for SiC_f-SiC_m and Cr-coated materials:

- SiC_f-SiC_m: for each type of material, two samples were tested at room temperature (RT) and two at 1200°C

- Cr-coated materials: for each type of material, two samples were tested at RT and two at 345°C

Real-time μXCT scans were taken at increasing loading stages. For high temperature tests, the experiments were conducted after the temperature stabilised at 1200 ± 5°C (for SiC_f-SiC_m materials) and 345 ± 2°C (for Cr-coated materials). For the process of tomographic acquisition, a white light X-ray beam in an energy range of 6 to 43 keV was utilised, along with a 2x long working distance Mitutoyo microscope lens, and a PCO Edge CCD camera (2560 × 2560 pixels) was used as a detector. Such setup resulted in a pixel size of 3.25 μm × 3.25 μm and a field of view of 8 mm × 4 mm, which centred on the middle section of the C-ring samples where maximum hoop stress occurred, as marked by dash line in Fig. 3.1. For each scan, 1969 projections were collected over a 180° rotation, the acquisition time for each projection is 30 ms and the total acquisition time is ~6 mins. The reconstruction of μXCT images was performed using a Gridrec algorithm [248] in the TomoPy package [249]. For each scan, the rotation centre was manually identified to remove any artefacts. To enhance the spatial resolution of each scan and reduce the fixed-pattern noise of the detector, a conventional flat field correction was applied [1].

During the experiment, the loading rig was operated in a displacement-control mode. Quasi-static loading was ensured by manually controlling of the loading speed of ~0.5 μm/s. During the scanning period (~6 mins) of each μXCT scan, the applied displacement was fixed, and load relaxations were observed for SiC_f-SiC_m materials tested at 1200°C, as well as Cr-coated materials tested at both RT and 345°C. For each specimen, a small pre-load (~5 N) was applied to prevent specimen movement during the scanning. Successive μXCT scans for each sample were collected at increasing load steps: in the case of SiC_f-SiC_m materials, five to eight scans were collected; for Cr-coated materials, four to six scans were collected.

3.3.1.3. μXCT data processing for 3D visualization

All the reconstructed scans were converted to stacks of 32-bit tiff images and were imported to open-source software ImageJ [250] for image pre-alignment and cropping to remove the background. For each type of the materials, the contrast of the cropped datasets was adjusted to a fixed dynamic range: -4.1 to 2.3 for SiC_f-SiC_m materials with single layer outer/inner SiC coatings, -3.2 to 1.8 for SiC_f-SiC_m materials with multi-layers outer SiC coating, and -2.7 to 2.1 for Cr-coated materials. The stacks of 32-bit tiff images are around 50 G in size. To markedly faster computing, all the adjusted datasets were converted to 8 bit and saved as raw data files (around 7 G of each dataset). Then, these raw data files were imported into Avizo

Lite software (version 2019.4) [251]. For improving volume renderings and reducing computation times, each scan was down-sampled by a factor of 2, which resulted in the increasing of effective voxel size to 6.50 µm.

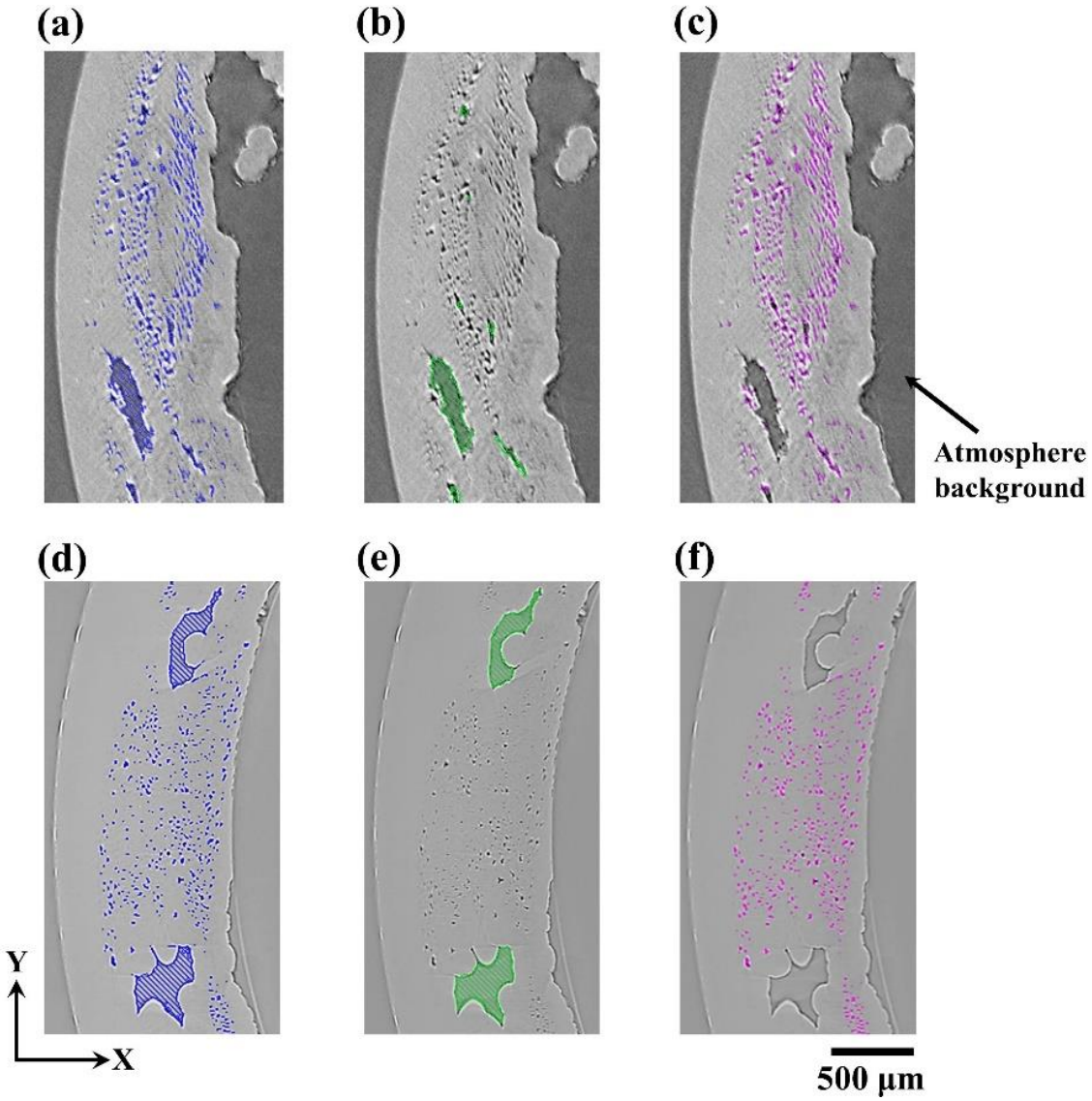

Figure 3-3. µXCT slices (of X-Y plane) taken from pre-load scan of C-ring samples for illustrating segmentation procedure of the pores inside SiC_f-SiC_m materials. (a) to (c) for the material with single-layer outer SiC coating: (a) all pores (delineated with a false blue colour; (b) macropores (delineated with a false green colour); (c) micropores (false pink colour); (d) to (f) for the material with multi-layer outer SiC coating: (d) all pores (delineated with a false blue colour); (e) macropores (delineated with a false green colour); (f) micropores (false pink colour).

The preload scan of each specimen of both types of SiC_f-SiC_m materials was used for manually segmentation and 3D visualization of the macro-size and micro-size pores via Image Segmentation Module [251]. The segmentation method is detailed described in the following text. For both types of SiC_f-SiC_m materials, the grey-levels of macropores and micropores are different when compared with other components (outer and inner SiC coatings, SiC matrices and remained atmosphere background) [158]. Therefore, by adjusting the threshold of the

masked voxels (0 to 255 in total) of material with single layer outer/inner SiC coatings into the range of 7 to 150, and material with multi-layers outer SiC coating in to 12 to 147, all the pores (including macropores and micropores) can be firstly segmented out, as presented in Fig. 3.3a and Fig. 3.3d, respectively. After that, a median filter in the Median Filter Module [251] is used for separating the macropores and micropores. The median filter is a non-linear digital filtering technique, often used for removing noise in the segmentation process. As the sizes of macropores are much larger than the micropores, by selecting the neighbourhood voxels of 26, and with three-time iteration , the macropores could first be segmented out from the dataset contains all pores, with examples presented in Fig. 3.3b and Fig. 3.3e. Then, by using the dataset contains all pores, minus out the dataset only contains macropores, the micropore can be selected out, Fig. 3.3c and Fig. 3.3f. The cracks inside all types of materials under loading were manually segmented out in the Segmentation Module [251], and visualized in 3D in Avizo Lite software (version 2019.4) [251].

3.3.1.4. Digital volume correlation

Local digital volume correlation (LA-DVC) method was utilized to generate 3D strain distribution maps at microstructural scale of SiC_f-SiC_m materials with single layer outer/inner SiC coatings under loading at both RT and 1200°C. For DVC analysis, all the reconstructed µXCT scans for the same specimen were aligned with the pre-load scan via the Image Registration Module [251], which is to remove any rigid body movement of the samples during loading. Then, they were cropped into the same dimensions (5213 × 2700 × 4913 μm^3) to ensure perfect positional overlap., and imported to the XdigitalVolumeCorrelation Module [251]. A three-step multipass approach was applied in this study where the side size of cubic sub-volume reduced from 208 voxels (676 µm, step one) to 104 voxels (338 µm, step two) and then 78 voxels (254 µm, step three) with 0 % overlapping of the dataset. For the DVC sensitivity analysis, the same pre-load scan for each sample was imported into XdigitalVolumeCorrelation Module [251] twice and correlated to each other, the three-step multipass approach was then applied to these scans. Therefore, the accuracy of DVC analysis was determined by using the mean calculated strain values, as zero strain was expected for the same pre-load scan.

3.3.2. Microstructural characterization techniques

3.3.2.1. Scanning electron spectroscopy

Fig. 3.4 displays the schematic of a typical SEM setup, which involves electron gun, anode, magnetic lens, backscattered electron detector, secondary electron detector, and sample stage. In the SEM, high-energy electrons are emitted by the electron gun, and subsequently converged by the magnetic lens. These converged electrons are then focused on the sample surface to generate signals [252].

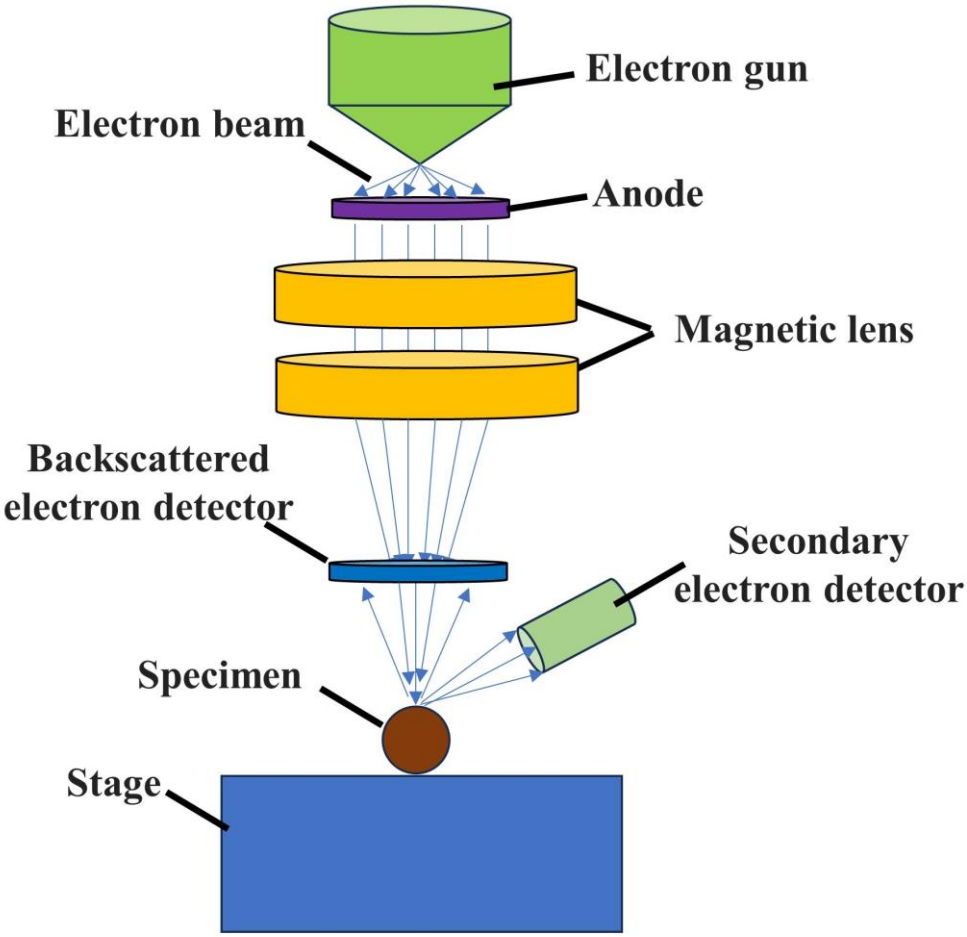

Figure 3-4. Schematic of a typical scanning electron microscope (SEM) set up. High-energy electrons are emitted by the electron gun, and subsequently converged by the magnetic lens and focused on the surface of the sample.

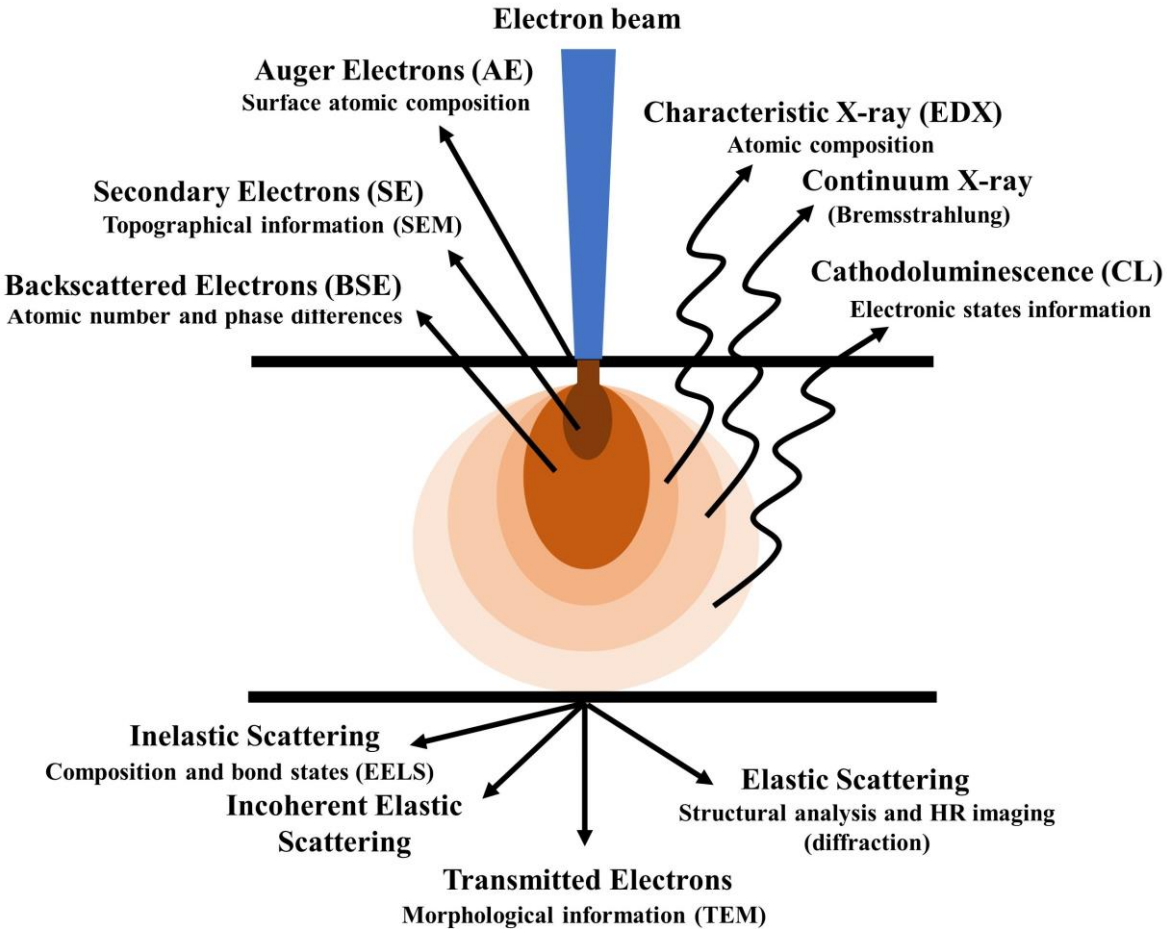

Figure 3-5. Schematic of the generation of different signals when electrons interacted with surface of the sample in a SEM.

When a high-energy electron beam impinges upon an object's surface, various signals are generated (Fig. 3.5), *e.g.*, secondary electrons (SE) for surface topographical information, backscattered electrons (BSE) for imaging sample's surface and contract of different phases, characteristic X-ray (EDX) for atomic composition, cathodoluminescence for electronic states information, transmitted electrons (TE) for structural information and others [253]. For the SE, they primarily originate from the excitation of electrons (by the primary beam) with weak bounding energies in the atomic close to the sample's surface [254], [255]. Therefore, they have a low kinetic energy (<50 eV). The SE are mainly used for imaging the surface morphology and topography [254], [255]; and the contrast difference in SE images is mainly affected by the variation of tomography, composition and channelling [255].

In current PhD project, for the SEM imaging of the as-received microstructures of both types of SiC_f-SiC_m materials, these samples were first mounted with a three-part fast-curing cold resin (Struers DuroCit 3 [256]). Mounted samples were automatically ground in a BUEHLER EcoMet™ 30 Semi-Automatic Grinder Polisher with 400-grit (~3 mins), 1200-grit (~4 mins)

and 2500-grit (~6 mins) sand grinding disks. Then, samples were polished by two water-based diamond suspensions: 3 μm (~5 mins, Struers MD-Dac polishing cloth) and 1 μm (~6 mins, Struers MD-Nap polishing cloth) and finally cleaned by water and ethanol, and dried in air for more than two days before the measurements. After these procedures, the surfaces of the samples are checked by the SEM imaging. They are smooth and flat with no obvious scratch can be observed, as presented in Chapter 4 and Chapter 5, respectively.

For the characterization of post failure crack patterns of all types of Cr-coated materials tested at both RT and 345°C, these samples were cleaned by water and ethanol, and dried in air for more than two days before the measurements.

In current PhD project, a Zeiss Evo MA10 LaB6 scanning electron microscope was used. For all the samples, the microscope was operated at a current of 62 μA, a 20 kV accelerating voltage, with a working distance of 8 to 11 mm. Specifically, for SiC_f-SiC_m materials, BSE mode was used; and SE mode was used for Cr-coated materials.

3.3.2.2. Electron backscatter diffraction mapping

Electron backscatter diffraction (EBSD) is a SEM-based technique, which has widely been used for characterization and quantification of crystallographic orientations, misorientations, texture trends, and grain sizes [257]. Fig. 3.6 displays a schematic showing the generation of EBSD patterns.

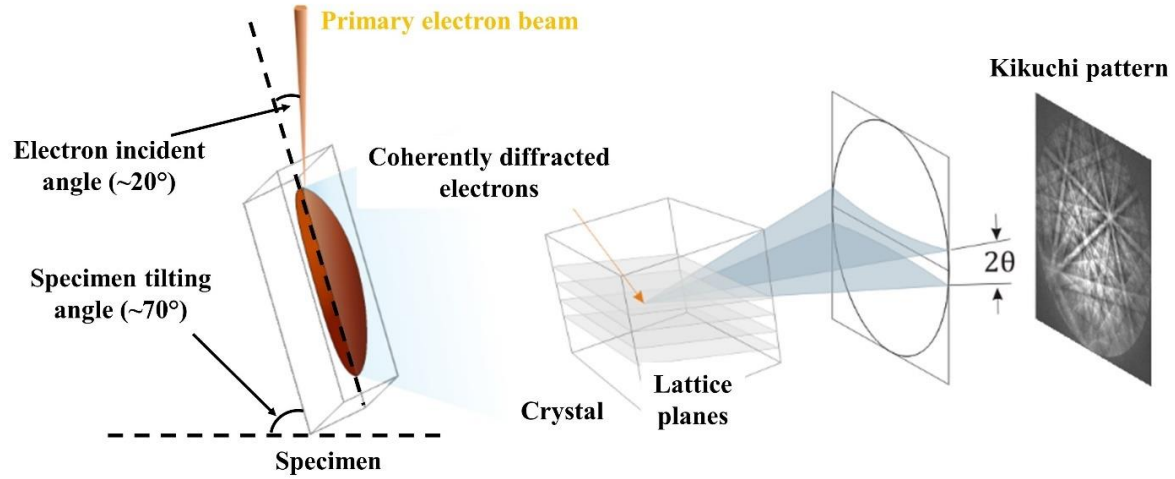

Figure 3-6. Schematic shows the formation of EBSD patterns. Figure is reproduced from ref [257].

In the SEM, the incident primary electron beam induces the emission of scattered electrons beneath the surface of the specimen, and these scattered electrons are distributed in all the directions in the interaction volume [258]. The incident scattered electron beams are

subsequently diffracted following the Bragg's law (Eq. 3.4), which corresponds to the local lattice plane arrangement:

$$n\lambda = 2dsin\theta, \tag{3.4}$$

Where n is an integer, λ is the wavelength of the electrons, d is the spacing between diffracting planes, and θ is the electron incident angle (typically ~20°). This diffraction results in the formation of a Kikuchi band that corresponds to the specific lattice plane, and this band exhibits an angular width of 2θ [257]. In the sample, all the lattice planes produce Kikuchi bands in the same manner, and subsequently generate the EBSD pattern. The EBSD pattern is, therefore, an analogue of crystal lattice planes in 2D projection, one representative example can be seen in Fig. 3.6. To maximize the yields of the diffracted electrons, a ~70° specimen tilling angle is commonly used. More detailed description of EBSD technique can be found in refs [259]–[263]. After the collection of EBSD patterns, a Hough transformation function was applied to transform the EBSD patterns from image space to Hough space, which eventually convert the straight Kikuchi bands to the more easily located points, following Eq. 3.5:

$$r = xsin\theta + ysin\theta, \tag{3.5}$$

Where r and θ are the parameters in the Hough space, and x and y are the parameters in the image space [264]. Subsequently, by comparing the measured data with the theoretically calculated inter-planar angles corresponding to specific lattice planes, the Kikuchi bands can be systematically indexed. This automated indexing process facilitates the determination of the phase structure and crystal orientation of the scanned materials [259].

In current PhD project, the EBSD is employed for the microstructural characterizations of several types of Cr coatings (*e.g.*, sizes, orientations and distributions of grains) of Cr-coated zircaloy-4 cladding materials. Samples are first mounted by a BUEHLER SimpliMet™ XPS1 hot compression mounting machine at a pressure of 3 MPa and temperature of 180°C with 180 s of both heating and cooling times. The mounted samples were then automatically ground in a BUEHLER EcoMet™ 30 Semi-Automatic Grinder Polisher with 400-grit (~2 mins), 600-grit (~2 mins), 800-grit (~4 mins), 1200-grit (~5 mins), 2500-grit (~5 mins) and 4000-grit (~5 mins) sand grinding disks, with each step grinded off the scratches from the previous step [265]. Then, samples were polished with 3 µm (MD-Nap cloth) in 1 µm water-based diamond suspensions (~4 mins at 260 rpm for each polishing step). After that, samples were further polished by a BUEHLER vibratory polisher for ~12 hrs with colloidal silica suspension, to achieve a flat surface with minimal surface deformation [266]. Finally, the surface of the samples was cleaned in water and ethanol and air-dried for more than three days prior to testing.

After these procedures, the surfaces of the samples are checked by the optical imaging. They are smooth and flat with no obvious scratch can be observed, as presented in Chapter 6 and Chapter 7, respectively. Surfaces are also checked by the EBSD mapping, with good Kikuchi patterns can be observed, Fig. 3.7.

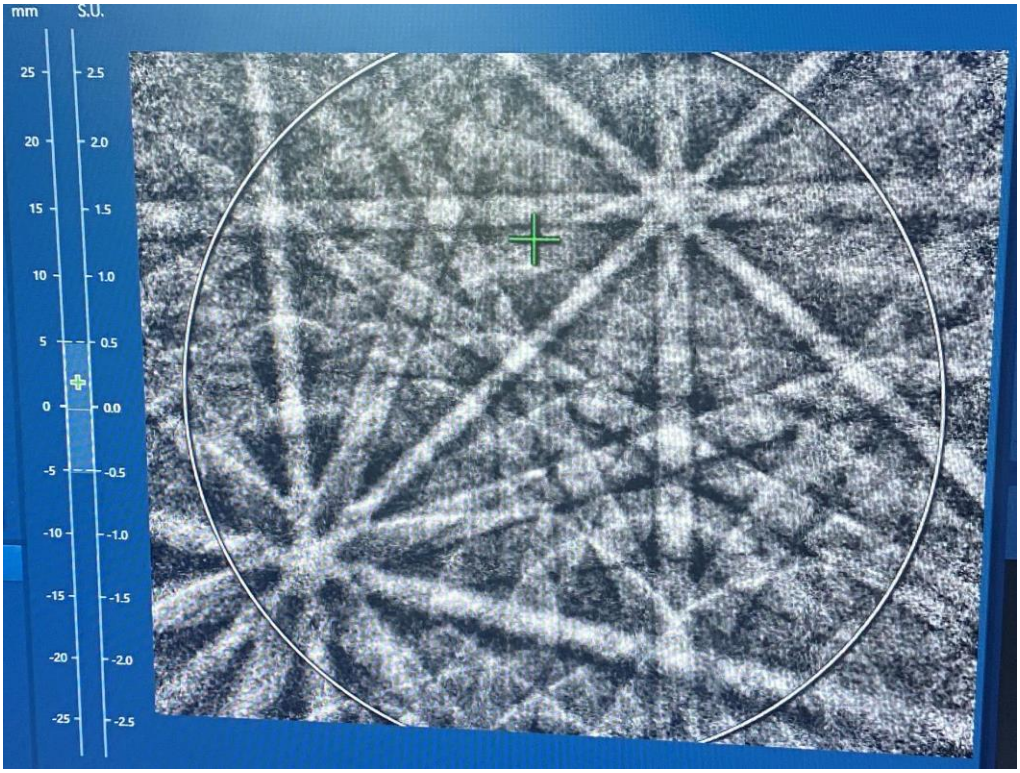

Figure 3-7. Kikuchi pattern of Cr coating after the polishing procedures.

A TESCAN Mira3 XMH variable pressure scanning electron microscope with an Oxford Instrument NordlyS EBSD detector was used to acquire the EBSD mapping of the polished cross-sections of the Cr coatings of the polished cross-sections of all types of Cr-coated Zircaloy materials. The equipment is in United Kingdom Atomic Energy Authority (UKAEA), It was operated in an accelerating voltage of 20 kV, and all each specimen was tilted to an angle of 70° during the test. The Oxford Instruments® HKL™ Channel 5™ software was utilised for the acquisition and analysis of the band contrast graphs, colour orientation imaging microscopy maps and the inverse pole figures (IPFs).

3.3.2.3. Focused ion beam scanning electron microscopy tomography

Focused ion beam scanning electron microscopy (FIB-SEM) tomography is another SEM-based technique [267]–[271], and a schematic of typical FIB-SEM dualbeam system is presented in Fig. 2.32. In the FIB-SEM dualbeam system, focused ion beam (commonly gallium ion, Ga+) is used for either imaging or micro-machining of the specimen, while

electron beam is used for SE/BSE imaging [258]. Ga+ ion beam is directed onto the material following its emission from the liquid metal Ga+ source with subsequently passing through a sequence of lenses. These energetic ion-material interactions lead to the generation of ions and secondary electrons emanating from the target material [272], [273].

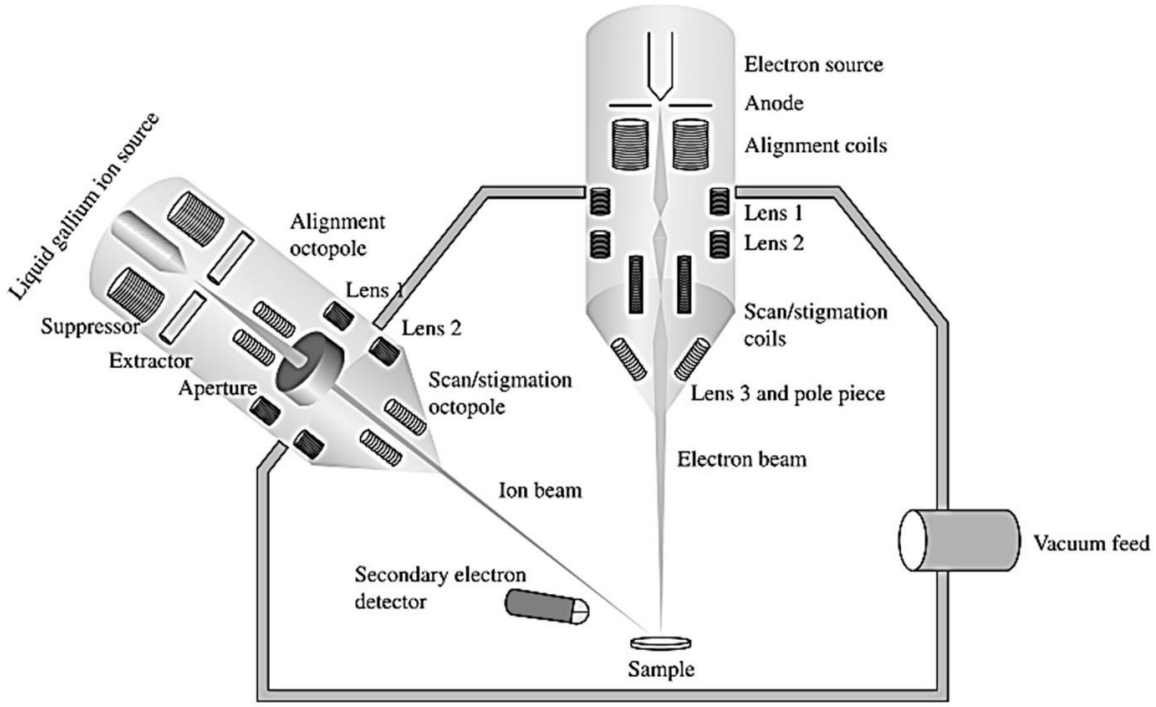

Figure 3-8. Schematic shows a typical focused ion beam scanning electron microscope (FIB-SEM) dualbeam system. Gallium (Ga) ion beams are emitted from a liquid metal ion source after traversing through a series of lenses. Simultaneously, electrons are emitted from an electron source positioned above and precisely focused onto the specimen's surface. SEM images of FIB-SEM tomography can be subsequently collected from secondary electron detector. Figure is reproduced from ref [274].

For the focused ion beam, when the current is low (*e.g.*, lower than 100 pA), the ion-induced low energy SE is sensitive to crystallographic orientation contrast (channeling contrast) [275]. However, when the current is high (*e.g.*, more than 6.5 nA), the ion beam can mill materials away from the surface of the sample through physical sputtering process resulting from atomic collision cascades. Therefore, micro-machining of the miniaturized features can be made via the FIB, including: microcantilevers [276], micropillars [277], trenches [278], and transmission electron microscope (TEM) foil [279].

In current PhD project, cross-sectional images are conducted by FIB-SEM, for investigating the crack behaviour in the Cr coatings of post-tested HCS and NCS materials at RT and 345°C. Samples were mounted on to an aluminium SEM specimen pin stubs (AGG301, Agar Scientific) by fast-drying silver suspension (Agar Scientific).

Plasma focused ion beam (P-FIB) milling combined with SEM imaging (FIB-SEM tomography) was conducted in a TESCAN AMBER X Plasma focussed ion beam scanning electron microscope in the UKAEA. The region of interest (ROI) was chosen at the coating crack areas for P-FIB sectioning. For protecting the surfaces and immediate sub-surfaces from being distorted and damaged by Ga+ bombardment during the FIB milling and imaging processes for each sample, a protective Pt layer (3 µm in thickness) was deposited over an 38 × 38 μm^2 area inside the ROI by the ion beam with a 30 kV voltage and a 1 nA current. A 38 × 40 × 30 μm^3 trench (in X-Y-Z dimension, with Z direction perpendicular to the sample surface) was then milled for each sample at 30 kV and 300 nA in the multiscan rectangular area milling mode for SEM imaging. After that, for each sample, a rough polishing procedure was performed at 30 kV and 100 nA at the milled cross-sections, followed by a final polishing procedure (performed at 30 kV and 30 nA). Finally, the cross-sectional SEM images of cracks were collected at a 20 kV accelerating voltage and with a 0.34 nA current in SE2 mode.

3.3.3. Measurement of local property by nanoindentation

The indentation technique was developed by Mohs in 1824 [280], who introduced a qualitative scale for assessing the hardness of diverse minerals based on the principle that a harder mineral could produce a scratch on a softer mineral [281]. Subsequently, various quantitative hardness testing methods were developed, by applying controlled indentations on a material of unknown mechanical properties using another material characterized by known geometrical and mechanical properties. By 1970s and 1980s, to meet the growing requirements for the characterization of mechanical properties of thin films and coatings, nanoindentation technique was developed [241], [282]–[285].

During the nanoindentation tests, the applied load and displacement are continually monitored and documented in the form of force-displacement curves [286], which enable the quantification of several mechanical properties of the tested materials. One typical load-displacement curve from nanoindentation test is presented in Fig. 3.9, where P_{max} is the maximum applied load; δ_{max} is the maximum displacement at the P_{max}; δ_c is the depth from the point of contact between the indenter and the specimen's surface to the apex of the indent, δ_{res} is the depth of residual impression after the indenter was removed; and S is the contact stiffness, derived from the gradient or slope of the upper part of the unloading curve [241], [287]. Additionally, based on the response of the tested material to the applied load, the load-displacement curve can be divided into the following regions [281]:

i. **Region AB**: elastic region, no residual impression remains on the surface following the removal of the applied load.
ii. **Region BC**: the mechanical behaviour changes from elastic to elastic-plastic.
iii. **Region CD**: completely plastic-region.
iv. **Region DE**: initial region of the unloading curve, the contact area remains constant as the displacement decreases.
v. **Region EF**: elastic recovery region, with the decreasing of the displacement, the impression's shape changes.

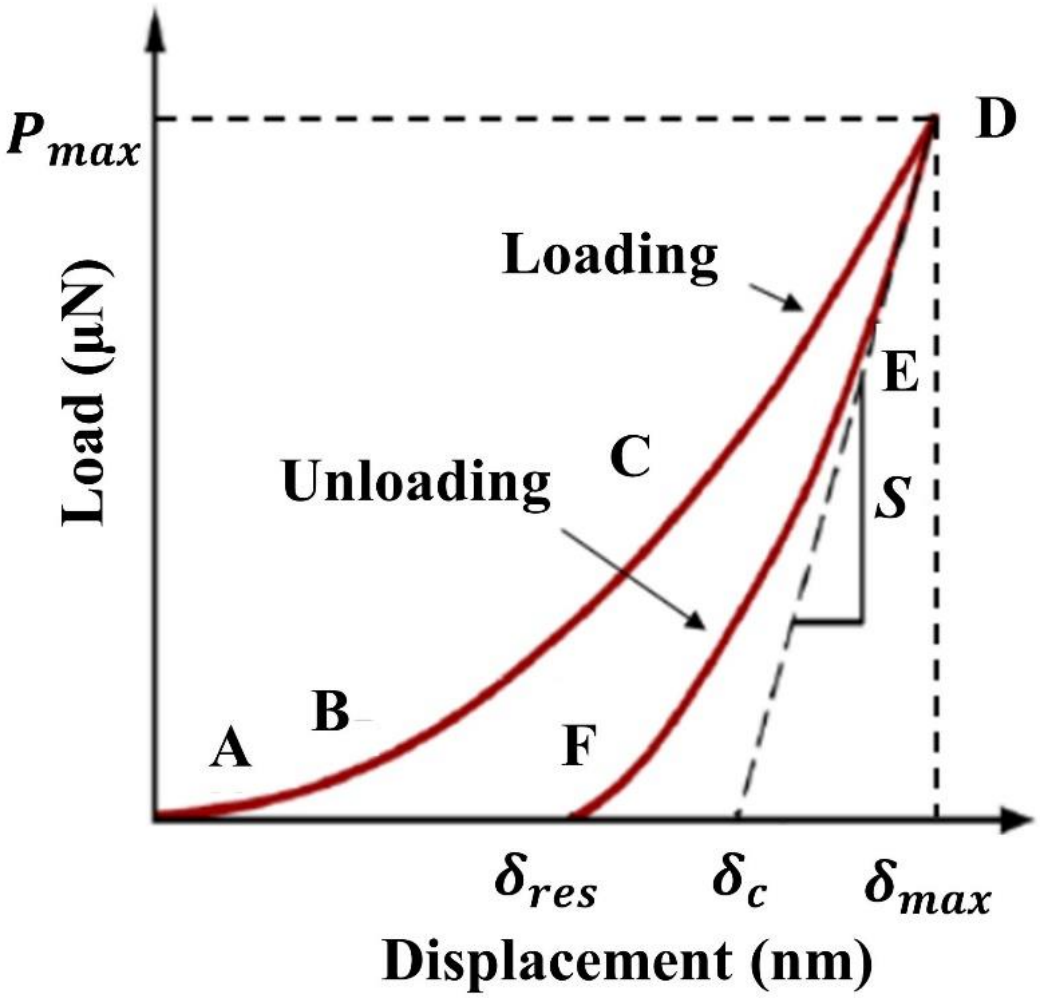

Figure 3-9. Schematic of a typical force and displacement curve of an elastic-plastic material indented by a pyramidal indenter. Figure is reproduced from ref [281].

Various methods have been used to derive the elastic modulus (*E*) and hardness (*H*) values from the load-displacement curve, including: slope-based method, energy-based method, dynamic method, loading curve method and unloading curve method (Oliver and Pharr method) [281]. Among them, Oliver and Pharr method [241] (proposed by Oliver and Pharr in

1992) is the most popular one. In the unloading curve method (Oliver and Pharr method), the E and H of the tested materials can be calculated via Eqs 3.6 to 3.8 [241], [288]:

$$H = \frac{P_{Max}}{A}, \tag{3.6}$$

$$\frac{1}{E_r} = \frac{1-\nu_i^2}{E_i} + \frac{1-\nu_s^2}{E}, \tag{3.7}$$

$$E_r = \frac{\sqrt{\pi}}{2\beta}\frac{S}{\sqrt{A}}, \tag{3.8}$$

where P_{Max} is the maximum load (mN), A is the projected contact area, E_i and ν_i are the Young's modulus and Poisson's ratio of the diamond tip, respectively. E_r and ν_s are the reduced modulus and Poisson's ratio of the tested specimen, respectively. β is a constant related to the indenter geometry.

In current PhD project, nanoindentation was used to measure the local properties of individual components in as-received SiC_f-SiC_m materials and as-received Cr-coated materials, respectively. For SiC_f-SiC_m materials, sample preparation procedure in Section 3.3.2.1 was used. As for Cr-coated materials, sample preparation procedure in Section 3.3.2.2 was used.

A Hysitron TI Premier nanoindenter with a Berkovich diamond tip (three-sided pyramidal shape) was used. Prior to all the measurements, A tip calibration process was conducted on standard fused silica, which generated a tip area function to correct for any geometrical deviations from an ideal Berkovich shape [14]. The polished specimen' cross-sections were mounted on the loading stage by a thin layer of crystalbond adhesive, and the location of each indent was then identified by using a 10 × objective lens. During the indentation process, a depth control mode was used with 100 nm s^{-1} of the loading/ unloading rate, and holding at the maximum indentation depth of 500 nm for 2 s. For the areas where multiple indents were conducted, the indents were spaced 10 μm apart. The hardness (H) and elastic modulus (E) were subsequently obtained via the Oliver and Pharr method [241], from Eqs. 2.11 and 2.12, respectively. In current study, E_i and ν_i are 1140 GPa and 0.07 for the Berkovich shape tip, respectively. And the widely reported ν_s of SiC (0.20 [289]), zircaloy-4 (0.30 [290]) and Cr (0.21 [5]) were used.

3.3.4. Measurement of residual stress

3.3.4.1. Residual stresses measured by Raman spectroscopy

Raman spectroscopy is a non-destructive technique and has widely used in various research areas, *e.g.*, material science [291], biology and life sciences [292], archeology [293],

environmental monitoring [294], and cultural heritage conservation [295]. The principle of Raman spectroscopy is based on the inelastic scattering of light during its interactions with the materials [296], which was theoretically predicted by Smekal in 1923 [297], and being experimentally observed by Raman in 1928 [298].

During the scattering process, the incident photons interact with the molecules, inducing perturbations in the electron cloud and leading to the formation of a transient energy state (virtual level), and immediately being scattered to another stable state [299]. Over 99% of the photons fall back to the initial energy state (ground level) with no energy exchange, resulted in the scattered light possesses the same frequency and wavelength as the incident light. This elastic scattering process is called Rayleigh scattering [300]. However, if the photons gain energy from the molecules, the frequency of the scattered light will be higher than the incident light, which is known as anti-Stokes Raman scattering [300]; if the molecules gain energy during the interaction, the scattered light's frequency will be lower than that of the incident light, and this process is known as Stokes Raman scattering [300]. A schematic of these three scattering processes is presented in Fig. 3.10. In the Raman spectra, the Raman shift (in wavenumber, cm^{-1}) can be calculated from the differences of incident and scattered light, following Eq. 3.9:

$$\Delta\omega = \omega_0 \pm \omega_R, \tag{3.9}$$

where ω_0 is the wavelength of incident light, ω_R is the wavelength of Raman scattered light.

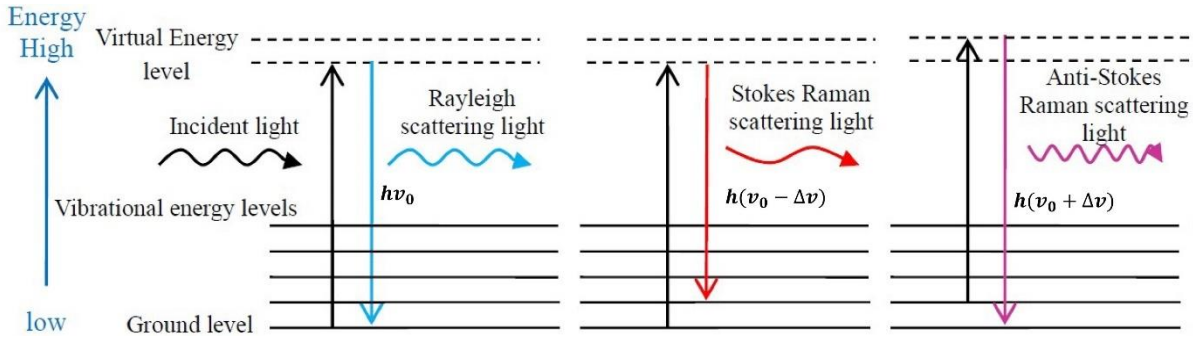

Figure 3-10. Schematic shows the scattering processes including: Rayleigh scattering, Stokes Raman scattering and anti-stokes Raman scattering. h is the Planck's constant, ν_0 is the frequency of the incident light, and $\Delta\nu$ is the variation of the frequency of scattered light (compared with that of incident light). Figure is reproduced from ref [301].

Fig. 3.11 displays the schematic of a typical setup of the Raman spectrometer. During the Raman measurements, monochromatic laser light emitted from various types of the sources (*e.g.*, Ar^+, He-Ne) is served as the incident light, and is directed into the microscope. This light subsequently passes through a objective lens and being focused on the specimen's surface, which consequently induces the emission of Raman scattering light from the specimen. This

Raman scattering light is then dispersed via a diffraction grating and directed to the charge-coupled-device (CCD). Note that, a filter is applied in this step to remove the Rayleigh scattering light. Finally, collected light intensity data are transmitted to a computer system, and the Raman spectrum is generated [302].

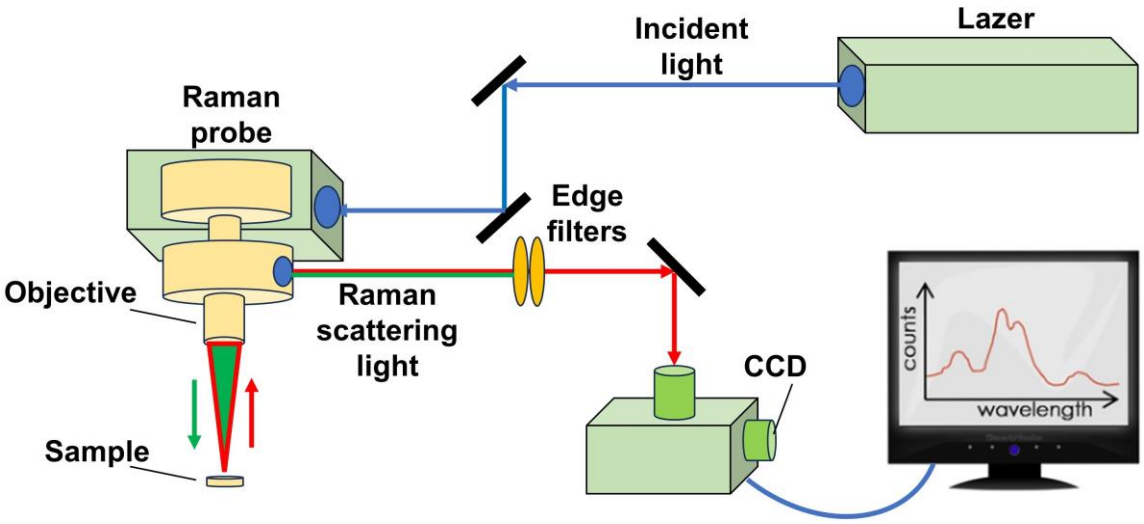

Figure 3-11. Schematic of a typical setup of the Raman spectroscopy system.

Generally, the peaks in Raman spectra contain material's information, for example, molecular vibration and crystal structure [303]. For instance, the Raman peak position could be used to determine the structure and for stoichiometric analysis. Specially, the shift of peak position has been widely used for determining residual stresses in various types of nuclear materials, including: SiC_f-SiC_m cladding materials [14], nuclear graphite [304] and TRISO particles [305]. The magnitude of residual stress (σ_R) can be calculated via Eq. 3.10:

$$\sigma_R = |\omega_0 - \omega_s| / \Delta C. \tag{3.10}$$

where ΔC is the stress conversion factor, ω_0 is stress-free peak position (cm^{-1}) and ω_s is measured peak position (cm^{-1}). Generally, a tensile stress shifts the Raman peak to a lower wavenumber, while a compressive stress shifts it to a higher wavenumber.

In current PhD project, Raman spectroscopy measurements were conducted on the polished cross-sections of as-received SiC_f-SiC_m materials to measure the residual stress of both SiC phase and carbon phase. Sample preparation procedure in Section 3.3.2.1 was used. A Renishaw inVia micro-Raman system with a 488 nm laser in a confocal mode was used. A long working distance 50 × Lecia lens was used to focus the laser light and collect the Raman scattered light within a ~0.6 to 0.7 μm diameter spot size in an ~20 mW incident power on the sample surface. Prior to the measurements, spectrometer was calibrated using a standard Si film with a known Si peak position at 520.3 cm^{-1}.

For both types of SiC_f-SiC_m cladding materials, the SiC phases in outer/inner SiC coatings, SiC matrix and SiC fibre mainly consist of β-SiC, with one type of transverse optical phonon mode (TO) at ~797 cm^{-1} [14], as well as small amount of α-SiC, with three types of TO at ~766 cm^{-1}, ~787 cm^{-1} and ~797 cm^{-1} [14]. Therefore, for SiC phase, the widely used ω_0 = 797 cm^{-1} of TO [14], and corresponding ΔC = 3.53 ± 0.21 cm^{-1}/GPa [306] of polycrystalline β-SiC were selected. As for carbon phase, the widely reported ω_0 = 1584.5 cm^{-1} graphitic mode (G) peak [14], and corresponding ΔC = 10 cm^{-1}/GPa [307] were used.

Measurements were performed on different locations of SiC_f-SiC_m materials and all the Raman spectra was scanned in the range of 200-2000 cm^{-1}. For the outer/inner SiC coatings and the multiple-layers outer SiC coating of SiC_f-SiC_m materials, respectively, the acquisition time was 10 s; for the SiC matrix between fibre bundles of both types of SiC_f-SiC_m materials, the acquisition time was 10 s; as for the SiC fibre (with excessive carbon phase inside), PyC interface area and SiC matrix next to the fibre of both types of SiC_f-SiC_m materials, the acquisition time was 20 s due to the relatively low SiC peaks' intensities compared with carbon parks. After the measurements, peak fitting was performed in Wire 5.3 software (with a combined Lorentzian + Gaussian function) to extract the wavenumber positions and Full-Width-at-Half-Maximum (FWHM), with one example presented in Fig. 3.12.

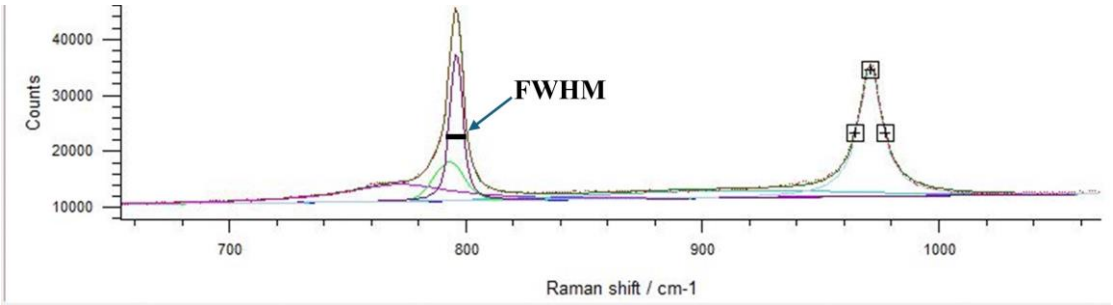

Curve Name	Centre	Width	Height	% Gaussian	Type	Area	ChiSq
Curve 1	771.414	54.4212	3122.22	0	Mixed	266901	0.934246
Curve 2	910.023	126.435	1368.45	100	Mixed	184174	
Curve 3	792.766	15.1531	7111.86	82.899	Mixed	124045	
Curve 4	795.849	6.38775	26889.4	47.9768	Mixed	228080	
Curve 5	971.344	12.3429	22894.3	0	Mixed	443879	

Figure 3-12. Representative example shows the peak fitting process.

3.3.4.2. Ring-core focused ion beam milling with digital image correlation

Focused ion beam-digital image correlation (FIB-DIC) method is a combination of various approaches, including: FIB milling, *in-situ* SEM imaging, digital volume correlation (DIC) and finite element modelling (FE); and has drawn growing interests for calculating residual strains and stresses in thin films and coatings [308]–[313].

Generally, FIB-DIC method involves four main steps:

i. Establishing patterning & image conditions. In this step, the sample's surface exhibit some random patterns (represented by the microstructural features), which serves as reference point for DIC displacement tracking; if the surface is too smooth, additionally random dot speckle patterns (usually by ion milling) are adopted on the surface [314]. Then, the milling conditions (*e.g.*, milling depth, milling rate) should be considered for the target materials mainly based on their composition and crystallinity [315], aiming at fully releasing the stresses in the materials, as well as minimizing the damages induced by ion beam [316]. Finally, to ensure the stability of both the machine and captured SEM images, it is imperative to turn on the system and keep it in an operational state for at least one hour before the experiment [316].

ii. FIB milling. The milling geometries are firstly selected, which commonly involve slot/trench [313], [317], double slot/H-bar [318], ring-core [319]–[321], and hole drilling [312], [322]. Then, for subsequent DIC analysis, SEM images are adjusted in a proper light and contrast range, as well as low noise [316]. Additionally, the drifting of sample could happen during the milling process. Therefore, it is recommended to conduct several repeat measurements on the sample to increase the accuracy of the results.

iii. DIC calculation. During this step, the images are compared with the reference image to generate the displacement fields, and subsequently calculate the residual strains [316]. If excessive drifting of sample happens during the milling, it will significantly affect the accuracy of the calculation of displacement and residual strain; thus, these data should be avoided.

iv. FE modelling & residual stress evolution. Various open-source FE models have been designed for corresponding milling geometries. The detailed principles and procedures for the calculation of stress during the milling process of various geometries (trench, double slot and ring-core) can be found in ref [316]. For the FE calculation, hardness and elastic modulus of the target material are two main factors to convert strain to stresses. However, for the target thin coating materials, their microstructures could be significantly different to the bulk materials; and the utilization of the macroscopic modulus value can be considered as an approximation but may not precisely reflect the underlying material behavior, consequently introducing inaccuracies in the determination of residual stresses [316]. Therefore, it is recommended to measure the

exact hardness and elastic modulus of the target materials, *e.g.*, using nanoindentation [1], [323] and microbeam bending method [324], [325].

In current work, FIB-DIC method with a ring-core geometry is used to calculate the residual stresses in the Cr coatings of HCS and NCS Cr-coated zircaloy-4 cladding materials. The sample preparation procedure described in Section 3.3.2.2 was used. After the polishing process, the samples were mounted on to an aluminium SEM specimen pin stubs (AGG301, Agar Scientific) by fast-drying silver suspension (Agar Scientific). The experiments were conducted in a FEI Helios NanoLab 600i Dualbeam workstation.

The first step is to locate a ROI in the centre part of the coating, after linking to the eucentric height and ensuring the X direction (horizontal) and Y direction (vertical) of the sample and the SEM image (in SE2 mode) were aligned. Electron deposition of random dot speckle patterns was then conducted using an Ga+ electron beam set at 10 kV and 0.34 nA, with a stage tilt of 52° and with SEM tilt correction enabled (disabled once electron deposition is completed). It takes ~90 s to finish the speckle pattern deposition process, with one example of the pattern after deposition presented in Fig. 3.13. Two concentric rings were drawn in the FIB view via circular patterning module, with 8.5 µm outer diameter, 6 µm inner diameter and 30 µm milling depth. The FIB ring core drilling process utilzed a Ga+ beam operated at 30 kV and 0.28 nA. To minimise any potential SEM imaging drift, SE2 imaging was set to fast scan mode of 50 ns dwell time, with a line time of 67.3 µs, frame time of 62.0 ms and a refresh rate 16.13 Hz. The resolution of all SEM images was set to 1024 × 884 pixels.

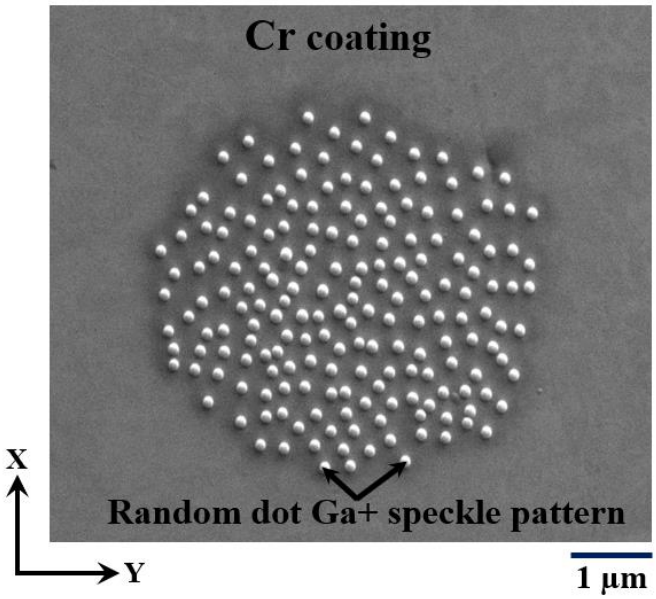

Figure 3-13. Image shows random dot speckle patterns deposited by Ga+ on the middle part of Cr coating of polished cross-sections of as-received HCS/NCS Cr-coated zircaloy materials.

During the experiment, the defined annulus region to be milled was moved over the ROI, and the drift of SEM imaging was checked again at the desired magnification of 12000x. An automated ring core drilling and image taking processes were applied, where the milling depth (30 µm) was divided into 100 steps, resulting in milling steps of ~ 0.3 µm thickness within the annulus region. Following each milling step, an SEM image was collected, which consisted if an average of 128 frames, enabling the less susceptible of the image to the charging-induced drift errors as the pixel dwell time was reduced. In each automated ring-core drilling process, around 90 SEM images were captured from both 0° and 90° scan rotation (~160 to ~180 images in total), resulting in the actual milling depth of ~27 µm.

The SEM images were subsequently imported into the open-source MATLAB-based 2D DIC programme NCORR [326] to calculate the relief of coating strain during the ring-core drilling process. Note that, drifting of the SEM images may occur during the milling process, and may milled off some dot patterns at the boundary. To minimize their influence of errors in DIC analysis, only the centre part of the dot patterns is selected for DIC analysis. Therefore, for DIC analysis, a subset-(interrogation window)-based local approach was employed in current work, which is a circular subset with 35 pixels of radius, 5 pixels of subset space and 5 pixels of strain interpolation radius.

For each ring-core, a strain relaxation profile was plotted against milling steps, ideally with the plateau in strain relief corresponding to total relaxation of residual stress in the gauge volume. The residual stresses inside the coating were then calculated from the average strains calculated by DIC method, and the measured E (measured by nanoindentation in current work) and v_s of Cr (0.21 [5]). These experiments were conducted on the middle of coating of the HCS and NCS materials, and three ring cores were performed for each type of the material.

3.4. Conclusion

This Chapter describes the materials investigated in current PhD project, including: two types of SiC_f-SiC_m cladding materials, and four types of Cr-coated zircaloy-4 cladding materials. The detailed experimental procedures are also included. The microstructures, local properties, residual stress distributions of two types of SiC_f-SiC_m cladding materials are investigated by several techniques, in the aim of illuminating the mechanical behaviours and failure processes of them tested at RT and 1200°C (by high temperature C-ring compression tests combined with real-time µXCT imaging). The results are presented respectively in Chapter 4 and Chapter 5. The microstructures and local properties of CS and PVD Cr-coated materials are studied via EBSD and nanoindentation, to understand their potential influences on the mechanical

behaviour and failure processes of these materials tested at RT and 345°C. These results are summarized in Chapter 6. As for the HCS and NCS Cr-coated materials, their mechanical behaviour and failure processes at RT and 345°C are investigated by high temperature C-ring compression tests with *in-situ* μXCT imaging, and the coating crack patterns are studied by SEM imaging FIB-SEM tomography, and with the results presented in Chapter 7. The local properties (by nanoindentation), microstructures (by EBSD), and residual stresses in the coating (by FIB-DIC) of HCS and NCS materials are also studied, which are to support the interpretation of the observations by μXCT imaging and SEM imaging, and the results are also presented in Chapter 7.

4. Mechanical behaviour of SiC_f-SiC_m cladding with single-layer outer/inner SiC coatings

In the current Chapter, the mechanical behaviour and failure processes of SiC_f-SiC_m cladding with single-layer outer/inner SiC coatings were investigated, with more comprehensive introductions of this material is presented in Section 3.2.1. The descriptions of C-ring compression experiments with *in-situ* μXCT imaging conducted at RT and 1200°C are presented in Section 3.3.1. The processing procedures of μXCT datasets are presented in Section 3.3.1.3. The procedures for measuring 3D strains by DVC methods is presented in Section 3.3.1.4. The procedures for estimating local properties by nanoindentation method is presented in Section 3.3.3. The procedure for estimating residual stresses by Raman spectroscopy is included in Section 3.3.4.1. The results are presented in the order of (i) the microstructure, local property and residual stress of as-received material; (ii) load-time curves, hoop strengths of outer coating and entire composite materials tested at each temperature; and (iii) failure processes and failure strengths of the materials tested at each temperature.

The results from current Chapter have been published in Materials & Design during the PhD project. The current Chapter contains minor additions and modifications compared to the published article by Yuan *et al.* [14]. Guanjie Yuan: Investigation, Formal analysis, Data curation, Writing – original draft, Writing – review & editing; J. Paul Forna-Kreutzer: Experiments; Peng Xu: Resources; Sean Gonderman: Resources, Review & editing; Christian Deck: Resources, Review & editing; Luke Olson: Resources, Review & editing; Edward Lahoda: Resources, Review & editing; Robert O. Ritchie: Resources, Funding acquisition, Supervision, Writing – review & editing; Dong Liu: Conceptualization, Resources, Methodology, Funding acquisition, Supervision, Writing – review & editing.

4.1. Microstructure of as-received material

Fig. 4.1 displays the typical microstructure of the as-received SiC_f-SiC_m material. As described in Section 3.2.1, single layer of SiC coating can be found on both outer and inner surfaces of the material, and they were measured to have a thickness of 201.13 ± 3.90 μm and 119.42 ± 6.38 μm, respectively. Note that the inner SiC coating is very torturous and hence it creates large voids at the inter surface of the cladding material, Fig. 4.1.

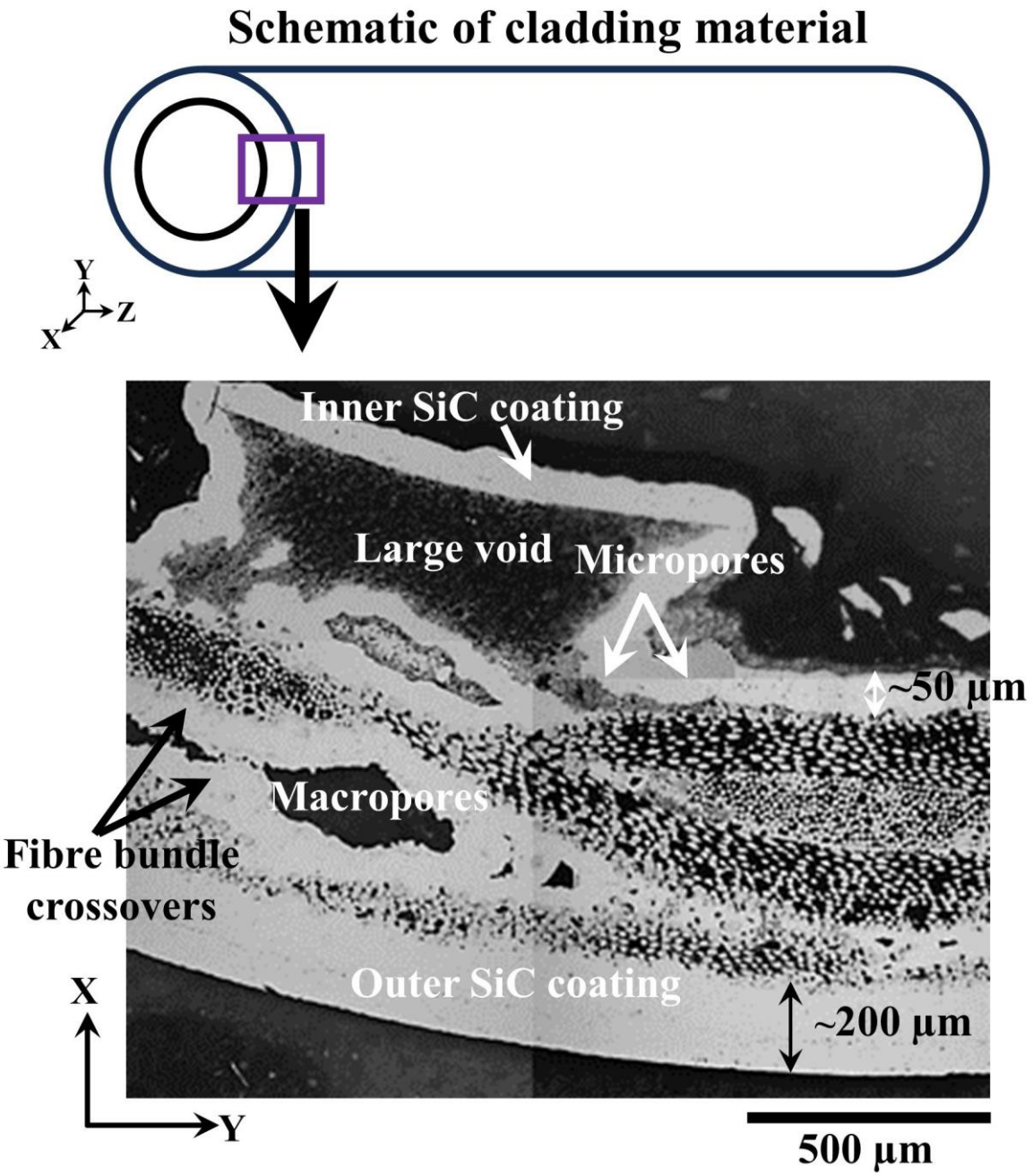

Figure 4-1. Optical image of the small polished cross-section of the as-received SiC_f-SiC_m material shows its typical microstructure. One schematic of the cladding material is also included to illustrate the location of the cross-section.

Two main types of pores were measured inside the material, including: (i) macropores are found in the matrix between fibre bundles (at the crossovers of fibre bundles), and (ii) micropores are found inside fibre bundles, Fig. 4.1.

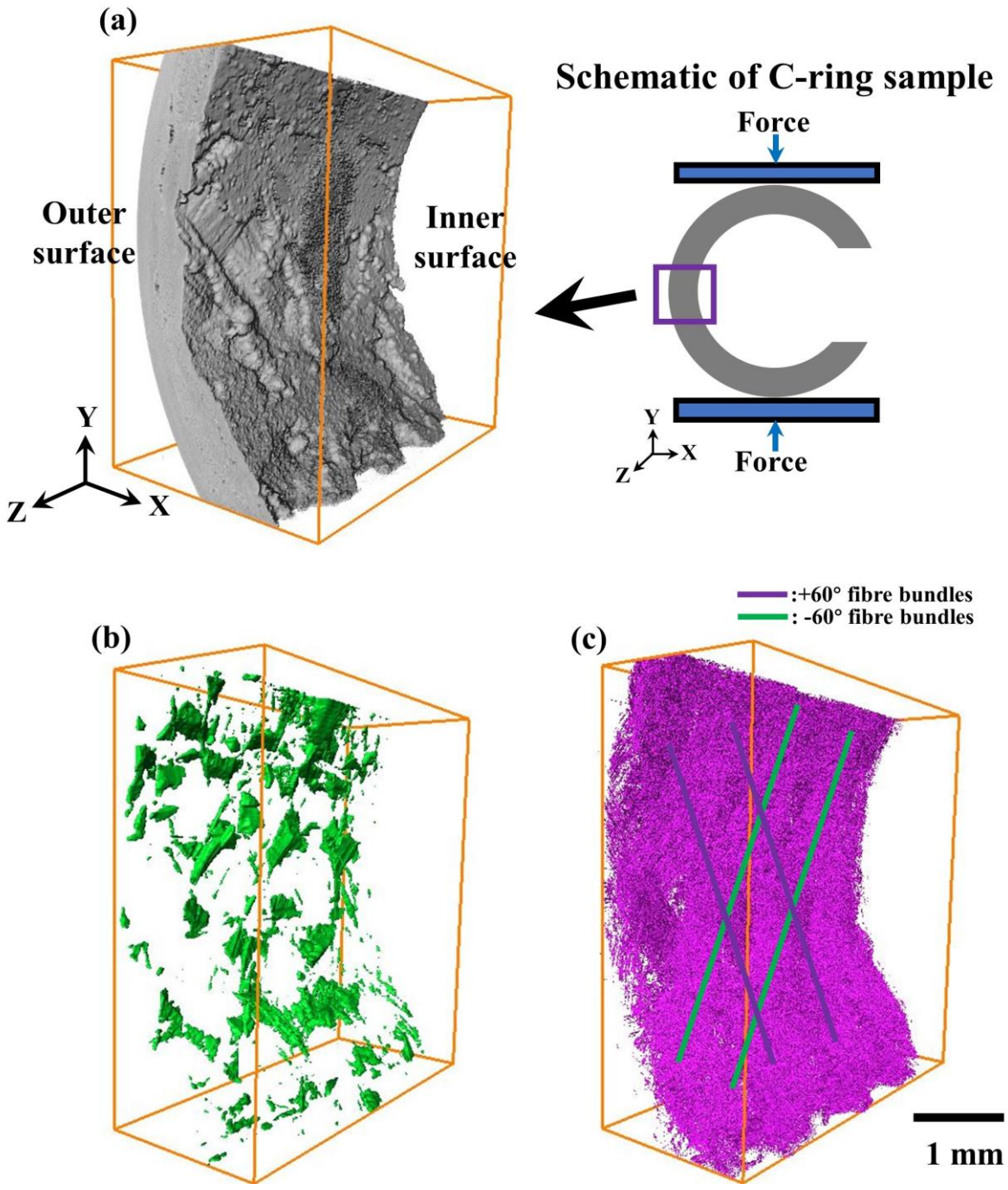

Figure 4-2. (a) to (c) are 3D visualization from reconstructed µXCT datasets of pre-load scan of the C-ring sample: (a) shows the material with tortuous inner surface, attributed to the large voids at the inner surface; (b) shows macropores and (c) shows micropores. Orientation of fibre bundles is also included.

The 3D visualization of the reconstructed µXCT scans of the as-received material, which collected at pre-load stage, is presented in Fig. 4.2a. Consistent with the observations from optical image (Fig. 4.1), the inner surface of the material is tortuous, Fig. 4.2a. For all the tested samples, the macropores and micropores in the as-received material have been segmented by the method described in Section 3.3.1.3, and they are visualized in 3D with examples are respectively shown in Figs. 4.1b and 4.1c. The volume fraction of these macropores and

micropores are estimated to be 2.56 ± 0.23% and 6.13 ± 0.52%, respectively. The larger voids, caused by the tortuous inner coating at the interface with the composite, were not included in the pore volume calculations. The pore structure/distribution and volume are consistent across all samples tested which indicates the volume studied is representative. This is further evident by the consistent mechanical behaviour in Section 4.3.

4.2. Local property and residual stress of as-received material

After the investigation of the microstructures of as-received material, a comprehensive analysis of the local property and residual stress distributions of individual components inside the as-received material were carried out, as they can potentially affect the mechanical properties and failure processes of the material.

4.2.1. Local property

Nanoindentation tests were performed on the polished cross-sections of the outer and inner SiC coating layers, the SiC fibres, the matrix within fibre bundles and the matrix between fibre bundles.

For both the outer and inner SiC coatings, a line-scan of indents, 10 μm apart, was collected across the thickness of the coating (from the coating's surface to the coating/composite interface), and 5 indents were performed in the same distance away from the surface of the coating. The results plotted in Fig. 4.3. It can be found that, across the thicknesses of both outer/inner SiC coating, no obvious difference in the values of hardness, H, and elastic modulus, E are measured, Fig. 4.3. Specifically, the outer coating has an average hardness of 31.9 ± 2.3 GPa and an elastic modulus of 338.8 ± 5.8 GPa, whereas for the inner coating the average hardness is 34.7 ± 0.6 GPa with an elastic modulus of 340.7 ± 3.3 GPa, *i.e.*, the outer and inner coatings have very similar properties.

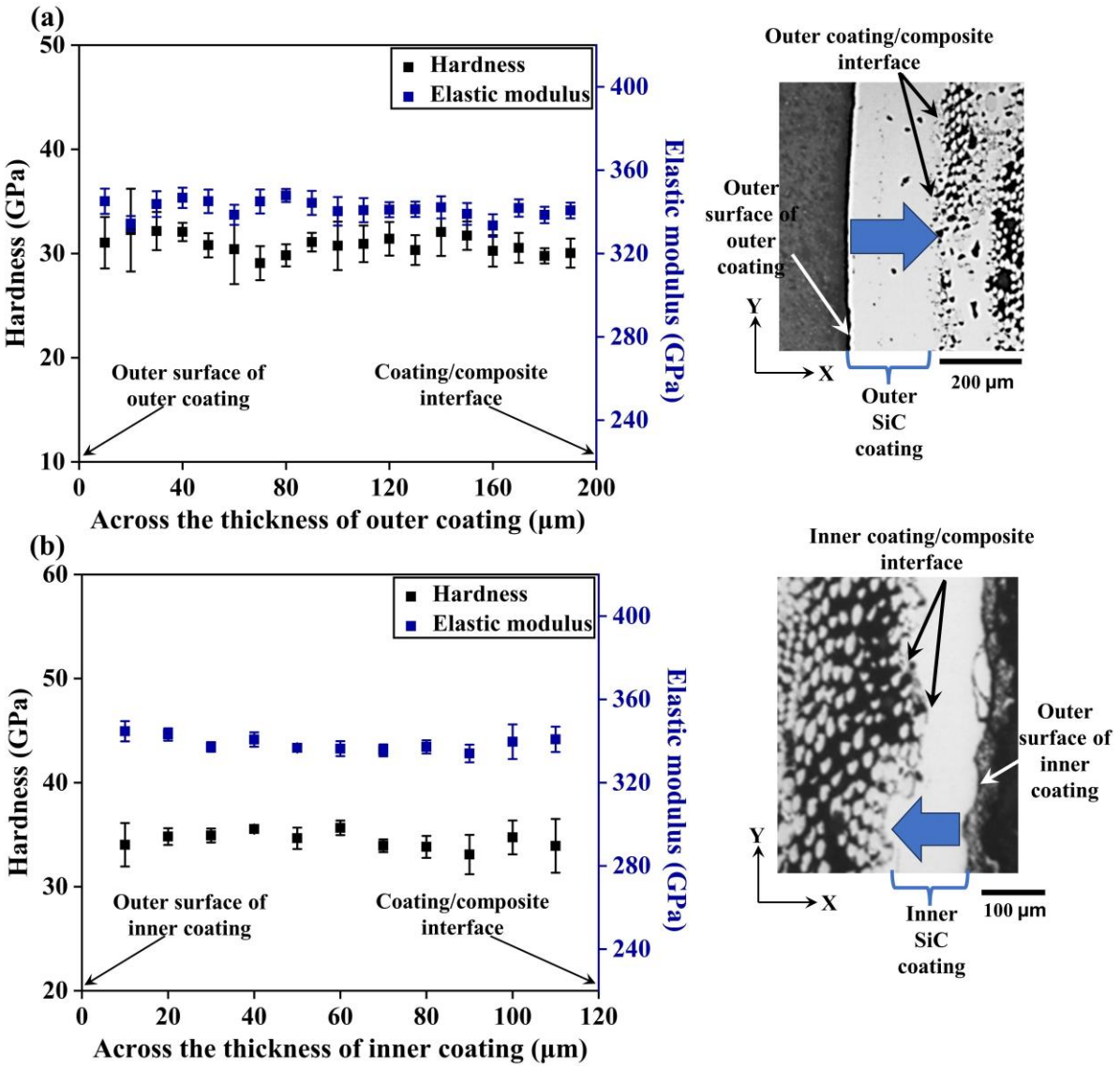

Figure 4-3. Hardness and elastic modulus values across the thickness of both outer and inner CVD SiC coatings of the polished cross-section of as-received material, with (a) for the outer SiC coating, and (b) for the inner SiC coating. Optical images of polished cross-sections of outer/inner SiC coatings are also included, with the blue arrows show the locations for line-indents.

For the matrix within a fibre bundle, the hardness and modulus were 33.2 ± 3.1 GPa and 331.0 ± 9.8 GPa, but for the matrix between fibre bundles, a slightly lower hardness of 32.0 ± 1.1 GPa and modulus of 310.7 ± 5.0 GPa were measured.

Table 4-1. Measured values of the hardness *H* and elastic modulus *E* in different areas of the polished cross-section of the as-received SiC_f-SiC_m cladding material.

Locations	*H* (GPa)	*E* (GPa)
Outer SiC coating	31.90 ± 2.26	338.82 ± 5.76
Inner SiC coating	34.68 ± 0.61	340.68 ± 3.29
Fibre	18.69 ± 3.18	174.64 ± 15.60
Matrix within a fibre bundle	33.21 ± 3.13	330.96 ± 9.78
Matrix between fibre bundles	31.99 ± 1.06	310.65 ± 5.03

4.2.2. Local residual stress

As described in Section 3.3.4.1, the SiC TO Raman peak at the position of 797 cm^{-1} is selected as the stress-free peak position, and the SiC TO peak at ~797 cm^{-1} is utilized to estimate the residual stress of the SiC phase of different components in the cladding material, including: outer SiC coating, inner SiC coating, SiC matrix and. Specially, for the both the outer and inner SiC coatings, a line-scan of measurements (in steps of 10 μm) was conducted across their thicknesses, as marked by blue arrow in the optical images in Fig. 4.4 and Fig. 4.5, respectively. 5 measurements were conducted at the same distance away from the surface of the coating.

Across the thickness of the outer SiC coating (with the measurement locations in Fig. 4.4), the detected Raman spectra are found similar, with one typical spectra presented in Fig. 4.4a. In the range of 500 cm^{-1} to 1000 cm^{-1}, three distinct TO peaks were observed: with one at ~764.8 cm^{-1}, one at ~788.2 cm^{-1} and one at ~795.8 cm^{-1}. One LO peak was observed at ~973 cm^{-1}. Some second order SiC peaks were detected in the range of 1300 cm^{-1} to 1800 cm^{-1}. As described in Section 3.3.4, CVD SiC mainly consists of β-SiC. Therefore, the TO peak at ~795.8 cm^{-1} was used to estimate the residual stress of β-SiC phase. Tensile residual stress is detected in the outer SiC coating, with the peak positions and corresponding residual stresses plotted in Fig. 4.4b. It can be found that, no obvious variation of the peak positions and corresponding residual stress across the thickness of the outer coating. The average peak position of the selected TO peak is 795.92 ± 0.43 cm^{-1}, with the average residual stress is 0.31 ± 0.13 GPa (via Eq. 3.10).

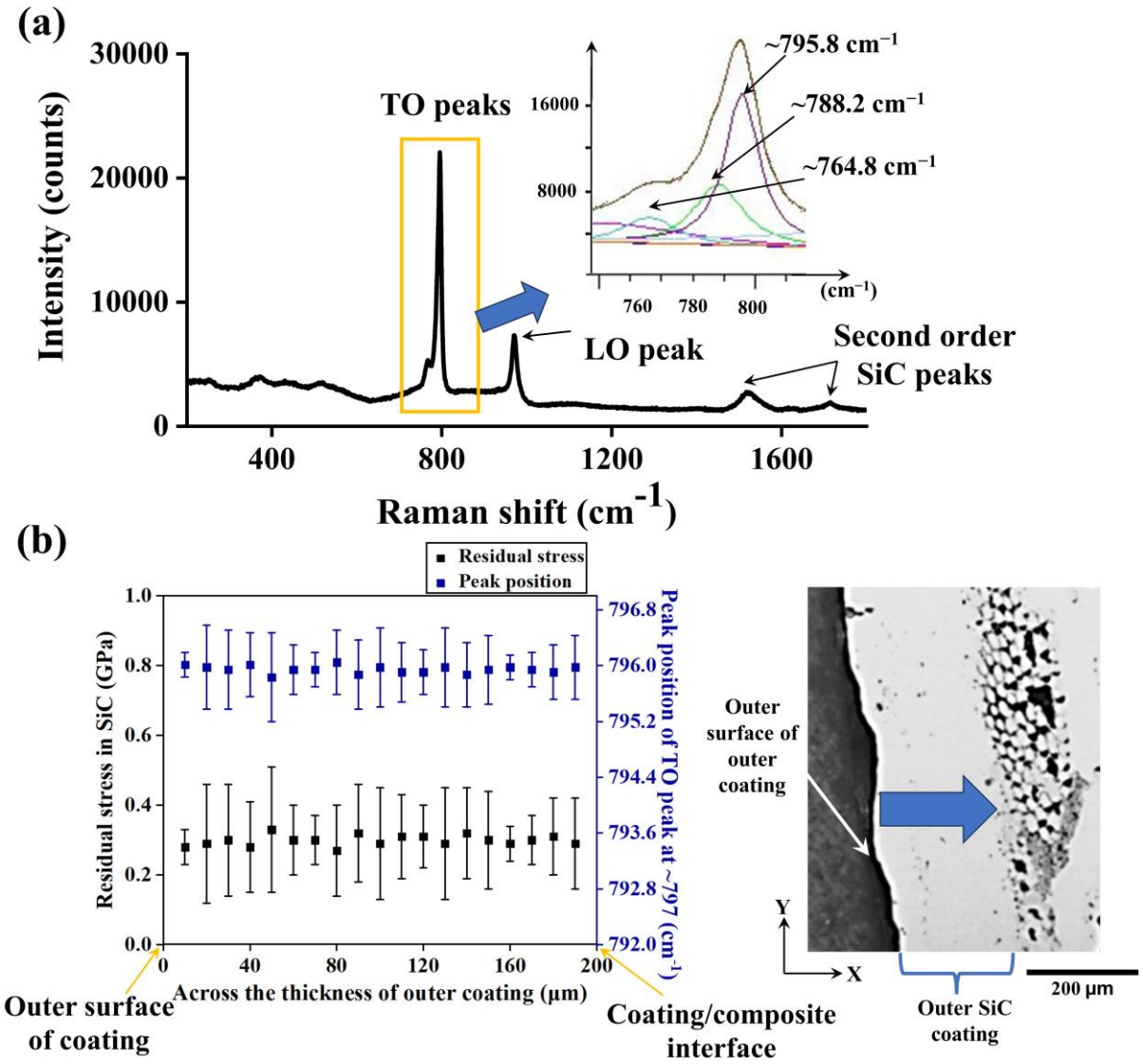

Figure 4-4. Raman measurements collected across the thickness of the outer SiC coating in the polished cross-section of as-received material. (a) Typical Raman spectra of SiC phase. (b) Peak positions of selected SiC TO peak (~797 cm^{-1}) and corresponding estimated tensile residual stresses of SiC phase across the thickness of the outer SiC coating.

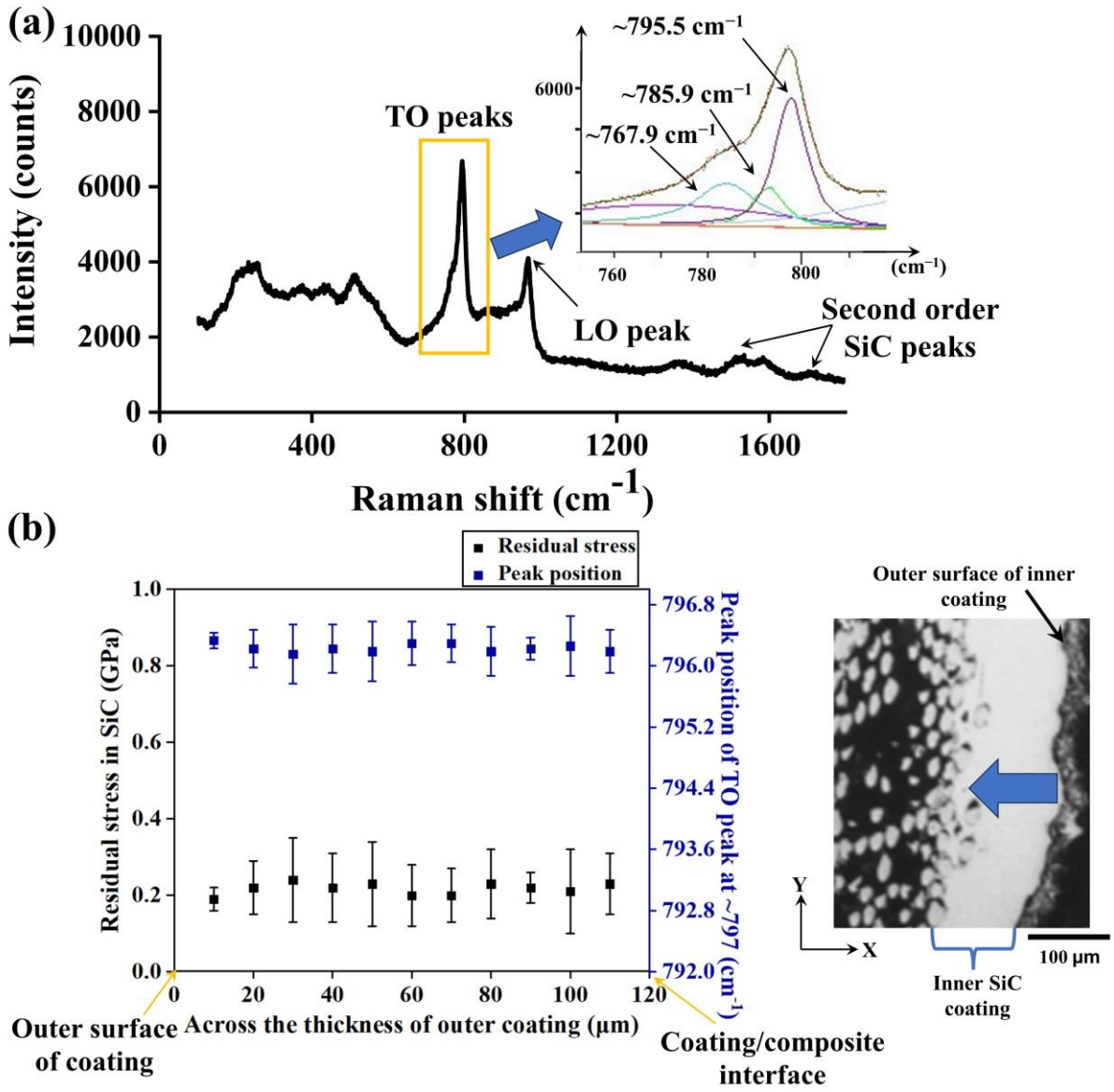

Figure 4-5. Raman measurements collected across the thickness of the inner SiC coating in the polished cross-section of as-received material. (a) Typical Raman spectra of SiC phase. (b) Peak positions of selected SiC TO peak (~797 cm^{-1}) and corresponding estimated tensile residual stresses of SiC phase across the thickness of the inner SiC coating.

The Raman spectra across the thickness of the inner coating were found similar, and Fig. 4.5a displays one typical spectra. Similar as the spectra in outer coating, three types of SiC TO peaks: at ~767.9 cm^{-1}, at ~785.9 cm^{-1} and at ~795.5 cm^{-1}, one type of SiC LO peak were also detected in the inner coating. Note that, obvious broadening of all the SiC TO peaks are detected in the inner coating, which indicates the relativity lower crystallinity of the SiC phase in the inner coating when compared with that in outer coating. Tensile residual stress is also detected in the inner SiC coating, and no obvious variation of the stress is found across the thickness of the inner SiC coating. The average peak position of the selected TO peak is 796.18 ± 0.42 cm^{-1}, with the average residual stress is +0.22 ± 0.12 GPa (via Eq. 3.10).

The Raman spectra collected for SiC matrix between fibre bundles are found similar (locations are marked in black arrows in Fig. 4.6), with one typical Raman spectra can be found in Fig. 4.6. In the range of 500 cm^{-1} to 1000 cm^{-1}, three types of TO peaks were also detected. However, significant broadening of the LO peak is observed, Fig. 4.6. The average peak position of the selected TO peak is 795.97 ± 0.35 cm^{-1}, with the average residual stress is +0.29 ± 0.10 GPa (via Eq. 3.10).

The detailed Raman peak position of selected SiC TO peak, and the corresponding residual stress values of SiC phase at these locations are tabulated in Table 4.2.

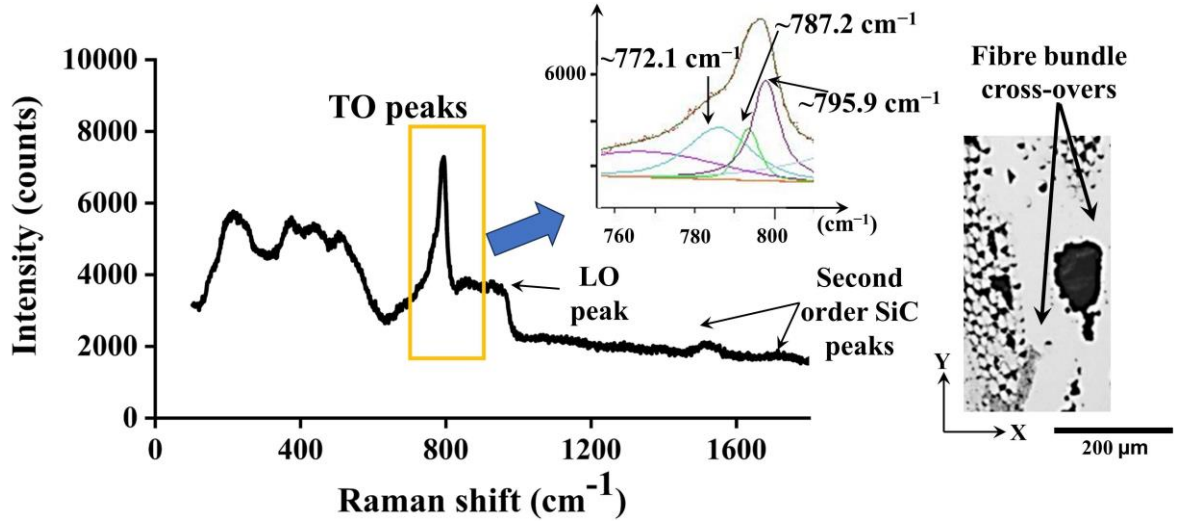

Figure 4-6. One typical Raman spectra collected in the matrix between fibre bundles in the polished cross-section of as-received material.

Table 4-2. Raman peak positions of the SiC TO band (at ~797 cm^{-1}) and carbon G band with the corresponding calculated residual stresses of β-SiC phase and carbon phase('+' for tensile stress and '−' for compressive stress).

Locations	**Raman peak position of SiC TO band (cm^{-1})**	**Residual stress in SiC phase[a] (GPa)**	**Raman peak position of carbon G band (cm^{-1})**	**Residual stress in carbon phase[b] (GPa)**
Outer SiC coating	795.92 ± 0.43	+0.31 ± 0.13	-	-
Inner SiC coating	796.18 ± 0.42	+0.22 ± 0.12	-	-
Matrix between fibre bundles	795.97 ± 0.35	+0.29 ± 0.10	-	-
Matrix next to fibre	796.17 ± 0.33	+0.24 ± 0.10	-	-
Fibre centre	794.54 ± 0.66	+0.70 ± 0.20	1587.89 ± 0.21	-0.34 ± 0.02
Fibre edge	794.67 ± 0.63	+0.66 ± 0.19	1588.29 ± 0.26	-0.38 ± 0.03
PyC interphase	795.01 ± 0.88	+0.56 ± 0.27	1590.07 ± 0.68	-0.62 ± 0.07

[a] calculated using Eq. 3.10, with ΔC being 3.53 ± 0.21 cm^{-1}/GPa [306]
[b] calculated using Eq. 3.10, with ΔC being 10 cm^{-1}/GPa [307]

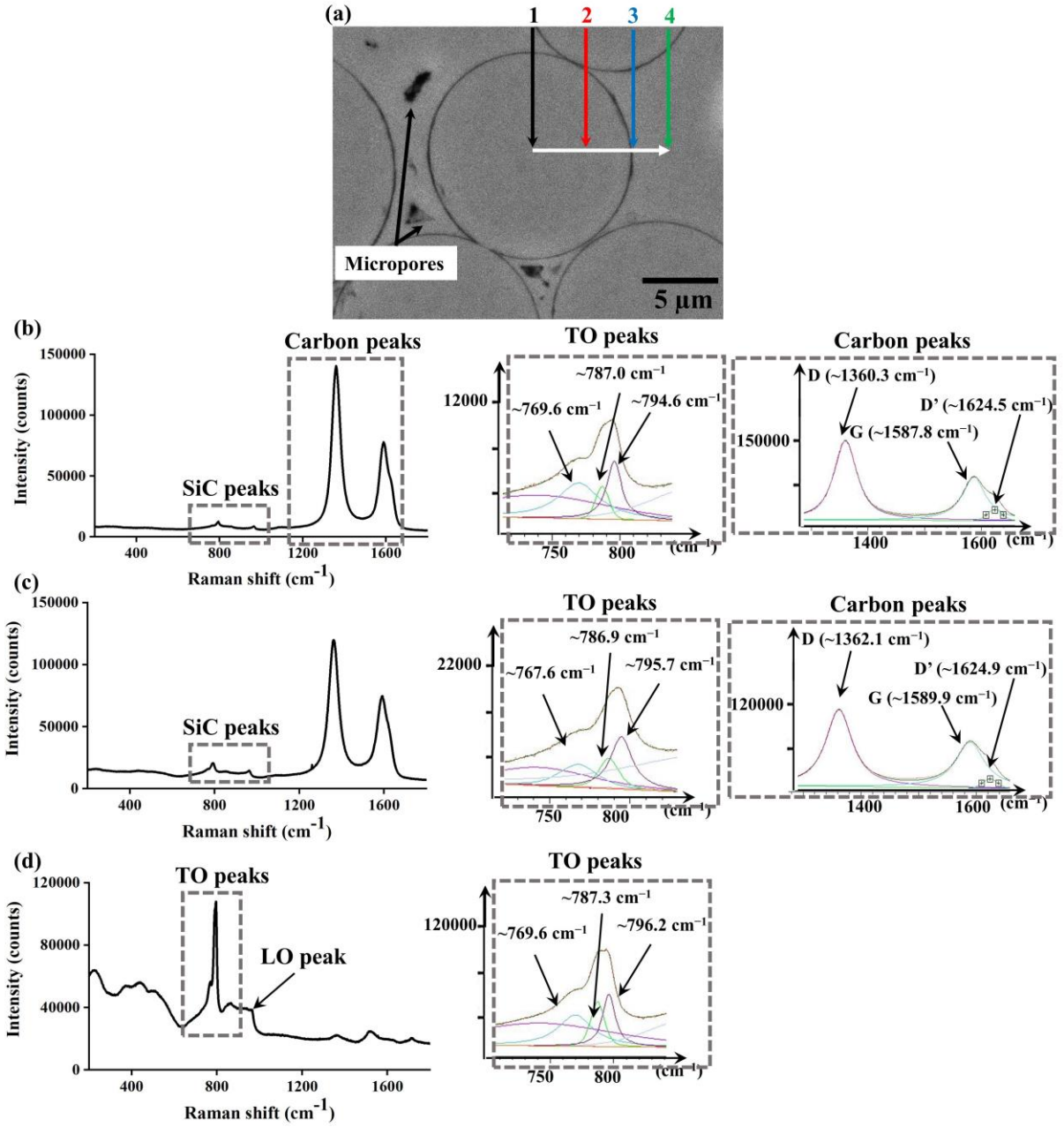

Figure 4-7. (a) Polished cross-sectional SEM image of one fibre showing the location of four measurements taken along the radial direction of the fibre; (b) to (d) are Raman spectra of different locations on the polished fibre cross-section: (1) centre of fibre, (2) middle point between the centre and the periphery of the fibre, (3) PyC interphase area and (4) matrix next to the fibre; with (b) for locations 1 and 2, (c) for location 3 and (d) for location 4. The insert images show the fitting of individual peaks of SiC phase and carbon phase.

For the SiC fibre and SiC matrix next to the fibre, Raman spectra were collected along the radial direction of the fibre at four locations: (1) at the centre of the fibre, (2) at the middle point between the centre and the periphery of the fibre, (3) on the PyC interphase layer, and (4) the matrix adjacent to the fibre, Fig. 4.7a. For locations 1 and 2, the Raman spectra were found similar, with one representative example presented in Fig. 4.7b. And the Raman spectra of locations 3 and 4 are presented in Fig. 4.7c and Fig. 4.7d, respectively. Inside the fibre at

locations 1, 2 and 3, three SiC TO peaks (700–1000 cm^{-1}) and three types of carbon peaks (disorder mode (D) peak at ~1360 cm^{-1}, graphitic mode (G) peak at ~1584.5 cm^{-1} and D' peak at ~1620 cm^{-1}) are apparent, but the carbon peaks are absent in the matrix (location 4) as there is no carbon phase, Fig. 4.7d. Moreover, shift of the SiC TO peak (~797 cm^{-1}) along the radial direction of fibre was observed, from ~794.6 cm^{-1} in location 1 to ~796.2 cm^{-1} in location 4. Shift of carbon G peak was also observed, from ~1587.8 cm^{-1} in location 1 to ~1589.9 cm^{-1} in location 3. These all indicate the variation of residual stress inside β-SiC phase and carbon phase along the fibre radial direction. Therefore, 5 Raman line scans were collected along the fibre radial direction (from location 1 to location 4), in steps of 1 μm, Fig. 4.8a.

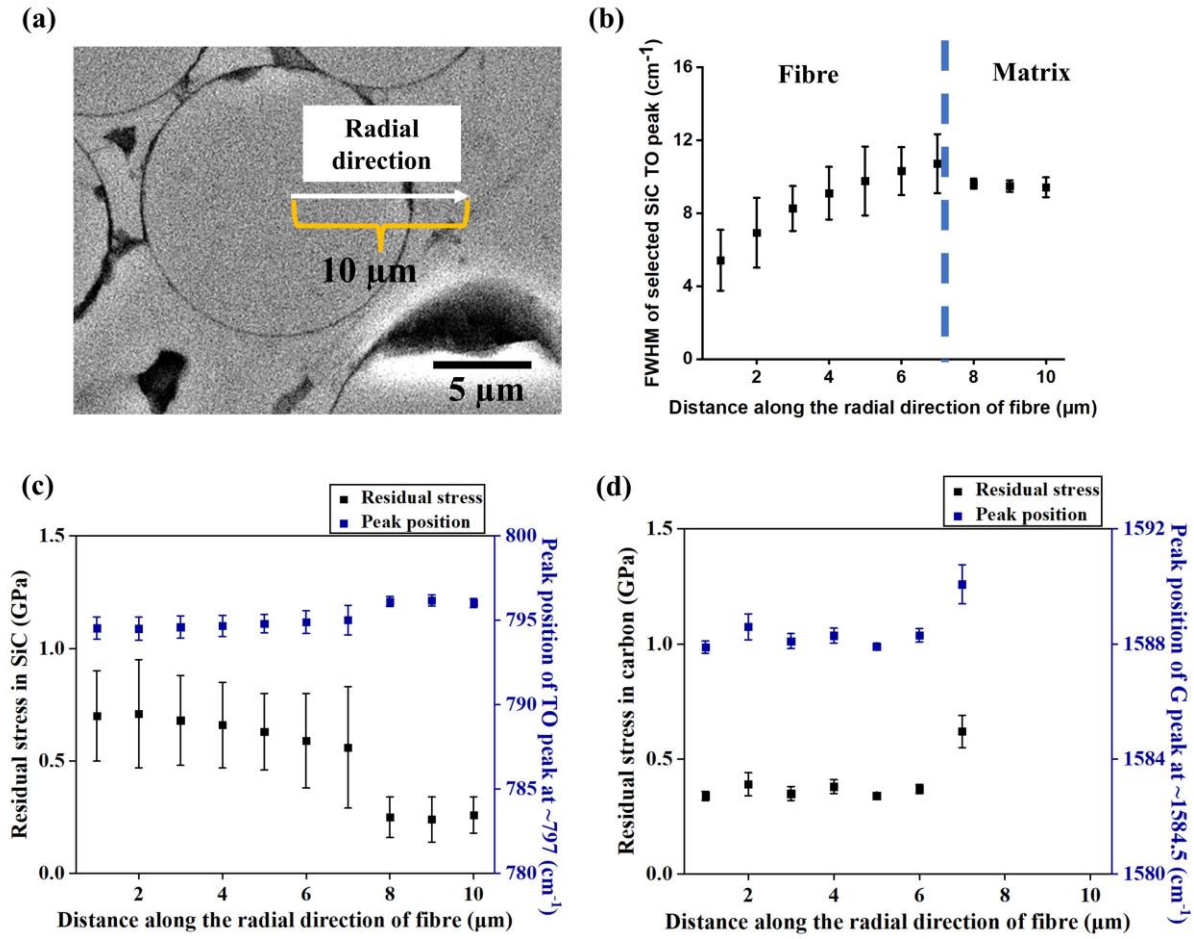

Figure 4-8. (a) Polished cross-sectional SEM image shows line-scan of Raman measurements taken along the radial direction of the fibre; (b) shows the FWHM of SiC TO peak at ~797 cm^{-1} along the fibre radial direction; (c) shows peak positions of selected SiC TO peak (~797 cm^{-1}) and corresponding estimated tensile residual stresses of SiC phase; and (d) shows peak positions of selected carbon G peak (~1584.5 cm^{-1}) and corresponding estimated compressive residual stresses of carbon phase.

The FWHM of SiC TO peak at ~797 cm^{-1} along the radial direction of fibre is presented in Fig. 4.8b. In the fibre, the FWHM of the peak steadily increases from fibre centre (~5.1 cm^{-1}) to the PyC interphase area (~11.9 cm^{-1}). It then become constant at ~9.4 cm^{-1} in the matrix

next to fibre, Fig. 4.8b. Tensile residual stress was measured of β-SiC phase inside the fibre. It steadily decreases along the radial direction of the fibre: from ~0.70 GPa at fibre centre, to ~0.56 GPa at the PyC interphase area; and then becomes consistent at ~0.24 GPa at the matrix next to fibre, Fig. 4.8c. Compressive residual stress was measured of carbon phase inside the fibre. It stays constant at around -0.4 GPa inside the fibre, and increases to around -0.6 GPa at the PyC interphase area, Fig. 4.8d. The measurements are compared with literature data in detail in Section 4.6.

4.3. Mechanical properties of SiC_f-SiC_m material at RT and 1200°C

The load-time curves for SiC_f-SiC_m materials under C-ring compression tests at RT and 1200°C, are plotted in Fig. 4.10. Samples S1-1 and S1-2 were tested at RT and samples S1-3 and S1-4 were tested at 1200°C. The detailed testing sequences in Table A.2 in the Appendices.

It can be found that, the measured behaviour was relatively consistent despite the limited number of samples tested. Load drops (sudden decrease in load when sample was in a fixed displacement) were observed for all tested samples (at both temperatures) during the loading process, which was found to correspond to the formation of cracks by the X-ray tomography results (will detailed presented in Section 4.4).

For sample S1-1 tested at RT, the first load drop (~5 N) occurred at ~21 N (~0.65 P_U), as marked in Fig. 4.9a, followed by the second load drop at ~25 N (~0.70 P_U), the third load drop at peak load 33.71 N (P_U) and a final post-peak load drop (more than 15 N) at 0.84 P_U. Similar behaviour was observed for another RT sample (S1-2), the first load drop occurred at ~22 N (~0.65 P_U, very similar to that occurred at ~0.62 P_U for sample S1-1); then the second load drop occurred at ~23 N (~0.68 P_U); two more load drops (~26 N, ~0.77 P_U and ~32 N, ~0.94 P_U) occurred before the peak load, until the final large load drop (more than 20 N) occurred at peak load (~34 N, P_U), Fig. 4.9a.

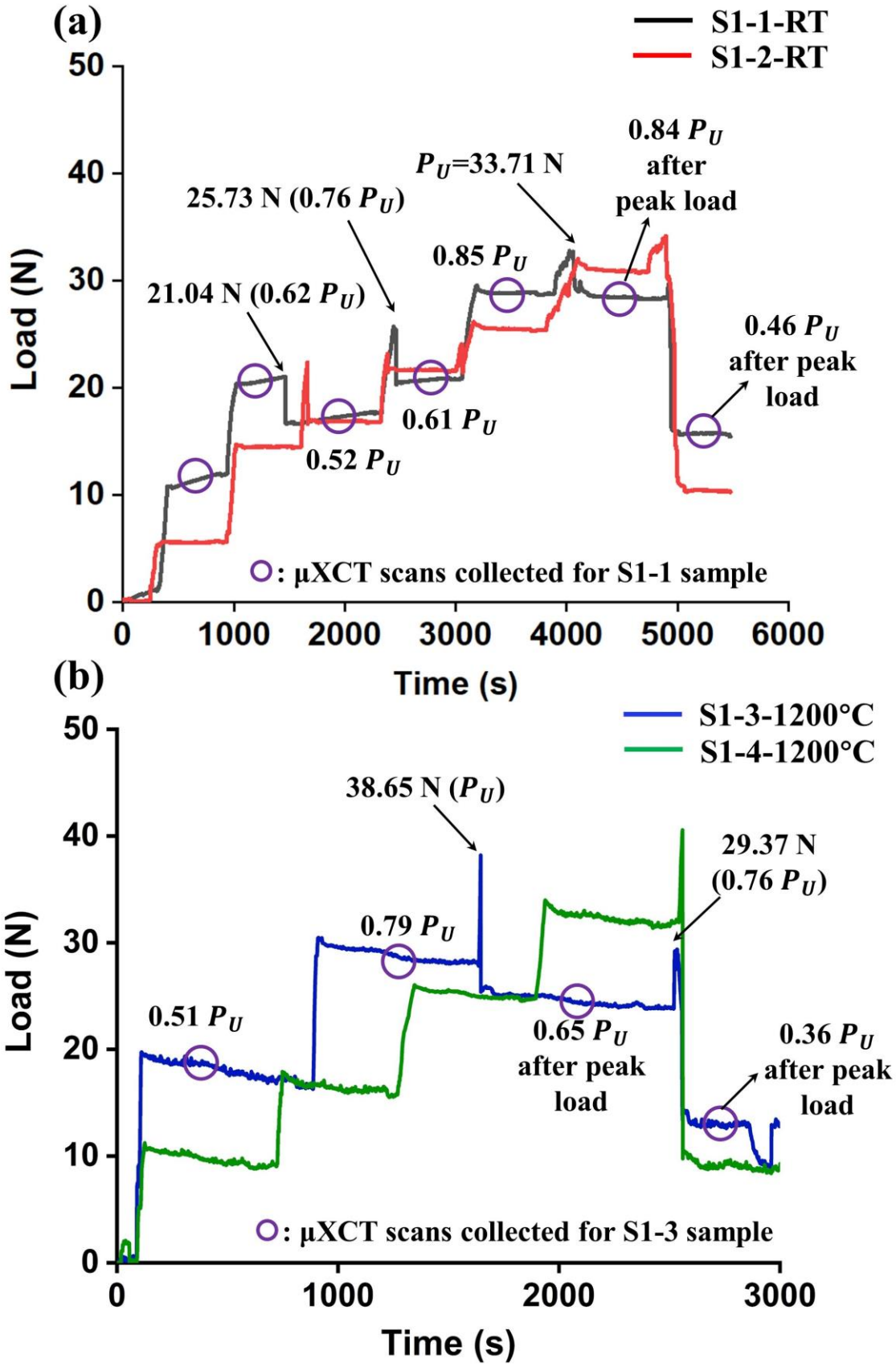

Figure 4-9. Load-time curves for the SiC_f-SiC_m materials under C-ring compression tests for (a) samples S1-1 and S1-2 tested at RT and (b) samples S1-3 and S1-4 tested at 1200°C. The open circles indicate locations of µXCT scans on samples S1-1 and S1-3; load drops and peak load are marked by arrows in S1-1 and S1-3 curves.

As for the materials tested at 1200°C, different mechanical behaviours were found (compared with tests at RT). The first such load drop were observed happened at peak load: ~39 N (P_U) for sample S1-3 and ~40 N (P_U) for sample S1-4, Fig. 4.9b. In all samples at both temperatures, the first crack always formed in the outer SiC coating corresponding to the first load drop (will be detailed presented in Section 4.4). The load at which this first coating crack/first load drop occurred was used to derive the outer coating failure strength via Eq. 3.1, which was 125–132 MPa at RT and 231–236 MPa at 1200°C. In other words, these tests consistently showed that a much higher stress is needed to create a first crack in the monolithic SiC coating in the C-ring compression configuration at 1200°C. Note that after the first coating crack, the stress distribution inside the sample will be modified, such that Eq. 3.1 may no longer be applicable. However, estimates of the maximum hoop stress have been derived based on this peak load and are listed in Table 4.3. The maximum hoop strength at 1200°C (~231–236 MPa) is consistently higher than that at room temperature (~200–202 MPa).

Table 4-3. Calculated coating failure strength and maximum hoop stress for SiC_f-SiC_m material under C-ring compression tests at RT and 1200°C.

Specimen	Sample width (mm)	First load drop (N)	Coating failure strength[a] (MPa)	Peak load (N)	Maximum hoop stress[a] (MPa)
S1-1-RT	4.85	21.04 (62% of peak load)	125.07	33.71	200.38
S1-2-RT	4.86	22.38 (66% of peak load)	132.76	34.13	202.46
S1-3-1200°C	4.81	Same as peak load	Same as maximum hoop stress	38.65	231.66
S1-4-1200°C	4.95	Same as peak load	Same as maximum hoop stress	40.57	236.29

[a] calculated using Eq. 3.1, ASTM C1323-16 [246].

In addition to load drops, during the time periods (~6 mins) when the samples were held at a constant displacement for µXCT scanning, load relaxations (progressive decreasing of load) were only observed at 1200°C tests but not apparent at RT. Specially, the load relaxations are in the range of 5.22% to 16.51% of the applied load before peak load, and 7.02% to 7.53% of the applied load after reaching peak load. While the in-depth analysis of these load relaxations was beyond the scope of current work, and detailed data of load relaxation values as a function of applied load are summarized in Table A.3 in the Appendices.

4.4. Failure processes of and crack toughening mechanisms at RT and 1200°C

After having analysed the microstructures, local properties, residual stresses of as-received SiC_f-SiC_m S1 materials and the load-time curves, the subsequent step towards achieving a more comprehensive understanding of the material behaviour at RT and 1200°C, with detailed analysis of the failure processes according to the *in-situ* μXCT datasets collected at increasing loading steps. The RT and 1200°C failure modes are described here using samples S1-1 and S1-3 as representative examples because the fracture processes in S1-2 and S1-4 are similar to S1-1 and S1-3, respectively.

4.4.1. Failure process at RT

At RT, the first load drop (from ~0.62 P_U to ~0.52 P_U) accompanies the formation of a surface crack (Crack #1) in the outer SiC coating, Fig. 4.10a. Once formed, this Crack #1 travelled across the total width of the sample (~4.85 mm), with the majority length of Crack#1 (selected range in a length of ~4.7 mm, which is ~97% of the sample's total width) was presented in Fig. 4.10a. It can be found that, Crack #1 is straight on the surface of outer coating, without any obvious deflection. The width of Crack #1 on the coating surface is measured to be ~10 μm. The first load drop in sample S1-2 (from ~0.65 P_U to ~0.53 P_U) occurred at a very similar load; the calculated outer coating strengths are accordingly consistent at ~125 to 132 MPa, as reported in Section 4.3.

The Crack #1 is subsequently segmented out and visualized in 3D, as presented in Fig. 4.11a. It can be found that, Crack #1 is a continuous crack across the C-ring sample width (b) and thickness (t). Crack #1 arrested the coating/composite interface without any obvious propagation into the underlying composite (Fig. 4.11a), where two μXCT slices (Slice 1 and Slice 2) of the X-Y plane were extracted to illustrate this, Fig. 4.10a.

Further loading did not enable the crack to propagate into the underlying composite but rather led to the formation of a second crack (Crack #2) in the outer coating, Slices 3 and 4 in Fig. 4.10b. This second crack appeared less straight on the coating surface with a discontinuity observed in the 3D segmented image (Fig. 4.11b); this crack also arrested at the outer coating/composite interface, even at the deepest area. The width of Crack #2 on the coating surface is measured to be ~10 μm.

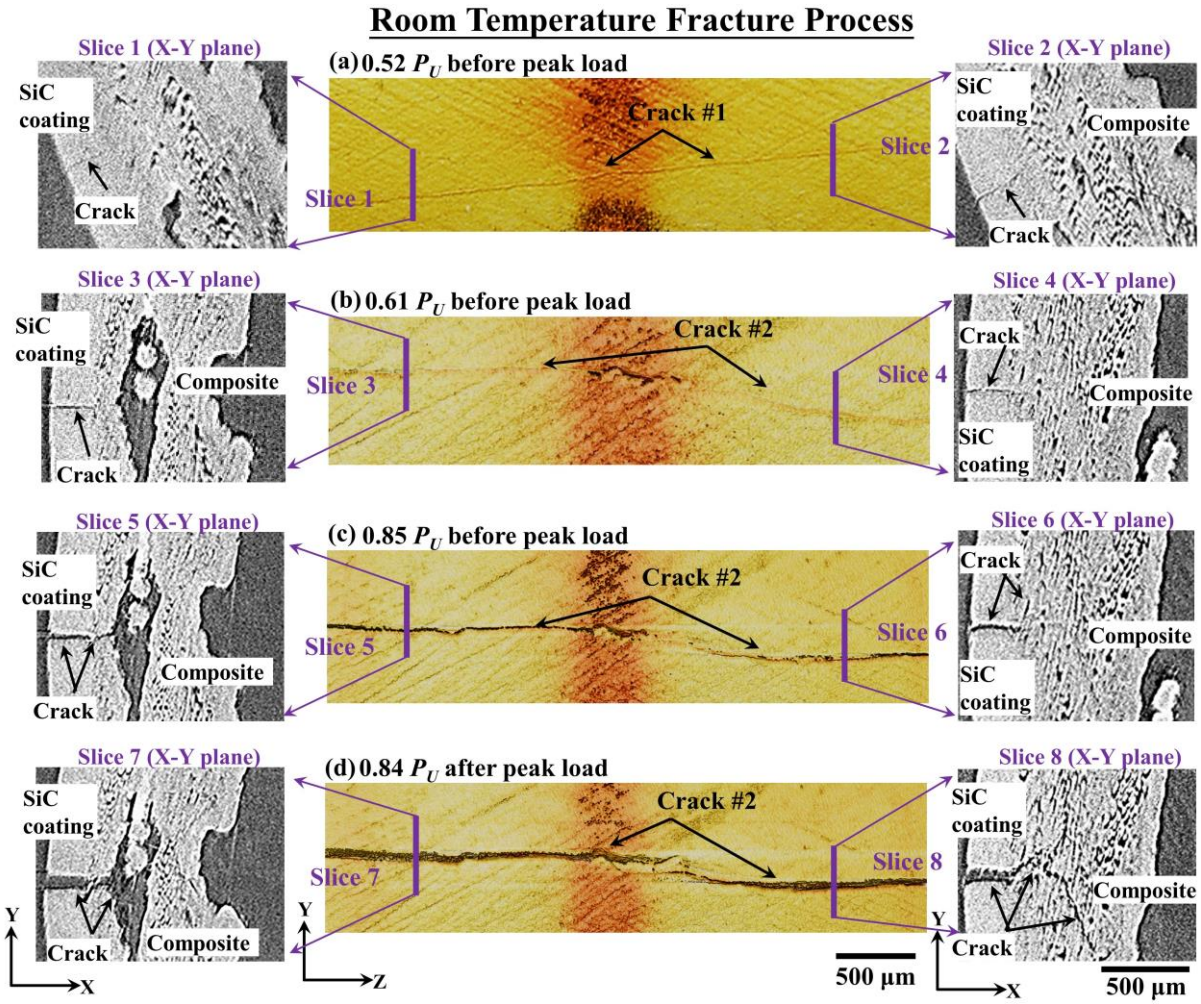

Figure 4-10. Crack formation and propagation processes at RT illustrated using sample S1-1: (a) formation of first coating crack (Crack#1) at 0.52 P_U before peak load (crack depth is illustrated by cross-sectional Slices 1 and 2), (b) formation of a second coating crack (Crack#2) at 0.61 P_U before peak load (crack depth is illustrated by cross-sectional Slices 3 and 4), (c) opening of second crack and joining at the middle of the sample at 0.85 P_U before peak load (crack depth is illustrated by cross-sectional Slices 5 and 6); (d) opening of second crack and penetration through the underlying composite reaching the inner SiC coating at 0.84 P_U after peak load (crack depth is illustrated by cross-sectional Slices 7 and 8).

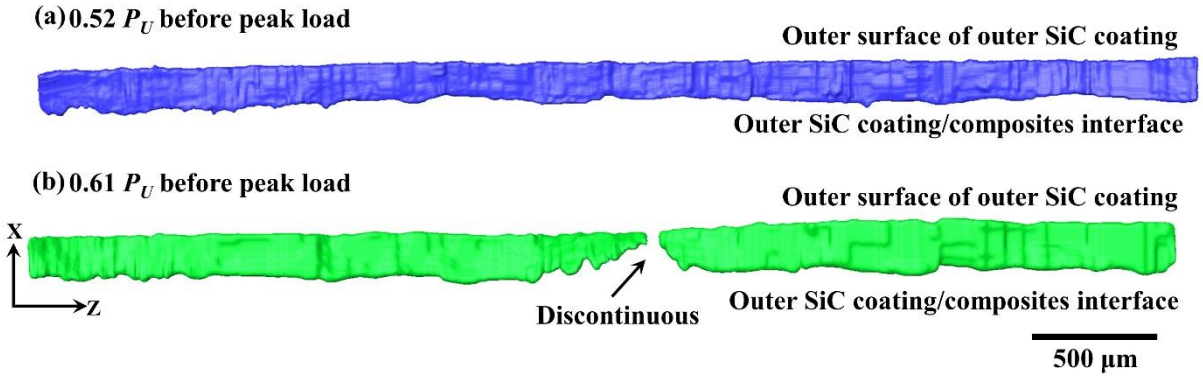

Figure 4-11. 3D visualizations (using Avizo software) of the room temperature outer SiC coating surface cracks for sample S1-1 at (a) 0.52 P_U before peak load with a full-thickness surface crack and (b) 0.61 P_U before peak load with a second surface crack. The colour represents the crack; the discontinuity is uncracked coating material.

Continued loading (up to 0.85 P_U before peak load) caused Crack #2 to open in width (from ~10 µm to ~30 µm), connect in the middle section, deflect at the coating/composite interface and propagate deeper into the underlying composite to link up with large matrix pores and interact with fibre bundles, as shown in Slices 5 to 6 in Fig. 4.10c. At this load step, the deepest depth of the propagation Crack #2 is ~40% (400 µm) of the total thickness of the material (~1 mm). These events all occurred before the peak load. With further loading after peak load, The width of Crack #2 opened up further to ~80 µm on the surface of outer SiC coating, Fig. 4.11d. Crack #2 penetrated through 80% (~700 µm) of the thickness of the cladding material and reached to the inner SiC coating (Slice 8 in Fig. 4.11d).

4.4.2. Failure process at 1200°C

At 1200°C, the µXCT scans collected prior to peak load revealed no crack formation (Fig. 4.12a). The first coating crack formed at a much higher load than at room temperature at the first load drop at peak load (from 38.65 N (P_U) to 25.65 N (0.65 P_U) for sample S1-3). Similar to the room temperature tests, the first crack also occurred in the SiC outer coating, Fig. 4.12b. However, distinct from the straight surface Crack #1 at RT, this first coating crack at 1200°C was discontinuous with uncracked ligaments and ~90° deflections within the coating along the hoop Y and Z directions of the C-ring sample (see the cross-sectional view in Fig. 4.12b for Slice 1 and Slice 2 of X-Y plane and X-Z plane).

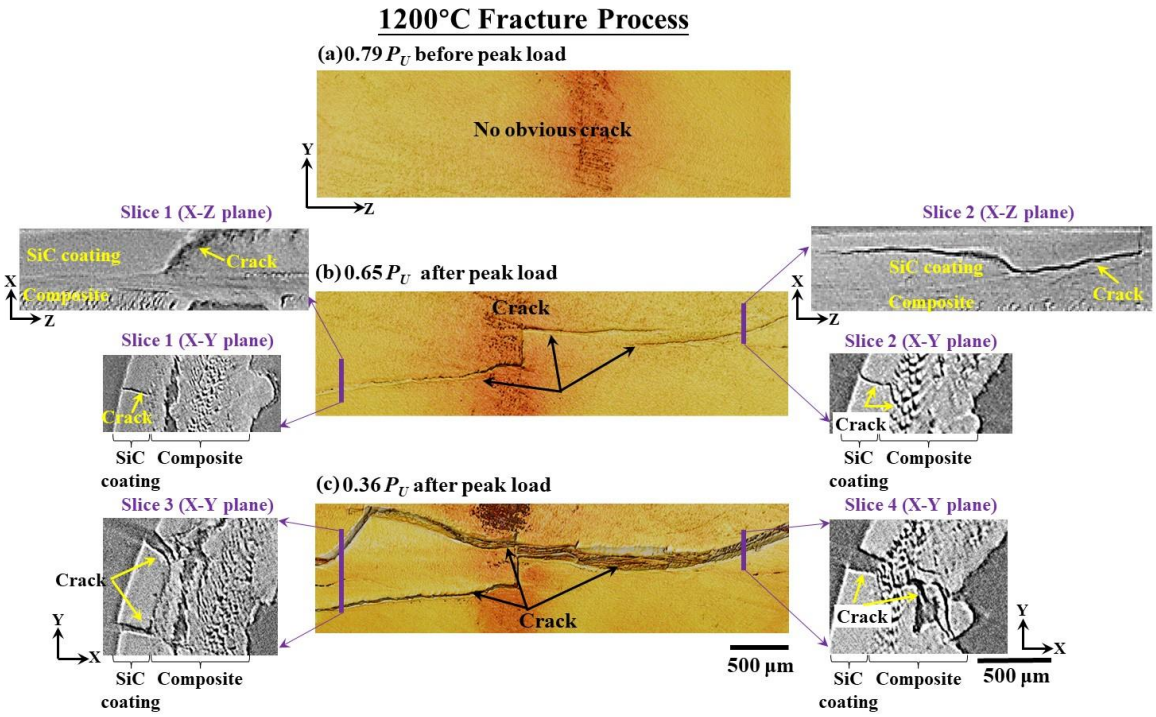

Figure 4-12. Crack formation and propagation processes at 1200°C illustrated using sample S1-3: (a) outer surface of sample at 0.79 P_U before peak load showing no crack formation; (b) formation of first discontinuous coating cracks at 0.65 P_U after peak load showing uncracked ligaments and 90° deflections within the coating (crack deflection either along coating/composite interface or inside coating are shown by cross-sectional Slices 1 and 2 of X-Z plane; crack depth is illustrated by cross-sectional Slices 1 and 2 of X-Y plane); (c) widening and joining of the outer coating crack at 0.36 P_U after peak load (crack depth is illustrated by cross-sectional Slices 3 and 4 of X-Y plane). The darker orange colour in the middle of the 3D images are artefacts related to the centre of rotation during reconstruction of the datasets.

3D visualization of this crack (Fig. 4.13) reviewed that, the penetration depth of the crack varies: the majority (~90%) of the crack length arrested before, or at, the coating/composite interface due to its shallow depth, or it deflected at the coating/composite interface. About 9.5% of the total crack length propagated through the coating/composite interface into the fibre bundle in the underlying composite – this crack either stopped inside a fibre bundle by deflection or connected with the matrix macropores (Fig. 4.12b and Fig. 4.13). Although the stress state is clearly modified by the presence of the first coating crack, a final scan after peak load at 0.36 P_U (Fig. 4.12c) was collected to demonstrate the widening and joining of the discontinuous surface cracks (Fig. 4.12b). These cracks also propagated deeper into the composite to connect with the macropores (Fig. 4.12c, Slices 3 and 4).

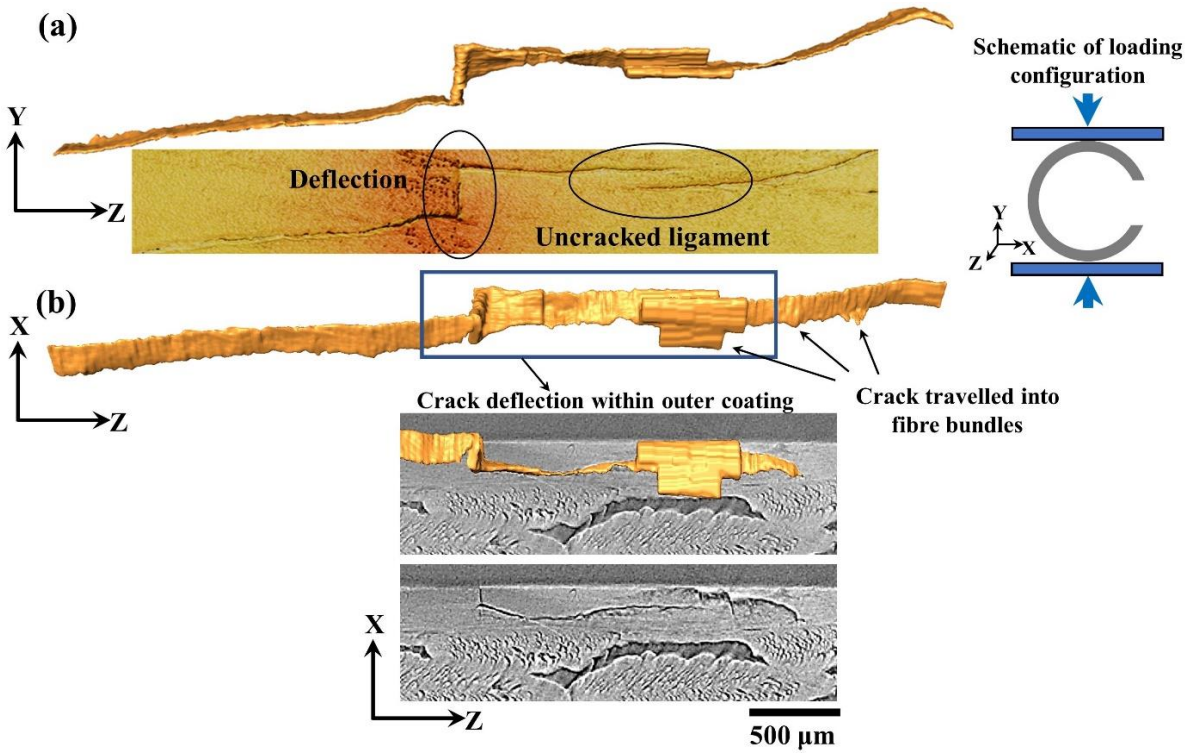

Figure 4-13. 3D visualization of the outer SiC coating crack of S1-3 sample tested at 1200°C at 0.65 P_U after peak load: (a) the YZ view of the crack highlighting features such as crack deflection and uncracked ligament; (b) XZ view of the 3D crack demonstrating the small fraction (~9.5%) of the total crack length that travelled across the coating/composite interface into the fibre bundle, with crack deflection within the SiC coating.

To summarize, compared to room temperature behaviour of the material, at 1200°C, the first crack formation still occurred within the outer SiC coating but at a much higher load and with a larger load drop (~15-25 N at 1200°C compared to ~5-6 N at RT). Mechanisms such as uncracked ligament bridging and 90° deflections within the monolithic SiC coating were only observed at 1200°C. At RT, further loading after the first load drop led to additional smaller load drops associated with more coating cracks prior to peak load. After the peak load, these cracks penetrated deeper into the underlying composite driven by complex stress-state in the C-ring compression configuration. At 1200°C, as the first load drop coincided with peak load, further loading after the first load drop/peak load also drove the cracks into the composite similar to the post-peak load behaviour at RT.

4.4.3. Crack toughening mechanisms at RT and 1200°C

At room temperature, toughening in the outer coating was associated with the formation of multiple separate cracks which increased the total crack surfaces/length before peak load (Fig. 4.14a Type O-I). At 1200°C, this was achieved by the simultaneous formation of discontinuous cracks separated by uncracked ligament bridges with crack deflection within the monolithic SiC coating (Fig. 4.14a Type O-II and Type O-III). At both temperatures before peak load,

crack deflection at the coating/composite interface was a major mechanism to stop the crack propagating into the underlying composite. At the tip of the deflected crack at the coating/composite interface, micro-scale crack bridging was also active as a toughening mechanism (Fig. 4.14b Type C-I).

In the underlying composite (primarily after peak load), crack bridging was active at both temperatures primarily within the fibre bundles (Fig. 4.14b Type C-I). Tortuous crack paths and crack bifurcation were generated as the cracks linked up with matrix pores and deflected at fibre bundle/matrix interfaces (Fig. 4.14b Type C-II). Microcracks ahead of a main crack were mostly found to form between fibres within a fibre bundle which acts as a mechanism to diffuse the main crack and arrest its extension (Fig. 4.14b Type C-III). These observations apply to both room temperature as well as 1200°C behaviour. It is emphasized that there was no particular order in terms which mechanism occurs first within the composite; these were observed simultaneously upon load drops in all samples investigated. Lastly, no fibre breakage or fibre pull out was observed in the current loading configuration.

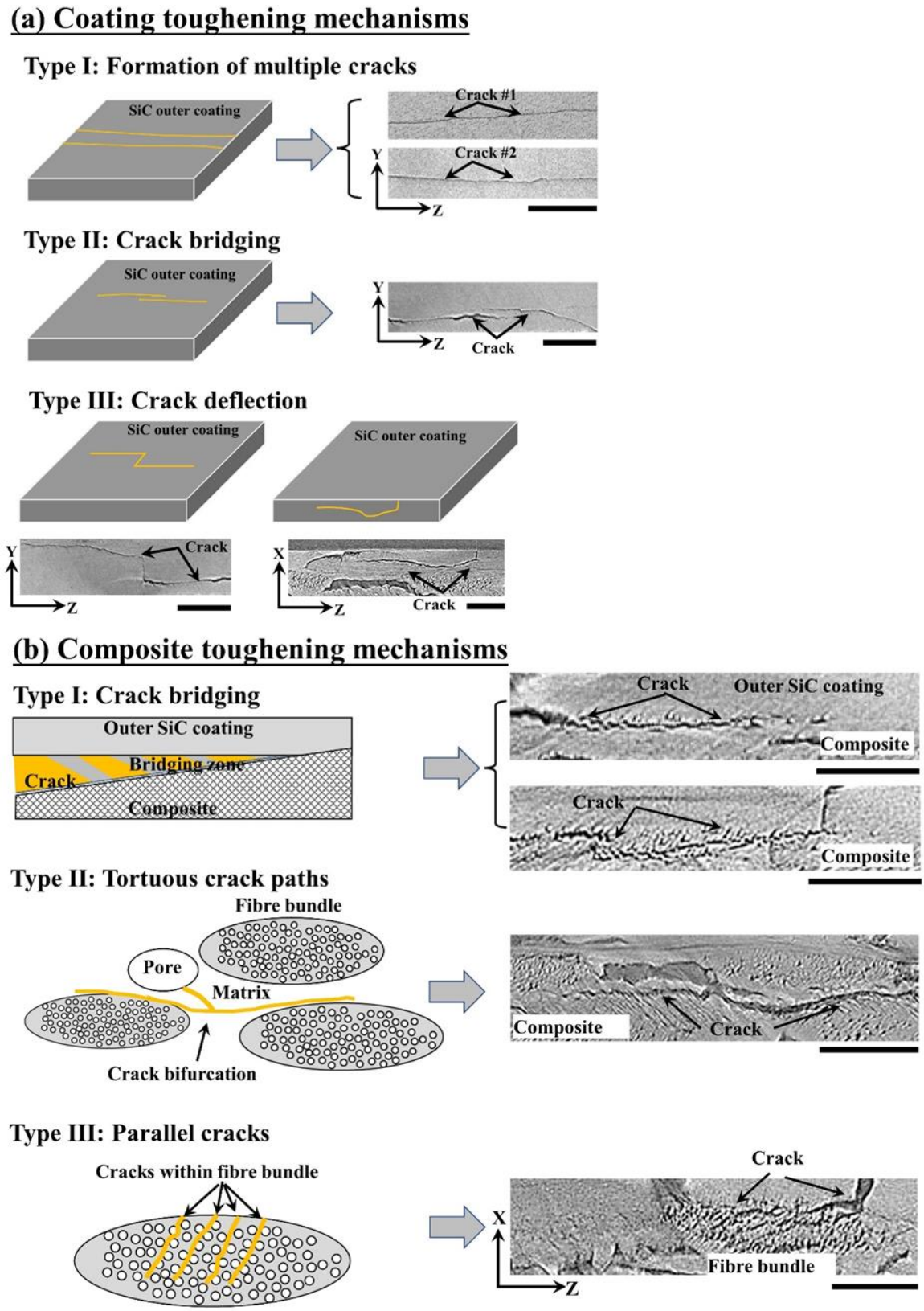

Figure 4-14. Schematics of the toughening mechanisms for the materials under C-ring compression test: (a) SiC outer coating including Type O-I (formation of multiple cracks), Type O-II (crack bridging) and Type O-III (crack deflection within coating and at coating/composite interface); (b) Composite toughening mechanisms including Type C-I (crack bridging), Type C-II (tortuous crack paths) and Type C-III (parallel cracks) with example μXCT slices of Y-Z plane and X-Z plane. All scale bars are 500 μm.

4.5. DVC analysis of 3D local strains of materials tested at RT and 1200°C

Before applying DVC methods to the loaded µXCT datasets from the *in-situ* C-ring compression tests, it is necessary to conduct sensitivity analysis to determine the errors and uncertainties associated with the calculation procedure of the investigated materials. In light of the different microstructures of studied composite materials, such sensitivity analysis is recommended for each material under investigation prior to the DVC calculation of loaded datasets [229]. In current work, the calculated strain uncertainties in the hoop direction (tensile hoop strain, ε_y) were found to be less than 0.01 % in all steps: 0.08 % for step 1, 0.05 % for step 2 and 0.02 % for step 3.

DVC analysis was subsequently utilised to determine local 3D displacements/strains by correlating deformed µXCT datasets to reference scans. Tensile hoop strains, ε_y, formed in the coating prior to and after the formation of the first coating crack were calculated at both room temperature and 1200°C. Samples S1-1 (at RT) and S1-3 (at 1200°C) are selected as representative examples because the calculated ε_y in S1-2 and S1-4 are similar to S1-1 and S1-3, respectively; with the calculated ε_y displayed on the X-Y plane of the C-ring samples in Fig. 4.15. It is evident that high ε_y strain concentration areas already formed inside the outer SiC coating before crack formation at both temperatures (Figs. 4.15a and 4.15b). At room temperature, the µXCT scan collected directly before the crack formation in the outer coating, at 0.62 P_U (Fig. 4.10a), indicated high ε_y strains of 1.88 ± 0.06 % (Fig. 4.15a); after the first load drop at 0.52 P_U these strains increased to 2.10 ± 0.14 % in the region where the first coating crack initiated (Fig. 4.15a). At 1200°C, a ε_y strain of 1.87 ± 0.12 % was formed at 0.79 P_U in the outer SiC coating (Fig. 4.15b) prior to the formation of the first coating crack at peak load; when the load dropped to 0.65 P_U after peak load, the ε_y strain increased to 4.92 ± 0.13 % (Fig. 4.165). The strains at which the first coating crack formed was derived from the measured strain before first load drop at both temperatures via a linear extrapolation. At RT, the first load drop happened at 0.62 P_U, therefore the coating failure strain at RT is ~1.88 %. At 1200°C, the first load drop happened at P_U, by using the measured strain (~1.87%) at 0.79 P_U, the coating failure strain at is estimated to be ~2.37 %.

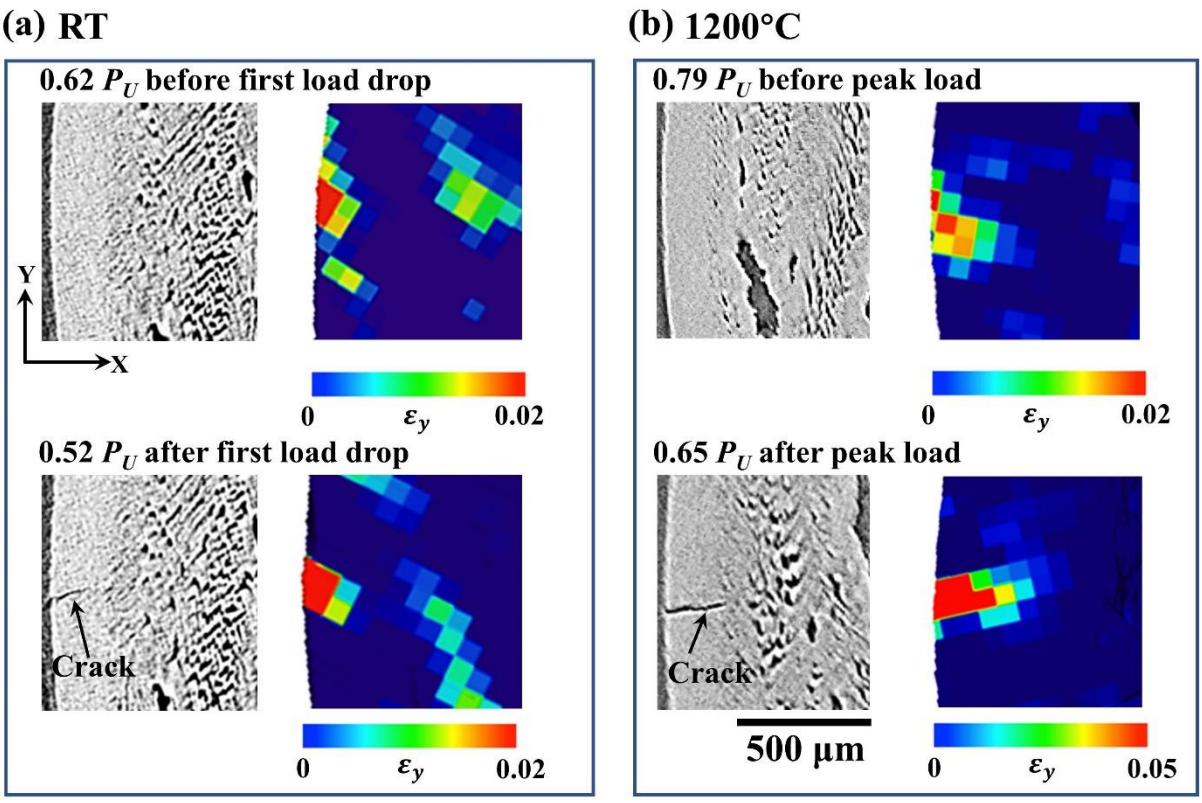

Figure 4-15. µXCT slices and the correspondingly calculated ε_y hoop strains of the X-Y plane at increasing loading steps (samples S1-1 (at RT) and S1-3 (at 1200°C) are selected as representative examples): for the room temperature S1-1 sample at (a) 0.62 P_U before first load drop/first coating crack formation, and 0.52 P_U after first load drop; for S1-3 1200°C sample at (b) 0.79 P_U before peak load, and 0.65 P_U after peak load.

4.6. Discussion

4.6.1. Microstructure and local property of SiC_f-SiC_m material

4.6.1.1. Porosity

The porosity (including the volume fractions of macropores and micropores) of SiC_f-SiC_m cladding tube material was estimated to be ~9%, which is in the reported range for similar nuclear grade SiC_f-SiC_m materials with the matrix produced by CVI method from open literatures: ~8.7 % to ~20.3%. The detailed information of these SiC_f-SiC_m materials and corresponding porosity values can be found in Table 2.7.

4.6.1.2. Local property

The overall hardness and modulus of the present SiC fibres (respectively ~19 GPa and ~175 GPa) were lower than that of the surrounding matrix (~33 GPa and ~330 GPa), which is also consistent with literature data. For instance, the indentation hardness and modulus of Hi-Nicalon™ type S fibres in CVI matrix SiC_f-SiC_m cladding materials have been reported to be ~24 GPa and ~270 GPa, compared to respective values of ~32 GPa and ~450 GPa for the

surrounding matrix [327]. Similar nanoindentation testing on Tyranno SA3 fibres in a CVI matrix SiC_f-SiC_m cladding yielded an overall fibre hardness of 26-30 GPa and ~38 GPa for the surrounding matrices [328]. This was attributed to the presence of carbon inside SiC fibre to lower the hardness and modulus and was verified the hypothesis using the 'rule of mixtures' based on the carbon volume fraction estimated from segmentation of fibre cross-sectional images (30% to 35%) in their materials [328].

4.6.2. Residual stress distribution

Residual stresses in the outer SiC coating will affect the strain at where first crack in the coating takes place. For instance, in the TRISO particle fuel, the SiC coating is put under compression to increase its failure strain [180]. The formation of crack or heating to elevated temperatures will subsequently modify the residual stress distribution which impacts the failure strain as well as the overall material's mechanical behaviour [223]. It is therefore critical to conduct a thorough analysis of the distribution of residual stresses in these cladding materials, both when interpreting their deformation and fracture behaviour, and when comparing different types of materials generated by different manufacturing processes.

In current Chapter, SiC was found to have tensile residual stresses in both the outer and inner coatings (0.31 ± 0.13 GPa and 0.22 ± 0.12 GPa, respectively), in the matrix between fibre bundles (0.29 ± 0.10 GPa) and in the matrix within a fibre bundle (0.35 ± 0.10 GPa), as summarized in Fig. 4.16. As these absolute stress values vary with the reference peak position selected, the relative variation in stress is compared. The stress in the inner coating is ~0.09 GPa less tensile than in the outer coating; it is also ~0.07 GPa less tensile than in the matrix between fibre bundles. The inference from this data is that the inner coating is under compression in absolute terms to balance out the tensile stresses in the nearby matrix, and that the outer coating could be under tension.

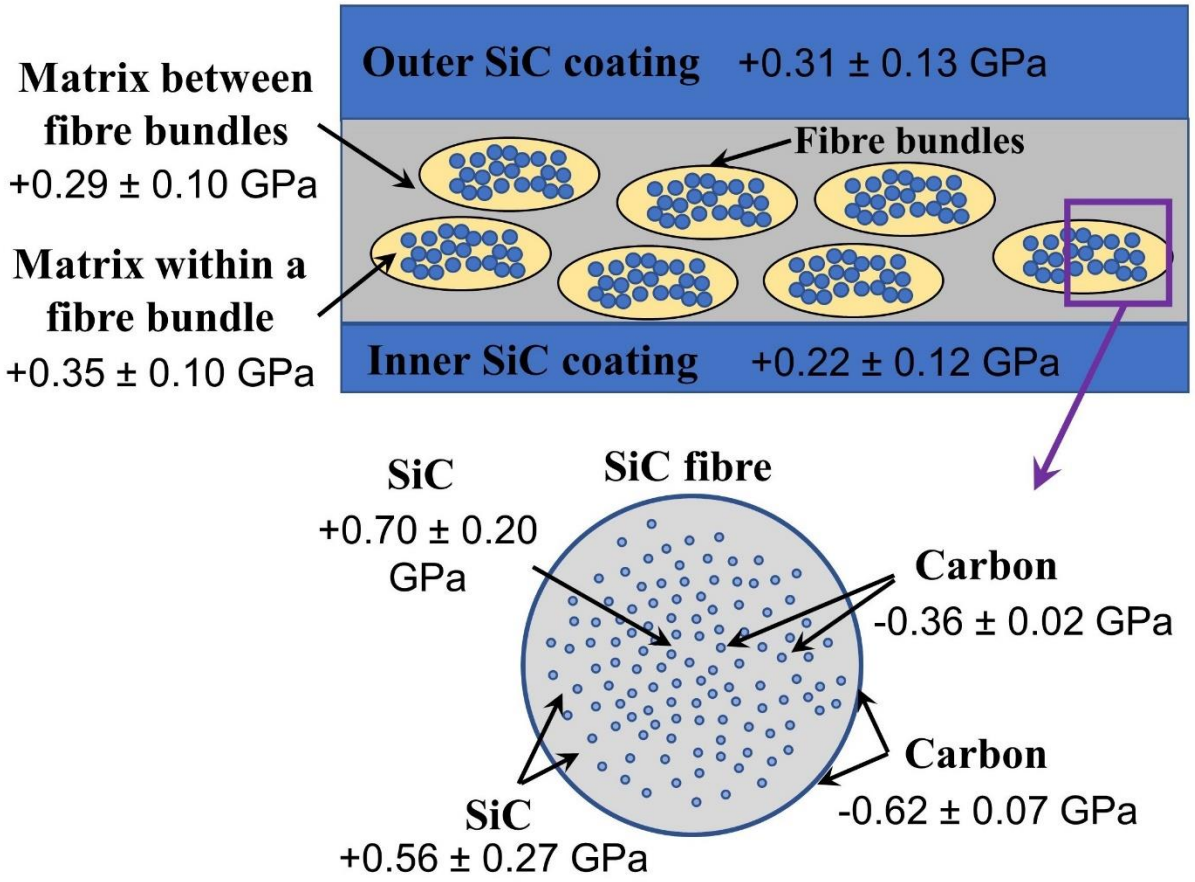

Figure 4-16. The variation in residual stresses in different components of the as-received SiC_f-SiC_m cladding material. ('+' for tensile stress and '-' for compressive stress).

Inside individual fibres, the SiC phase has a higher tensile residual stress at the centre of fibre (~0.70 GPa) than at the outer edge (~0.56 GPa). Such a variation across the fibre cross-section is not unexpected, as the fibre undergoes complex compositional and microstructural changes during the fibre spinning and heat treatment. Though this is consistent with results in the literature for Raman data collected from a CVD SiC fibre with a tungsten-rich core where the highest tensile residual stress (~0.55 GPa) was measured at the fibre centre [329]. Note that the SiC TO peak has a low FWHM at these high stress areas; as the FWHM is considered to be inversely proportionally to grain size, this implies larger grains at the fibre centre and smaller grains at the edges, again consistent with literature reports [329], [330].

Nance *et al*. [163] utilized Raman spectroscopy to measure the residual stresses in the SiC phase inside Hi-Nicalon Type-S SiC fibres (same type of fibre as current project, which mainly consist of β-SiC) at different stages of their manufacture: (i) in the as-received fibre (using a reference stress-free position of 788 cm^{-1} which is different from commonly used value of 797 cm^{-1}), (ii) after mechanical braiding of fibre bundles, and (iii) after 33%, 66% and 100% CVI densification processes. These authors reported that processing introduced compressive

stresses into the SiC fibres of a magnitude from -0.70 GPa (after mechanical braiding of the fibre bundles) to -1.08 GPa (after the 100% CVI densification process). Although a different reference peak position was used, their Raman peak position of the SiC TO band (~794 cm^{-1}) matched well with the band position in current study. These and other measurements of the residual stresses of SiC phase in SiC fibres are summarized in Table 4.4.

Table 4-4. Measured stress-free Raman peak positions and Raman peak positions of the SiC TO band, with the corresponding calculated residual stresses of SiC phase inside different types of SiC fibres. ('-' indicates a compressive stress).

Type of fibres	Selected stress-free peak position (cm^{-1})	Raman peak shift of SiC TO peak (cm^{-1})	Residual stress of SiC phase (GPa)
Hi-Nicalon type-S fibre (as-received) [163]	788 ± 0.07 (TO)	0	0
Hi-Nicalon type-S fibre (after braiding) [163]	788 ± 0.07 (TO)	792 ± 0.14 (TO)	-0.72
Hi-Nicalon type-S fibre (after 33% CVI densification process) [163]	788 ± 0.07 (TO)	793 ± 0.14 (TO)	-0.90
Hi-Nicalon type-S fibre (after 66% CVI densification process) [163]	788 ± 0.07 (TO)	794 ± 0.08 (TO)	-1.08
Hi-Nicalon type-S fibre (after 100% CVI densification process) [163]	788 ± 0.07 (TO)	794 ± 0.27 (TO)	-1.08
One type of SiC fibre produced by CVD method (W-rich core in the centre of fibre) [330]	790 (TO)	-	From -0.1 to -2.4

While the SiC phase in the fibre was under highest tensile residual stress, the carbon phase in the fibre was in compression (measured using the G band shift in the Raman spectrum as described in Section 3.3), specifically at a stress of approximately -0.36 GPa at the fibre centre. Using the G band peak position analysis, the PyC interphase area was found to be even more compressive at about -0.62 GPa (Fig. 4.16). This was attributed to volume expansion during processing according to Niu *et al.* [330]. The compressive stress in the carbon phase balances with the tension in the SiC phase. Indeed, compressive stresses in the carbon phase of -1.22 GPa have also been measured at the C-rich boundary between fibre and matrix in SiC/Ni-Cr-Al composites by Raman spectroscopy [330]. Therefore, the data measured in the current work

in the SiC fibres are consistent with literature and can be used as input for future constituent materials performance modelling.

4.6.3. Failure strength/strain of SiC_f-SiC_m material tested at RT and 1200°C

Before detailed discussion of the hoop strength data, it is important to differentiate 'maximum hoop strength' from 'coating failure strength'. The former is used to select the peak load to derive a maximum strength based on Eq. 3.1 from ASTM Standard C1323-16 [246] which is used by the majority of studies in the open literature data. However, at RT, cracks formed in the cladding materials before peak load under C-ring compression loading. They can lead to the release of energy at the crack tips, as well as stress-state in the C-ring sample during the crack deflection in the composite. Therefore, the hoop strength of material derived from Eq. 3.1 by the peak load is likely to be no longer valid. In current work, the load at first coating crack occurs is used to calculate the coating failure stress. No obvious stress-state variation happened in the C-ring sample before the coating crack happened (hoop stress is the dominant stress), therefore the calculated coating failure strength is more reliable.

The room temperature maximum hoop strength of SiC_f-SiC_m composite (with and without an outer coating) measured by C-ring compression test, has been reported in the range of 174 MPa to 413 MPa. A detailed summary of this information is given in Table 2.7. In current project, the coating failure strain at 1200°C was measured to be ~2.37%, which is higher than that at RT: ~1.88%. One potential reason is, when the materials were tested at high temperature (*e.g.*, 1200°C), the relaxation of tensile stress in the outer SiC coating enables it survive higher failure strains. From literature, 12-20% 3D local strain (measured by DVC) in the outer coating was reported by Saucedo-Mora *et al.* [132] in their coated SiC_f-SiC_m claddings related to local failure.

In present work, the room temperature maximum hoop stresses (based on the peak failure load) of SiC_f-SiC_m cladding material were estimated to be ~200 MPa, which may be an overestimate of the strength due to deviation from linearity caused by prior crack formation; nevertheless, this value is still within the reported range. The room temperature coating failure strength of SiC_f-SiC_m material was lower at 125-132 MPa, although there are no published data directly reporting the coating failure stress (first load drop) of similar SiC materials under C-ring compression (as far as the author are aware). However, reviewing the published load/stress-displacement curves for a range of materials, the stresses at first load drop are in the range of ~180 to ~240 MPa (Table 2.7 and Fig. 4.18) [119], [131]. This range is broadly similar to the

current work but the variation in these values can be associated with the differing sample volumes, materials fabrication, overall material stiffness and coating thicknesses.

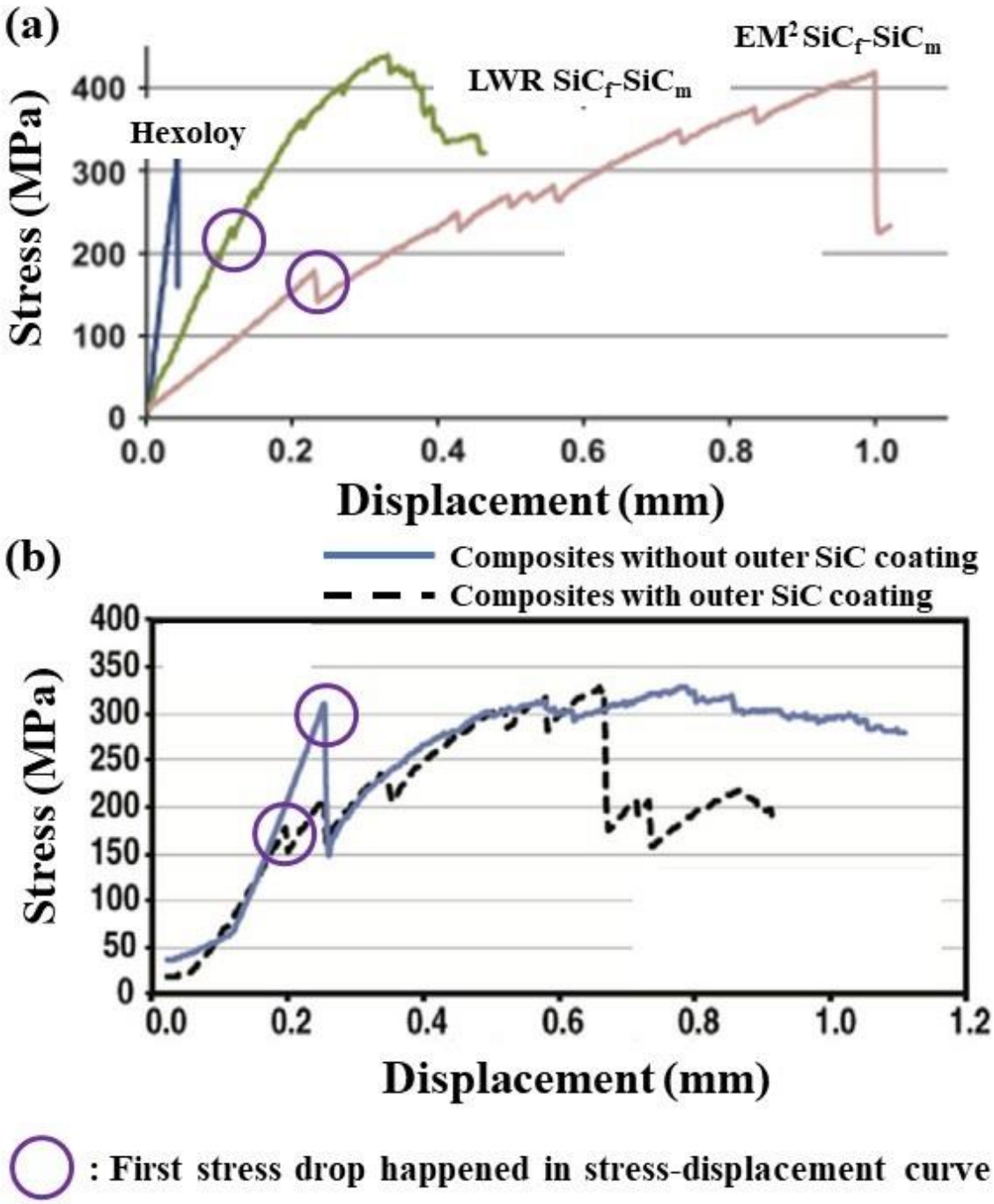

Figure 4-17. Stress-displacement curves for room temperature C-ring compression tests of different types of SiC_f-SiC_m cladding tube materials from literature, shows stresses at first load/stress drops for that with outer SiC coating, as marked by open circles; to be noted that, stresses at first load drops are not reported, and authors extracted them from their reported stress-displacement curves; (a) LWR SiC_f-SiC_m cladding tube materials (with outer SiC coating), EM^2 SiC_f-SiC_m cladding tube materials (with outer SiC coating) and monolithic Hexoloy SiC [131], (b) SiC_f-SiC_m cladding tube materials with and without outer SiC coating [119].

In general, there are fewer high temperature experiments on tubular SiC_f-SiC_m cladding composites in open literatures; a detailed summary of literature values can be found in Table 2.9. Hironaka *et al.* (2002) [331] and Nozawa *et al.* (2014) [9] reported good strength retention of SiC_f-SiC_m composites at temperatures up to 1200°C which is consistent with the results of the current work. A notable study in this regard is by Shapovalov *et al*. [130], where high-temperature C-ring compression tests were performed on two types of Hi-Nicalon™ Type S fibres reinforced SiC_f-SiC_m cladding materials, one with a CVD outer SiC coating (~100 µm in thickness) and tested in air up to 1100°C, the other without outer SiC coating and tested in air (up to 1100°C) and Ar environments (up to 1900°C). For the coated samples, they reported a failure load of ~16 N tested at 1100°C in air. This value is half of the failure load measured in current study at 1200°C, but the width of their C-ring samples was also half that of the current samples; this implies that the current results are consistent with their measurements. In addition, they found that the peak loads (~16 N) for the coated samples did not decrease at temperatures up to 1100°C in air, as well as un-overcoated samples up to 1900°C in Ar (~10 N) [130]; again, this is consistent with the current findings up to 1200°C.

The retention and/or increase in failure strength is not unexpected; for instance, Gulden [332] reported the fracture strength of dense SiC being approximately constant between room temperature and about 900°C and then to increase sharply up to the maximum test temperature of 1215°C to 1400°C. These imply that the room temperature property tests can be considered as a conservative assessment of the coating failure for such materials systems. However, for accurate modelling of the materials fracture processes, it is noted that the coating failure strength should be differentiated from the maximum peak strength in C-ring compression configuration. Additionally, load relaxation was only found for the materials tested at 1200°C (Fig. 4.9). This phenomenon has commonly reported in CMCs materials [229]. Several factors could potentially contribute to such load relaxation at high temperatures: (i) creep of fibre [333]; (ii) redistribution of residual stress of individual components [229]; and (iii) the weaken of fibre/matrix interface [334].

4.6.4. Failure processes and active toughening mechanisms at RT and 1200°C

The documented failure modes of SiC_f-SiC_m composites at room temperature are generally considered to occur in three stages [129], [131], [179]: (i) during the initial linear (elastic) region of the stress-strain curve, the load is shared by both the fibres and matrix with little to no cracks within the material; (ii) at the proportionality limit (akin to the yield strength in a metal), cracks initiated in the matrix propagate along the fibre/matrix interface to result in the

nonlinear mid-region of the stress-strain curve (akin to the plastic region in a metal); (iii) with the matrix significantly fractured, load is transferred to the fibres which can lead to fibre pull-out and eventually to fibre fracture, thus correlating with the remainder of the stress-strain curve. However, the real time 3D imaging in the current study suggested very different failure processes (summarised in Fig. 4.18) in the SiC_f-SiC_m cladding material under C-ring compression loading. Specifically, (i) the matrix crack was not the first fracture to occur, (ii) several different toughening mechanisms in the coating and composites were activated simultaneously rather than in sequence, and (iii) no fibre fracture/pull out was observed. This suggests that the fracture processes may vary when different loading configurations are applied such as bending, C-ring compression and/or biaxial/triaxial loading; it is inappropriate to presume that the same failure processes in one test configuration will apply to all others. Accordingly, to accurately model material performance, *in-situ* testing with 3D imaging on representative samples is essential to identify the specific failure processes for the relevant loading configuration.

In summary, for the current C-ring compression of SiC_f-SiC_m cladding material, at room temperature the failure processes can be classified as follows (Fig. 4.18a): *Stage 01* - a linear region with no obvious crack formation; *Stage 02* - the first load drop occurs corresponding to crack formation in the outer SiC coating; *Stage 03* - additional crack formation in the coating on further loading (these coating cracks in *Stage 02* and *Stage 03* primarily stay within the coating, either due to their shallow depth or deflection at the coating/composite interface, and do not yet fully propagate to the underling composite); *Stage 04* - upon load drop at peak load, a primary coating crack propagates into the underlying composite, where various toughening mechanisms (crack deflection, crack bridging, bifurcation and micro-cracking) are activated simultaneously in the composite to resist the damage [335]. Beyond *Stage 04*, the outer SiC coating further fragments with cracks propagating further into underlying composites signifying final failure.

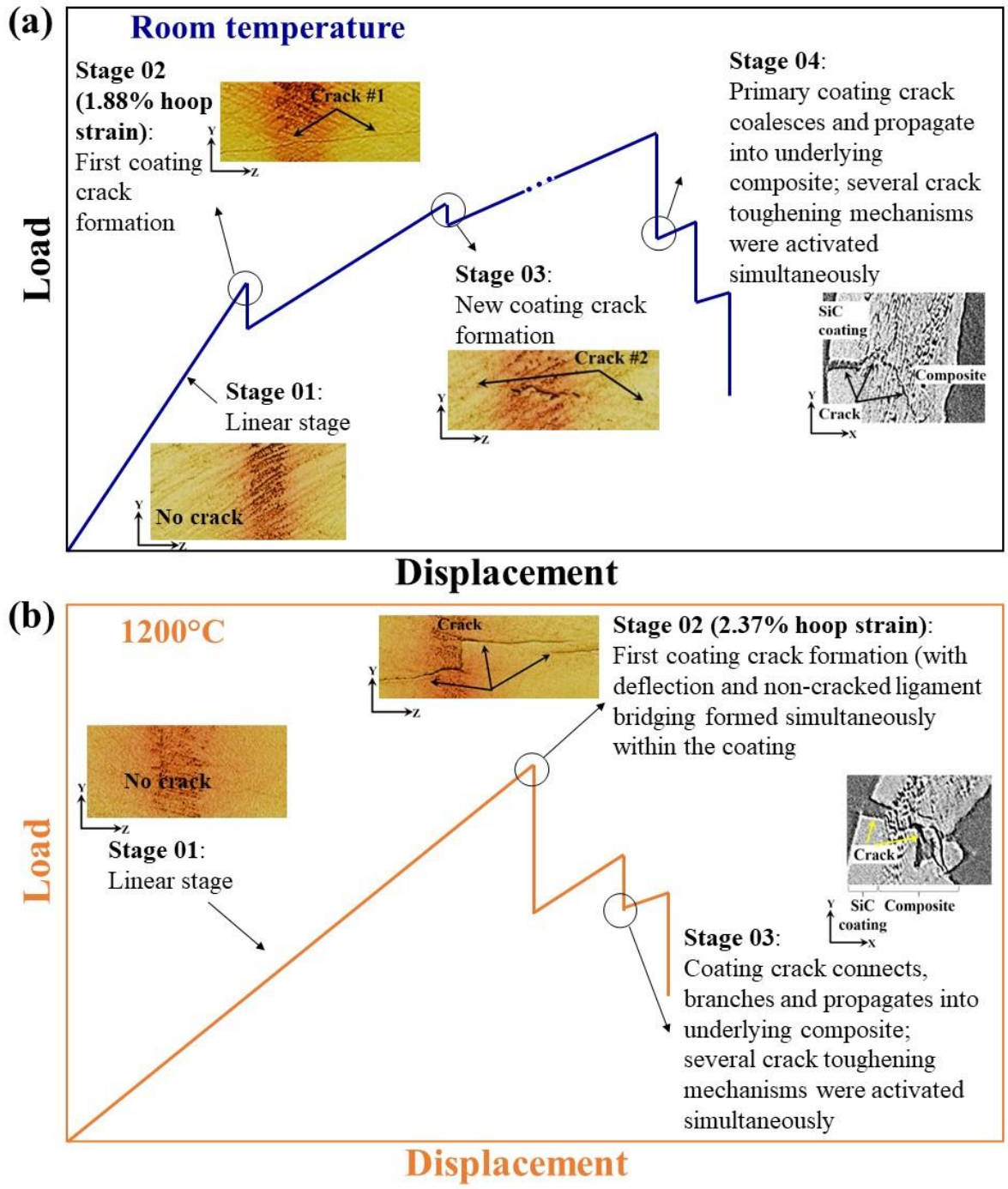

Figure 4-18. Schematic illustrations of load-displacement curves to display the progressive failure of SiC_f-SiC_m cladding material under C-ring compression at (a) room temperature and (b) 1200°C. Corresponding μXCT slices are representative examples illustrating failure processes.

The corresponding failure modes at 1200°C can be classified as shown in Fig. 4.18b: *Stage 01* - a linear region with no crack formation or load drops; *Stage 02* - first coating crack forms at peak load in the SiC outer coating with uncracked ligament bridging and crack deflection within the coating layer activated simultaneously; the majority of the cracking stays within the coating and does not yet propagate into the underlying composite; *Stage 03* - further loading leads to a connection of coating cracks and their propagation into the underlying composite.

Inside the composite, crack deflection (either at the fibre bundle/matrix interface or at the fibre/matrix interface within a fibre bundle due to the built-in weak interphase), crack bridging and bifurcation act simultaneously to resist damage. It is important to note here that no obvious fibre pull-out nor fibre fracture was observed in this study at both room temperature and 1200°C.

4.7. Conclusion

The local properties, in terms of modulus and hardness were measured for individual components inside the SiC_f-SiC_m cladding material. The results are consistent with literature values with one key message being that the fibre has a lower modulus and hardness than that of the matrix, due to the residual carbon phase inside the fibre.

A higher hoop strength and coating failure strain was measured for the SiC_f-SiC_m cladding material at 1200°C compared to that at room temperature; this suggests room temperature tests can be potentially used as a conservative estimate of the high temperature performance for the SiC_f-SiC_m cladding tube materials.

The residual stresses were mapped using Raman spectroscopy and suggested a relative tensile residual stress inside the outer SiC coating at RT, which could be a potential factor contributing to the high coating failure strain at 1200°C.

The failure processes at room temperature are different from 1200°C although in both cases, the first crack initiated in the outer SiC_f-SiC_m coating leading to a load drop. As the crack propagated into the underlying composite, various toughening mechanisms (*i.e.*, crack bridging, crack deflection and bifurcation, parallel cracks and tortuous crack pathways) in the composite were activated simultaneously at both room temperature and 1200°C to resist the damage. Crack deflection within the SiC coating, however, was only observed at 1200°C. No obvious fibre pull-out or breakage were observed in this C-ring compression configuration at both temperatures.

It must be emphasized that these observations, with real time imaging using XCT under load at different temperatures, offer new first-hand insights into the failure processes in these composites under C-ring compression condition, which as noted above are different from the conventional wisdom of how SiC_f-SiC_m composites are presumed to fail [336]. For microstructural-based modelling, these different experimental observations must be considered for a faithful description of the mechanical behaviour of these critical materials for future nuclear applications.

5. Mechanical behaviour of SiC_f-SiC_m cladding with multi-layer outer SiC coating

In this Chapter, the mechanical behaviour and failure processes of SiC_f-SiC_m cladding with multi-layer SiC coating were explored, and more detailed introductions of this material are included in Section 3.2.1. The descriptions of C-ring compression tests with real-time μXCT conducted at both RT and 1200°C are included in Section 3.3.1.2. The procedures of μXCT data processing are included in Section 3.3.1.3. The procedure for measuring local properties by nanoindentation is presented in Section 3.3.3. The procedure for measuring residual stresses by Raman spectroscopy is presented in Section 3.3.4.1. The results are presented in the order of (i) the microstructures, local properties and residual stresses of as-received materials, (ii) load-time curves, hoop strength and failure processes of the material tested at each temperature. Note that, the materials in this Chapter use the same type of fibre (Hi-Nicalon™ Type S) as the materials in Chapter 4; therefore, the local properties and residual stresses of the fibres in both types of materials are very similar.

5.1. Microstructures of as-received materials

The typical microstructure of as-received material is presented in Fig. 5.1. The material comprises of the outer SiC coating and underlying CMC layer, and there is no inner SiC coating. The thicknesses of the outer SiC coating and underlying CMC layer were measured to be 260.59 ± 7.71 μm and 775.11 ± 13.44 μm, respectively. As marked in Fig. 5.1b, 11 sub-layers can be observed in the outer SiC coating. For sub-layers 1 to 9, their thickness was measured to be similar: 19.58 ± 1.35 μm. Sub-layer 10 has a higher thickness: 31.58 ± 0.93 μm, and sub-layer 11 has the highest thickness: 39.24 ± 0.85 μm. Additionally, pores can be commonly observed at the interface between adjacent sub-layer in outer coating, with two representative examples presented in Fig. 5.1b. These pores are unexpected. For the CMC layer, inside fibre bundles, PyC interphase can be observed surrounding the SiC fibre (at the fibre/matrix interface), Fig. 5.1c.

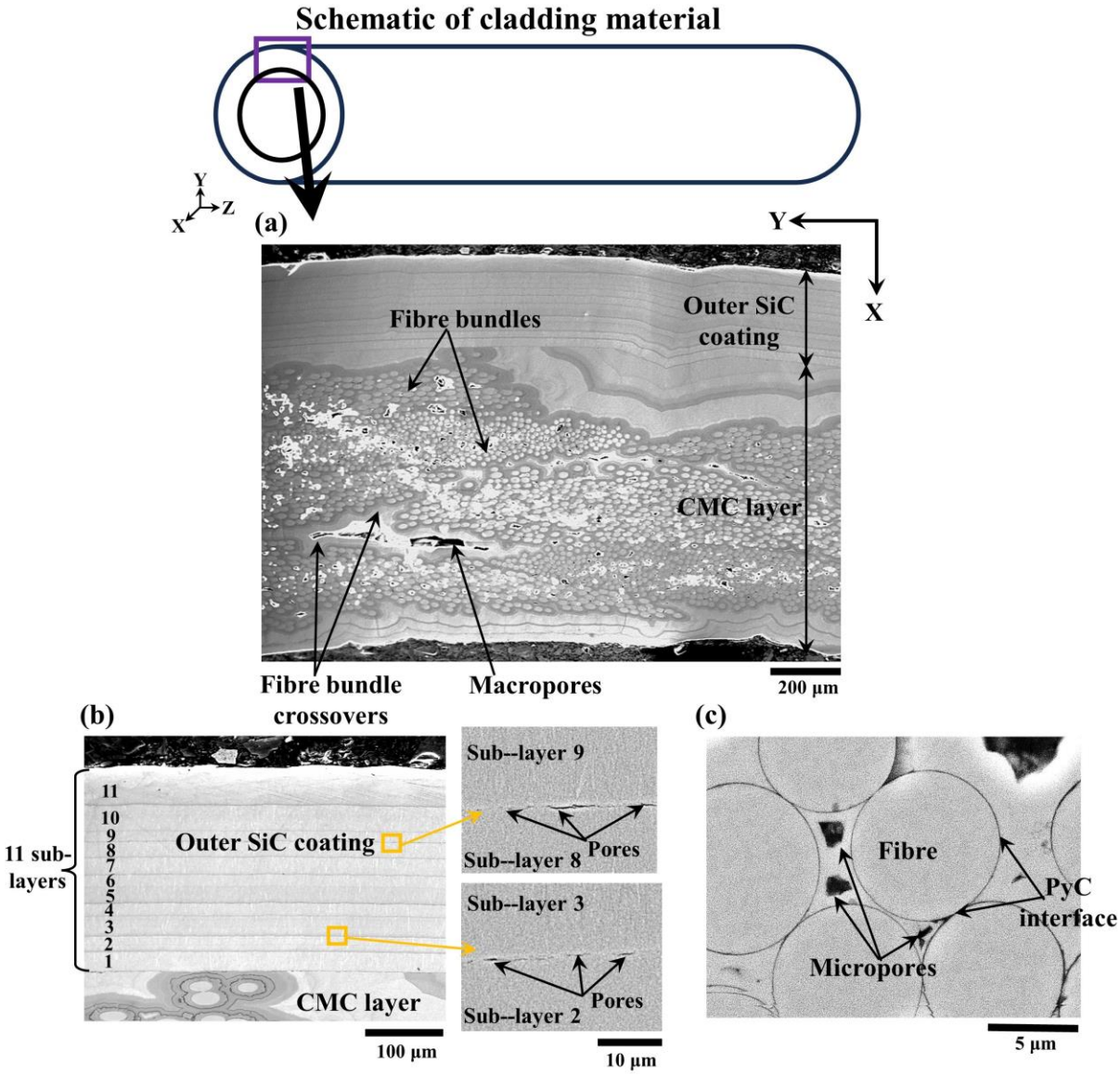

Figure 5-1. SEM images collected from the polished cross-sections (of X-Y plane) of the as-received material, presenting the its typical microstructures: (a) shows the material consists of outer SiC coating and underlying CMC layer; (b) are magnified images showing 11 sub-layers can be observed in the outer SiC coating, and pores can be commonly observed at the interface of adjacent sub-layers; (c) presents the microstructure inside fibre bundles. One schematic of the cladding material is also included to illustrate the location of the cross-section.

Fig. 5.2a displays 3D visualization of as-received material. Three types of fibre bundles can be observed in the CMC layer, including (i) 90° fibre bundles, braided along the longitudinal of the cladding; and (ii) and (iii) ±45° braiding angle against the cladding's hoop direction, respectively, Fig. 5.2b. These fibre bundles were braided in a 3D orthogonal braiding pattern.

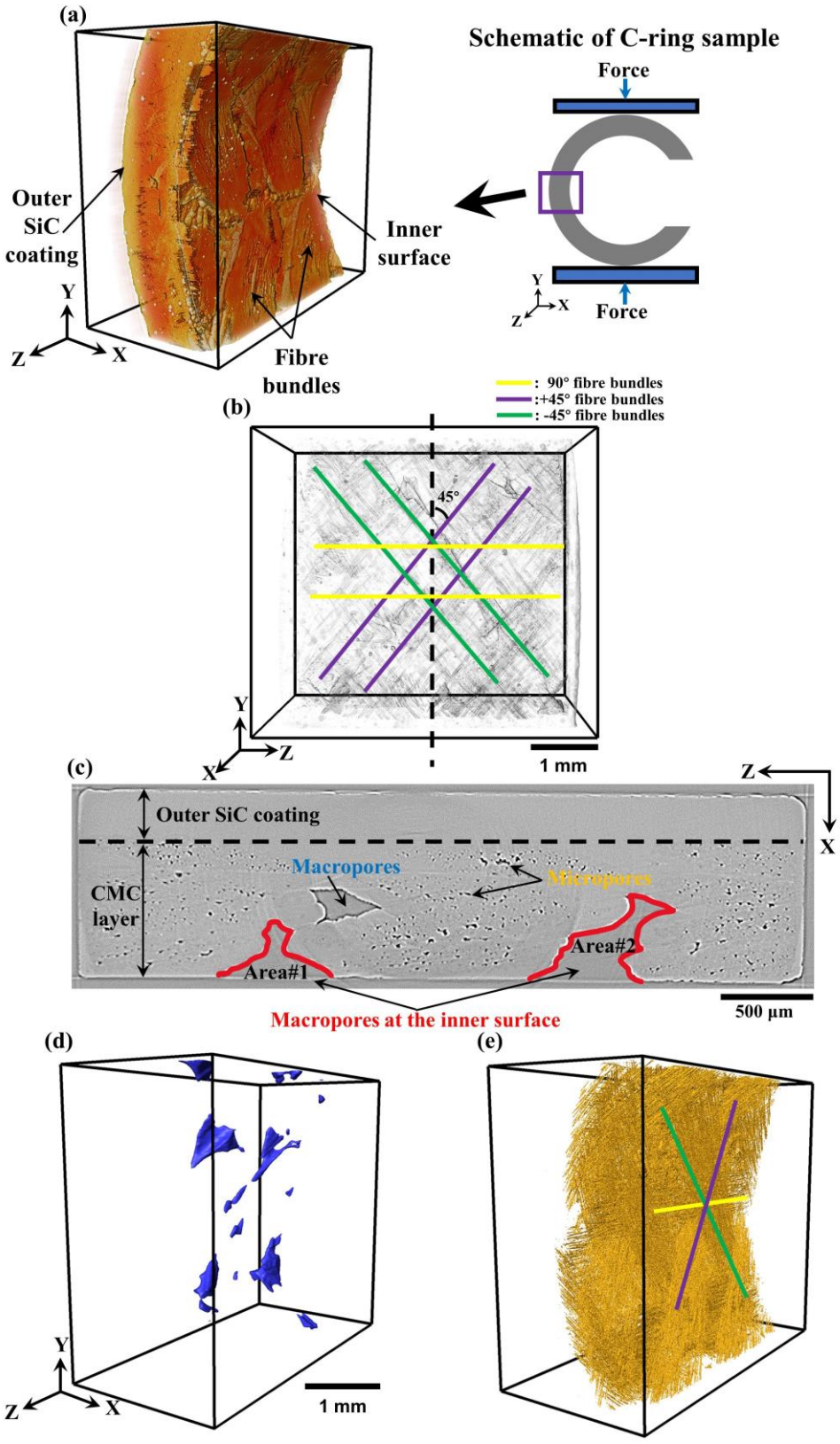

Figure 5-2. Microstructures of as-received material from reconstructed µXCT datasets of pre-load scan: (a) 3D visualization of the material; (b) 3D visualization of the fibre bundles; (c) one representative µXCT slice of X-Z plane shows macropores and micropores inside the CMC layer; some macropores can be found at the inter surface, and they were excluded from the volumetric calculation of the macropores; (d) 3D visualization of macropores in the CMC layer and (e) 3D visualization of micropores in the CMC layer.

Two types of pores can be seen in the CMC layer: (i) macro-size pores located in the SiC matrix at the crossovers of the fibre bundles; (ii) micro-size pores located inside fibre bundles, Fig. 5.2c. Some macropores can be observed at the inner surface of the material, as marked in Fig. 5.2c. Note that, at such areas (macropores at the inner surface), their wall-thickness (t) are less than the average wall-thickness (t) of the cladding material (~1.04 mm). For instance, the t at Area#1 is 0.70 mm, ~67.7% of the cladding' average wall-thickness; at Area#2, the t is 0.54 mm, which is only ~51.6% of the cladding' average wall-thickness, Fig. 5.2c. Subsequent investigations reveal these areas showed significantly influence on the materials' failure processes tested at both temperatures, as will be presented in Section 5.4.

It can be found, the macropores did not obviously connect to each other, Fig. 5.2d. As for the micropores, they distributed along the braiding angle of the fibre bundles (marked in Fig. 5.2e), and they had some connections with each other.

The volume fraction of pores (porosity) of the cladding material was calculated to be 3.45 ± 0.21%, where macropores at the inner surface and pores in the outer SiC coating were excluded from the volumetric calculation. The volume fractions of macropores and micropores were calculated to be 0.52 ± 0.09% and 2.93 ± 0.26%, respectively. The consistency in the structures, distributions, and volume fractions of the porosity among all the examined specimens indicates the representativeness of the calculated volume. This is further substantiated by the uniform mechanical behaviour described in Section 5.3.

5.2. Local property and residual stress of as-received material

Subsequent to the examination of the as-received material's microstructures, a comprehensive investigation was conducted to obtain the local mechanical properties and residual stresses of individual components in the as-received material, as they could potentially affect the material's mechanical properties and failure processes at both temperatures.

5.2.1. Local property

Nanoindentation were conducted via the methods described in Section 3.3.3. The results are summarized in Table 5.1.

For the outer SiC coating, only very slightly variation of hardness, H, and elastic modulus, E were measured across its thickness, with the lowest hardness (~30.2 GPa) and elastic modulus (~398.1 GPa) values both measured at the location of 50 μm away from coating/CMC interface, Fig. 5.3. This indicates the local properties of individual sub-layers in the outer coating are

similar. In general, the outer SiC coating has an average value of hardness and elastic modulus of 32.2 ± 0.7 GPa and 407.2 ± 5.5 GPa, respectively.

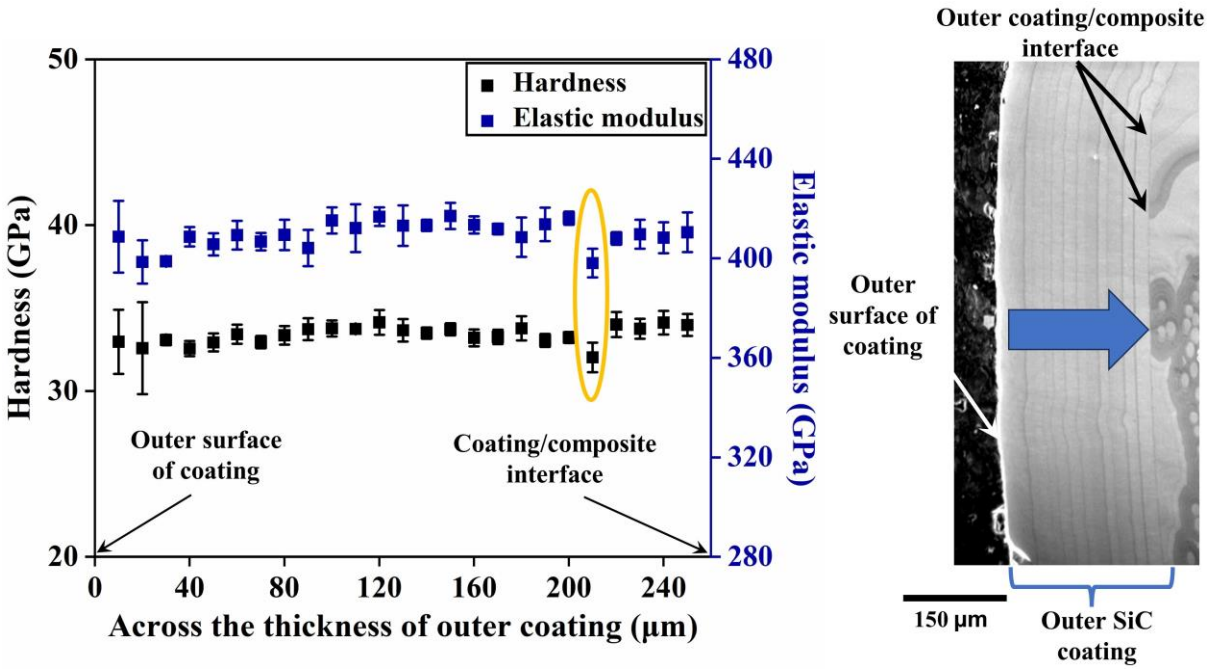

Figure 5-3. Hardness and elastic modulus values across the thickness of outer CVD SiC coating of the polished cross-section of as-received material. Optical image of polished cross-sections of outer SiC coating is also included, with the blue arrows show the locations for line-indents.

In underlying composite, the elastic modulus of matrix next to fibre bundles is 90% of that in the SiC matrix between fibre bundles. For the SiC fibres, they have an average hardness of 19.3 ± 3.2 GPa and elastic modulus of 189.4 ± 11.4 GPa, which were much lower (by ~60% and ~45%, respectively) than that of matrix and the outer coating. The measurements in this section will be subsequently compared with literature values in Section 5.5.

Table 5-1. Measured values of the hardness *H* and elastic modulus *E* in different areas of the polished cross-section of the as-received material.

Locations	*H* (GPa)	*E* (GPa)
Matrix next to fibre	33.21 ± 3.13	356.78 ± 16.90
Matrix between fibre bundles	33.45 ± 0.70	391.93 ± 10.77
Fibres	19.28 ± 3.22	189.40 ± 11.41
Outer SiC coating	32.23 ± 0.68	407.21 ± 5.52

5.2.2. Residual stress

By using the method described in Section 3.2.3, the residual stress of SiC phase of individual components of the cladding material, including: outer SiC coating, SiC fibres and SiC matrix were measured.

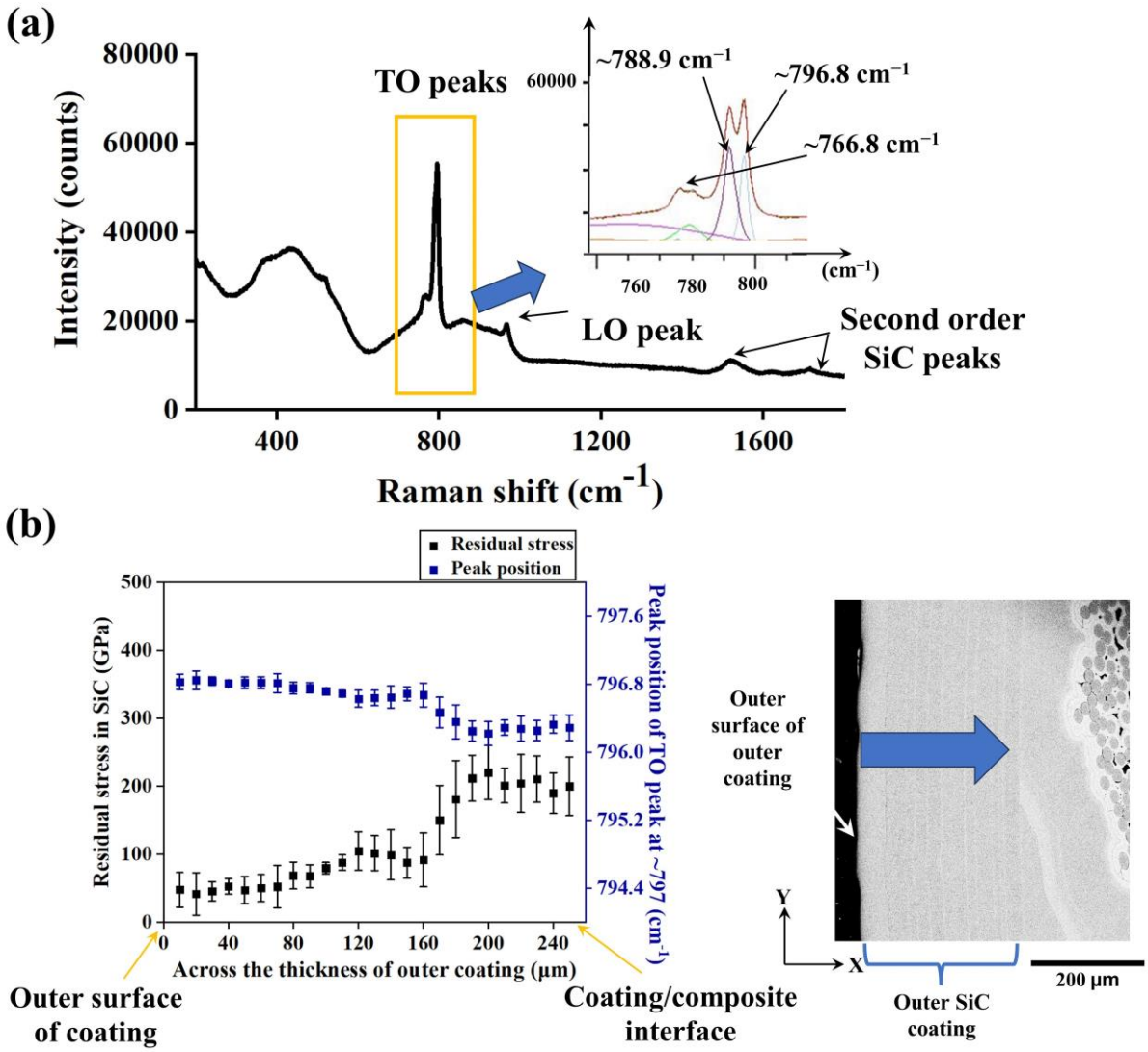

Figure 5-4. Raman measurements collected across the thickness of the multi-layer outer SiC coating in the polished cross-section of as-received material. (a) Typical Raman spectra of SiC phase. (b) Peak positions of selected SiC TO peak (~797 cm^{-1}) and corresponding estimated tensile residual stresses of SiC phase across the thickness of the outer coating.

For the outer coating, Raman spectra collected in different locations in the coating are found similar, with one representative example presented in Fig. 5.4a. Some random SiC peaks can be observed in the spectrum range of 400 cm^{-1} to 500 cm^{-1}. In the range of 500 cm^{-1} to 1000 cm^{-1}, three types of TO peaks were found: at ~766.8 cm^{-1}, at ~788.9 cm^{-1} and at ~796.8 cm^{-1}. Compared with the outer coating of the material in Chapter 4, the ~788.9 cm^{-1} TO peak in outer coating in current Chapter is sharper. One LO peak was found at ~973 cm^{-1}. In 1300 cm^{-1} to 1800 cm^{-1}, some second order SiC peaks were observed. Note that, no obvious Si peak (at ~520.3 cm^{-1}) was detected in the outer coating, indicates the outer coating in current work consists of high purity level of SiC phase without obvious Si phase.

The residual stress in outer SiC coating is plotted in Fig. 5.4b. Tensile stress was measured, it stayed quite constant (~50 MPa) from 10 μm to 70 μm away from the surface of the outer

coating, and steadily increased from 70 µm (~50 MPa) to 120 µm (~100 MPa). Then, it remained constant (120 µm to 160 µm) at ~100 MPa, increased to ~210 MPa (170 µm to 190 µm); and final remained constant at ~210 MPa from 190 µm to 260 µm (coating/composite interface), Fig. 5.4b. In general, the average tensile residual stress in outer coating was measured to be 112 ± 70 MPa (0.12 ± 0.07 GPa), and the potential reason for the variation of residual stress in the coating will be discussed in Section 5.5.

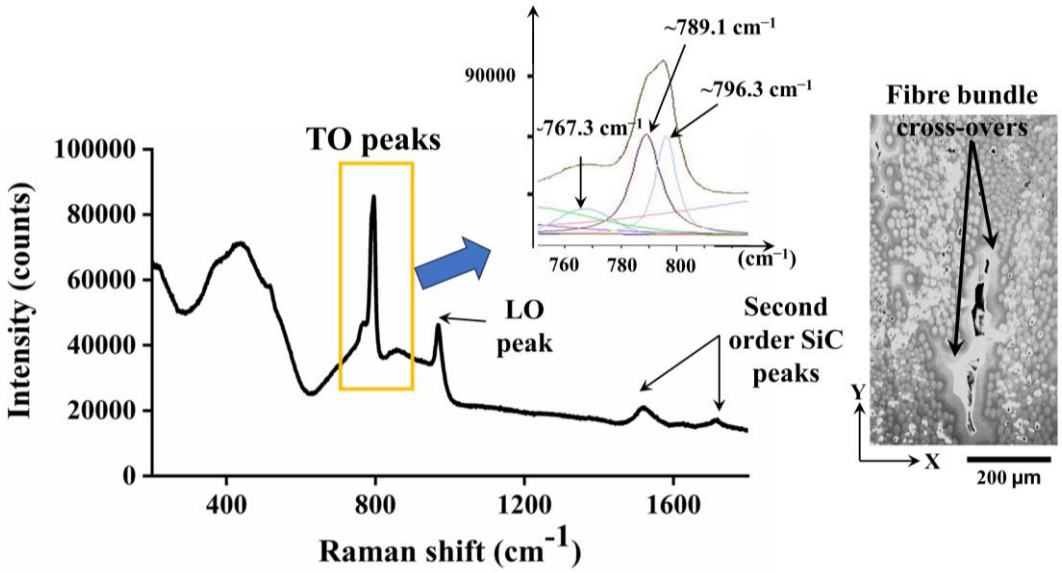

Figure 5-5. One typical Raman spectra collected in the matrix between fibre bundles in the polished cross-section of as-received material.

In the composite, the Raman spectra of SiC matrix between fibre bundles were found similar, and one representative example is presented in Fig. 5.5. Similar to that of the material in Chapter 4, three types of SiC TO peaks and one LO peak were also observed. No significant broadening of LO peak is detected. Generally, tensile residual stress was estimated in matrix between SiC fibre bundles, 0.10 ± 0.06 GPa, as tabulated in Table 5.2.

For residual stresses of SiC fibre and SiC matrix in SiC fibre bundles (matrix next to the fibre), the Raman spectra were collected at four locations along the fibre radial direction (Fig. 5.6a), which is similar to that in Chapter 4. The results are plotted in Figs. 5.6b and 5.6c, where Fig. 5.6a presents typical SiC peaks in the range of 0 to 1200 cm^{-1} and Fig. 5.6b presents typical carbon peaks in the range of 1200 cm^{-1} to 1800 cm^{-1}. The spectra of locations 1 and 2 were very similar and overlapped in Figs. 5.6b and 5.6c. These results are similar to that in Chapter 4 (Fig. 4.7) as same type of fibres was used. Compared with the material in Chapter 4, the main difference is for matrix next to the fibres. Significant broadening of TO and LO peaks were

observed, as presented in Fig. 5.6b. This broadening effect complicates the precise fitting of individual SiC TO peaks and the estimating of residual stress in this location.

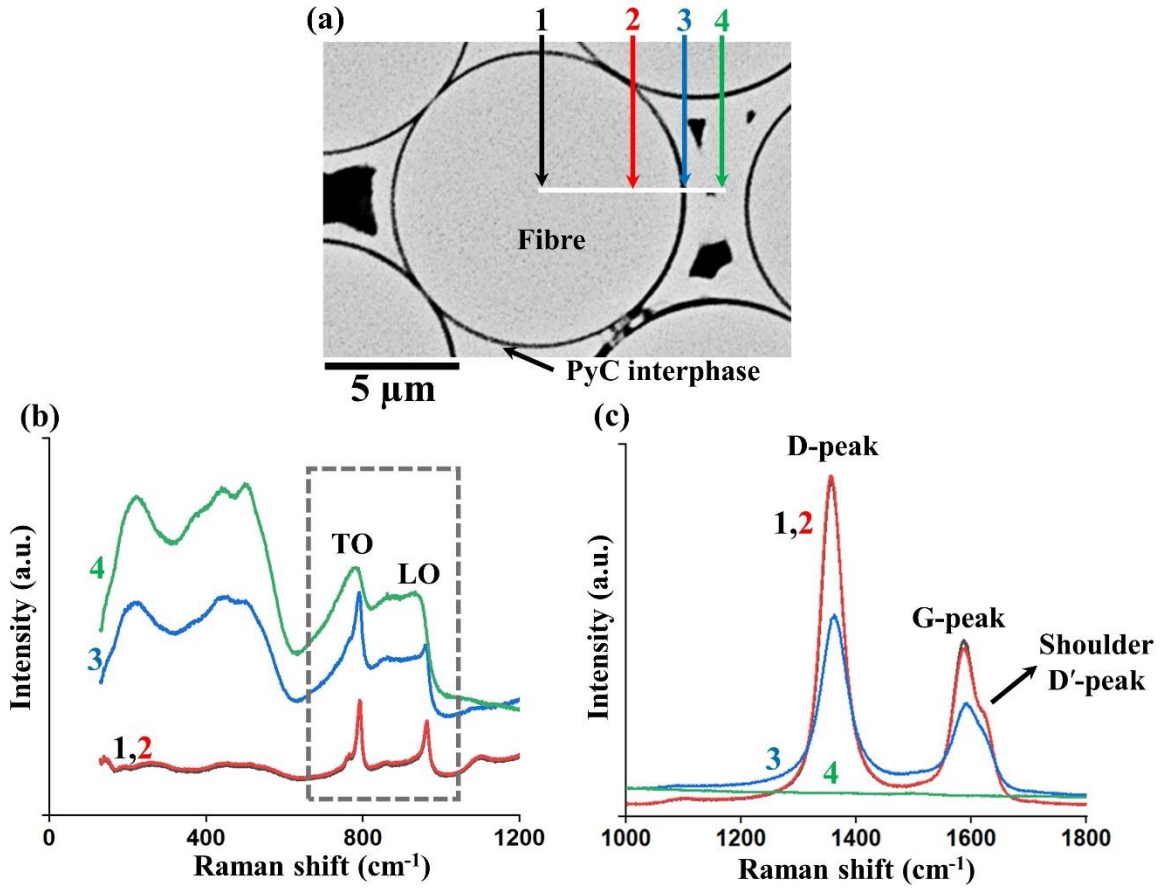

Figure 5-6. (a) Polished cross-sectional SEM image of one fibre showing the location of four measurements taken along the radial direction of the fibre; (b) and (c) are Raman spectra of different locations on the polished fibre cross-section: (1) centre of fibre, (2) middle point between the centre and the periphery of the fibre, (3) PyC interphase area and (4) matrix next to the fibre; with (b) collected in the range of 0 to 1200 cm^{-1} showing SiC peaks and (e) collected in the range of 1200 cm^{-1} to 1800 cm^{-1} showing carbon peaks

5 Raman line scans were collected along the fibre radial direction (from location 1 to location 3), in steps of 1 µm, as presented in Fig. 5.7. For SiC phase, tensile stress steadily decreases from fibre centre (~0.9 GPa) to PyC interphase (~0.5 GPa), Fig. 5.7b. The carbon phase is in compression: -0.3 GPa in fibre and -0.6 GPa in PyC interphase area, Fig. 5.7c.

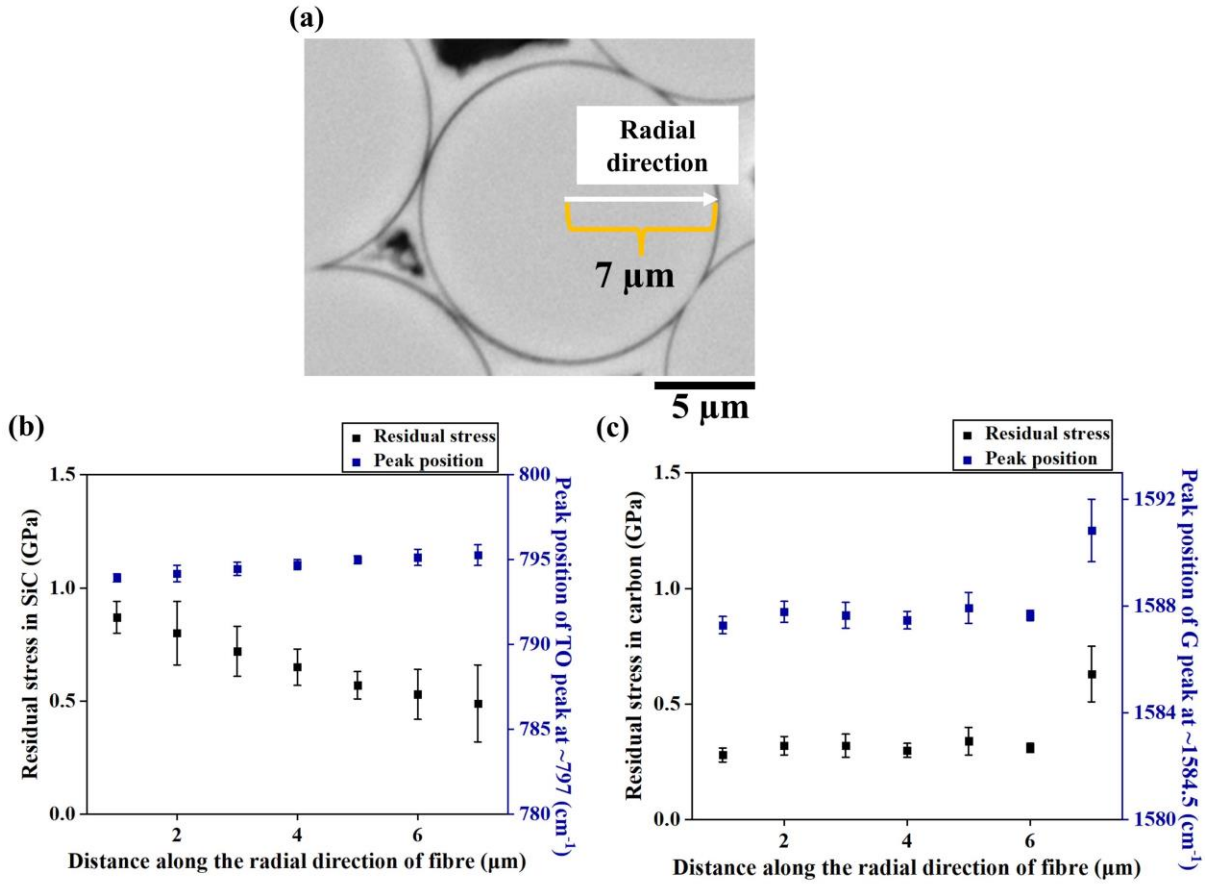

Figure 5-7. (a) Polished cross-sectional SEM image shows line-scan of Raman measurements taken along the radial direction of the fibre; (b) shows peak positions of selected SiC TO peak (~797 cm^{-1}) and corresponding estimated tensile residual stresses of SiC phase; and (c) shows peak positions of selected carbon G peak (~1584.5 cm^{-1}) and corresponding estimated compressive residual stresses of carbon phase.

Table 5-2. Raman peak positions of the SiC TO band and carbon G band with the corresponding calculated residual stresses ('+' for tensile stress and '−' for compressive stress).

Locations	Raman peak position of SiC TO band (cm^{-1})	Residual stress in SiC phase[a] (GPa)	Raman peak position of carbon G band (cm^{-1})	Residual stress in carbon phase[b] (GPa)
Outer SiC coating	796.58 ± 0.25	+0.12 ± 0.07	-	-
Matrix between fibre bundles	796.63 ± 0.21	+0.10 ± 0.06	-	-
Fibre centre	793.92 ± 0.24	+0.87 ± 0.07	1587.29 ± 0.32	-0.28 ± 0.03
Fibre edge	794.71 ± 0.29	+0.65 ± 0.08	1587.48 ± 0.33	-0.30 ± 0.03
PyC interphase	795.26 ± 0.61	+0.49 ± 0.17	1590.84 ± 1.17	-0.63 ± 0.12

[a] calculated using Eq. 3.10, with ΔC being 3.53 ± 0.21 cm^{-1}/GPa [306]

[b] calculated using Eq. 3.10, with ΔC being 10 cm^{-1}/GPa [307]

5.3. Mechanical behaviour at RT and 1200°C

Fig. 5.8 shows the load-time curves of materials under C-ring compression experiments at room temperature and 1200°C. Samples S2-1 and S2-2 were tested at RT and S2-3 and S2-4 were tested at 1200°C. Detailed testing sequences are listed in Table A.4 in Appendices.

During each μXCT scan the specimen was maintained at a fixed displacement for around 6 mins (the acquisition time of μXCT scan). Progressive reducing of load at such fixed displacement (load relaxations) were not evident for the samples tested at RT (Fig. 5.8a), but were found for 1200°C samples, Fig. 5.8b. These observations are similar with the SiC_f-SiC_m cladding materials reported in Chapter 4, with obvious load relaxations were only found for samples tested at 1200°C. The detailed load relaxation as a function of load of the materials investigated in current Chapter are tabulated in Table A.5. Specially, the load relaxations are in the range of 12.17% to 25.96% of the applied load, which were higher than that of the materials investigated in Chapter 4 (5.22% to 17.45%). Note that, such load relaxations during the fixed displacement is suggested to be affected by three main factors, including testing temperature, type of the material and acquisition time for the μXCT scan [229].

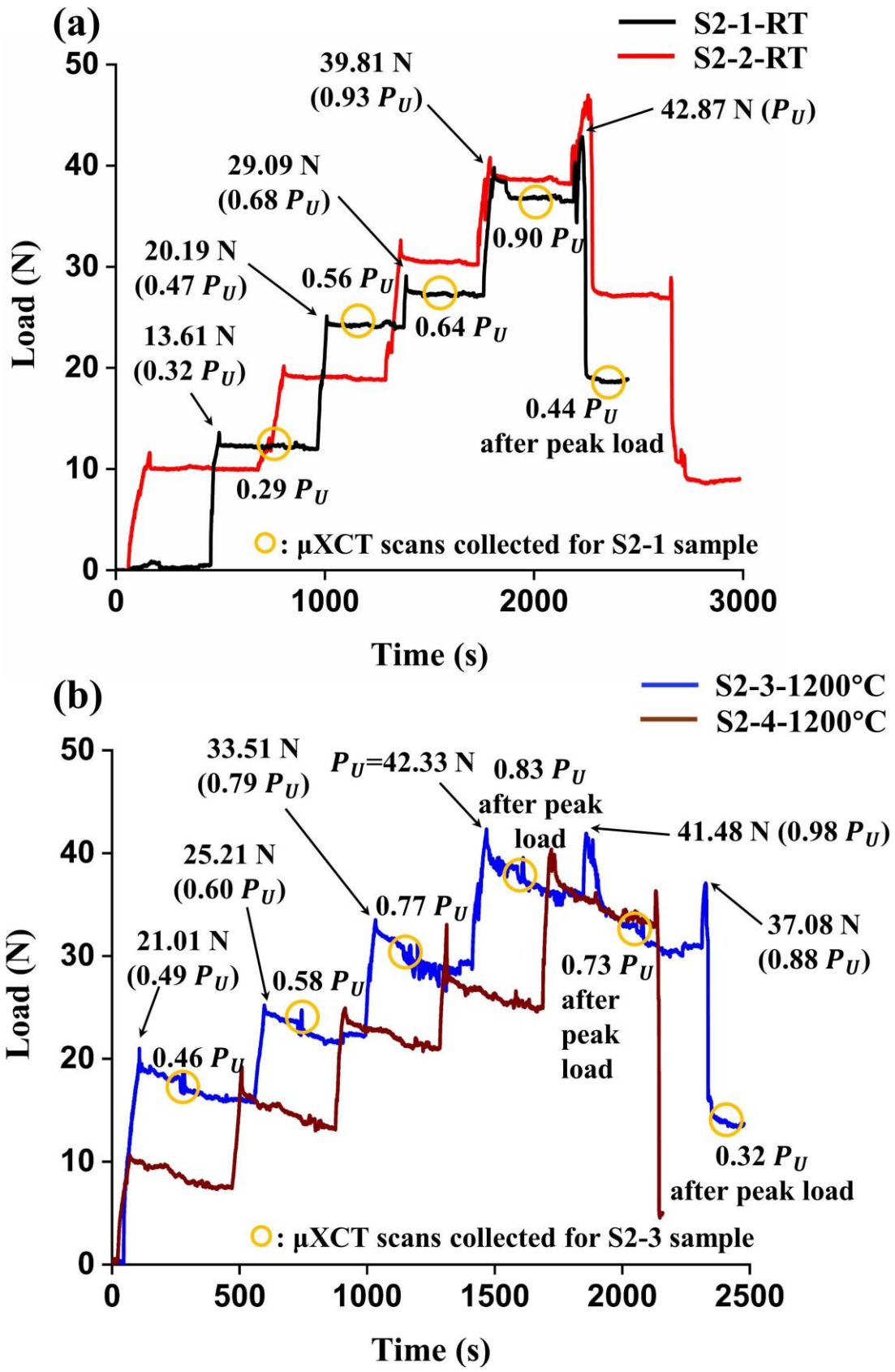

Figure 5-8. Load-time curves for the SiC_f-SiC_m cladding materials under C-ring compression tests for (a) samples S2-1 and S2-2 tested at RT and (b) samples S2-3 and S2-4 tested at 1200°C. The open circles indicate locations of μXCT scans on samples S2-1 and S2-3; load drops and peak load are marked by arrows in S2-1 and S2-3 curves.

In addition to load relaxations, it was observed that load drops, characterized by an abrupt reduction in applied load while the sample is maintained at a fixed displacement, occurred for all the samples tested at both RT and 1200°C. Subsequent investigation by the real-time μXCT imaging revealed, these load drops were associated with the initiation and propagation of cracks in the SiC_f-SiC_m cladding materials under loading at both temperatures, as will be detailed shown in Section 5.4. Note that, prior to the C-ring compression tests, cracks already formed in all the tested C-ring samples caused by the cutting process. However, despite these presented cracks, similar mechanical behaviour was observed for samples at same testing temperature. Moreover, such cracks did not prevent the materials from bearing more load (stress) with further loading.

For the materials tested at RT, several small load drops (1 N to 5 N) occurred before reaching peak load, and the large load drop (by more than 20 N) occurred at P_U, Fig. 5.8a. As for the materials tested at 1200°C, several small load drops occurred prior to and at the peak load (Fig. 5.8b), before the large load drop happened after P_U. These observations are different from the materials tested at RT.

Note that, following the formation of cracks in the materials at RT and 1200°C, stress distribution in the C-ring sample could be modified; thus, Eq. 3.1 could be unsuitable. However, the maximum hoop stresses have been estimated via the peak load of each sample and these values are tabulated in Table 5.3. The maximum hoop stresses at RT were calculated to be ~243.5 MPa, with similar values at 1200°C: ~237 MPa.

Table 5-3. Calculated maximum hoop stress for SiC_f-SiC_m cladding materials under C-ring compression tests at RT and 1200°C.

Specimen	Sample width (mm)	Peak load (N)	Maximum hoop stress[a] (MPa)
S2-1-RT	3.78	42.87	237.20
S2-2-RT	3.92	46.97	250.60
S2-3-1200°C	3.83	42.33	235.27
S2-4-1200°C	3.74	40.38	239.01

[a] calculated using Eq. 3.1, ASTM C1323-16 [246].

5.4. Failure processes and toughening mechanisms at room temperature and 1200°C

The progressive failure processes and crack toughening mechanisms of the SiC_f-SiC_m cladding materials at both RT and 1200°C were investigated by analyzing the *in-situ* μXCT scans collected at different loading steps. Consistent failure processes were observed for the materials tested at same temperature, therefore, the samples S2-1 and S2-3 are selected as representative examples to illustrate the failure processes at RT and 1200°C, respectively.

5.4.1. Progressive failure process at room temperature

Fig. 5.9 represents the initial damage of S1 sample. One surface crack (Crack#1) was found in the outer coating, and travelled across the sample's total width (~3.8 mm). YZ view of Crack#1 (selected range in a length of ~3.6 mm, which is ~95% of the sample's total width, Fig. 5.9a) revealed Crack#1 is straight without obvious deflection or bifurcation on the surface of outer coating, and the width of Crack#1 on the coating surface is ~10 μm, Fig. 5.9a.

The 3D visualization of Crack#1 from different views, and corresponding representative μXCT slices of X-Y plane are presented in Fig. 5.9b. Generally, there are 1233 μXCT slices of X-Y plane in the dataset, represents the total length of the Crack#1 (same as the width of the sample: ~3.8 mm). ~121 slices (~10% of the total length of the crack) showed Crack#1 deflected along the coating/composite interface, and propagated into the fibre bundles, with one representative example presented in Slice 1 in Fig. 5.9b. ~360 slices (~29% of the total length of the crack) showed Crack#1 propagated into the fibre bundles with connection with the macropores, reached to around 50% of the total thickness of the sample (~1 mm), with one representative example presented in Slice 2 in Fig. 5.9b. ~752 slices (~69% of the total length of the crack) showed Crack#1 arrested at the coating/composite without any obvious deflection along such interface or propagation into the underlying composite, one representative example is presented in Slice 3 in Fig. 5.9b. In summary, for the initial Crack#1, ~39% of the total crack length travelled into and interacted with underlying CMC layer (marked by open rectangles Fig. 5.9b), with the remaining part (~61%) arrested at coating/CMC interface, Fig. 5.9b. Note again, such initial damage did not prevent samples from bearing more load.

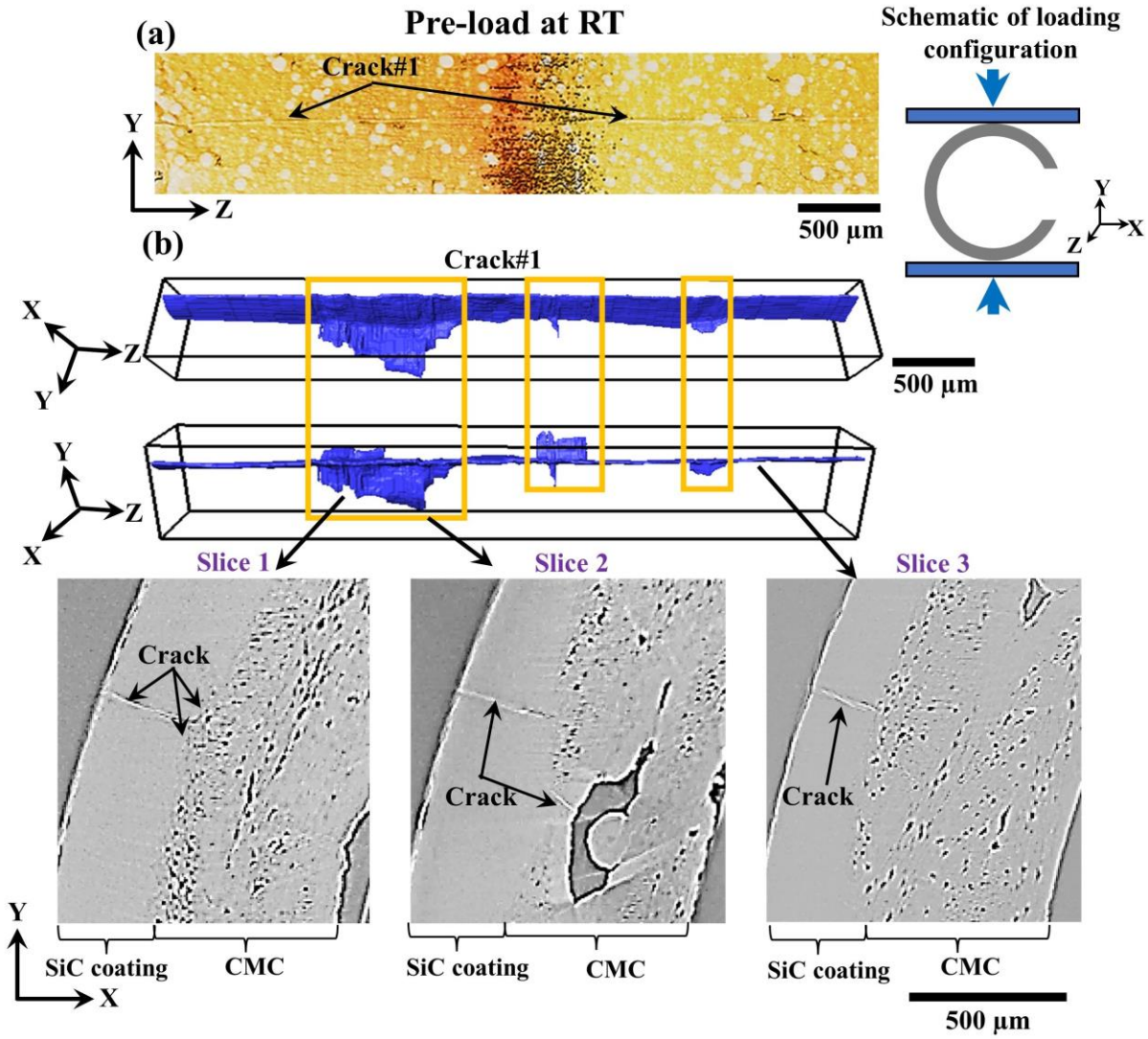

Figure 5-9. 3D visualization of the majority length of surface crack (Crack#1) in the outer SiC coating tested at RT (sample S2-1 is selected as representative example) from the scan collected at pre-load: (a) the YZ view shows the formation of Crack#1; (b) 3D visualization of Crack#1 from different views Representative Slices 1 to 3 of X-Y plane present different features of Crack#1: Slice 1 for crack deflection and bifurcation along the coating/composite interface; Slice 2 for crack linked up with large macropores in the matrix; Slice 3 for crack arrested at the coating/composite interface.

With further increasing of load, the load drops occurred at ~0.32 P_U and ~0.47 P_U correspond with the further opening of Crack#1 on the coating surface (~15 µm and ~25 µm in width, respectively). At ~0.47 P_U, the total length of Crack#1 propagated into underlying CMC layer.

Once load reached to 0.68 P_U, another load drop happened (from 0.68 P_U to 0.64 P_U), led to the formation of a second surface crack (Crack#2) in the outer coating. Crack#2 was subsequently found to be the fatal crack caused the failure of the C-ring sample. Once Crack#2 formed, it simultaneously travelled across the sample's total width. Fig. 5.10a displays the YZ view of Crack#2 (selected range in a length of ~3.5 mm, ~92% of the sample's total width). The width of Crack#2 on the surface of outer SiC coating is ~30 µm. 3D visualizations of

Crack#2 are presented in Fig. 5.10b. The total length of Crack#2 went into the underlying CMC layer. It deflected and bifurcated along the coating/CMC interface, and propagated into the fibre bundles, Slice 1 in Fig. 5.10b. Some part of it connected with the matrix macropores, Slice 2 in Fig. 5.10b. Some part of Crack#2 propagated in the matrix between fibre bundles, Slice 3 in Fig. 5.10b. Deflection of Crack#2 in the outer SiC coating was also observed (marked by open purple circle), Slice 4 in Fig. 5.10b.

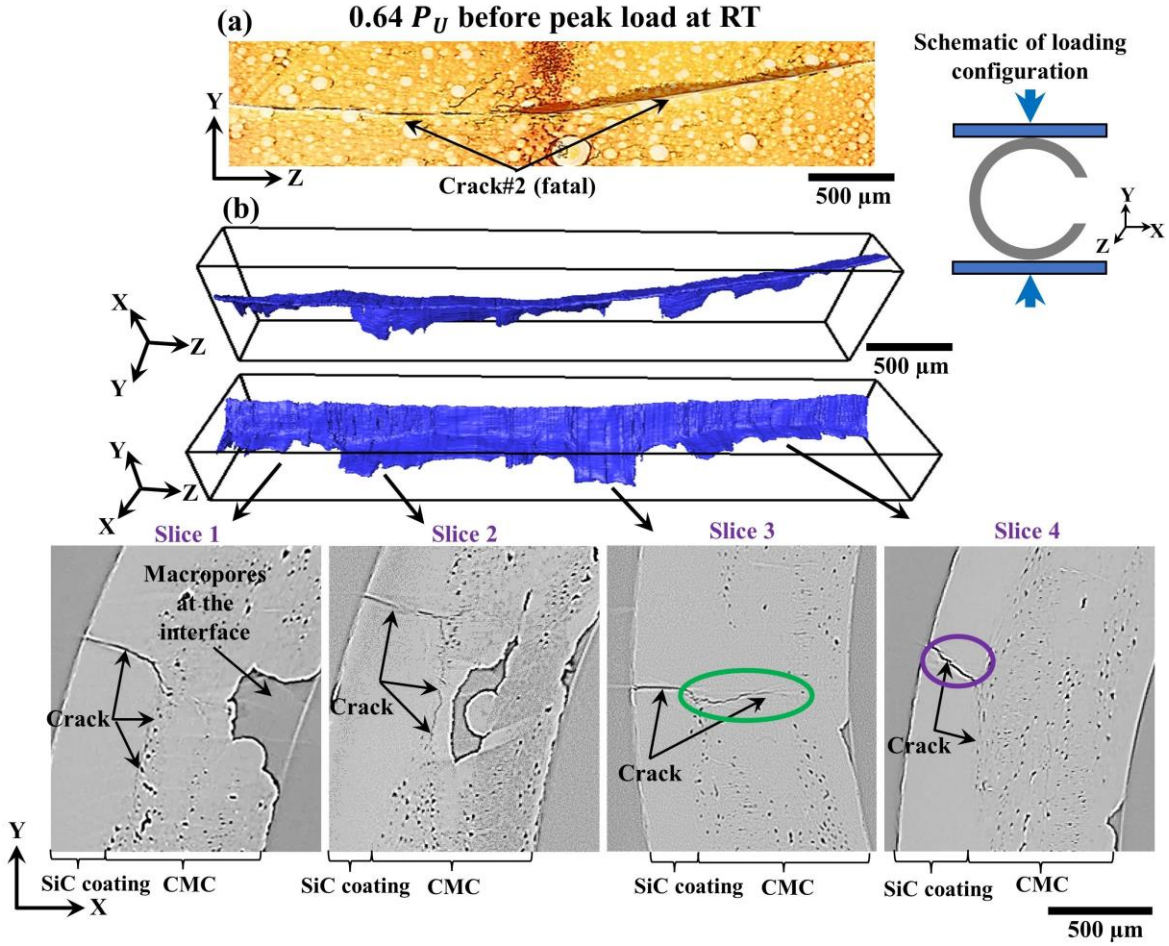

Figure 5-10. 3D visualization of the majority length of surface crack (Crack#2, fatal crack) in the outer SiC coating tested at RT (sample S2-1 is selected as representative example) from the scan collected at pre-load: (a) the YZ view shows the formation of Crack#2; (b) 3D visualization of Crack#1 from different views demonstrating that, once Crack#1 formed, all of the total crack length travelled into and interacted with the underlying composites. Representative µXCT Slices 1 to 4 of X-Y plane present different features of Crack#2 and the composite material.

Note that, as described in Section 5.1, certain areas in the material exhibited variations in wall-thickness (t) due to the presence of macropores at the inner surface, and the t reduced to approximately 60% of the average t of the material (Slice 1 in Fig. 5.10b). Furthermore, in the areas where have scarcity or absence of fibre bundles, crack extended into approximately 80% of the cladding material's total t once formed, Slice 3 in Fig. 5.10b. These areas in the CMC layers were unexpected.

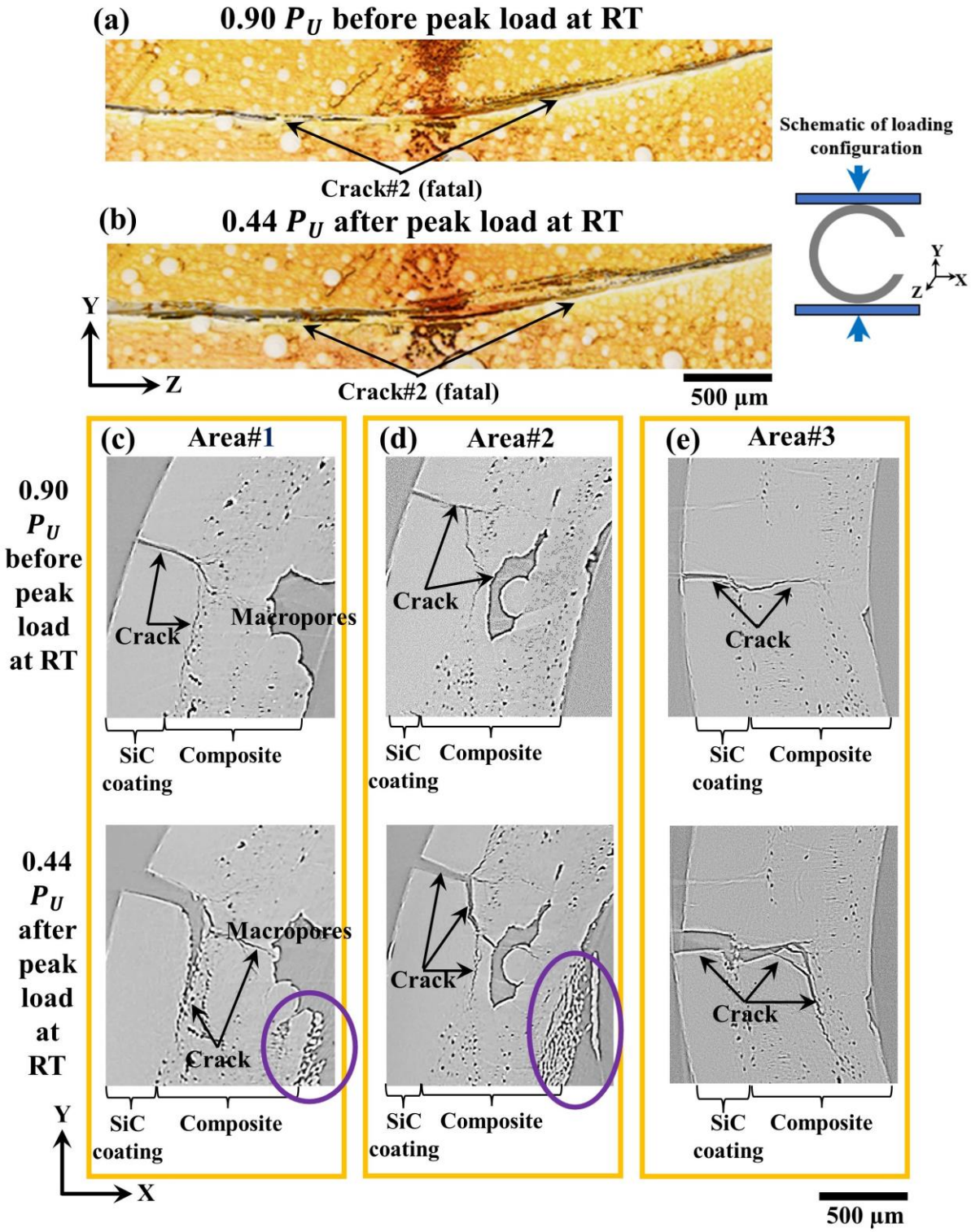

Figure 5-11. Propagation processes of Crack#2 (fatal crack) at RT. (a) and (b) are reconstructed µXCT scans respectively at 0.90 P_U before peak load and 0.44 P_U after peak load of Y-Z plane showing Crack#2 opening up in width with further loading. Crack depth is illustrated by cross-sectional µXCT slices of X-Y plane collected at three typical areas in the composites, including (c): Area#1, and slices in (c) are collected at the same position of Slice 1 in Fig. 5.10b; (d): Area#2, slices in (d) are collected at the same position of Slice 2 in Fig. 5.10b; and (e): Area#3, slices in (e) are collected at the same position of Slice 3 in Fig. 5.10b.

With further loading to ~0.90 P_U before P_U, Crack#2 opened up further on the surface of outer coating to ~45 μm in width, Fig. 5.11a. Crack depth is illustrated by the corresponding XCT slices of X-Y plane at three areas, including: Area#1, where macropores exist at the inner surface (slices in Fig. 5.11c are collected at the same position of Slice 1 in Fig. 5.10b); Area#2, where macropores exist in this area (slices in Fig. 5.11d are collected at the same position of Slice 2 in Fig. 5.10b); and Area#3, where has scarcity or absence of fibre (slices in Fig. 5.11e are collected at the same position of Slice 3 in Fig. 5.10b). At current loading stage (~0.90 P_U), Crack#2 did not travel across the entire thickness (~1 mm) of the cladding material.

After reaching P_U, the width of Crack#2 opened up to ~150 μm on outer coating's surface, Fig. 5.11b. Carefully investigation indicates that, Crack#2 travelled across the sample's entire thickness only at Area#1, linked up with macropores at inner surface, Fig. 5.11c. The deepest propagation depth of Crack#2 occurred at Area#2, more than ~90% of the thickness (~900 μm) of the material, Fig. 5.11d. At other areas, Crack#2 travelled across less than 80% of the thickness (~800 μm) of the material, with one representative example presented in Fig. 5.11e. Additionally, cracks were commonly observed inside the fibre bundles at the inner surface of the material, see examples in Figs. 5.11c and 5.11d. These cracks did not exhibit obvious connection with the fatal crack (Crack#2), indicates the initiation and propagation of these cracks were not caused by the propagation of Crack#2.

In summary, at RT, the presence of initial coating crack in the testing material did not prevent it from sustaining further loading. And subsequent loading led to the formation of fatal crack prior to the P_U. At P_U, the fatal crack travelled across the sample's total thickness at the areas where macropores existed at the inner surface, caused the final fracture of the sample.

5.4.2. Progressive failure process at 1200°C

Fig. 5.12 represents the initial damage of S3 sample. Two cracks (Crack#1 Crack#2) were observed in the outer coating, Fig. 5.12a. Carefully investigation revealed that Crack#1 was the fatal crack leading to the failure of the material, and propagation of Crack#1 under loading was detailed investigated in this section. The width of Crack#1 on the coating surface is ~20 μm, and it travelled across sample's total width (~3.8 mm), Fig. 5.12a.

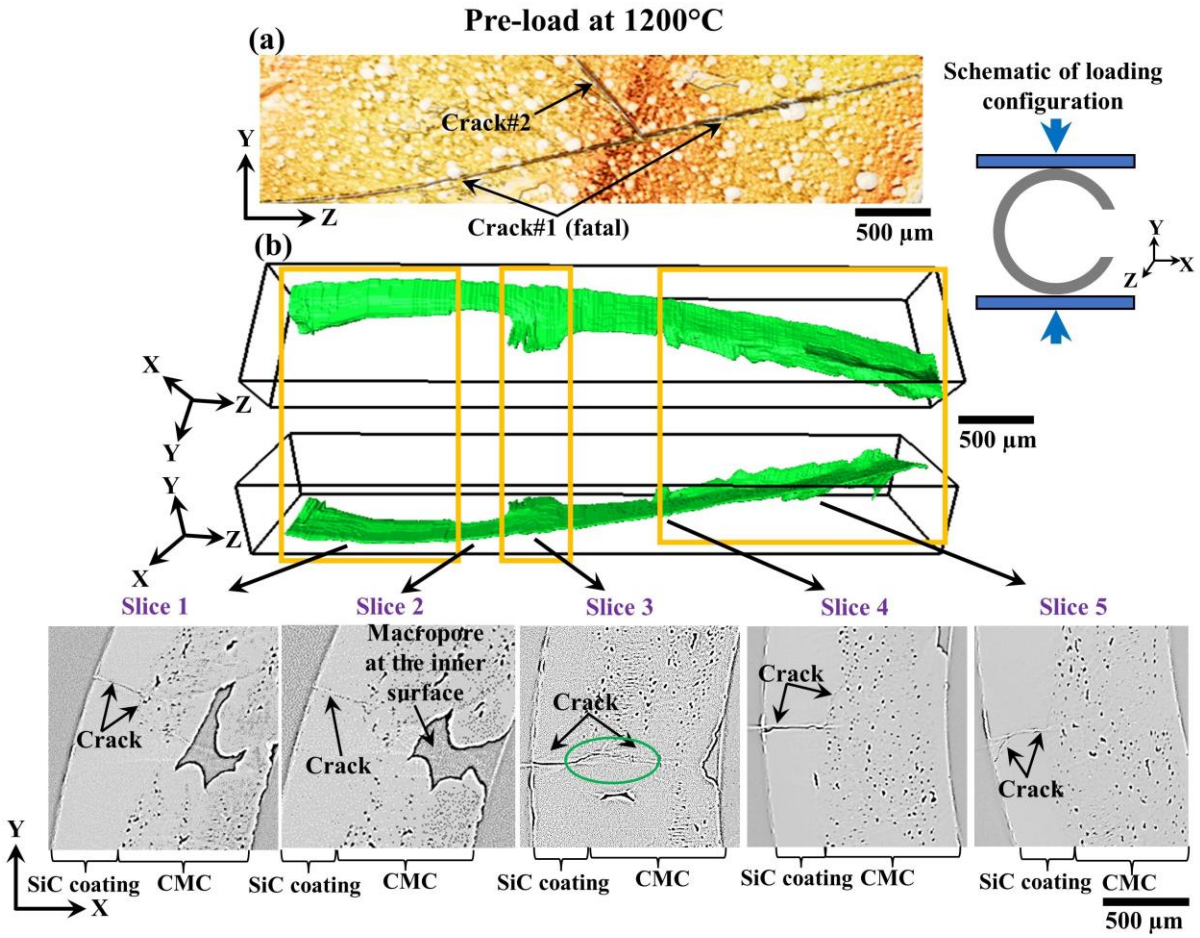

Figure 5-12. 3D visualization of the majority length of surface crack (Crack#1, fatal crack) in the outer SiC coating tested at 1200°C (sample S2-3 is selected as representative example) from the scan collected at pre-load: (a) the YZ view shows the formation of Crack#1; (b) 3D visualization of Crack#1 from different views. Representative Slices 1 to 5 of X-Y plane present different features of Crack#1.

Slices 1 to 5 in Fig. 5.12b represents different features of Crack#1.Slice 1 for crack deflection and bifurcation along the coating/composite interface. Slice 2 for crack arrested at the coating/composite interface. Note that, the macropores at the inner surface led to the wall-thickness at this area is only 60% of the average wall-thickness of the cladding material). Slice 3 for crack travelled into around 70% of the wall-thickness of the cladding material once formed, in the area with scarcity or absence of fibre bundles in the composites (marked by open green circle). Slice 4 for crack deflection along the coating/composite interface and travelled into the fibre bundles. Slice 5 for crack deflection in the outer SiC coating.

From the total 1233 µXCT slices of X-Y plane, ~788 slices (~64% of the crack's total length) showed Crack#1 deflected along the coating/CMC interface, and propagated into the fibre bundles, Slices 1 and 4 in Fig. 5.12b. ~122 slices (~10% of the crack's total length) showed Crack#1 travelled into more than 70% of wall-thickness (~700 µm) of the material in the area with scarcity or absence of fibre bundles, Slice 3 in Fig. 5.12b. ~323 slices (~26% of the crack's

total length) showed Crack#1 arrested at the coating/CMC interface, Slice 2 in Fig. 5.12b. In summary, the majority (~74% of crack length) of Crack#2 travelled into and interacted with the underlying CMC layer (marked by open rectangles Fig. 5.12b), with ~26% of the total length of Crack#1 arrested at the coating/CMC interface, Fig. 5.12b. Such damage is larger than the initial coating crack in room temperature sample (61% of crack length arrested at the interface). However, under such level of initial damage, high temperature samples could still sustain more loading before final fracture, and reached to similar peak load as the materials tested at RT.

With further loading, no newly formed cracks were observed. The Crack#1 (fatal crack) opened up in width on the surface of the outer coating, with ~25 μm at 0.58 P_U before P_U (Fig. 5.13a), ~40 μm at 0.77 P_U before P_U (Fig. 5.13b), ~60 μm at 0.83 P_U before P_U (Fig. 5.13c), and ~170 μm at 0.73 P_U after P_U, Fig. 5.13d.

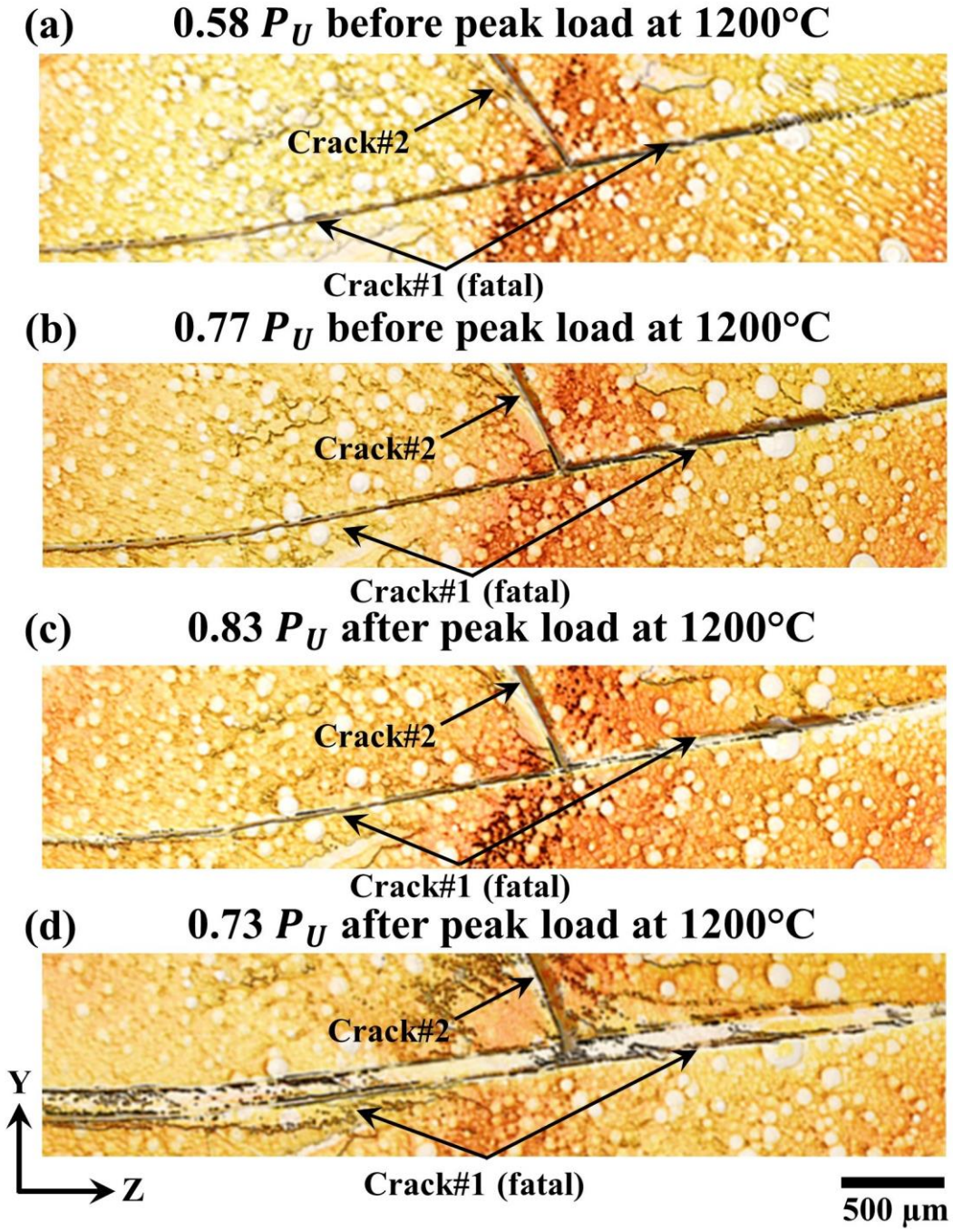

Figure 5-13. Failure processes of the cladding material at 1200°C, illustrated by reconstructed µXCT scans of Y-Z plane, including: (a) 0.58 P_U before peak load, (b) 0.77 P_U before peak load, (c) 0.83 P_U before peak load and (d) 0.73 P_U after peak load.

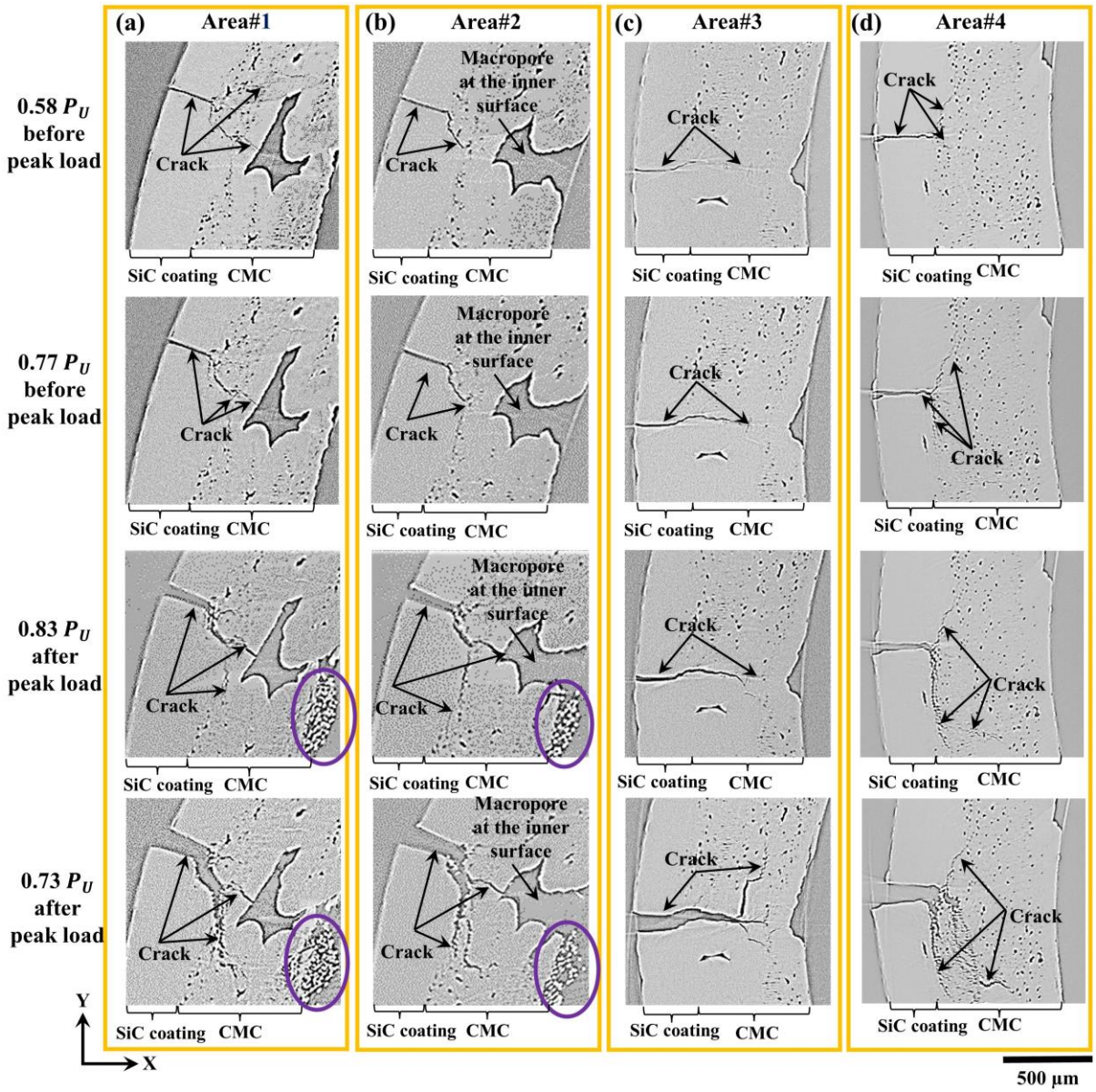

Figure 5-14. Cross-sectional μXCT slices of X-Y plane collected at four typical areas in the composites to illustrate the failure process, including (a): Area#1, same area of Slice 1 in Fig. 5.12a); (b): Area#2, same area of Slice 2 in Fig. 5.12b; (c): Area#3, same area of Slice 3 in Fig. 5.12b; and (d) Area#4, same area of Slice 4 in Fig. 5.12b.

The propagation depths of Crack#1 with continuously loading are illustrated by the collected μXCT slices of X-Y plane at four areas, including: Area#1, where macropores exist in the composite (slices in Fig. 5.14a are collected at the same position of Slice 1 in Fig. 5.12a); Area#2, where macropores exist at the inner surface of the material, and the wall-thickness at this area is only 60% of the average wall-thickness of the cladding material (slices in Fig. 5.14b are collected at the same position of Slice 2 in Fig. 5.12b); Area#3, where has scarcity or absence of fibre bundles in the composite (slices in Fig. 5.11c are collected at the same position of Slice 3 in Fig. 5.12c); and Area#4, where no obvious macropores and scarcity or absence of

fibre bundles area exist in the composite (slices in Fig. 5.11d are collected at the same position of Slice 4 in Fig. 5.12d).

At Area#1, Crack#1 connected with the macropores with further loading, and did not travel across the total thickness of the material even after peak load, with the deepest depth (~750 μm) is ~75% of the material's thickness at 0.73 P_U after P_U, Fig. 5.14a. However, for Area#2, after reaching P_U, Crack#1 connected with macropores at the inner surface and travelled across material's thickness at such area at 0.83 P_U after P_U, Fig. 5.14b. The across-thickness crack is only observed at Area#2 after peak load. At each loading step, the deepest propagation depths of Crack#1 were all found occurred at Area#3 (at where scarcity or absence of fibre bundles in the CMC layer): with more than 75% (~750 μm) of the sample's total thickness at 0.77 P_U before P_U; more than 85% (~850 μm) of the sample's total thickness after reaching P_U (0.83 P_U after P_U); and more than 90% (~900 μm) of the sample's total thickness at 0.73 P_U after P_U, Fig. 5.14c. For the crack propagation process at the areas without macropores and scarcity or absence of fibre bundles, Area#4 is selected as representative example, with the crack propagation depth less than 50% (~500 μm) of the sample's total thickness just after reaching P_U (0.83 P_U after P_U), and < 750 μm at the last loading step (0.73 P_U after P_U), Fig. 5.14d. Additionally, similar to the materials tested at RT, cracks were commonly observed inside the fibre bundles at inner surface of the material, Figs. 5.14a and 5.14b. These cracks did not exhibit obvious connection with the fatal crack (Crack#1), indicates the initiation and propagation of these cracks were not caused by the propagation of Crack#1.

In summary, at 1200°C, the load drops corresponded with the further propagation of initial coating cracks, and further loading did not result in the newly formation of coating cracks. Similar as the materials tested at RT, across-thickness crack only occurred at the area where macropores presented at the inner surface of the material. At both temperatures, fibre pull-out was commonly observed, with representative examples presented in Fig. 5.15.

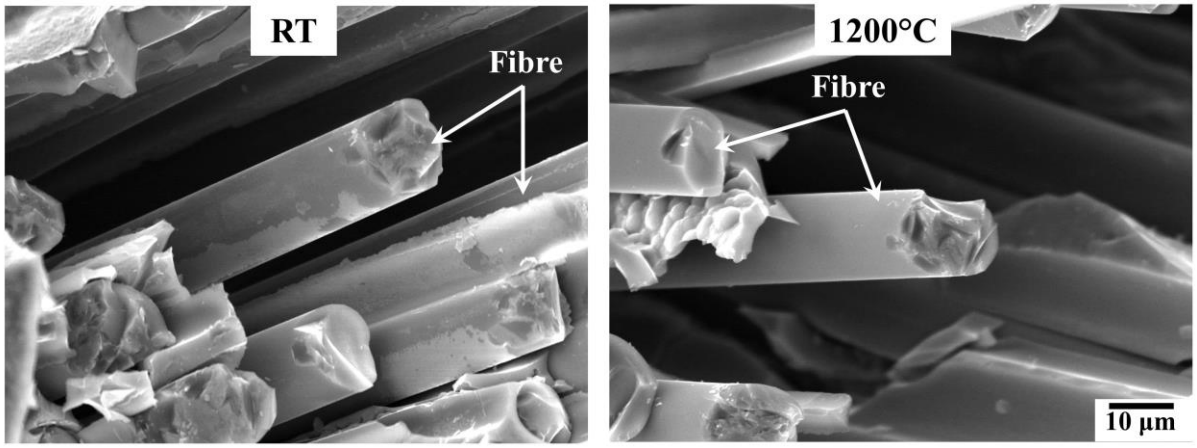

Figure 5-15. SEM images showing fibre pull-out of the materials tested at RT and 1200°C.

5.5. Discussion

5.5.1. Microstructures

5.5.1.1. Outer multi-layer SiC coating

In current study, the presence of pores at the interfaces of adjacent sub-layers in the outer SiC coating are commonly observed, which were unexpected and not reported in monolithic SiC coating of similar SiC_f-SiC_m claddings [14]. Such pores could potentially diminish the hermicity of the entire cladding system. Moreover, in current work, crack deflection in the outer multi-layer coating was commonly observed at both RT and 1200°C. This contrasts with observations in Chapter 4, where such deflection was only observed at 1200°C in monolithic SiC coating of similar SiC_f-SiC_m cladding under C-ring compression loading [14]. This indicates the weak interfaces of adjacent sub-layers could potentially facilitate the deflection of cracks in the coating, rather than their immediate propagation through the entire thickness of the coating, which potentially enhances the damage tolerance of the cladding system under C-ring compression loading. It is worth noting that, under different loading configurations (*e.g.*, uniaxial tension and compression), cracks could potentially initiate from these pores [147] in the outer coating, and consequently affect the structural integrity of the entire cladding material. Therefore, future work will be conducted for the thoroughly investigation of the influence of pores on strength and damage initiation areas in the multi-layer outer coating under different loading configurations, as well as their influence on the hermicity of the cladding system.

5.5.1.2. Fibre braiding patterns and pores in CMC layer

In current Chapter, the fibre bundles were in 3D braiding pattern with ±45° of fibre braiding angle to the tube axis. However, some unexcepted areas with scarcity or absence of fibre bundles were observed in the CMC layer, which unignorably showed influences on the failure

processes of the materials tested at both RT and 1200°C. Such areas were not observed in similar SiC_f-SiC_m materials (Chapter 4) in 3D fibre braiding patterns with ±60° of fibre braiding angle to the tube axis [14]. This indicates the variation of fibre braiding patterns could avoid the appearance of areas with scarcity or absence of fibre bundles in the CMC layer.

Additionally, the fibre braiding pattern could affect the porosity level of the SiC_f-SiC_m claddings. For instance, the volume fraction of macropores of the material in current Chapter is ~0.52%, which is only 20% of that (~2.56%) in the material in Chapter 4. Moreover, in current study, the total porosity of the SiC_f-SiC_m material is measured to be 3.45 ± 0.21%, which is significantly lower than the porosity level reported of similar CVI-densified SiC_f-SiC_m cladding materials: 8.7 to 20% [119], [128], [161], [162], [171], Table 2.7. The low porosity could be attributed to different parameters (*e*,*g*, deposition rate and temperature [159]) of CVI densification process in current work when compared with that in open literature; and such lower porosity could potentially enhance material's hermeticity [14], [119].

As described in Section 5.1, the macropores at the inner surface significantly reduce the materials' wall-thickness at such area, and consequently affect the failure processes of the materials under C-ring compression loading at both temperatures. Furthermore, it was reported that, for SiC_f-SiC_m cladding materials (without outer/inner coating) under uniaxial tension test, the sharp boundary of macropores commonly generated stress concentrations and caused damage initiation in such area [158]. Conversely, micropores only introduce localized fluctuations of minor magnitudes to the stress distribution, exerting negligible influence on the overall stress heterogeneity induced by macropores [158]. Therefore, for a thoroughly understanding of mechanical behaviour and failure processes of the SiC_f-SiC_m claddings, a thoroughly investigation of macropores in CMC layer is of virtual importance.

In summary, the variations in outer SiC coating, fibre braiding angles, and CVI densification processes result in distinct microstructures the SiC_f-SiC_m materials in Chapter 4 and current Chapter. A brief summary of their microstructures is tabulated in Table 5.4.

Table 5-4. Summary of the variations of microstructures of the SiC_f-SiC_m materials in Chapter 4 and Chapter 5.

	SiC_f-SiC_m in Chapter 4	**SiC_f-SiC_m in Chapter 5**
Outer SiC coating	Monolithic without pores	Multi-layers with pores at the interface of adjacent layers
Inner SiC coating	Monolithic without pores	-
Fibre braiding patterns	±60° of fibre braiding angle to the tube axis	±45° of fibre braiding angle to the tube axis
Volume fraction of macropores	2.56 ± 0.23%	0.52 ± 0.09%
Volume fraction of micropores	6.13 ± 0.52%	2.93 ± 0.26%
Porosity	8.69 ± 0.35%	3.45 ± 0.21%
Un-expected areas in CMC layer	-	(i) scarcity or absence of fibre bundles (ii) macropores at the inner surface

5.5.2. Local properties

For the outer SiC coating, very slightly variation of the hardness and elastic modulus values across its thickness, indicates the consistency of the local properties of the 11 sub-layers in the outer coating. As for the lowest hardness (~30.2 GPa) and elastic modulus (~398.1 GPa) values measured in the coating (Fig. 5.3), the indents could be performed at the week interface of layer 3 and layer 4.

The modulus of the matrix next to fibre (~357 GPa) was ~90% of that of outer coating and matrix between fibre bundles (~400 GPa), which could be attributed to the relativity lower crystallinity (detected by Raman spectroscopy, Fig. 5.6b) in these areas [337]. And such lower crystallinity in the matrix could potentially reduce the irradiation tolerance of the cladding material [338].

5.5.3. Residual stress

For the outer SiC coating, tensile residual stress of SiC phase steadily increased across the thickness of the coating: around 50 MPa (0.05 GPa) at the surface of outer coating to around 210 MPa (0.21 GPa) at the coating/composite interface. These observations are significant different with the residual stresses in the single layer of outer and inner SiC coatings of the material investigated in Chapter 4, with consistent residual stresses measured across the thickness of the coating, with 0.31 ± 0.13 GPa and 0.22 ± 0.12 GPa for the outer and inner SiC coatings, respectively. The variation of residual stress across the thickness of outer coating in current Chapter could be potentially resulted from the fabrication process of multiple SiC layers

in outer coating: the layers were deposited sequentially, with the innermost layer (highest measured tensile stress) formed by the initial deposition [339], [340].

As discussed in Section 4.6.3, the relaxation of tensile stress in single layer of outer coating could potentially affect the failure strength and strain of the coating at high temperatures [14]. Therefore, the relaxation of such complexed stress in multi-layer outer coating at high temperatures may result in different mechanical properties and failure processes under C-ring compression loading, when compared with the monolithic coating. Hence, further mechanical experiments will be conducted for materials without initial damage in multi-layer outer coating.

For the SiC matrix next to fibre, significant broadening of SiC TO and LO peaks were measured (Fig. 5.6b). This could be attributed to the relativity lower crystallinity of the matrix at such areas [337]. Moreover, the diminished crystallinity in the matrix has the potential to diminish the irradiation tolerance of the entire cladding material [338]. As for the SiC matrix between fibre bundles, 0.10 ± 0.06 GPa tensile residual stress was measured, which is lower (~66%) than the tensile stress of matrix between fibre bundles in the material in Chapter 4 (0.29 ± 0.10 GPa). This could be attributed to the different CVI densification processes of these two types of materials. As the variations of CVI parameters (*e.g.*, temperatures, times) could affect the microstructure and local property of the matrix [341], and consequently affect the residual stress of the matrix. A summary of residual stresses in individual components in the SiC_f-SiC_m materials in Chapter 4 and current Chapter is tabulated in Table 5.5.

The material in current Chapter use the same type of fibre (Hi-Nicalon™ type S fibre) as the material in Chapter 4. Therefore, the residual stresses of SiC phase and carbon phase inside the fibre in the same areas of these two types of materials are compered. For the SiC phase of fibre in current Chapter, the residual stresses in the centre and edge are respectively ~24% and ~16% higher than that of the fibre in Chapter 4 (~0.70 GPa and ~0.56 GPa, respectively); and for carbon phase, the residual stresses in the centre of fibre is ~19% lower than the that of fibre in Chapter 4 (around -0.36 GPa), and similar values at the PyC interphase area are measured: around -0.62 GPa. It is suggested that [163], different CVI densification processes of the matrix showed significantly influences on the residual stresses in the SiC fibre. As discussed in Section 4.6.2, in the SiC_f-SiC_m cladding material reported by Nance *et al*. [163], the residual stress of both SiC phase and carbon phase in their Hi-Nicalon Type-S SiC fibre varied with the CVI densification processes: with respectively −0.90 GPa and -3.2 MPa after 33% densification, −1.08 GPa and -4.0 MPa after 66% densification and −1.08 GPa and -4.7 MPa after 100% densification. This indicates that, for different types of SiC_f-SiC_m cladding materials, even

though the utilized fibre type is the same, the variation of manufacturing processes could lead to the variation of residual stress in the fibre. Therefore, for a faithful modelling of the mechanical behaviours of the SiC_f-SiC_m cladding materials, a comprehensive analysis of residual stresses in individual components should be conducted.

Table 5-5. Comparison of the residual stress in individual components in the SiC_f-SiC_m materials in Chapter 4 and Chapter 5.

Individual components	**SiC_f-SiC_m in Chapter 4**	**SiC_f-SiC_m in Chapter 5**
Outer SiC coating	For SiC phase: +0.31 ± 0.13 GPa	For SiC phase, varied across the coating thickness: ~50 MPa at the coating/CMC interface to ~210 MPa.
Inner SiC coating	For SiC phase: +0.22 ± 0.12 GPa	For SiC phase: +0.31 ± 0.13 GPa
Matrix between fibre bundles	For SiC phase: +0.29 ± 0.10 GPa	For SiC phase: +0.10 ± 0.06 GPa
Matrix next to fibre bundles	For SiC phase: +0.24 ± 0.10 GPa	For SiC phase, due to the significant broadening of TO peaks, hard to perform the peak fitting, and can not estimate the stress
Fibre centre	For SiC phase: +0.70 ± 0.20 GPa For carbon phase: -0.34 ± 0.02 GPa	For SiC phase: +0.87 ± 0.07 GPa For carbon phase: -0.28 ± 0.03 GPa
Fibre edge	For SiC phase: +0.66 ± 0.19 GPa For carbon phase: -0.38 ± 0.03 GPa	For SiC phase: +0.65 ± 0.08 GPa For carbon phase: -0.30 ± 0.03 GPa
PyC interphase area	For SiC phase: +0.56 ± 0.27 GPa For carbon phase: -0.62 ± 0.07 GPa	For SiC phase: +0.65 ± 0.08 GPa For carbon phase: -0.63 ± 0.12 GPa

5.5.4. Mechanical behaviour at RT and 1200°C

As described in Section 5.3, at both temperatures, the initial coating cracks (caused by the sample preparation process) did not significantly affect the mechanical behaviour of materials, as all tested samples could sustain a peak load of 40 N to 47 N. Although very limited mechanical experiments of SiC_f-SiC_m cladding materials testing at high temperatures can be found from open literature, the retention of materials' failure hoop strength (peak load) at elevated temperatures (up to 1900°C in Ar atmosphere) has been reported [14], [130]. For instance, Shapovalov *et al*. [130] conducted C-ring compression tests on their SiC_f-SiC_m cladding materials (without outer SiC coating) in Ar environment. The peak load of their materials reminded quite consistent at elevated temperatures: ~10 N at RT, ~8 N at 1040°C, ~11 N at 1360°C, ~10 N at 1760°C and ~9 N at 1900°C.

However, the failure hoop strength of the multi-layer outer coating cannot be derived from current work due to the presence initial coating cracks. In comparison with the monolithic outer

coating, the different microstructures and residual stress distribution of the multi-layer coating could potentially result in different mechanical behaviour and failure hoop strength of the coating under loading at elevated temperatures. Therefore, it is worth noting again that, for a faithful investigation of the influence of the application of multi-layer outer coating on the mechanical performances of the entire SiC_f-SiC_m cladding materials, further experiments are needed with proper sample preparation processes without the presence of initial damage.

Additionally, in current Chapter, the hoop strength (derived from peak load) of the material (with ±45° fibre braiding angle) was measured to be ~240 MPa at RT. Such strength is ~20% higher than similar material in Chapter 4 (with ±60° fibre braiding angle) under same testing conditions: ~200 MPa at RT. This indicates the fibre braiding pattern could potentially affect the hoop strength of the material. Similar phenomenon has been reported by Chen *et al*. [147] in their SiC_f-SiC_m cladding materials (2D braiding pattern, without outer/inner coating) under uniaxial tension at RT. Significant decreasing of strength was found with increasing fibre braiding angles: ~380 MPa for ±30°, ~200 MPa for ±45° and ~60 MPa for ±60°. It is suggested the tensile strength of the SiC_f-SiC_m cladding materials is more sensitive to the variation of fibre braiding angle [147]. Therefore, for a thoroughly investigation of the mechanical behaviour of current material, future work will be conducted focusing on the tensile behaviour of the material.

5.5.5. Summary of crack toughening mechanisms at RT and 1200°C

For the materials tested at both temperatures, several crack toughening mechanisms occurred in the outer SiC coating (Fig. 5.16), and underlying CMC layer (Fig. 5.17).

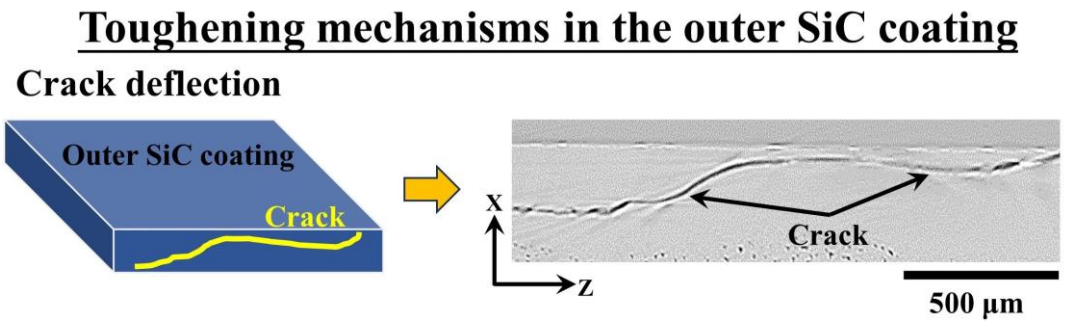

Figure 5-16. Schematics of the crack toughening mechanisms in the outer SiC coating of materials tested at both RT and 1200°C, with Type I: crack deflection within the coating.

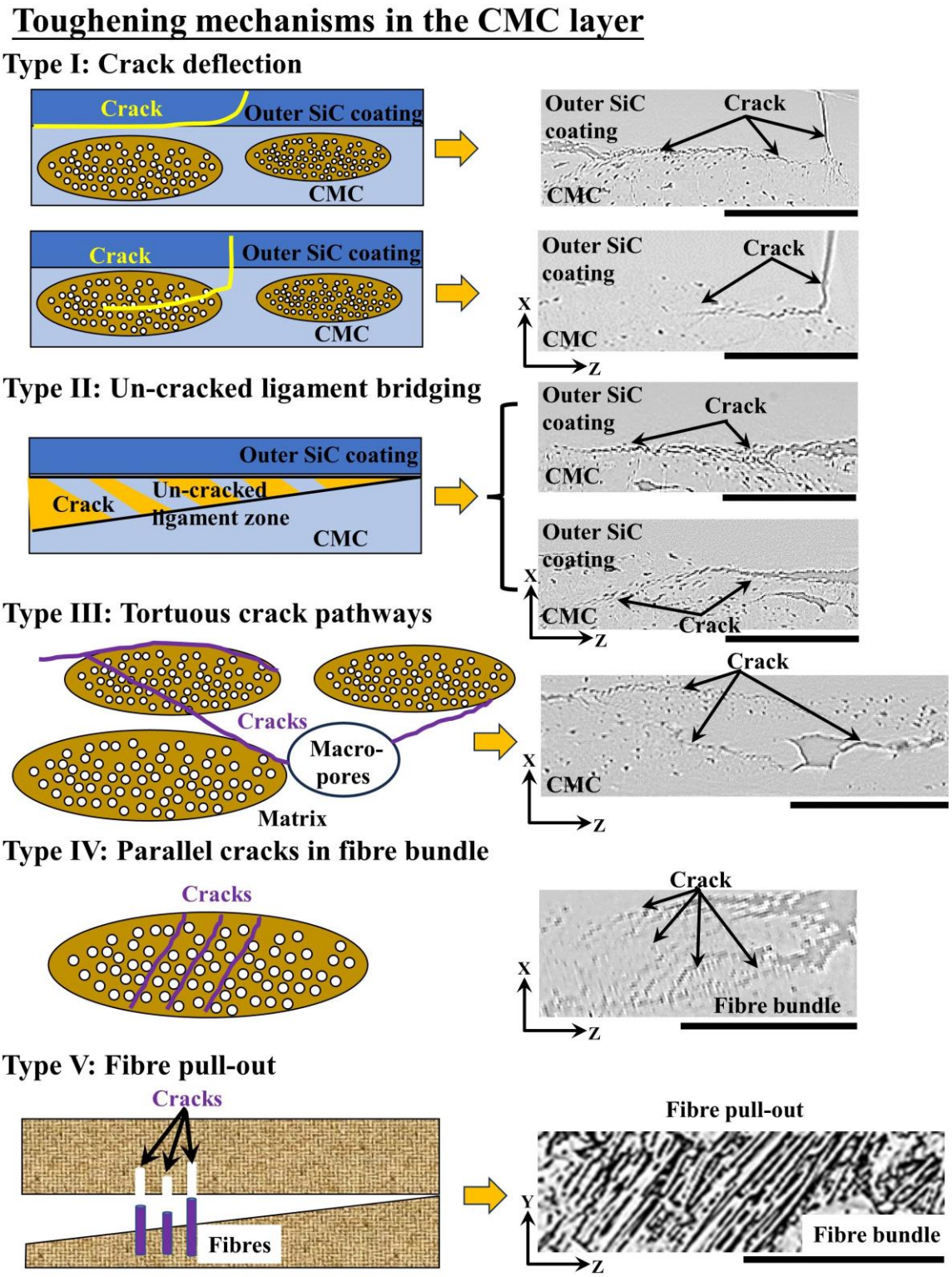

Figure 5-17. Schematics of the crack toughening mechanisms in the underlying composite of cladding materials tested at both RT and 1200°C, including: Composites Type I (crack deflection along the interface of coating/composites, crack deflection within fibre bundles), Composites Type II (un-cracked ligament bridging at the interface of coating/composites and within fibre bundles), Composites Type III (tortuous crack pathways), Composites Type IV (parallel cracks within fibre bundles) and Composites Type V (fibre pull-out). All the scale bars are 500 μm.

At both temperatures, one main crack toughening mechanism could be commonly observed in the multi-layer outer SiC coating: crack deflection in the coating, Fig. 5.16. It is worth noting again such defection was only observed in the materials with single layer outer coating (Chapter 4) under C-ring compression at 1200°C [14].

Once cracks reached the underlying CMC layer, the main crack toughening mechanism (before peak load) was crack deflection, along the coating/CMC interface (Fig. 5.17, Type I), as well as inside fibre bundles along the PyC interface (Fig. 5.17, Type I), transfer the growth paths of cracks away from the direction of maximum driving force.

At the tips of these deflected cracks, un-cracked ligament bridging (Fig. 5.17, Type II) at both the interface of coating/CMC and within fibre bundles was activated. Tortuous crack pathways were formed as cracks connected with the macropores, with deflection and bifurcation at the interfaces between fibre bundle and surrounding matrix (Fig. 5.17, Type III). Once cracks propagated into the fibre bundles, instead of broken individual fibres, they preferred to deflect along the PyC coatings, prevented the formation of catastrophic large cracks in fibre bundles (Fig. 5.17, Type IV). After reaching peak load, PyC coatings and matrices inside fibre bundles could not sustain a higher stress, and fibres were pulled out [131] (Fig. 5.17, Type V), enhanced the ductility of the cladding material. These observations apply to the materials tested at both temperatures. Note that, obvious fibre-pull out was not observed in similar materials (Chapter 4) with single layer outer coating under C-ring compression loading at both RT and 1200°C. And such fibre-pull out was also not being captured by real-time μXCT imaging in three types of SiC_f-SiC_m cladding materials (2D braiding pattern, with different fibre braiding angle; ±30°, ±45° and ±60°) under uniaxial tensile at RT [147]. A comparison of crack toughening mechanisms of the SiC_f-SiC_m materials in Chapter 4 and current Chapter tested at both temperatures is tabulated in Table 5.6.

These observations indicate the crack toughening mechanisms of different types of SiC_f-SiC_m materials could be different, and again highlight the importance of applying *in-situ* 3D μXCT imaging to investigate crack toughening mechanisms and failure processes of SiC_f-SiC_m claddings, which offer first-hand insights into the microstructural evolution of these materials.

Table 5-6. Comparison of crack toughening mechanisms in individual components of the SiC_f-SiC_m materials in Chapter 4 and Chapter 5 tested at both temperatures.

Toughening mechanisms	**SiC_f-SiC_m in Chapter 4**	**SiC_f-SiC_m in Chapter 5**
Crack deflection in outer SiC coating	Only at 1200°C	At both RT and 1200°C
Fibre pull-out	-	At both RT and 1200°C
Parallel crack inside fibre bundles	At both RT and 1200°C	At both RT and 1200°C
Crack deflection inside fibre bundles	At both RT and 1200°C	At both RT and 1200°C
Un-cracked braiding	At both RT and 1200°C	At both RT and 1200°C
Crack braiding in outer SiC coating	At both RT and 1200°C	-
Tortuous crack pathway	At both RT and 1200°C	At both RT and 1200°C

5.5.6. Optimizing the design of cladding material

The observations by real-time μXCT imaging in current Chapter could help to optimise the design of such SiC_f-SiC_m cladding materials.

Firstly, in specific areas in the material, scarcity or absence of fibre bundles was observed; cracks travelled across >70% of the sample's total thickness at these areas once formed at both temperatures, and propagated across more than 90% of the sample's total thickness after reaching peak load. The presence of such area is evidently detrimental to the structural integrity of the material. Therefore, for further optimizing the design of cladding material, an appropriate braiding angle of fibre bundles should be taken into consideration to avoid the presence of such area.

Moreover, macropores existed at the inner surface of the material, which significantly reduced the material's thickness at such area (~50% to 70% of the average thickness of the material). Under loading at both temperatures, through-thickness cracks were only observed at such areas, which is harmful to the structural integrity and hermeticity of the material, as well as increasing the risk of gas leakage. These observations indicate the importance of the application of protective inner coating layer, which could compensate for the lower materials' thickness at the areas with macropores at the inner surface. Once cracks connected with these macropores,

the inner coating can effectively impede their propagation through the entire thickness of the cladding materials in these areas.

Lastly, the presence of cracks in the fibre bundles at the inner surface were observed in the materials tested at both temperatures after reaching peak load. And these cracks were not cause by the propagation of fatal crack (as they did not have obvious connection with the fatal crack). This could be caused by the compressive stress at sample's inner surface under C-ring compression loading. These observations were unexpected and were not found in similar materials with an protective inner SiC coating under C-ring compression loading at both temperatures in Chapter 4. Therefore, this again indicates the importance of the application of inner SiC coating, which not only serves as gas barrier, but also protect the fibre bundles and matrix near inner surface, and enhancing the overall integrity of the materials.

5.6. Conclusion

Pores are commonly observed at the interfaces of adjacent sub-layers in the outer coating, which could potentially diminish the hermicity of material. The weak interfaces could potentially facilitate crack deflection in the outer coating, which was observed at both temperatures. Variation of residual stress was measured across the coating's thickness. These observations are different from that of similar SiC_f-SiC_m material with monolithic outer coating in Chapter 4.

The CVI process of the SiC matrix successfully yielded a relatively low porosity of the SiC_f-SiC_m cladding material. However, the resulting matrix exhibited lower crystallinity, which has the potential to diminish the irradiation-resistance of the cladding material. Additionally, variation of CVI parameters could affect the residual stress distribution in the SiC fibres.

Similar mechanical behaviour was observed at RT and 1200°C for the samples with initial damage (caused by sample preparation process) under loading, indicates the materials showed good damage tolerance under current level of initial damage. Further experiments will be conducted on the materials without such initial damage, as the application of multi-layers outer SiC coating could potentially affect the mechanical performances of the entire SiC_f-SiC_m cladding material when compared with that with monolithic outer coating.

Two specifical un-excepted areas in the SiC_f-SiC_m cladding materials demonstrated detrimental impacts on the structural integrity and hermeticity of the materials at both temperatures, including the area with scarcity or absence of fibre bundles and the area where macropores

existed at the inner surface. Solutions may involve the enhancements to the braiding patterns of fibre bundles, as well as the application of a protective inner SiC coating.

6. Mechanical behaviour of CS and PVD Cr-coated zircaloy-4 claddings

In the current Chapter, the mechanical behaviour and failure processes of two types of Cr-coated (with the coating manufactured by CS and PVD, respectively) zircaloy-4 cladding material were investigated, with more comprehensive introductions of these two types of materials presented in Section 3.2.2. The experimental procedures of C-ring compression tests with *in-situ* μXCT conducted at both RT and 345°C are introduced in Section 3.3.1.2. The processing procedures of μXCT data analysis are presented in Section 3.3.1.3. The experimental procedures for local property measurements by nanoindentation method are included in Section 3.3.3. The procedure for analysis grain distributions in the Cr coatings by EBSD mapping is presented in Section 3.3.2.2. The procedures for analysis failure pattens of post-tested materials by SEM imaging are presented in Section 3.3.2.1. The results are presented in the order of (i) the microstructures and local properties of the as-received materials, (ii) load-displacement curves, hoop strength and progressive failure processes of these two types of materials tested at both RT and 345°C.

The results from current Chapter have been published in the literature during the PhD project. The current Chapter is based on the published article by Yuan *et al.* [1]. Guanjie Yuan: Investigation, Formal analysis, Data curation, Writing – original draft, Writing – review & editing; J. Paul Forna-Kreutzer: Experiments; Jon Ell: Experiments; Harold Barnard: Resources, Review & editing; Benjamin R. Maier: Resources, Review & editing; Edward Lahoda: Resources, Review & editing; Jorie Walters: Resources, Review & editing; Robert O. Ritchie: Resources, Funding acquisition, Supervision, Writing – review & editing; Dong Liu: Conceptualization, Resources, Methodology, Funding acquisition, Supervision, Writing – review & editing.

6.1. Microstructures of as-received materials

The optical images of the polished cross-sections of the as-received CS and PVD Cr-coated materials are respectively present in Figs. 6.1a and 6.1b, showing their typical microstructures. It can be found that, for the CS material, the Cr coating/substrate interface is tortuous, with some small pores scattered in the coating, as marked by the black arrows in Fig. 6.1a. As for the PVD material, the coating/substrate interface is relatively flat, with no obvious defects in the form of cracks or porosity found in the coating, at the resolution shown in Fig. 6.1b. The thickness of the CS and PVD Cr coatings were measured to be 20.03 ± 3.93 μm and 14.36 ± 0.16 μm, respectively.

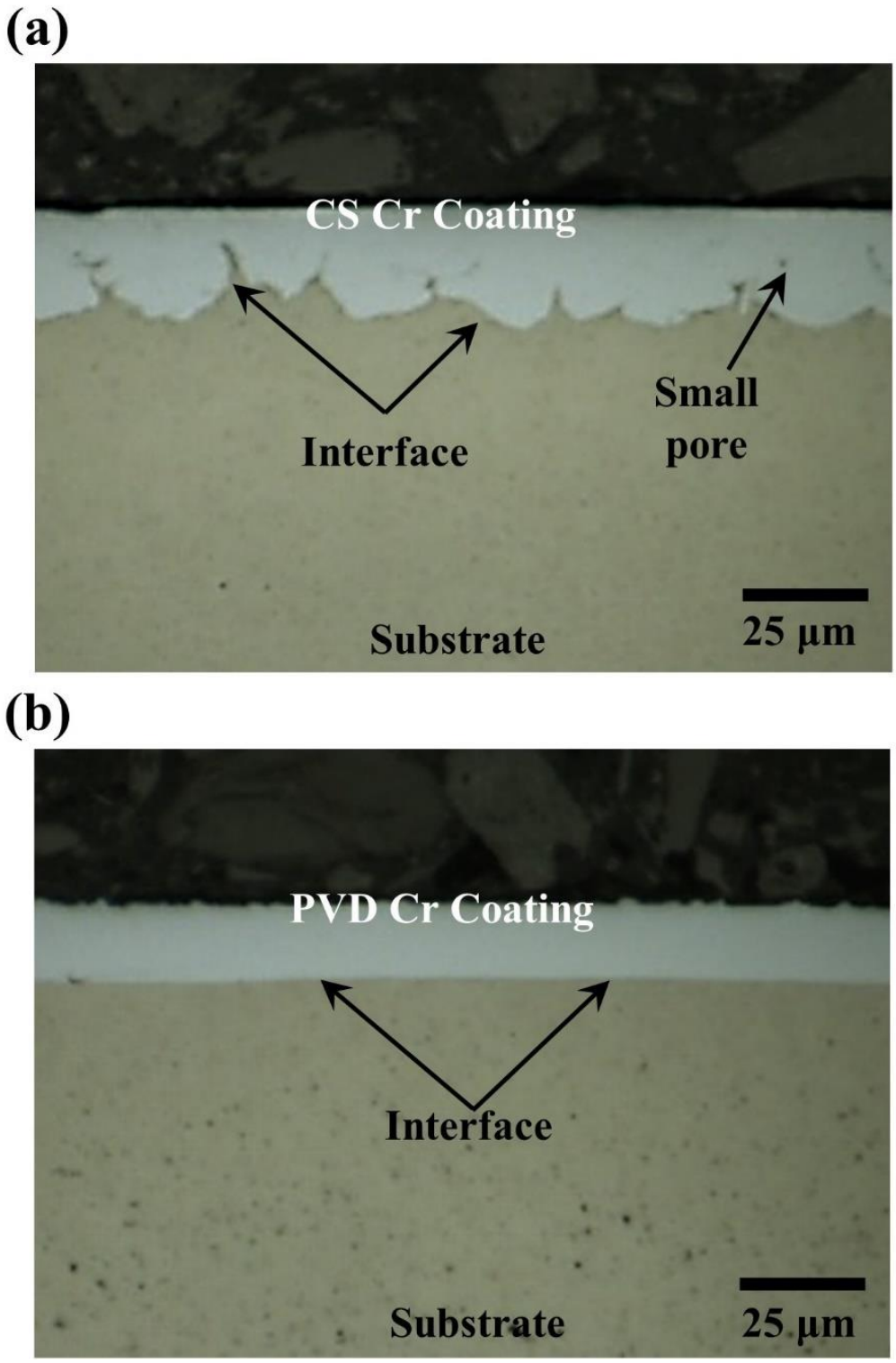

Figure 6-1. Optical images of the polished cross-sections of the as-received Cr-coated zircaloy-4 cladding materials: (a) CS Cr-coated materials and (b) PVD Cr-coated materials.

The EBSD band contrast graphs and corresponding orientation image microscopy maps of the CS and PVD coatings are presented in Fig. 6.2a and Fig. 6.2b, respectively. It can be found that, the CS Cr coating has the typical splat structure with small, closed gaps or pores in between (Fig. 6.2a). The orientation image microscopy map shows that the CS Cr grains have a random orientation in each splat (Fig. 6.2a) in the coating; and there is no obvious preferred Cr grain orientation in the CS coating as evident in the IPF map (Fig. 6.2c).

For the PVD Cr coating, the Cr grains are primarily columnar in shape, with smaller grains can be found clustered near the coating/substrate interface (Fig. 6.2b). Compared with the CS coating, no obvious porosity/gaps between grains are found (Fig. 6.2b), which is consistent with the observations from Fig. 6.1b. The PVD Cr grains show strong texture, in the X and Y directions; most of them are along [1 1 1] direction (Fig. 6.2d).

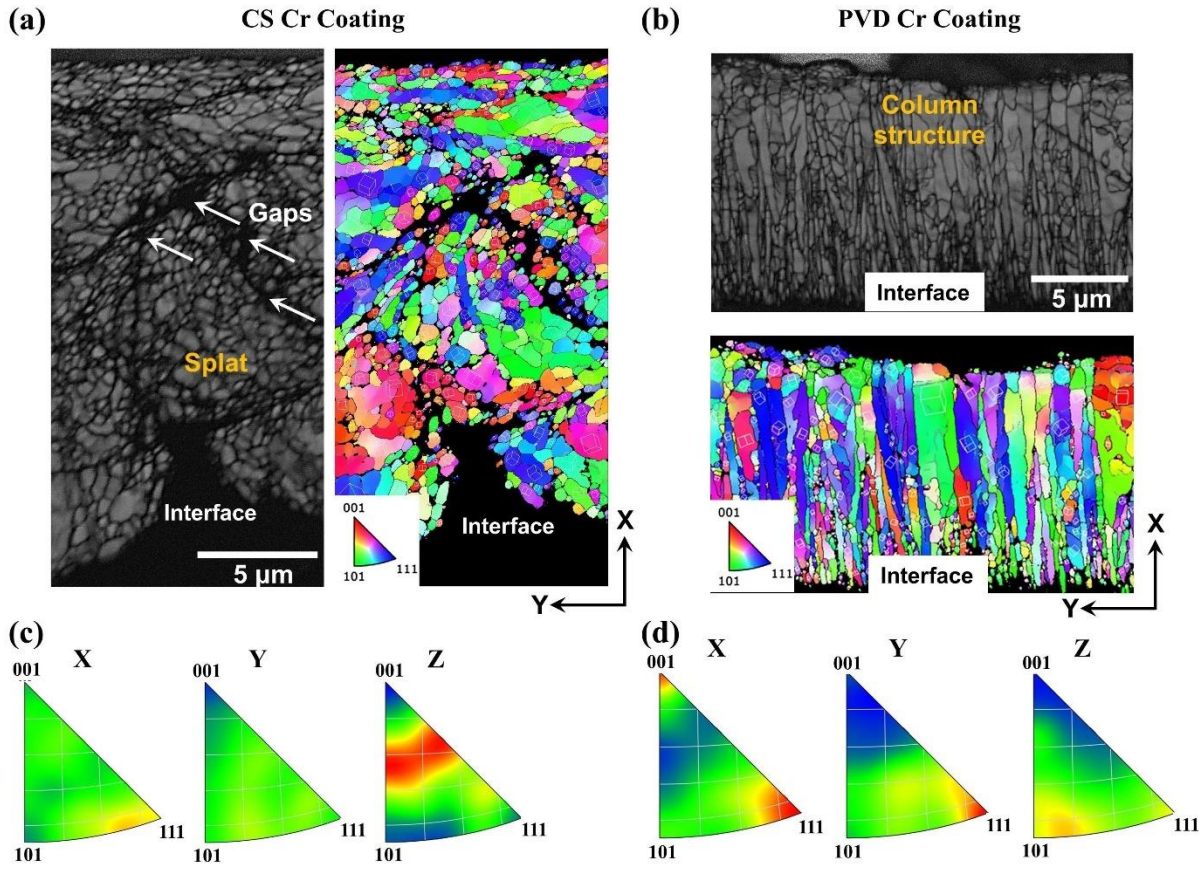

Figure 6-2. (a) and (b) are EBSD maps of the Cr coatings showing band contrast graphs; the colour orientation imaging microscopy maps show the Cr grains of X-Y plane. (a) the CS Cr coating shows splat structures and small gaps/pores (marked by white arrows) between splats; (b) the PVD Cr coating shows columnar structured Cr grains with no obvious porosity; (c) and (d) are inverse pole figures (IPFs) show textures of the Cr grains in the coatings, respectively.

Measurements of the areas of the Cr grains in the CS and PVD coatings are conducted automatically by EBSD mapping. And it can be found that the Cr grains in the CS coating are in the range of 0.01 to 7.25 μm^2, whereas the grains in the PVD coating are in the range of 0.01

to 16.35 μm^2. The area distribution of the Cr grains (selected range of 0 to 1 μm^2 where most grains are distributed) in the CS and PVD Cr coatings are presented in Fig. 6.3a and Fig. 6.3b, respectively. For both types of Cr coatings, more than 50% of the Cr grains are in the range of 0 to 0.1 μm^2. The average area of the Cr grains in the CS coating is 0.16 ± 0.42 μm^2, while the PVD Cr grains have a higher (~140%) average area of 0.39 ± 1.22 μm^2.

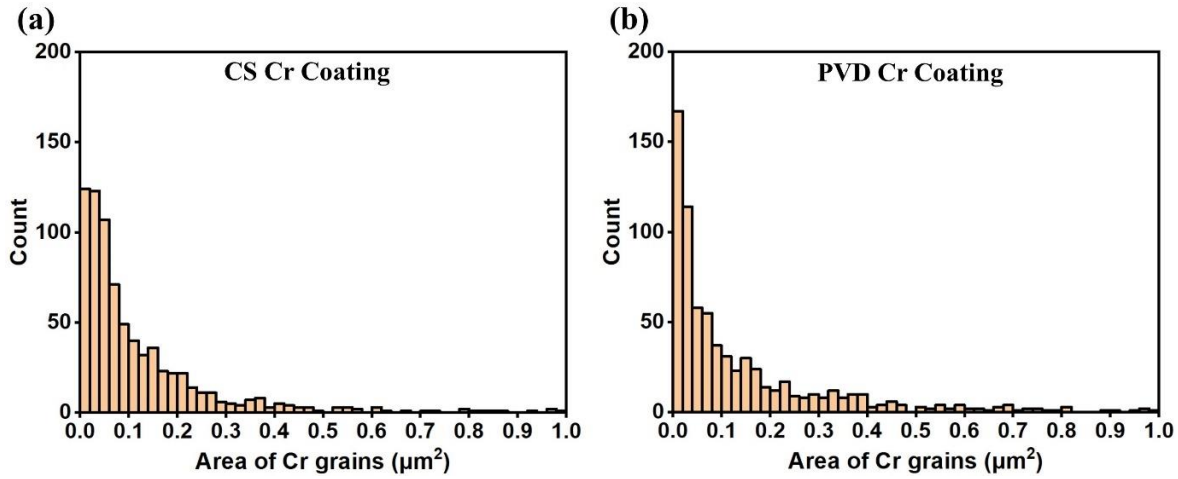

Figure 6-3. (a) and (b) are measured area distribution graphs of Cr grains in the two types of coatings (in the range of 0 to 1 μm^2) for the (a) CS Cr coating, and (b) PVD Cr coating.

6.2. Local properties of as-received materials

Nanoindentation tests were conducted on the polished cross-sections of both the CS and PVD Cr-coated materials in four areas: (i) in the middle of the Cr coating (termed as ‘Area #1′), (ii) in the Cr coating but located 3 μm or less to the coating/substrate interface (‘Area #2′), (iii) in the substrate but located within 5 μm of the interface (‘Area #3′), and (iv) in an area in the substrate away from the interface, *i.e.*, an area where properties are potentially not impacted by the coating process (‘Area #4′). Examples of the four indent areas are shown in Fig. 6.4. The data points are tabulated in Table 6.1, as well as plotted in Fig. 6.5.

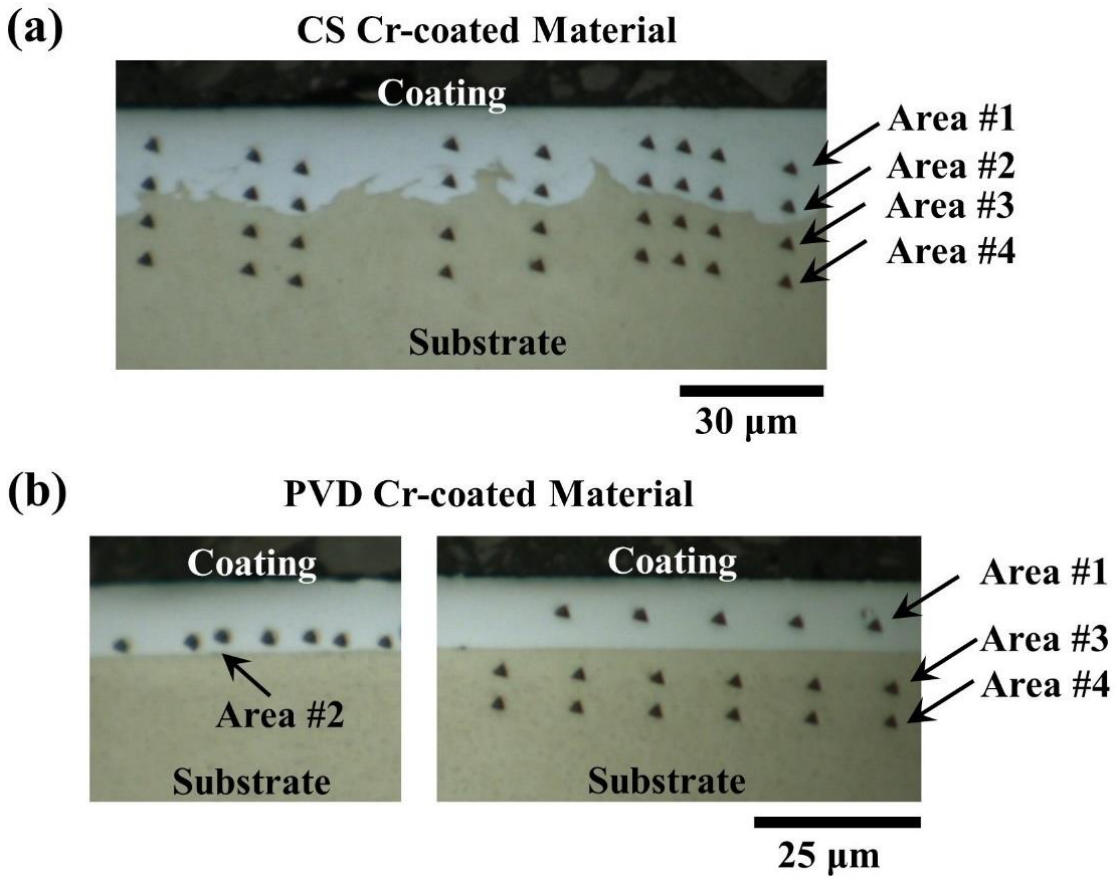

Figure 6-4. Optical images of the polished cross-sections of the as-received Cr-coated materials showing the four areas of the indents: (a) CS Cr-coated materials and (b) PVD Cr-coated materials.

Table 6-1. Measured values of the hardness H and elastic modulus E in different areas of the polished cross-sections of the CS and PVD Cr-coated materials.

Areas	CS material		PVD material	
	H (GPa)	E (GPa)	H (GPa)	E (GPa)
Coating Area #1	4.49 ± 0.65	266.06 ± 7.96	4.47 ± 0.35	268.31 ± 6.92
Coating Area #2	3.79 ± 0.34	249.47 ± 8.85	5.20 ± 0.45	260.03 ± 4.88
Substrate Area #3	3.02 ± 0.18	109.53 ± 5.25	2.72 ± 0.25	113.41 ± 5.26
Substrate Area #4	2.62 ± 0.13	105.61 ± 4.99	2.64 ± 0.23	109.52 ± 3.97

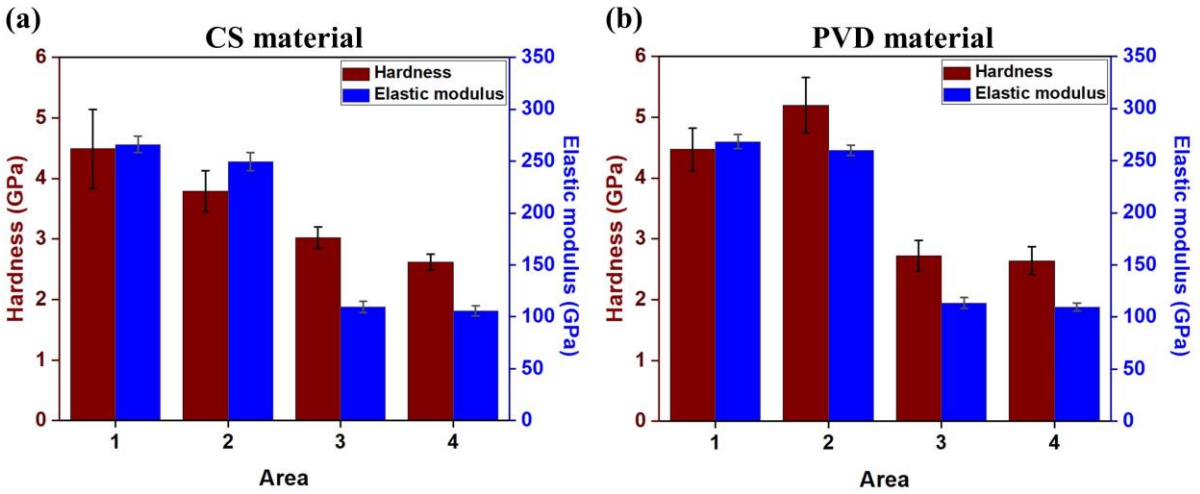

Figure 6-5. Hardness and elastic modulus of the different values in the polished cross-sections of (a) CS material and (b) PVD material.

For the CS Cr-coated material, compared to Area #1, Area #2 displays 15.6% lower hardness. And Area #3 has a higher hardness (~15.3%) compared to that in Area #4. These imply that the cold spraying process has hardened the surface layer of the substrate.

For the PVD Cr-coated material, compared to Area #1, Area #2 displays 16.3% higher hardness. For the substrate, no significant differences in either value were found for Area #3 and Area #4. This demonstrates that the PVD coating process did not cause obvious changes in the substrate close to the coating interface.

6.3. Hoop strength at RT and 345°C

As little change was found in the mechanical behaviour of two (repeat) samples of either the CS or PVD materials tested at each temperature, one representative load–displacement curve for each type of material at each condition (RT and 345°C) are plotted in Fig. 6.6. And the detailed testing sequences are listed in Table A.6 in the Appendices.

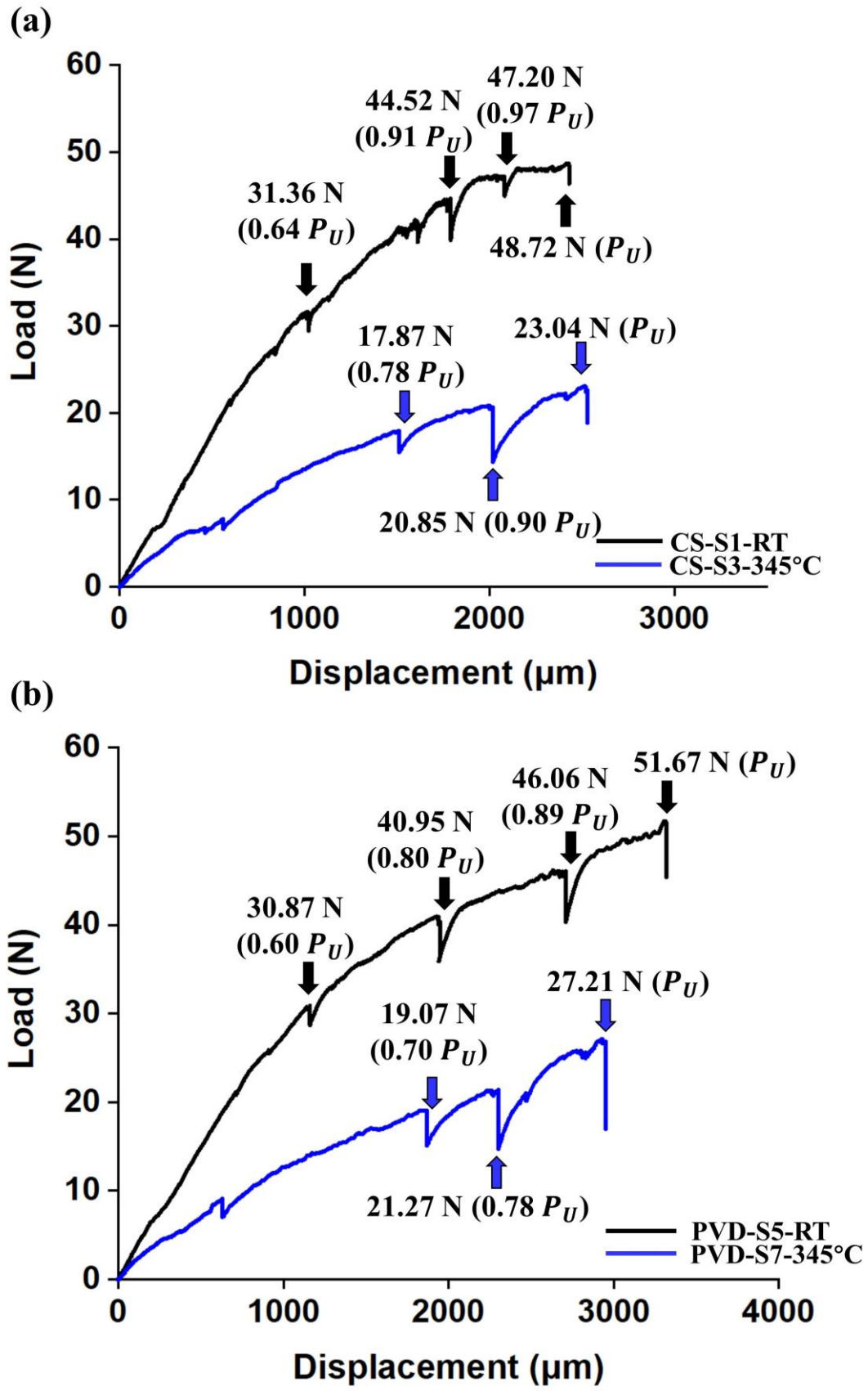

Figure 6-6. Representative load–displacement curves for the C-ring compression tests of two types of Cr-coated materials at both room temperature and 345°C: (a) CS Cr-coated materials including sample S1 tested at RT and sample S3 tested at 345°C; (b) PVD Cr-coated materials including sample S5 tested at RT and sample S7 tested at 345°C. The coloured arrows indicate locations of the μXCT scans.

The maximum hoop strength derived from Eq. 3.1 are listed in Table 6.2. Note that as the sample deformation in the current test was larger than the validity criteria cited in ASTM Standard C1323-16 [246], the calculated values may be taken as overestimates. The maximum hoop strength of CS materials at RT is ~77 % higher than that at 345°C. The same trend is found for PVD materials where the maximum hoop strengths at RT is ~88% higher than that at 345°C. Additionally, as described in Section 3.3, real-time radiography projections were used to monitor coating cracks during loading; the loads and corresponding hoop stresses (derived from Eq. 3.1) when these cracks were first observed by radiography projection (also confirmed with µXCT images) are listed in Table 6.2. For CS Cr-coated materials tested at both RT and 345°C, coating cracks were first seen at ~90% P_U. As for PVD Cr-coated materials tested at both RT and 345°C, coating cracks were detected at ~80% P_U. Moreover, the hoop strain when coating cracks firstly being observed and at peak load were calculated by the corresponding hoop stress and measured elastic modulus (by nanoindentation method), as summarized in Table 6.2. Note that, the elastic modulus of Cr coating could decrease at elevated temperatures, so the calculated strain at 345°C could lower than the actual value. Moreover, after crack initiated, samples are under large deformation than the validity criteria cited in ASTM Standard C1323-16 [246], so the calculated strain at peak load could be different with the actual values.

Table 6-2. The width of specimens, loads and corresponding hoop stresses and strains where coating cracks were first observed, peak loads and calculated maximum hoop stresses for CS Cr-coated and PVD Cr-coated materials tested at both RT and 345°C.

Specimen	Sample width (mm)	Load, corresponding hoop stress[a] (MPa) and strain where coating cracks were first observed	Peak load (N)	Maximum hoop stress[a] (MPa) and strain
CS-S1-RT	2.36	44.52 N/1091.17 MPa/0.41%	48.72	1194.11/ 0.45%
CS-S2-RT	2.15	35.27 N/948.90 MPa/0.36%	42.42	1141.26/0.43%
CS-S3-345°C	2.21	20.85 N/542.73 MPa/0.20%	23.04	603.03/0.22%
CS-S4-345°C	2.40	25.95 N/625.57 MPa/0.24%	28.84	695.08/0.27%
PVD-S5-RT	2.51	40.95 N/921.33 MPa/0.34%	51.67	1151.66/0.43%
PVD-S6-RT	2.47	38.66 N/873.26 MPa/0.33%	50.73	1149.02/0.43%
PVD-S7-345°C	2.41	21.27 N/492.68 MPa/0.18%	27.21	631.64/0.23%
PVD-S8-345°C	2.18	18.66 N/527.94 MPa/0.20%	23.04	591.27/0.25%

[a] calculated using Eq. 3.1, ASTM C1323-16 [246].

In addition to load drops (sudden decreasing of load at a fixed displacement), load relaxations (progressive decreasing of load at a fixed displacement, marked by coloured arrows in Fig. 6.6) were observed for both types of cladding materials tested at both temperatures during the µXCT scanning periods (~6 mins) when samples were held at constant displacement. Such load relaxations were also reported by Nguyen *et al.* [112] on room temperature tensile tests on PVD Cr-coated (coating thickness: ~15 µm) sheet zircaloy-4 samples (example presented in Fig. A.1 in the Appendices). The load relaxation values in current work may have some relationship with the mechanical properties of underlying substrate. While the in-depth analysis of these load relaxations was beyond the scope of current work, and detailed data of load relaxation values as a function of applied load are summarized in Table A.6 in the Appendices.

6.4. Failure processes and crack toughening mechanisms at RT and 345°C

The failure processes of both types of Cr-coated materials were investigated by analysing the real-time µXCT scans collected at different loading steps. One representative sample from each coating type at each temperature was presented to provide a description of the failure process. Moreover, the ductility and crack resistance of Cr coatings can be effectively assessed through the observation of surface crack evolution, specifically the number of coating cracks [53]. In a system characterized by a brittle coating on a ductile substrate, the development of coating cracks typically progresses through three distinct stages: i) nucleation stage: channel cracks initiate under a relatively low tensile strain; ii) propagation stage: the number of cracks increases, albeit at a decelerating rate; iii) saturation stage: the number of cracks reaches a plateau, where the initiation of new channel cracks becomes markedly difficult. Therefore, in current project, the number of coating cracks at increasing loading stages are measured to investigate the crack resistance of Cr coatings.

6.4.1. CS Cr-coated materials

For the CS sample S1 (tested at RT), the first µXCT scan was collected at 0.64 P_U (estimated hoop stress 723.23 MPa). However, no obvious cracks in the coating were visible in the real-time radiography projection, as well as in the µXCT scan (Fig. 6.7a). With continued loading, no cracks were seen in the radiography projection until 0.91 P_U (1091.17 MPa of stress; 0.41% of strain) where a µXCT scan was collected. Multiple coating cracks were found to have formed simultaneously, Fig. 6.7b. These cracks had similar behaviours; therefore, three of them (Crack#1 to #3, see magnified image in Fig. 6.7e) were selected as representative examples, and 3D visualization of part of them (selected range in a length of ~ 360 µm, which is ~15% of the sample's total width: ~2.4 mm) were presented in Fig. 6.7e.

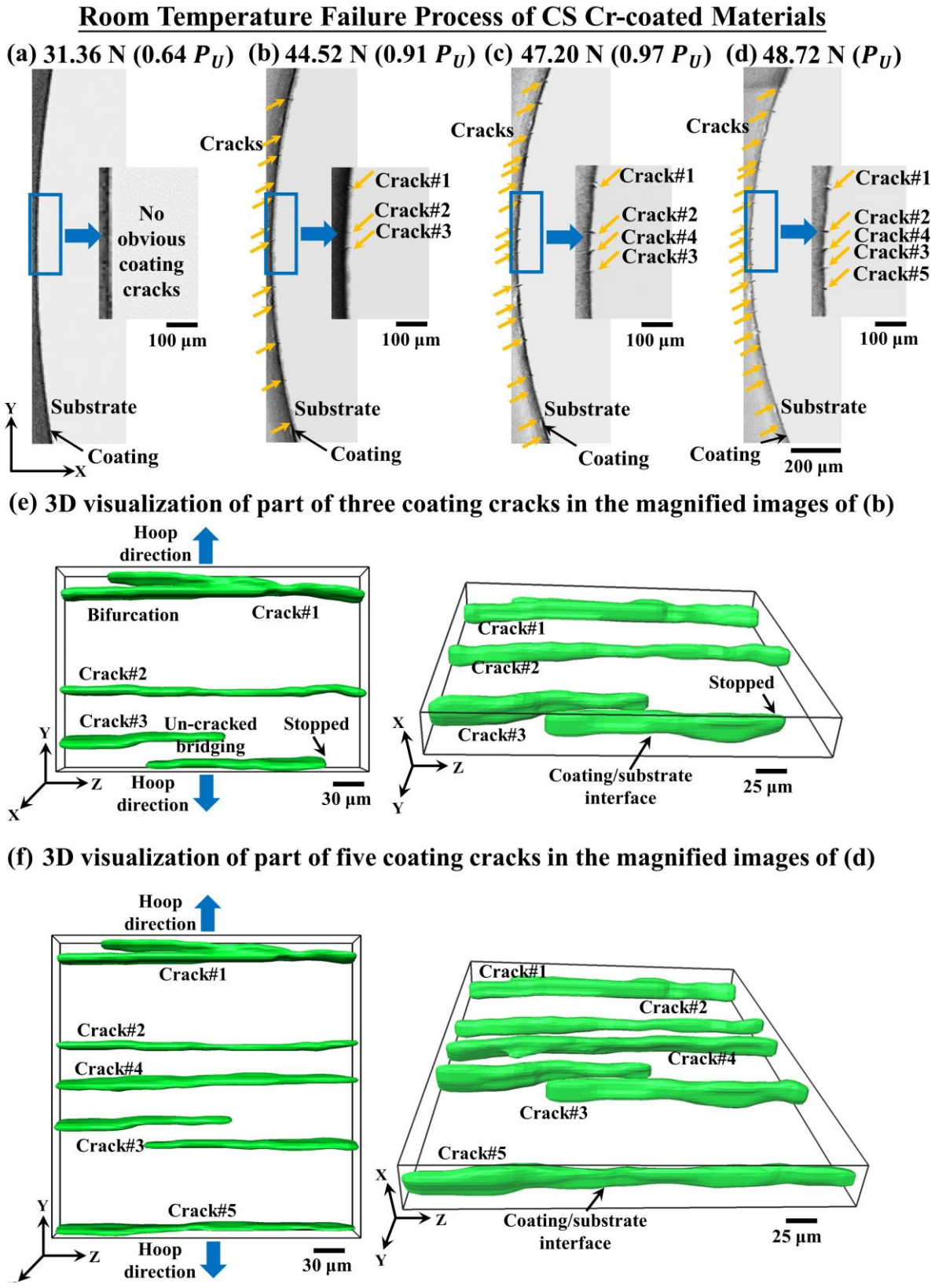

Figure 6-7. (a) to (d) are *in-situ* μXCT slices of the X-Y plane (including magnified images extracted from the same location in the sample at increasing loading steps) illustrated from CS sample S1: (a) scan at 31.36 N (0.64 P_U) before peak load, (b) scan at 44.52 N (0.91 P_U) before peak load, (c) scan at 47.20 N (0.97 P_U) before peak load, and (d) μXCT scan at peak load 48.72 N (P_U). (e) and (f) are 3D visualization of part of the representative coating cracks in the magnified images of (b) and (d) respectively.

Once formed, all the coating cracks arrested at the coating/substrate interface, Fig. 6.7e. The majority of coating cracks travelled across the sample's total width (~2.4 mm) once formed, but some cracks were found stopped in the coating, see Crack#3 in Fig. 6.7e. All the coating cracks formed nearly perpendicular to the tensile hoop direction (Y direction). The average distance between the coating cracks at this loading step was measured to be 98.89 ± 34.71 μm. With increasing load to 0.97 P_U (1158.29 MPa; 0.44%), the number of cracks increased, and a new crack (Crack#4) was observed in the selected range, Fig. 6.7c. Accordingly, the average distance between coating cracks reduced to 77.60 ± 25.41 μm.

At P_U (1194.11 MPa; 0.45%), the number of coating cracks further increased with a new crack (Crack#5) showed up in the selected range in Fig. 6.7d. The coating cracks were found still arrested at the coating/substrate interface (Fig. 6.7f). The newly formed cracks also travelled across the sample's total width (Crack#4 and Crack#5 in Fig. 6.7f), with the further extended in length of the cracks formed in previous loading stages being observed (Crack#3 in Fig. 6.7f). The distance between the coating cracks was measured to reduce further to 58.38 ± 17.21 μm (Fig. 6.7f).

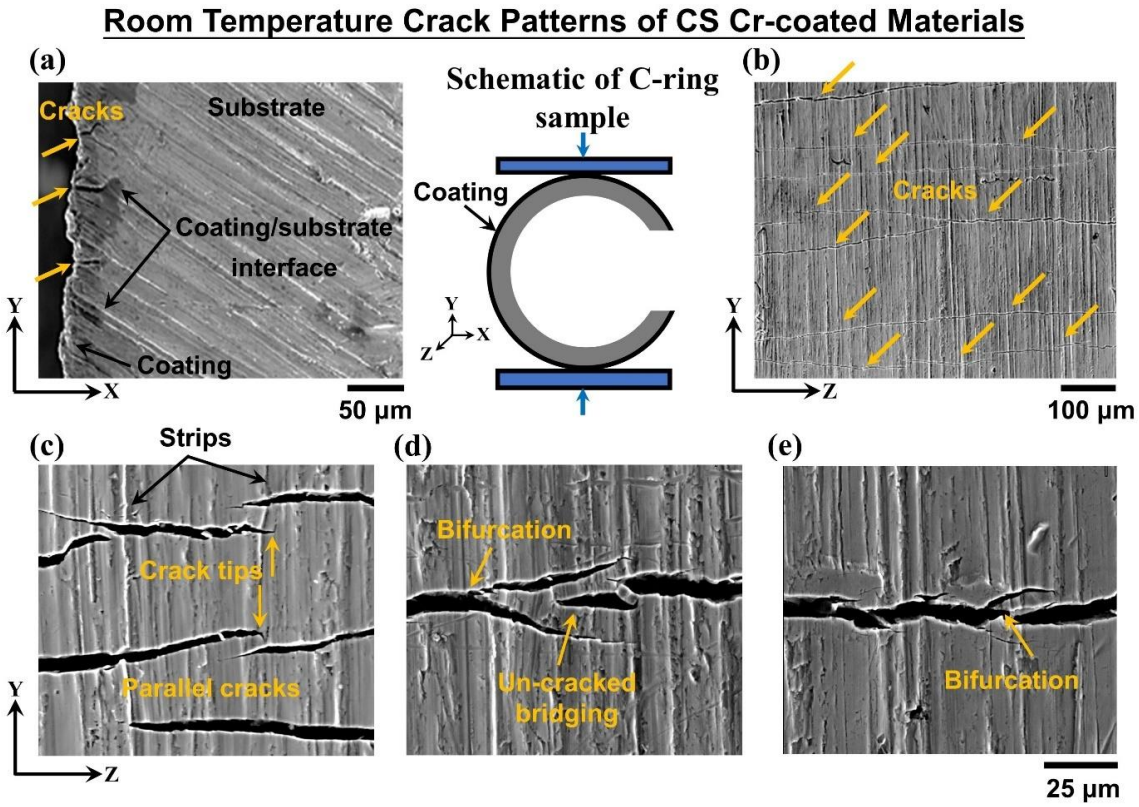

Figure 6-8. SEM images showing crack patterns of post-failure CS Cr-coated materials tested at RT, illustrated using sample S1: (a) image collected from the side surface of the sample (X-Y plane); (b) low magnification view of the outer surface of the sample (Y-Z plane); (c) to (e) are high magnification views of the outer surface of the sample (of the Y-Z plane). One schematic of C-ring sample with loading is included.

Crack patterns of the CS sample S1 tested at RT are shown in Fig. 6.8. Cracks were found not penetrate through to the substrate (Fig. 6.8a), which is consistent with the observations from µXCT imaging (Fig. 6.7). These cracks formed nearly perpendicular to the tensile hoop direction in the coating surface, at an angle of 80° to 95°, Fig. 6.8b. High magnification SEM images revealed various crack toughening mechanisms, including the creation of parallel cracks (Fig. 6.8c), uncracked ligament bridging (Fig. 6.8d) and cracks bifurcation (Figs. 6.8d and 6.8e). Crack deflection at the crack tips was also found, which can be as much as ~90° from the crack growth direction, typically along the strips on the coating formed during the CS manufacturing process (Fig. 6.8c). The width of these coating cracks was in the range of 1-5 µm.

For the CS Cr-coated sample S3 tested at 345°C, the first µXCT scan collected at 0.78 P_U showed no obvious crack formation (Fig. 6.9a). With continued loading, no cracks were observed in the radiography projection until 0.90 P_U (542.73 MPa; 0.20%), Fig. 6.9b. Distinct from the CS materials tested at RT, only three cracks showed up simultaneously (Fig. 6.9b); these three cracks were found showing similar behaviours, and Crack#1 (magnified image in Fig. 6.9b) was selected as representative examples. 3D visualization of Crack#1 showed it confined within the coating without penetrating the underlying substrate (Fig. 6.9d), and travelled across the sample's total width: ~2.2 mm (21% of the total crack length was presented in Fig. 6.9d). Additionally, in some parts of Crack#1, crack deflection and bifurcation at the coating/substrate interface area was observed, Figs. 6.9b and 6.9d. The average distance between the coating cracks was measured to be 334.67 ± 154.31 µm.

With further loading to P_U (695.08 MPa; 0.22%), no markable change was found for the average distance between the coating cracks of 314.89 ± 141.77 µm (Fig. 6.9c). Coating cracks still arrested at the coating/substrate interface (Fig. 6.9e); with crack merging being observed (Fig. 6.9e) at the bifurcation and deflection area (same area in Fig. 6.9d) at the coating/substrate interface.

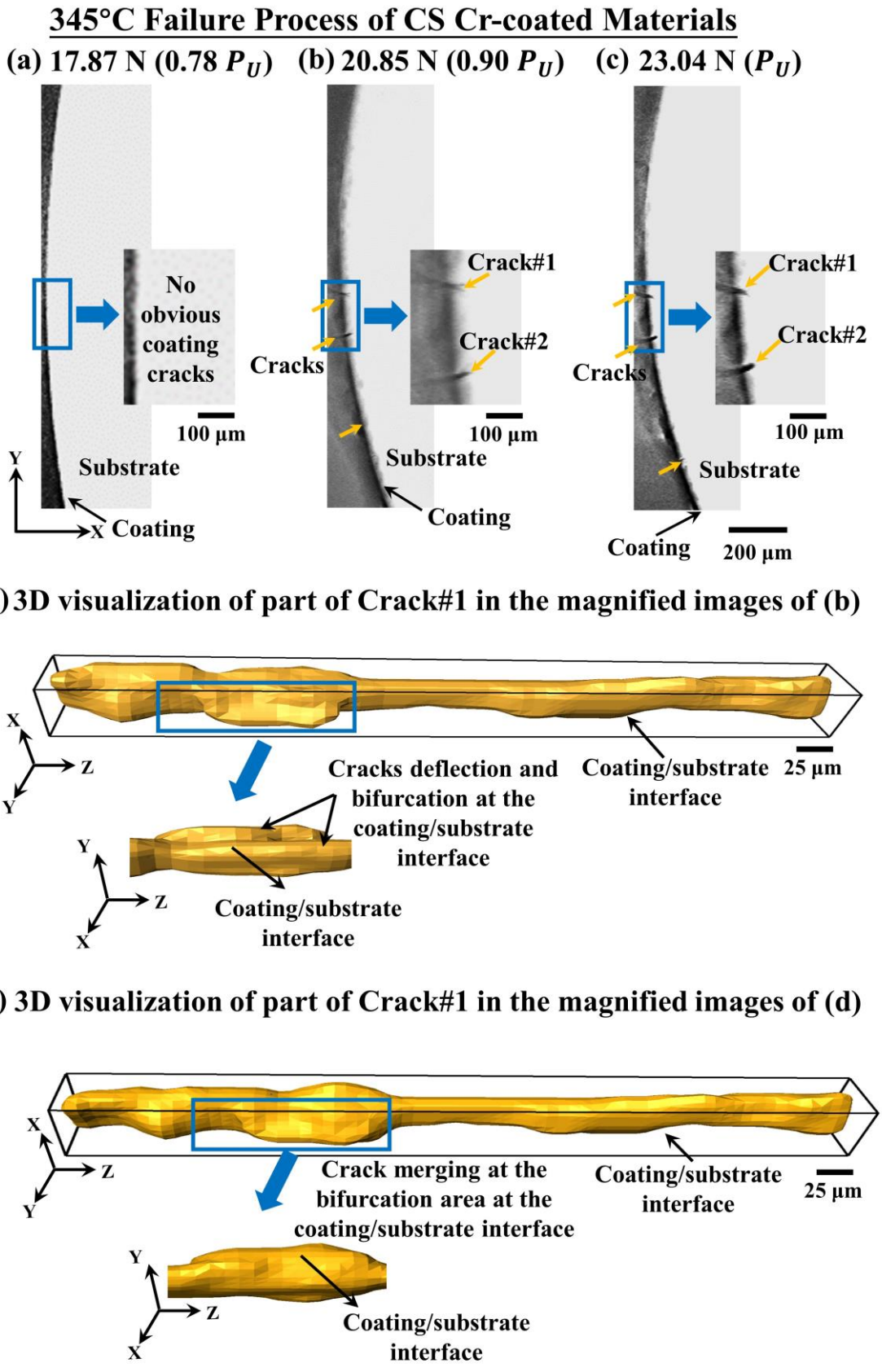

Figure 6-9. (a) to (c) are *in-situ* µXCT slices of the X-Y plane (including magnified images extracted from the same location in the sample at increasing loading steps) showing crack formation and propagation processes of the CS Cr-coated materials tested at 345°C, from sample S3: (a) scan at 17.87

N (0.78 P_U), (b) scan at 20.85 N (0.90 P_U), (c) scan at peak load 23.04 N (P_U). (d) and (e) are 3D visualization of part of the representative coating crack (Crack#1).

SEM images of the crack patterns of the CS sample S3 tested at 345°C are shown in Fig. 6.10. Similar to the CS materials tested at RT, the cracks at 345°C arrested within the coating (consistent with µXCT images in Fig. 6.9); crack defection in the coating was also observed (Fig. 6.10a). From the surface of the Cr coating, primary coating cracks (with a width of ~ 6 µm) formed perpendicular to the tensile hoop direction, Fig. 6.10b. However, cracks with a finer width (less than 3 µm, which is below the detection resolution of µXCT and the radiography projection) were also observed as discontinuous and tortuous (Fig. 6.10b). SEM images indicated that deflection (Fig. 6.9d) and bifurcation (Fig. 6.9e) were observed at the tips of finer cracks. Similar observations were also found in CS sample S4 tested at the same temperature.

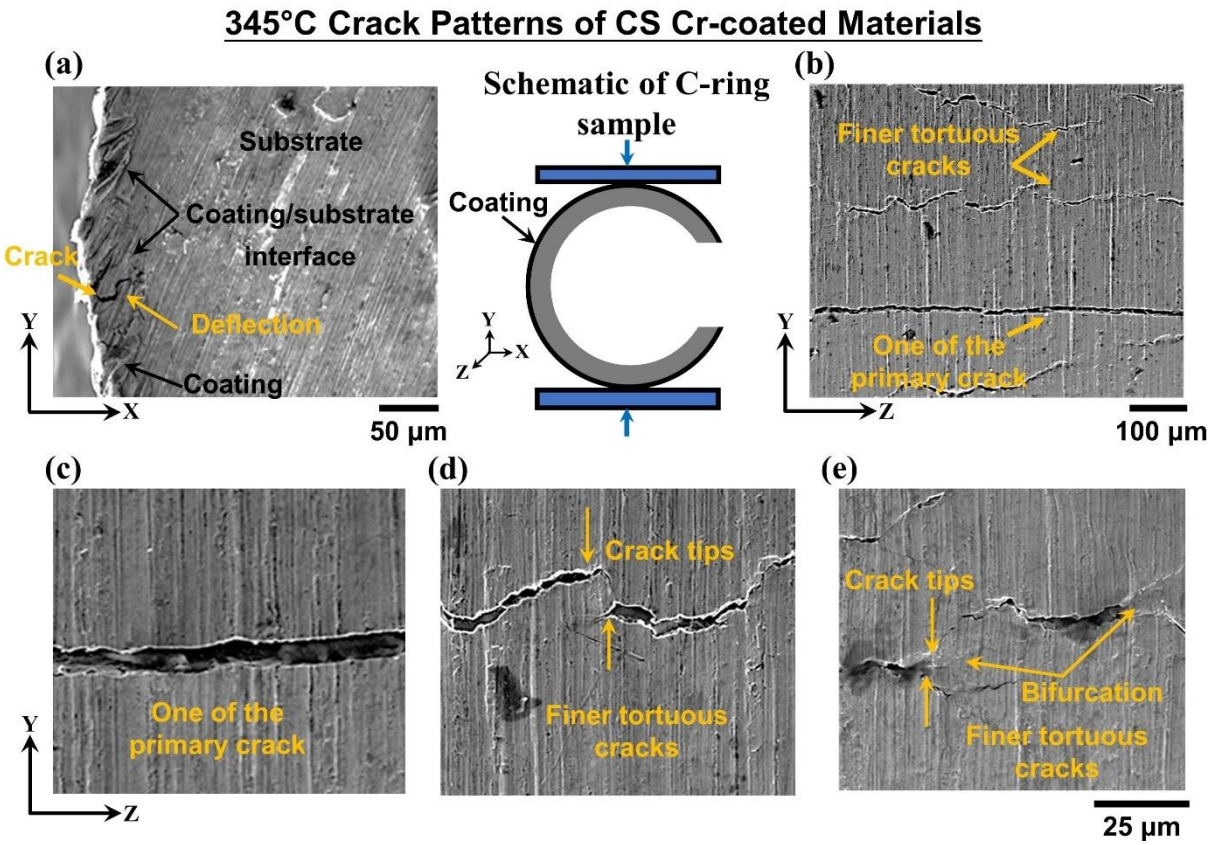

Figure 6-10. SEM images showing crack patterns of the post-failure CS Cr-coated materials tested at 345°C, from sample S3: (a) image collected from the side surface of sample (X-Y plane); (b) low magnification view from the outer surface at the sample's middle plane (Y-Z plane). (c) to (e) are high magnification views of the outer surface of the sample (Y-Z plane). One schematic of C-ring sample with loading is included.

To summarize, for CS materials tested at both RT and 345°C, the first onset of multiple cracks was found at ~90% peak load in the coating, these cracks arrested at the coating/substrate interface. At RT, once formed, the majority of coating cracks tended to travel across the

sample's total width; cracks formed almost perpendicular to the hoop direction. With further loading, number of cracks increased, and semi-across width cracks formed at previous loading stages further grew up in length. However, at 345°C, only three primary cracks formed perpendicular to the hoop direction, accompanied by finer tortuous cracks.

6.4.2. PVD Cr-coated materials

For the PVD Cr-coated sample S5 (tested at RT), the μXCT scan at 0.60 P_U showed no obvious coating cracks observed, Fig. 6.11a. With further loading to 0.80 P_U (954.58 MPa; 0.34%), multiple cracks were first observed to have formed simultaneously. Similar behaviours were observed for these coating cracks, four of them (Crack#1 to Crack#4, as marked in the magnified image in Fig. 6.11b) were selected as representative examples, and part of these four representative cracks (selected length of ~540 μm, which is ~22% of the total sample's width: ~2.5 mm) was visualized in 3D to illustrate the crack behaviours, Fig. 6.11e.

It was found that, all the cracks arrested at the coating/substrate interface once formed, see examples in Fig. 6.11e. The majority of coating cracks travelled across the sample's total width, with some of them arrested in the coating (Crack#1 and Crack#3 in Fig. 6.11e). Note that, no direct correlation between the formation of Crack#3 and the sample boundary was found, which is direct evidence that not all the coating cracks generated from sample's edge. Some toughening mechanisms were also observed, including un-cracked ligament bridging and deflection, see Crack#2 in Fig. 6.11e. The average distance between the coating cracks at this load was measured to be 62.13 ± 14.55 μm.

With further loading to 0.89 P_U (1061.97 MPa; 0.38%), the distance between coating cracks reduced to 50.67 ± 14.92 μm, Fig. 6.11c. At P_U (1193.22 MPa; 0.43%), the number of coating cracks further increased with Crack#5 newly formed, Fig. 6.11d. 3D visualization showed these five representative cracks arrested at the coating/composite interface, Fig. 6.11f; and the increasing of load led to Crack#1 and Crack#3 extended further in length with un-cracked ligament bridging. Additionally, at peak load, a new crack branched out from Crack#4, Fig. 6.11f. The distance between coating cracks further reduced to 29.27 ± 11.84 μm, Fig. 6.11d.

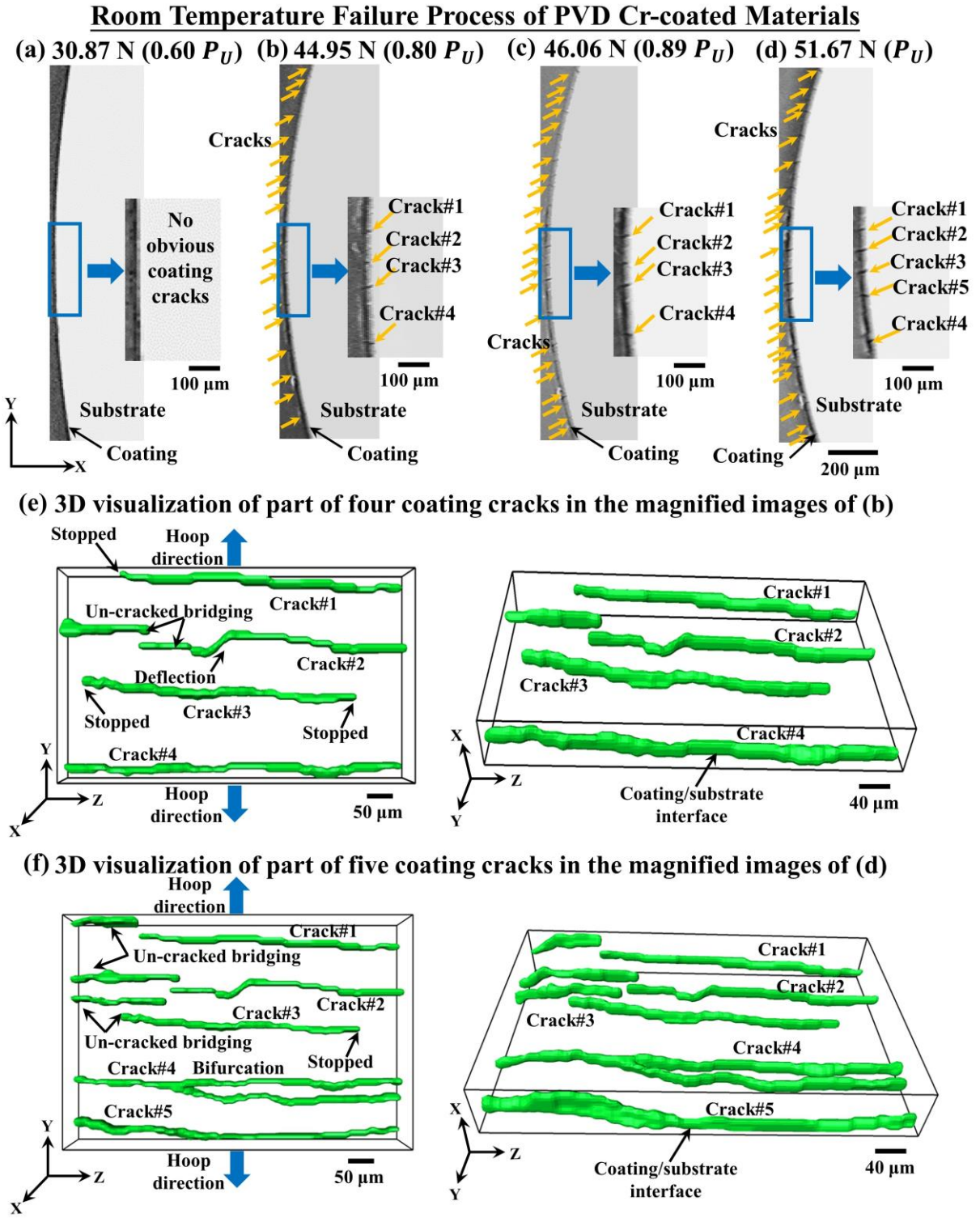

Figure 6-11. (a) to (d) are *in-situ* µXCT slices of the X-Y plane (including magnified images extended from the same location in the sample at increasing loading steps) showing crack formation and propagation processes in the PVD Cr-coated materials tested at RT, from sample S5: (a) scan at 30.87 N (0.60 P_U), (b) scan at 44.95 N (0.80 P_U, (c) scan at 46.06 N (0.89 P_U) and (d) scan at 51.67 N (P_U). (e) and (f) are 3D visualization of part of the representative coating cracks in the magnified images of (b) and (d) respectively.

SEM images conducted on the PVD materials tested at RT are presented in Fig. 6.12. The deflection of coating cracks at the coating/substrate interface was observed, Fig. 6.12a. On the coating surface, these cracks are discontinuous in places and not all strictly perpendicular to the tensile hoop stress direction, specifically at an angle range of 80° to 105° (the maximum angle between coating cracks is ~25°) with the hoop direction, Fig. 6.12b. Magnified SEM images revealed that these cracks were mostly intergranular, Fig. 6.12. Several toughening mechanisms that include parallel cracks (Fig. 6.12c), cracks bifurcation (Fig. 6.12d) and un-cracked ligament bridging (Fig. 6.12e) were observed. The width of coating cracks was in the range of 1–4 μm.

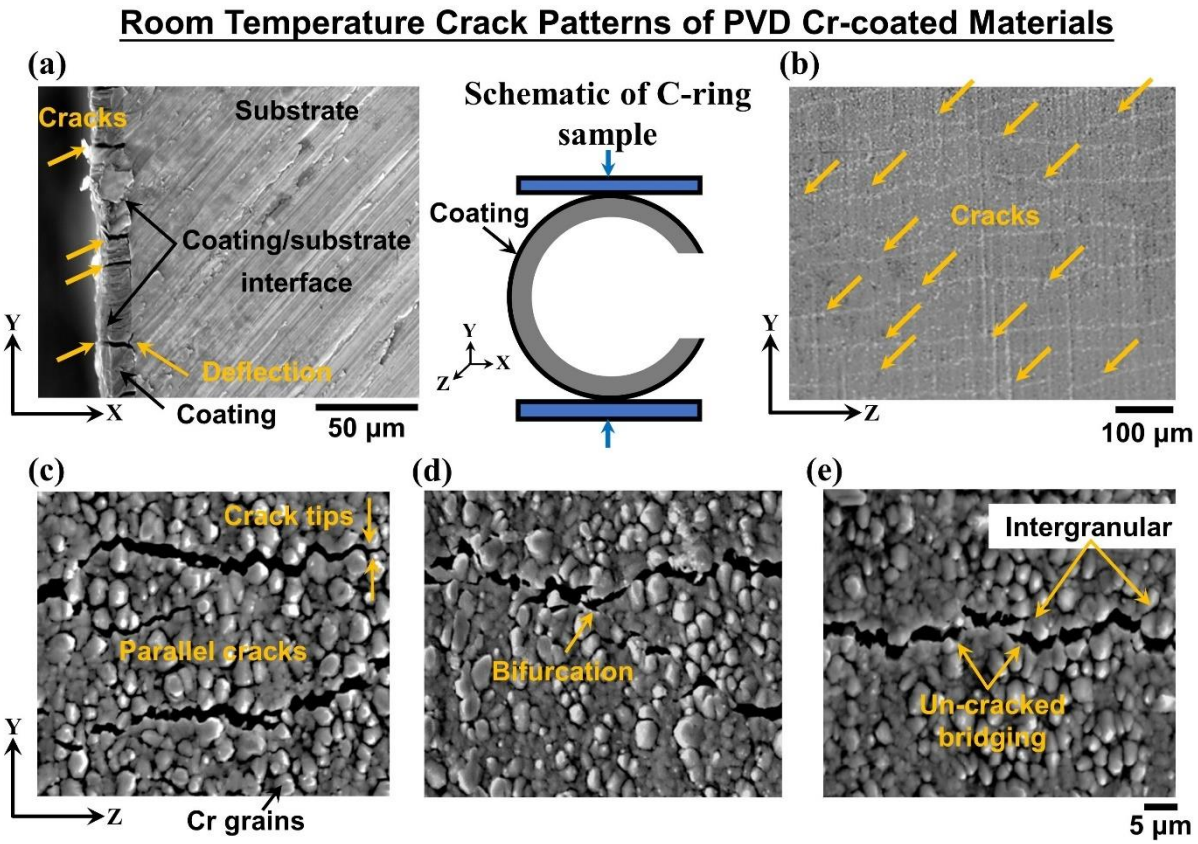

Figure 6-12. SEM images showing crack patterns of the post-failure PVD Cr-coated materials tested at RT, from sample S5: (a) image collected from the side surface of sample (X-Y plane); (b) low magnification view of the outer surface of the sample (Y-Z plane); (c) to (e) are high magnification views of the outer surface of the sample (of the Y-Z plane): (c) shows parallel cracks and cracks deflected along the Cr grain boundaries; (d) shows crack bifurcation and (e) uncracked ligament bridging, with most cracks in an intergranular mode. One schematic of C-ring sample with loading is included.

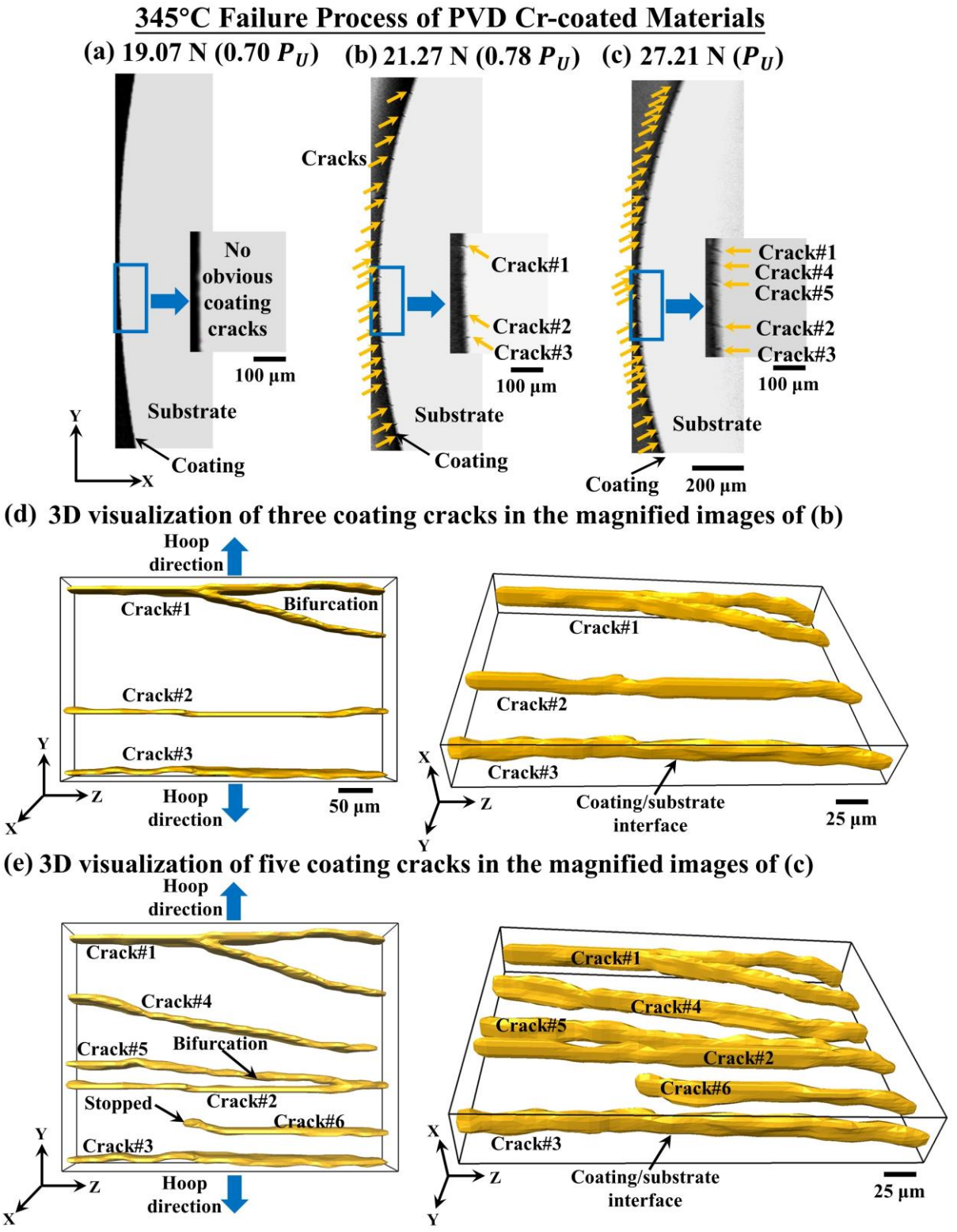

Figure 6-13. (a) to (c) are *in-situ* µXCT slices of the X-Y plane (including magnified images extracted from the same location in the sample at increasing loading steps) showing crack formation and propagation processes in the PVD Cr-coated materials tested at 345°C, from sample S7: (a) scan at 19.07 N (0.70 P_U) (b) scan at 21.27 N (0.78 P_U), (c) scan at peak load 27.21 N (P_U). (d) and (e) are 3D visualization of part of the representative coating cracks in the magnified images of (b) and (c) respectively.

For the PVD Cr-coated sample S7 tested at 345°C, the µXCT scan collected at 0.70 P_U (442.15 MPa) shows no obvious coating cracks, Fig. 6.13a. With further loading to 0.78 P_U (492.68 MPa; 0.18%), the µXCT images collected at this point showed multiple coating cracks forming simultaneously (Fig. 6.13b). All these cracks arrested at the coating/substrate interface; with majority of them travelled across the total width of the C-ring sample (~2.4 mm), representative cracks (Crack#1 to Crack#3) are shown in Fig. 6.13d. The average distance between the coating cracks was measured to be 71.20 ± 21.87 µm.

At P_U (660.72 MPa; 0.23%), the number of coating cracks increased (Fig. 6.13c) with Crack#4 and Crack#5 being observed, Fig. 6.13c; and the 3D visualization of part of Crack#1 to Crack#5 is presented in Fig. 6.13e. Note that, as mark in Fig. 6.13e, the newly formed Crack#6 did not travel across the sample's total width, and was not observed in the selected µXCT slice (X-Y plane) in Fig. 6.13c. At P_U, all the coating cracks were still found arrested at the coating/substrate interface, Fig. 6.13e; and the distance between the coating cracks further reduced to 43.27 ± 11.84 µm.

Crack patterns of the PVD sample S7 tested at 345°C are shown in Fig. 6.14a. A cross-sectional view (Fig. 6.14a) showed that these coating cracks did not penetrate into the substrate. Compared to the coating cracks at RT which formed (of the Y-Z plane) at an angle range of 80° to 105° to the hoop direction, some cracks in the coating surface at 345°C were found to form at a larger angle (75° to 109°) to the hoop direction (the maximum angle between coating cracks is ~34°, Fig. 6.14b). Magnified SEM images revealed these coating cracks mostly propagated intergranularly, with an almost doubled crack width (1–8 µm) compared to that (1–4 µm) at RT (Figs. 6.14c-e). As shown by the SEM images, toughening mechanisms again included parallel cracks (Fig. 6.14c), bifurcation (Fig. 6.14d) and deflection (Fig. 6.14e), with uncracked ligament bridging observed to be either at the bifurcation areas (Fig. 6.14d) or within the cracks (Fig. 6.14e).

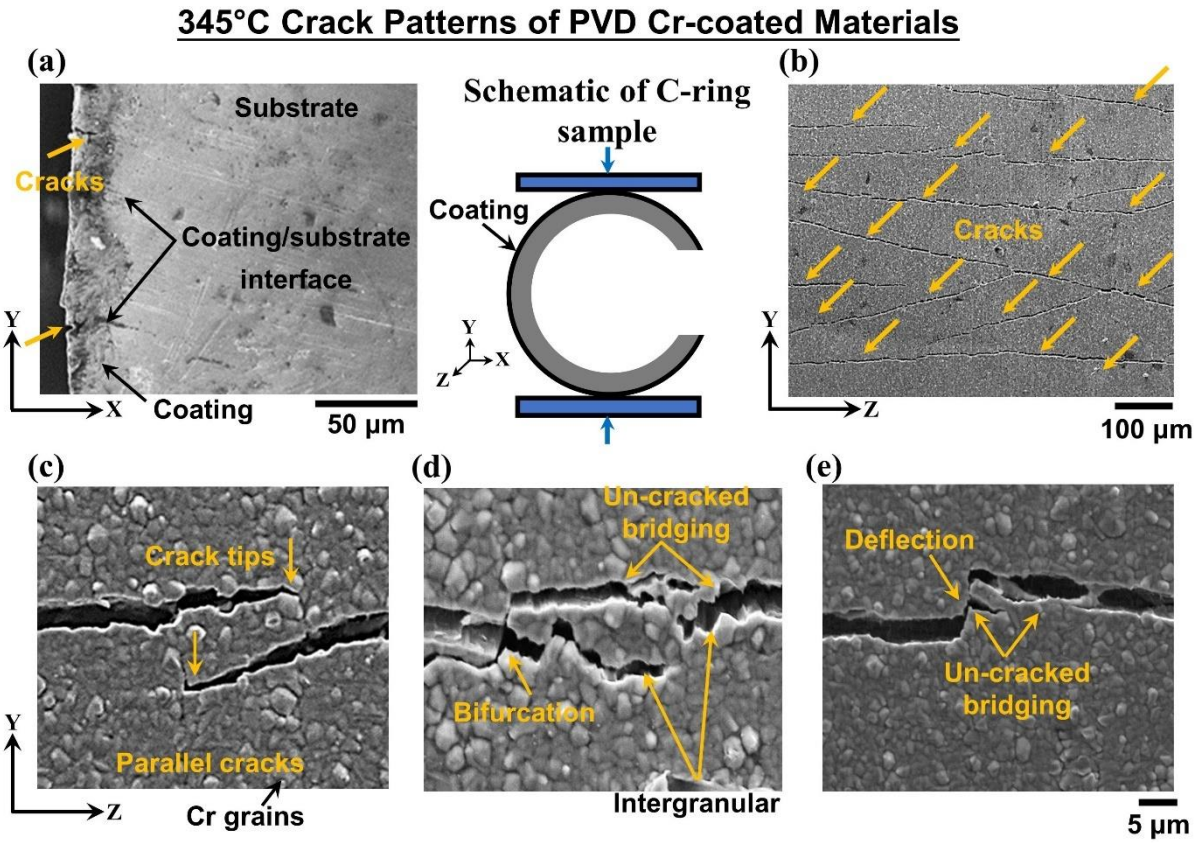

Figure 6-14. SEM images showing crack patterns of the post-failure PVD Cr coated materials tested at 345°C, from sample S7: (a) image collected from the side surface of sample (X-Y plane); (b) low magnification view of the outer surface of the sample (Y-Z plane); (c) to (e) are high magnification views of the outer surface of the sample (Y-Z plane). One schematic of C-ring sample with loading is included.

To summarize, for PVD Cr-coated materials tested at both RT and 345°C, multiple coating cracks formed simultaneously at ~ 80% peak load in the Cr coating. No evidence revealed that these cracks penetrated the substrate after reaching peak load. At both RT and 345°C, once coating cracks formed, the majority of them tended to travel across the sample's total width; further loading led to the formation of new coating cracks, as well as further extended in length of the semi-across width cracks formed at previous loading stages. At RT, the cracks were at a width of 1–4 μm at the coating surface and formed almost vertically (at an angle of 80° to 105°) to the hoop direction. However, at 345°C, the coating cracks displayed a larger width (1–8 μm), as well as a larger angle range (75° to 109°) from the tensile hoop direction. No coating spallation was found at either temperature.

6.5. Discussion

6.5.1. Microstructures of CS and PVD Cr-coated materials

For the CS Cr-coated materials, the tortuous Cr coating/substrate interface is a typical morphology of the cold spraying process [3], [63]. The thickness of these coating can be quite varied, as reported by Fazi *et al.* [100]. Small pores distribued in the CS coating in optical images (Fig. 6.1a) were confirmed by band contrast EBSD maps in Fig. 6.2a. These are attribued to the deposition process of the CS method, and are commonly found between former Cr powder particles [63], [100]. Fazi *et al.* [63], [100] pointed out that as these small pores are isolated from outer environment, they have a negligible effect on the coating oxidation resistance. The crack pathways in the CS coating could be potentially affected by the spalted Cr grains in the coating; which consequently affects the strength of the coating. These will be further discussed in Section 6.5.3.

For PVD Cr-coated materials, compared to CS materials, the PVD Cr coating/substrate inetrface was found to be smoother (Fig. 6.1b), with the coating almost fully dense with no obvious porosity (Fig. 6.2b). The Cr grains were columnar in shape, with a strong texture along [111] direction in both hoop and axial direction. Smaller grains at the coating/substrate interface were found, which is consistent with typical PVD coatings [112]. The PVD Cr grains were often observed to exhibit either, or both, strong [110] and [111] crystallographic textures with direction normal to the deposition surface [53], [112], [342]. The columnar Cr grains in the PVD coating could affect the pathways of coating cracks, as well as the strength when coating cracks firstly being observed, as furtehr discussed in Section 6.5.3. Due to these larger columnar Cr grains, the average size of the Cr grains inside PVD coating (with an area of 0.39 ± 1.22 μm^2) is ~1.4 times higher than that in the CS coating (0.16 ± 0.42 μm^2).

6.5.2. Local properties of CS and PVD Cr-coated materials

For CS Cr-coated materials, the local properties of both the coating and substrate were found to become significantly varied close to the interface. Specifically, for the coating, the hardness of Area #1 (~4.5 GPa) was ~18.4% higher than that in Area #2, ~3.8 GPa. As for the substrate, the hardness of Area #3 (~3.0 GPa) was ~15.3% higher than in Area #4 (~2.6 GPa). Similar trends have been reported by Fazi *et al.* [100] in a CS Cr-coated ZIRLO™ cladding material. The nanoindentation hardness measured in the middle of their Cr coating (at a location similar to the Area #1 in current project) was ~ 27.8% higher than that measured at locations close to the interface (at a location similar to those tested in our Area #2). Similarly, the hardness of the

substrate close to the interface, *i.e.*, within 5 µm (at a location akin to our Area #3) was ~40% higher than that measured in the substrate away from the interface. As discussed in Section 2.3, during the CS manufacturing process, a intermixed bonding region could generate at the coating/composite interface (~40 nm in thickness), with one example of concentration profile across the intermixed bonding region at one CS Cr-coating/Optimized ZIRLO™ interface, Fig. 6.14a. This is caused by the diffusiom of Cr and Zr elements into each other [100].

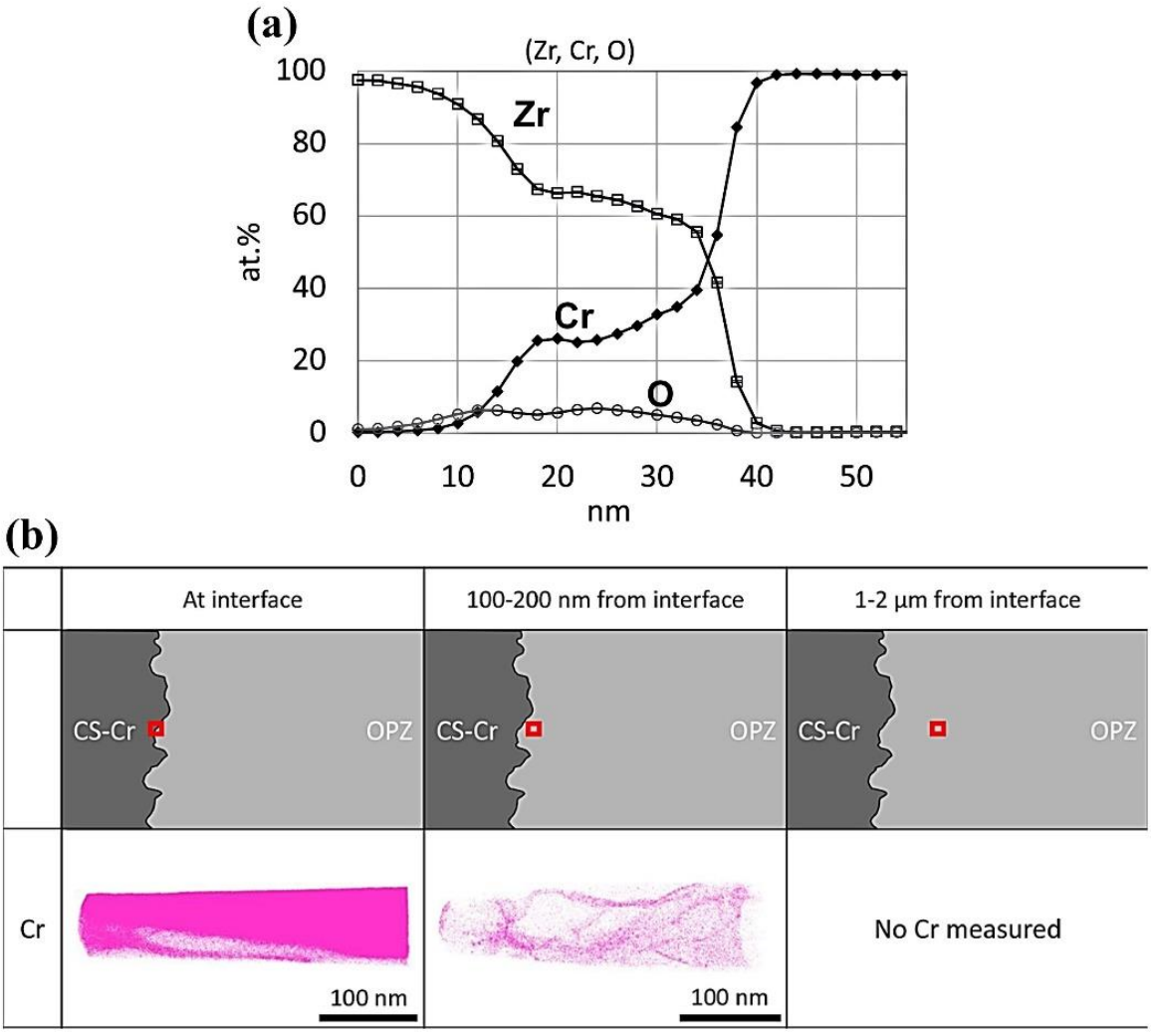

Figure 6-15. (a) Concentration profiles across the intermixed bonding region (in a thickness of around 40 nm) found at the CS Cr-coating/Optimized ZIRLO™ interface, performed by energy dispersive X-ray spectroscopy (EDX); (b) 3D reconstruction of the elemental distribution of Cr element at the CS Cr-coating/Optimized ZIRLO™ interface (in a distance of 100 nm to 200 nm), performed by atom probe tomography (APT). Figures are reproduced from ref [100].

It was reported that the maximum diffusion distance of Cr and Zr into each other is ~100 nm to ~200 nm [100], with one example presented in Fig. 6.15b. In current work, the nanoindentation tests performed in the substrate were ~3 µm to ~5 µm away from the interface (far away from the such intermixed bonding region and element diffusion region), therefore the influence of such intermixed bonding region to the variation of local properties could be

considered negligible. As such the variations in measured data were most likely the result of plastic deformation in the coating and substrate close to the interface during the manufacturing process [100], which can cause deformed and elongated Cr grains [101], [102], smaller grain sizes and a higher dislocation concentration in the substrate near the interface. Such plastic deformation during CS coating manufacturing could also impact its interfacial toughness. This is discussed below in Section 6.5.3.

For PVD Cr-coated materials tested in the current study, the hardness of Area #2 (~ 5.2 GPa) is also higher (by about 16%) than Area #1 (~4.5 GPa). This is attributed to the smaller size of the Cr grains located close to the interface (Fig. 6.2b), which is typical for PVD Cr coatings [79]. In contrast to the CS materials, there is no significant variation in hardness in the substrate of PVD materials as the PVD process does not lead to any plastic deformation.

In summary, for both the CS and PVD Cr-coated materials in current study, the hardness and elastic modulus values measured for Cr coatings are in the range of 3.8 GPa to 5.2 GPa, and 249.5 GPa to 268.3 GPa, respectively; and for zircaloy-4 substrate are in the range of 2.6 GPa to 3.0 GPa, and 105.6 GPa to 113.4 GPa, respectively. These values are broadly consistent with the values of the hardness and elastic modulus of the Cr coating and substrate from open literatures: the hardness and modulus of Cr coatings are respectively in the range of 2.9 to 14.2 GPa and 140–300 GPa; corresponding values for the zircaloy substrate are typically 1.8–3.0 GPa and 95–115 GPa [343]. This suggests the local properties measured in current work is comparable with others.

6.5.3. Strength and strain of CS and PVD Cr-coated materials at RT and 345°C

Using various testing methods, such as plug-expansion, uniaxial tension and tensile tests, the room temperature maximum hoop strength of similar CS and PVD Cr-coated zircaloy-4 materials have been reported in the open literature to be in the range of ~700 MPa to ~1322 MPa [53], [79], [104], [105], [112]; detailed summaries of these values is presented in Table 2.4 and Table 2.5 in Section 2.3. In the present study, the maximum hoop stresses at RT are ~ 1168 MPa and ~1150 MPa respectively for the CS and PVD Cr-coated materials. Although such calculated maximum hoop stresses are approximate values based on Eq. 3.1, they are still in the reported range. And such variations could be caused by the different properties of Cr coatings, *e.g.*, variations in surface roughness. And these properties could potentially affect the mechanical properties of the entire Cr-coated cladding materials, *e.g.*, initiation of coating cracks. Therefore, future work will be conducted on the investigation of surface roughness of these materials.

In current work, the estimated maximum hoop stresses tested at 345°C for both types of cladding materials were all found to be lower than those at RT by ~50%; with ~631 MPa (~54% of RT value) for CS Cr-coated materials, and ~611 MPa (~53% of RT value) for PVD Cr-coated materials. Similar phenomena have been reported by Roache *et al.* [104], [105] on their CS Cr-coated zircaloy-4 cladding materials, tested at both RT and 315°C using a plug-expansion test. The maximum hoop stresses of samples tested at 315°C (~500 MPa) were 60% to 70% of the RT values (700-800 MPa). Jiang *et al.* [53] also reported the tensile strength at 350°C (~240 MPa) of their PVD Cr-coated zircaloy-4 sheet samples as ~55% of the strength tested at RT (~440 MPa). These are all consistent with the findings in present work suggesting that the C-ring compression test is comparable with other test configurations.

In current study, for the CS coating, the hoop strain when first coating cracks being observed is 0.36% to 0.41% at RT, and 0.20% to 0.24% at 345°C. Roache *et al.* [104], [105] conducted plug-expansion tests for similar CS Cr-coated zircaloy-4 claddings with ~24 μm coating thickness at RT and 315°C. They employed both AE and DIC methods to measure the hoop strain at the initiation of coating cracks. The hoop strain values obtained were consistent at both temperatures, ranging from 0.3% to 0.5% at RT and approximately 0.34% at 315°C. In current study, the measured hoop strain at RT aligns with these previously reported values. However, a lower strain was observed at 345°C. A potential explanation for this discrepancy is that the strain calculations in this study, for both RT and 345°C, were based on the RT elastic modulus of the Cr coating, as determined by nanoindentation. The actual elastic modulus of the Cr coating at 345°C is likely lower than the RT value, resulting in a lower calculated strain. To obtain more accurate hoop strain values at elevated temperatures, future research will involve high temperature nanoindentation to determine the actual elastic modulus of the Cr coating at these temperatures. For the PVD coating, the hoop strain when first coating cracks being observed is 0.33% to 0.34% at RT, and 0.18% to 0.20% at 345°C. Very limited hoop strain value of similar materials were reported from literature. Jiang *et al.* [53] (2021) conducted *in-situ* tensile tests on simialr PVD Cr-coated (coating thickness: ~15 μm) zircaloy-4 sheet specimens at elevated temperatures (from RT to 450°C). The tensile strains at the initiation of coating cracks were found increased with temperature: steadily increasing from around 0.44% at RT to around 2.10% at 450°C [53]. In current study, the measured hoop strain at RT aligns well with these previously reported values. However, a lower strain was observed at 345°C, which could also be caused by the over estimated elastic modulus at 345°C. In

summary, for CS material, the RT hoop strain at the initiation of coating crack is 14.7% higher than the PVD material, indicate the CS coating possesses higher crack-resistance.

In current study, the hoop strength of the first formation of coating cracks of CS coating was ~1020 MPa at RT and ~584 MPa at 345°C, which were respectively 13.7% and 14.5% higher than the PVD coating (~897 MPa at RT and ~510 MPa at 345°C). Note that the accurate strength of first coating cracks' formation of CS materials at 345°C could lower than ~584 MPa, as finer coating cracks could form prior to the primary coating cracks and were not detected by µXCT imaging. Similar phenomenon has been reported by Burden *et al.* [14] from their CS (~25 µm in thickness) and PVD (~20 µm in thickness) Cr-coated zircaloy cladding tube materials under C-ring compression at RT. Although no exact stress values were reported, the coating crack initiation point (captured by real-time SEM imaging) for their CS materials is ~10.5 N/mm, which is ~23.5% higher than that of PVD materials (~8.5 N/mm).

Additionally, from the reported cross-sectional SEM images of the post-tested samples, compared with the cleavage crack behaviours of PVD coating (cracks travelled along the boundaries of columnar grains, which served as a smoother crack pathways, see example in Fig. 2.12), the pathways of CS coating cracks were more torturous as they travelled along the individual splatted grain boundaries, enabling them to potentially be arrested and deflected prior to reach the interface and generate large cracks (Fig. 2.12) [14]. Such crack deflection in the CS coating was also observed in current work, see example in Fig. 6.9a. Moreover, as suggested by Burden *et al.* [14], the high roughness of CS coating/substrate interface resulted in a strong mechanical interlocking of the coating and substrate increasing the complexity of load redistribution. Therefore, in current study, the potential reasons for the higher strength (first coating cracks' formation) of CS coating (compared with PVD coating) could be attributed to splatted grains in the coating and its higher interfacial roughness.

6.5.4. Interfacial toughness and interfacial failure modes at RT

In this work, for CS and PVD Cr-coated materials tested at both RT and 345°C, once coating cracks reached the coating/substrate interface, they were arrested or deflected at the interface without penetrating the underlying substrate; this was confirmed both by µXCT and SEM imaging. One typical example is presented in Fig. 6.11a, from the SEM image of the side surface (X-Y plane) of a sample after failure, where some doubly deflected cracks can be observed along the interface for the PVD material tested at RT. As no obvious coating spallation was found for the CS and PVD materials tested at both RT and 345°C, there was clearly good adhesion of the Cr coating to the substrate.

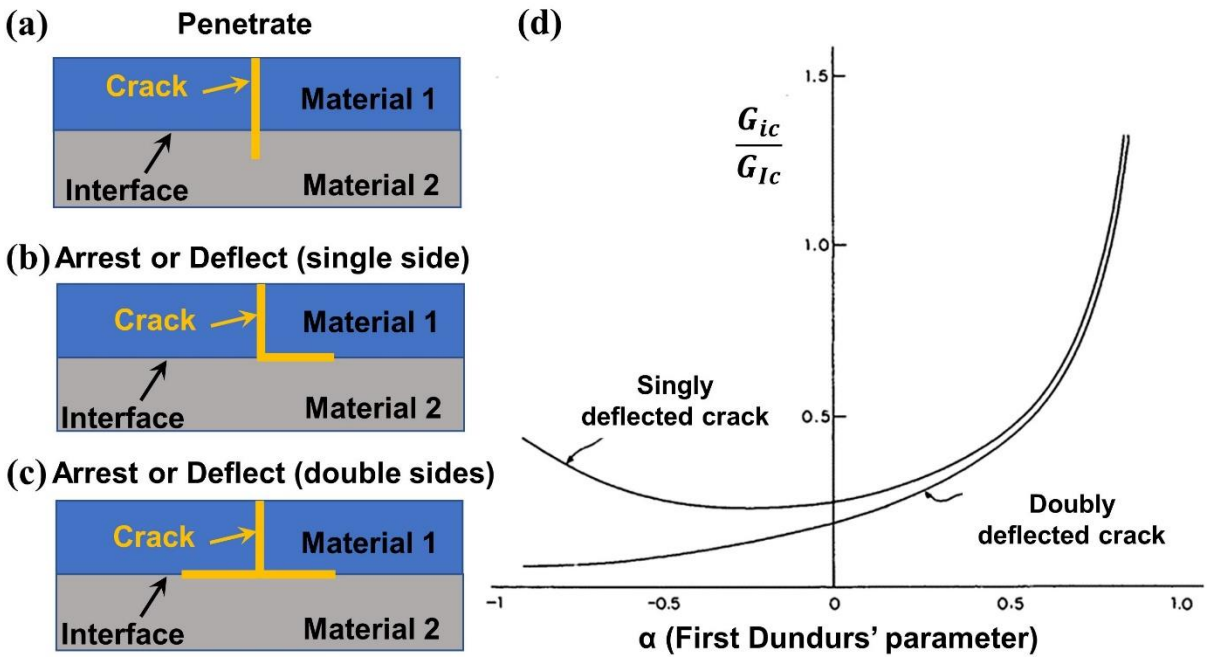

Figure 6-16. Schematic illustrations to demonstrate how when a crack runs from material 1 and impinges on the interface with a dissimilar material 2, it can have three ways to propagate: (a) penetrate the substrate (material 2), (b) arrest or with single-side deflection or (c) arrest or with double-side deflection. (d) Diagram of He and Hutchinson's linear-elastic analytical solution [344], [345], once a crack in one material impinges the interface with a different material, the behaviour is a function of the elastic modulus mismatch across the interface. As is defined by the interfacial toughness, G_{ic}, the critical strain energy release rate, G_{Ic}, of material 2 (substrate) and the first Dundurs' parameter (α).

As the local modulus of the coatings and substrate were measured in the present study, with the mode I fracture toughness or strain energy release (K_{Ic} or G_{Ic}) of zircaloy cladding material known, the upper bound of the mixed mode coating-substrate interfacial fracture toughness or strain energy release rate (G_{ic}, including singly interfacial deflected cracks and doubly interfacial deflected cracks) at room temperature can be determined from the He and Hutchinson method based on first Dundurs' parameter (α) [344], [345], assuming largely elastic conditions (Fig. 6.15). As a coating crack approaches and impinges on the coating/substrate interface, it can penetrate the underlying material (Fig. 6.15a) or become arrested at the interface with either a single-side (Fig. 6.15b) or double-side interfacial deflection (Fig. 6.15c). Fig. 6.11a presents an example for the situation described in Fig. 6.15c for a nominally perpendicular impingement. The first Dundurs' parameter (α) represents the elastic modulus mismatch across the interface of two dissimilar materials (details on this can be seen in refs [344], [345]), and is defined by:

$$\alpha = \frac{E_1' - E_2'}{E_1' + E_2'}, \tag{6.1}$$

where E_1' and E_2' are the plane-strain elastic modulus of the zircaloy-4 and Cr, respectively, as can be calculated from:

$$E_i' = \frac{E_i}{1 - v_i^2}, \tag{6.2}$$

where E_i and v_i are the elastic modulus and Poisson's ratio of the corresponding material, respectively. The critical strain energy release rate, G_{Ic}, can be correlated to the critical stress intensity K_{Ic} by assuming primarily mode I cracking:

$$G_{Ic} = \frac{K_{Ic}^2}{E_1}, \tag{6.3}$$

where E_1 is the elastic modulus of substrate close to the interface. Eq. 6.3 is used to convert the reported zircaloy-4 mode I fracture toughness to critical strain energy release rate to correlate the mixed-mode interfacial toughness, G_{ic}, using the first Dundurs' parameter, α (Eq. 6.1).

Ren [346] used a modified Vallecitos embedded Charpy (VEC) technique to acquire the mode I stress-intensity factor, K_{Ic}, of zircaloy-4 (similar type of substrate material with current work) cladding tube materials at RT. The geometry of the cladding tube (r_o being ~4.7 mm and r_i being ~4.1 mm) in their work is also similar to that of current study (r_o being ~4.6 mm and r_i being ~4.0 mm). The reported K_{Ic} (101.1 MPa/m^2 at RT) [346] is therefore selected to estimate the interfacial toughness G_{ic}. Using Eq. 6.3, the converted critical strain energy release rate of the substrate of CS and PVD Cr-coated materials were calculated to be 93.33 J/m^2 and 90.13 J/m^2, respectively. By inputting the measured elastic modulus of the coating and substrate close to the interface (Areas #2 and #3, Table 6.1) of both CS and PVD materials, the first Dundurs' parameter (α) of singly and doubly deflected interfacial cracks, and corresponding upper-bound of interfacial toughness (G_{ic}) were calculated, as listed in Table 6.3.

Table 6-3. Calculated first Dundurs' parameter (α), as well as corresponding upper bound of the interfacial toughness (G_{ic}) for the situations of singly and doubly deflected interfacial cracks of both CS and PVD Cr-coated materials tested at RT.

Deflection types	**CS material**		**PVD material**	
	$\boldsymbol{\alpha}$	$\boldsymbol{G_{ic}}$ **(J/m^2)**	$\boldsymbol{\alpha}$	$\boldsymbol{G_{ic}}$ **(J/m^2)**
Singly deflected cracks	-0.37	22.39	-0.37	21.62
Doubly deflected cracks		11.20		10.81

Based on Fig. 6.15d, both the CS and PVD Cr-coated materials tested at RT were investigated. For interfacial crack deflection, the first Dundurs' parameter (α) is -0.37, such that the interfacial toughness (G_{ic}) should be respectively more than 0.24 and 0.12 times that of the zircaloy-4 substrate for both singly and doubly interfacial crack deflection. It can be found the

upper bound of the interfacial toughness (G_{ic}) at RT for single (22.39 J/m^2) and double (11.20 J/m^2) deflected cracks of the CS materials are both ~3.6% higher than that for the PVD materials (21.62 J/m^2 and 10.81 J/m^2). It is suggested that the higher interfacial toughness for the CS materials could result from the relatively strong interfacial locking of the coating and substrate [3], caused by plastic deformation close to the interface area during the CS manufacturing process [100].

6.5.5. Failure processes and crack patterns of CS and PVD materials at RT and 345°C

In the current work, for both the CS and PVD Cr-coated cladding materials tested at RT and 345°C, the formation and progressive development of coating cracks were successfully imaged by *in-situ* µXCT imaging. More importantly, the µXCT slices (2D images and 3D reconstructed slices) presented in current work provided crack pathways in the coating; such information could not be offered by 2D SEM images, as SEM only provides information of either the surface of coating cracks or the coating cracks at the cross-sections at sample's edge. These all demonstrated the current resolution of µXCT images (3.25 µm/pixel) is sufficient to provide the crack information in the Cr coating.

6.5.5.1. CS Cr-coated cladding materials tested at RT and 345°C

For the CS materials tested at RT, multiple coating cracks formed at ~90% of the peak load (Fig. 6.6). The distance between coating cracks, crack density (number of cracks per area), and corresponding hoop strain are summarized in Table 6.4.

Table 6-4. Distance between the coating cracks, crack density and corresponding hoop strain at different loading steps of CS Cr-coated materials tested at RT and 345°C.

	Loading stage	Distance between coating cracks (µm)	Crack density (#/µm^2)	Hoop strain
RT	0.91 P_U	98.89 ± 34.71	0.007	0.41%
	0.97 P_U	77.60 ± 25.41	0.009	0.44%
	P_U	58.38 ± 17.21	0.012	0.45%
345°C [a]	0.90 P_U	334.67 ± 154.31	0.002	0.20%
	P_U	314.89 ± 141.77	0.002	0.22%

[a] The distance between coating cracks and crack density at 345°C are only for the primary coating cracks, these finer tortuous cracks are not included in the calculation.

At RT, multiple coating cracks formed simultaneously at 0.41% hoop strain, and crack density increased with increasing load. After peak load, the crack number becomes saturated at 0.012/ μm^2. These cracks were found to be nearly perpendicular to the hoop direction (Fig. 6.7), indicating that the hoop stress is the main contributor to the coating fracture at RT. Some crack toughening mechanisms (*e.g.*, crack deflection and bifurcation) were observed for the CS coating cracks, Fig. 6.6e and Fig. 6.7. Similar phenomenon was also reported by Roache *et al.* [104], [105] (under plug-expansion tests at RT) and Burden *et al.* [14] (under C-ring compression tests at RT) of their CS Cr-coated zircaloy cladding tube materials; and one potential reason is that when coating cracks travelled along the boundaries and gaps between the splatted Cr grains inside CS coating, enabled them have more potentials to transfer their growth paths away from the direction (hoop direction in current work) of maximum driving force [14]. At some crack tips, cracks deflections along the striations in the coating (~90° to their growth direction) were observed (Fig. 6.7a) but they did not have any major impact to the overall crack direction patterns. The failure process of the CS Cr-coated cladding materials tested at RT can be classified into three stages: (i) initial collective deformation in the coating/substrate system without crack formation; (ii) multiple coating cracks formed simultaneously at 0.41% hoop strain oriented perpendicular to the tensile hoop direction with toughening mechanisms presented; (iii) with increasing load, the distance between the coating cracks steadily decreased to about 60% of the initial distance at formation when reaching peak load.

However, at 345°C, in addition to the three primary cracks (vertical to the hoop direction), tortuous small cracks (finer in width) were also observed (Fig. 6.7). These finer cracks were likely formed prior to the primary cracks. Based on the SEM imaging, the distance between coating cracks (includes both finer cracks and primary cracks) and corresponding crack density are measured to be 92.42 ± 37.92 μm and 0.006/ μm^2, respectively. As discussed in Section 2.3, such tortuous fine coating cracks have been reported on CS Cr-coated zircaloy-4 cladding tubes under plug-expansion tests at 315°C [104], [105] with angles oriented at ~65° to ~75° to the axial direction (Fig. 2.8). From their FEA analysis [105], tensile residual strains between Cr coating and substrate were measured at both axial (0.026%) and circumferential (0.031%) directions, as respectively presented in Fig. 6.17 and Fig. 6.18.

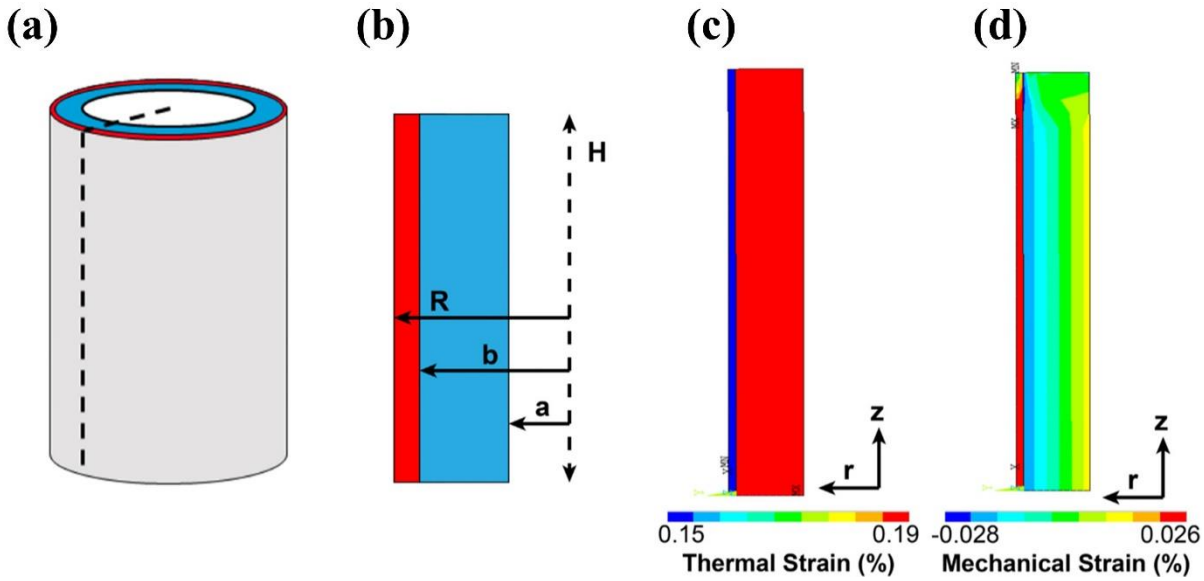

Figure 6-17. Finite-element calculation of residual stress distribution in the axial direction of CS Cr-coated zircaloy cladding tube. (a) The expanding plug specimen with an axial slice marked by a black dashed line. (b) A graphical representation of an axial slice of the coated zirconium alloy. Representative (c) thermal strain and (d) mechanical strain maps of that slice resulting from heating from room temperature to 315°C. Figures are reproduced from reference [105].

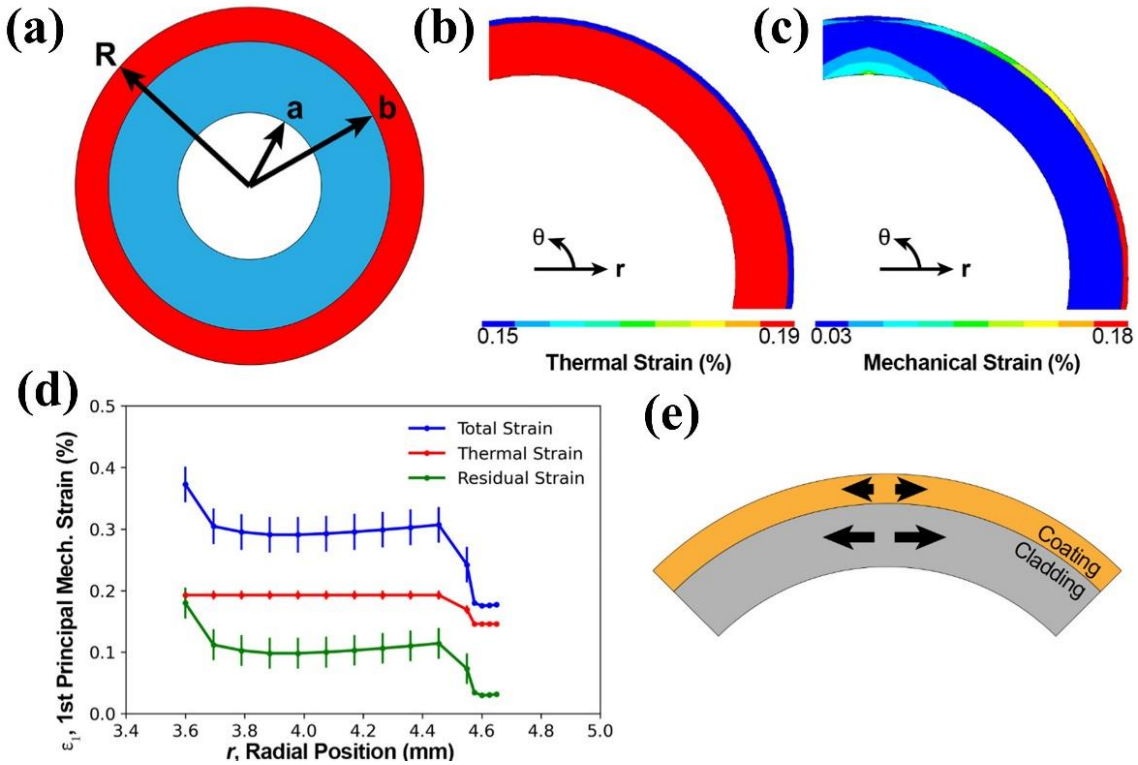

Figure 6-18. Finite-element calculation of residual stress distribution in the circumferential direction of CS Cr-coated zircaloy cladding tube materials. (a) A graphical representation of the cross-section ANSYS model. Representative (b) thermal strain and (c) mechanical strain maps and (d) the corresponding strain values through the radial thickness of the substrate and coating at the orientation leading to the max coating strain when heating from room temperature to 315°C. From the model, the coating will possess a slight (e) tensile residual strain. Figures are reproduced from reference [105].

Such tensile stresses were caused by the thermal expansion mismatch of Cr (4.9 to 8.2 × 10^{-6}/°C [347], [348]) and zircaloy-4 substrate (6.6 × 10^{-6}/°C [349], [350]) when temperatures rising from RT to 315°C. It was suggested that such tensile residual strains could create a shear stress state predisposed to off axis cracking and generate a multi-dimensional stress-state in the coating [105], which led to the tortuous small coating cracks in current work. Compared with the PVD materials, such tortuous small coating cracks in the CS materials at high temperatures could potentially divert the stress at the crack tips from the main driving force; and therefore, potentially prevent the formation of large fatal coating cracks at the early stage of coating fracture.

As with increasing load, the tensile hoop stress generated in C-ring compression will exceed the thermal multi-dimensional stresses [105], this is considered to be a potential reason for the two-stages of crack formation observed in the present work: (i) the formation of finer coating cracks caused by multi-dimensional stresses from the thermal mismatch, and (ii) the formation of primary cracks caused by the tensile hoop stress. Accordingly, the failure processes in the CS materials tested at 345°C can be classified into four stages: (i) initial collective deformation in the coating/substrate system without crack formation; (ii) formation of finer tortuous coating cracks due to the multi-directional stress distribution upon heating with a low hoop stress; (iii) with increasing tensile hoop stress, several primary cracks (vertical to hoop direction) form at ~90% of peak load; (iv) with further loading the number of primary cracks did not increase but their width did.

6.5.5.2. PVD Cr-coated cladding materials tested at RT and 345°C

For PVD materials tested at RT, multiple coating cracks formed simultaneously at 80% of peak load. The distance between coating cracks, crack density (number of cracks per area), and corresponding hoop strain are summarized in Table 6.5.

Table 6-5. Distance between the coating cracks, crack density and corresponding hoop strain at different loading steps of PVD Cr-coated materials tested at RT and 345°C.

Materials	Loading stage	Distance between coating cracks (μm)	Crack density (#/μm^2)	Hoop strain
RT	0.80 P_U	62.13 ± 14.55	0.008	0.34%
	0.89 P_U	50.67 ± 14.92	0.012	0.38%
	P_U	29.27 ± 11.84	0.017	0.43%
345°C	0.78 P_U	71.20 ± 21.87	0.009	0.18%
	P_U	43.27 ± 9.18	0.012	0.23%

At RT, multiple coating cracks formed simultaneously at 0.34% hoop strain, and crack density increased with increasing load. After peak load, the crack number becomes saturated at 0.017/ μm^2.Note the crack density (upon formation as well as with increasing load) were higher than that of the CS materials. These coating cracks were almost perpendicular to the tensile hoop stress (in an angle range of 80° to 105°) and propagated mostly in an intergranular manner (Fig. 6.11).

There are two main differences of the crack patterns in PVD coatings at 345°C compared with the RT tests: (i) the orientation of the coating cracks showed a larger deviation from the hoop direction (75° to 109° at 345°C), Fig. 6.13, and (ii) the width of these cracks were larger (1-8 μm) after peak load (Fig. 6.13); (iii) the crack density was also smaller. The exact reason for these two types of behaviour is not fully understood, but this could be related to a similar thermal mismatch on heating, as observed in the cold sprayed coatings. This would result in change of stress-state, as well as a potential transition from brittle to ductile behaviour with increasing temperature which would lead to larger crack width and a reduced saturated crack density [53]. Indeed, further experiments with intermediate temperature steps should be conducted in the future to investigate the brittle to ductile transition temperature of such coating materials.

In general, the failure process of the PVD materials tested at both RT and 345°C can be classified into three stages: (i) the initial collective deformation in the coating/substrate system without crack formation; (ii) multiple coating cracks formed simultaneously at ~80% of peak load, with crack orientations diverged away from tensile hoop direction at higher temperature, and (iii) coating crack density saturated at peak load.

For both CS and PVD materials, crack density decreased with increasing temperatures. Similar phenomenon has been reported, Jiang *et al.* [53] (2021) performed *in-situ* tensile tests on their PVD Cr-coated (coating thickness: ~15 µm) zircaloy-4 sheet specimens at elevated temperatures (from RT to 300°C), and the distance between coating cracks were also reported to be increasing from ~66 µm at RT to ~166 µm at 300°C (in current work, it is ~30 µm at RT and ~50 µm at 345°C for PVD materials). Although different values were reported, which may be due to the variation of Cr coatings (coating thicknesses, fabrication processes) and testing configurations, similar trend was observed, again indicated the C-ring compression tests in current work is comparable with other test configurations, and indicated the quantitative analyses of the distance between coating cracks (crack density) in current work is an effective method to investigate the coating crack behaviours.

6.5.6. Vibrations and handling of Cr-coated zircaloy claddings in LWRs

Vibrations of zircaloy claddings could occur during operation in light water reactors, which could affect the mechanical properties of the claddings [351]. Such vibrations could be mainly classified into two types, the first types is mechanical vibration, which could cause by the seismic events (earthquakes) and external disturbances [352]. Kitano *et al.* [352] recently (2020) investigated the seismic resistance of ruptured and oxidized zircaloy claddings (40% of hoop strain at the rupture opening, as presented in Fig. 6.19) after LOCA condition (at 135°C) by finite element analysis (FEA). The maximum principal stress (68 MPa) was reported along the axial direction, occurred at the rupture opening, Fig. 6.19. They suggested that such materials could be prevented against structural failure resulting from bending stresses induced by seismic activity during post-LOCA conditions [352]. For the industrial applications of CS and PVD Cr-coated materials in LWRs, future work will be conducted on the investigation of the failure of coatings at such mechanical vibration conditions.

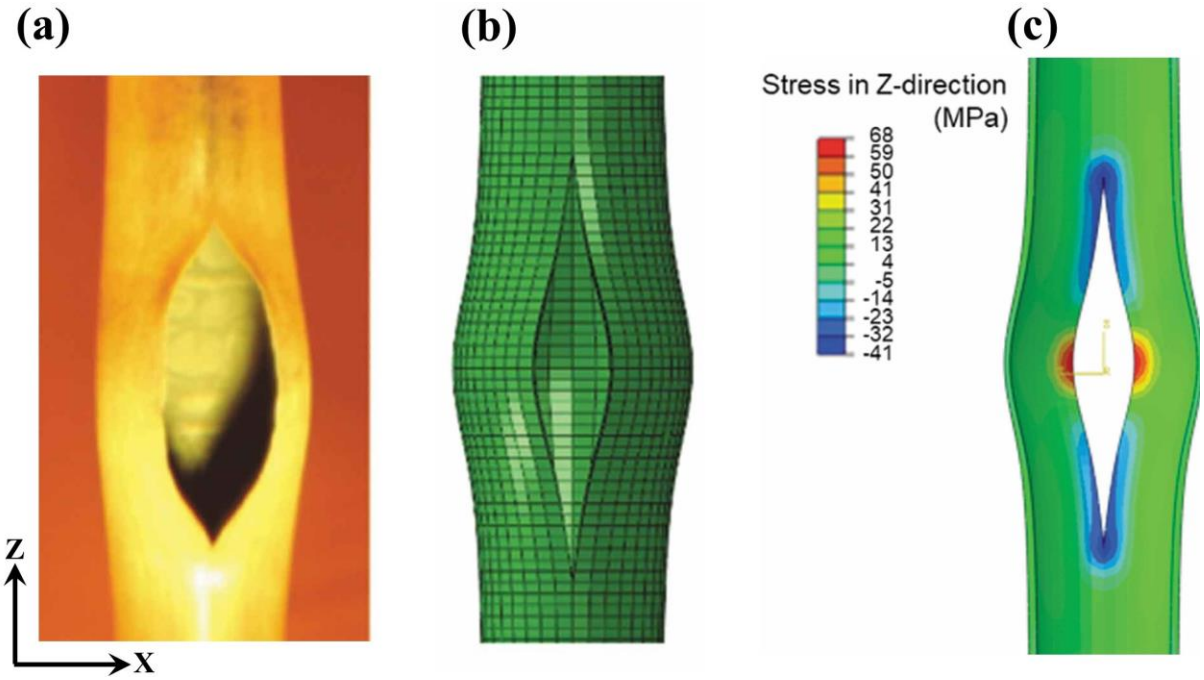

Figure 6-19. (a) Appearance of a ruptured and oxidized zircaloy cladding tube material; (b) finite element mode of the ruptured zircaloy cladding tube material; (c) calculation of the distribution of the axial (Z direction) stress in the ruptured zircaloy cladding tube material by FEA at 135°C, when the vibration and rupture opening have the same azimuthal angle (0 degree), and at a conservative displacement of 58 mm. Figures are reproduced from ref [352].

The second type of vibration is flow-induced vibration [353]. Such vibration is caused by the flow of water circulating through the core of the LWRs [354]. As presented in Fig. 6.19, cladding rods are supported by the grid assembly. Springs (or metallic vanes) are designed between the cladding and the grid assembly to fix the location of the claddings [354]. However, under irradiation conditions, the springs could relax and lose their spring force, which consequently result in gaps between assembly and claddings. The vibration caused by flow of coolant could subsequently increase the possibly of wear of the claddings' surface against the assembly, which is widely known as 'grid-to-rod fretting (GTRF)'. As reported by Kitano *et al.* [353], in USA, more than 70% of the fuel failure in PWRs are caused by the GTRF. Based on that, in addition to the modelling for predicting GTRF in LWRs [353], several studies have focused on the wear properties of CS and PVD Cr-coated zircaloy claddings [3], [80]. These works indicated the Cr-coated zircaloy claddings have superior wear resistance compared with the un-coated ones. For instance, as reported by Bischoff *et al.* [80], after being exposed to 300°C for 100 hrs (PWR water condition), the un-coated (selected as reference) and PVD Cr-coated M5 claddings were under wear tests (Fig. 6.20a, 1.5 N normal load, linear displacement of ± 200 μm, with a frequency of 20 Hz) by the Inconel spring. It was reported that, compared with the un-coated materials, the total wear volume of coated materials was significantly decreased by two orders of magnitude, Fig. 6.20b.

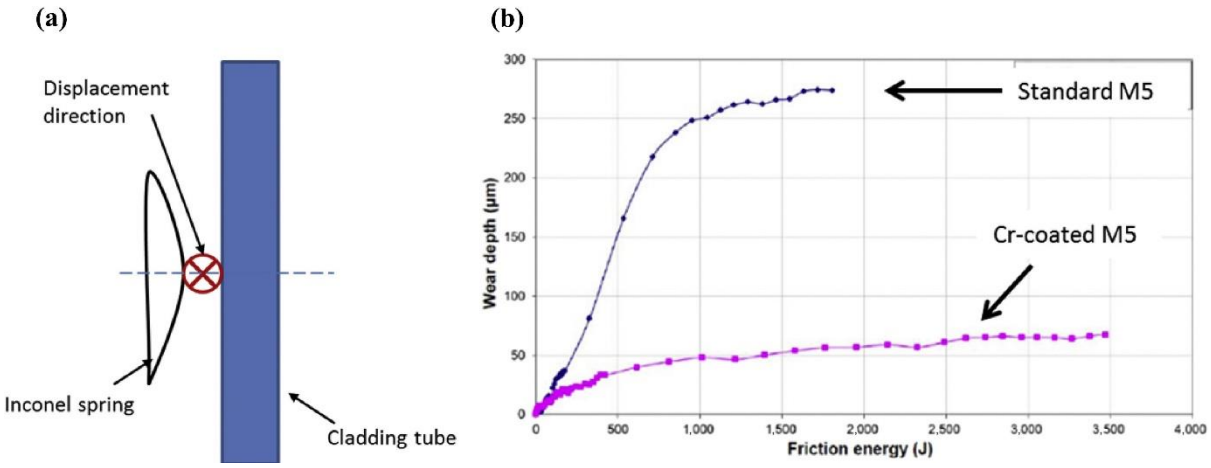

Figure 6-20. (a) Schematic representation of the experimental setup for the parametric wear tests on un-coated (reference) and PVD Cr-coated M5 claddings; (b) total wear depth as a function of friction energy for the clad/spring case for the un-coated (reference) and PVD Cr-coated M5 claddings. Figures are reproduced from ref [80].

For the CS and PVD materials in current project, the hoop strains when coating cracks initiated were measured to be ~0.41% and ~0.38%, respectively. Therefore, when handling these cladding, the strain at hoop direction should not exceed these critical values. Moreover, as described in Section 2.1.1, the zircaloy-4 cladding material is ~4 m in length [24]. During the handling of the claddings, bending could occur in the claddings due to their self-weight, as well as the stress and strain in the axial direction. Additionally, when the claddings are fixed by the grid assembly, stresses in the hoop direction are applied in the claddings. In current study, the CS and PVD Cr coatings could respectively sustain a hoop stress of ~1020 MPa and ~897 MPa at RT, and respectively ~584 MPa and ~510 MPa at 345°C without the formation of coating cracks. These indicate, during handling the claddings, as well as fixed them by the grid assembly, the applied hoop stresses of CS and PVD Cr-coated materials should respectively below ~1020 MPa and ~897 MPa, for preventing the damage of the coatings and formation of coating cracks. Future work will be focus on conducting bending tests on these materials to investigate the strength of the failure of the coatings in the axial direction of the claddings.

6.6. Conclusion

The different manufacturing processes of CS and PVD methods resulted in different local microstructures and properties of the Cr coatings: for CS Cr-coated materials, high speed spraying process resulted in hardening in the substrate close to the interface; as for PVD Cr-coated materials, smaller Cr grains close to interface caused higher hardness in the coating.

For both CS and PVD cladding materials, the measured hoop strengths at 345°C were ~50% of the room temperature strengths; compared with PVD materials, ~14% higher strength of

first coating cracks' formation, as well as ~8% higher hoop strain for coating crack initiation were found for CS materials tested at the same temperature, These can be potentially attributed to the higher interfacial roughness and splatted Cr grains inside CS Cr coatings.

For CS and PVD materials tested at both temperatures, all the coating cracks arrested at the coating/substrate interface and did not penetrate the substrate; using first Dundurs' parameter, based on measured local properties in current work and literature values on fracture toughness, the interfacial toughness of the CS material was estimated to be higher than the PVD materials at room temperature, and this was deemed to be plausible as the cold sprayed coating-substrate system had a more tortuous interlocking interface.

The failure processes of both types of coatings were investigated. CS coatings have a much lower overall crack density at both RT and 345°C compared to the PVD coatings; in particular, the average distance between primary cracks for the CS coatings at 345°C was much larger than that at RT. The formation of tortuous fine cracks was found in the CS coatings only at 345°C during initial stage of loading. Once the primary cracks formed at 345°C due to the high tensile hoop stress, they did not increase in numbers but increased in width as the load was raised to peak load.

For PVC coatings, the average distances between cracks at both RT and 345°C showed decreasing trend to 50–60% in the crack distance at peak load compared to the situation at their initial formation; in addition to the increase in the number of cracks, the PVD coatings at 345°C showed a widening of cracks with increasing load that demonstrated more ductile behaviour. The orientation of the cracks in the PVD coatings also showed larger deviation from the perpendicular direction of the tensile hoop stress. In both the CS and PVD coatings, the primary cracks (except those tortuous fine cracks in CS at 345°C) were all formed simultaneously at about 80–90% of the peak load, a situation that did not change with temperature.

In summary, nuclear-grade CS and PVD Cr coatings demonstrate different microstructures, local properties, as well as very different behaviour with testing temperature in a C-ring compression test configuration. A brief summary of their properties is tabulated in Table 6.6. The experimental observations in the current work are critical for the understanding of mechanical behaviour and failure processes of these materials at elevated temperatures, and improving the design of these coated zircaloy-4 cladding materials for future nuclear application.

Table 6-6. Summary of the different properties of CS Cr-coated and PVD materials tested at both RT and 345°C.

Properties		CS materials	PVD materials
Microstructures of as-received materials	-	Splat structures; pores in the coating; no preference grain orientation; tortuous interface	Grains in columnar shape with smaller grains clustered near interface; no obvious pores in the coating; strong texture in [111] direction; smooth interface
Area of Cr grain in the coating	-	0.16 ± 0.42 μm^2	0.39 ± 1.22 μm^2
Local properties of as-received materials (GPa)	In the middle of the coating	4.49 of H; 266.06 of E	4.47 of H; 268.31 of E
	In the coating close to the interface	3.79 of H; 249.47 of E	5.20 of H; 260.03 of E
	In the substrate close to the interface	3.02 of H; 109.53 of E	2.72 of H; 113.41 of E
	In the substrate away from the interface	2.62 of H; 105.61 of E	2.64 of H; 109.52 of E
Interfacial toughness G_{ic} (J/m^2)	Singly deflected cracks	22.39	21.62
	Doubly deflected cracks	11.20	10.81
Hoop strength (MPa) and strain at the initiation of coating cracks	RT	~1020/0.41%	~897/0.34%
	345°C	~584/0.22%	~510/0.19%
Maximum hoop stresses (MPa) and strain	RT	~1168/0.45%	~1150/0.43%
	345°C	~649/0.25%	~611/0.24%
Crack pathways in the coating	-	Tortuous crack pathways	Cleavage behaviour
Coating crack patterns	RT	Cracks formed nearly perpendicular to the tensile hoop direction; cracks arrested at the interface	Cracks formed nearly perpendicular to the tensile hoop direction (at an angle range of 80° to 105°); cracks arrested at the interface
	345°C	2 to 3 primary cracks formed nearly perpendicular to the tensile hoop direction; finer tortuous cracks being observed; cracks arrested at the interface	Cracks formed nearly perpendicular to the tensile hoop direction (at an angle range of 75° to 109°); cracks arrested at the interface

7. Mechanical behaviour of HCS and NCS Cr-coated Zircaloy claddings

In the current Chapter, the mechanical behaviour and progressive failure processes of two types of Cr-coated (with the Cr coating produced by HCS and NCS methods, respectively) zircaloy-4 cladding material were studied at RT and 345°C. More detailed introductions of these materials are presented in Section 3.2.2. The experimental procedures of high-temperature C-ring compression tests combined with real-time μXCT at RT and 345°C are presented in Section 3.3.1.2. The processing methods of the analysis of μXCT data can be found in Section 3.3.1.3. The testing methods of nanoindentation experiments for the measuring of local properties are presented in Section 3.3.3. The experimental procedure of the analysis of Cr grain distributions in the HCS and NCS Cr coatings by EBSD method can be found in Section 3.3.2.2. The experimental procedure of the measurement of residual stress distributions in these two types of Cr coatings by FIB-DIC method is presented in Section 3.3.4.2. The experimental procedures for the analysis of coating crack pattens of post-tested samples by SEM imaging can be found in Section 3.3.2.1. The results are presented in the order of (i) the microstructures, local properties and residual stresses of the as-received HCS and NCS materials; (ii) load-displacement curves, hoop strength and progressive failure processes of these two types of materials tested at both room temperature and 345°C; (iii) coating crack patterns and crack toughening mechanisms of the materials tested at both RT and 345°C; (iv) interfacial toughness of both types of materials at RT.

7.1. Microstructures of as-received materials

The typical microstructure of HCS material is presented in Fig. 7.1a and NCS material is presented in Fig. 7.1b. It can be found that, similar to the CS materials in Chapter 6, the interfaces of both HCS and NCS materials are tortuous. Small pores are also found to be scattered in both types of Cr coatings, Fig. 7.1. The thicknesses of the HCS and NCS Cr coatings are found to be similar, as measured to be 25.11 ± 6.2 μm and 24.22 ± 3.57 μm, respectively.

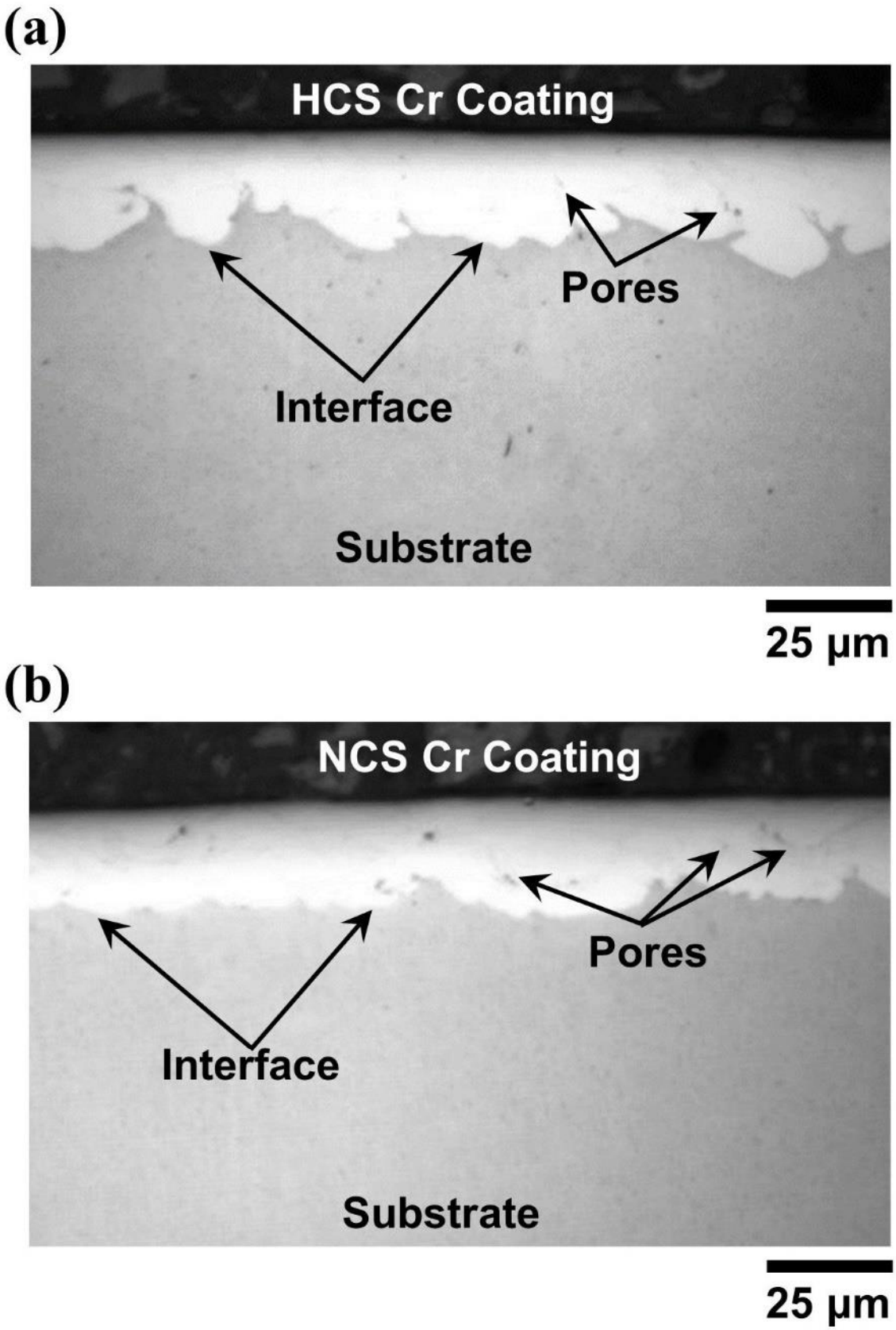

Figure 7-1. Optical images of the polished cross-sections of the as-received HCS and NCS Cr-coated, with the tortuous coating/substrate interfaces and pores inside the Cr coatings found for both types of the materials: (a) HCS Cr-coated materials and (b) NCS Cr-coated materials.

Fig. 7.2a and Fig. 7.2b present the EBSD band contrast figures and corresponding orientation image microscopy mapping of HCS and NCS Cr coatings, respectively. In both the HCS and NCS Cr coatings, pores can be found between the splatted Cr grains (Fig. 7.2), such results are consistent with that observed by optical imaging. The IPF maps of HCS and NCS Cr coatings are displayed in Fig. 7.2c and Fig. 7.2d, respectively. For both HCS and NCS Cr coatings, the Cr grains in the coating did not have any preferred orientation.

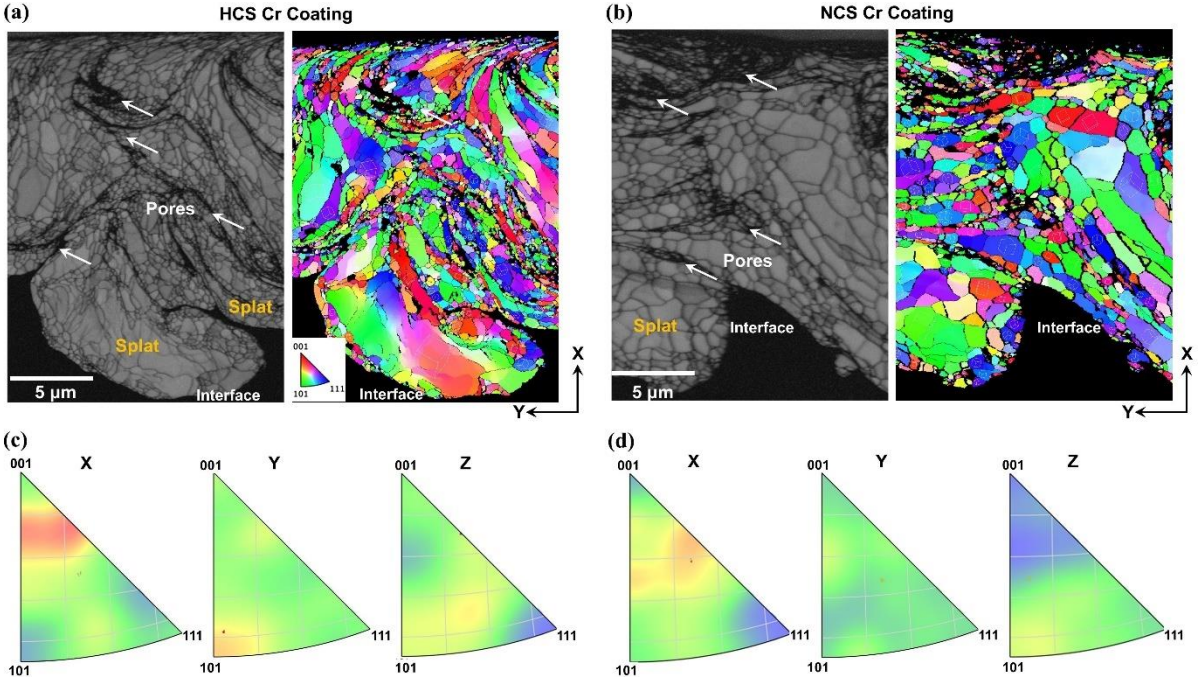

Figure 7-2. (a) and (b) are EBSD maps of the HCS and NCS Cr coatings contain band contrast graphs, and corresponding orientation imaging microscopy maps of the X-Y plane; for both types of Cr coatings, splat structures of Cr grains and small gaps/pores (marked by white arrows) between splats can be found: (a) HCS Cr coating; and (b) NCS Cr coating. (c) and (d) are inverse pole figures (IPFs) show textures of the Cr grains in both the HCS and NCS coatings, and random orientation of Cr grains in both types of coatings were found: (c) HCS Cr coating; and (d) NCS Cr coating.

Measurements of the areas of the Cr grains in the CS and PVD coatings are conducted automatically by EBSD mapping. For HCS Cr coating, the areas of Cr grains are measured to be 0.01 to 8.43 μm^2; similar results are found in the NCS Cr coating, with the area of Cr grains are measured in the range of 0.01 to 8.52 μm^2. For HCS and NCS Cr coatings, most of the Cr grains' area are distributed in the range of 0 to 1 μm^2, and the distribution of the Cr grains' areas in both HCS and NCS Cr coatings in such range (0 to 1 μm^2) are plotted in Fig. 7.3a and Fig. 7.3b, respectively. For both HCS and NCS Cr coatings, the majority (over 60%) of the Cr grains are measured to be below 0.1 μm^2. The average Cr grains' areas in the HCS Cr coating is measured to be 0.16 ± 0.31 μm^2, with similar value found for the NCS Cr coating: 0.18 ± 0.36 μm^2.

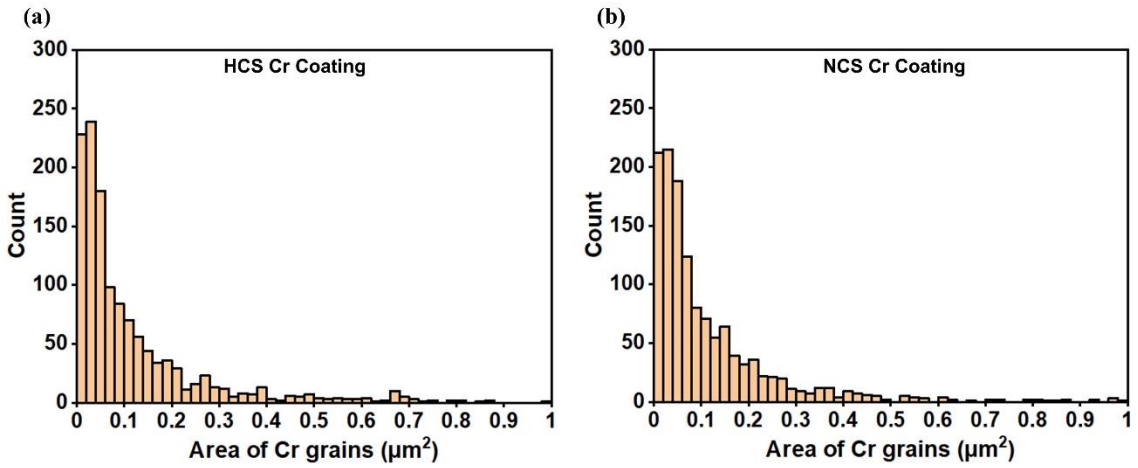

Figure 7-3. The distributions of the Cr grains' areas in the HCS and NCS Cr coatings, the selected range is 0 to 1 μm^2: (a) HCS Cr coating, and (b) NCS Cr coating.

7.2. Local properties of as-received materials

Nanoindentation experiments were conducted on the as-received HCS and NCS materials. Similar with the nanoindentation tests conducted on CS and PVD materials in Chapter 6, the tests in current Chapter were also performed on four areas, as described in Section 6.2. The indent points of the HCS and NCS materials are presented in Fig. 7.4. The hardness and elastic modulus values are tabulated in Table 7.1, as well as plotted in Fig. 7.5.

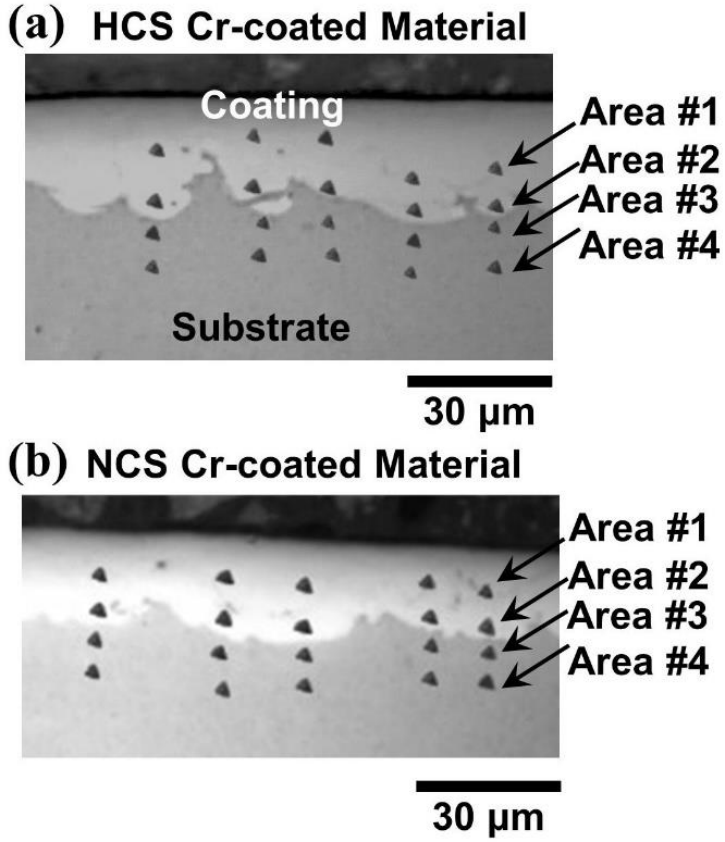

Figure 7-4. Optical images of the polished cross-sections of the as-received Cr-coated zircaloy cladding tube materials showing the four areas of the indent points: (a) HCS materials and (b) NCS materials.

Table 7-1. Measured values of the hardness H and elastic modulus E in different areas of the polished cross-sections of the HCS and NCS Cr-coated materials.

Areas	HCS material		NCS material	
	H (GPa)	E (GPa)	H (GPa)	E (GPa)
Coating Area #1	4.22 ± 0.69	230.32 ± 9.75	4.77 ± 0.68	200.82 ± 5.78
Coating Area #2	3.75 ± 0.80	213.59 ± 8.34	3.73 ± 0.67	203.81 ± 5.02
Substrate Area #3	3.08 ± 0.33	106.79 ± 7.99	3.06 ± 0.13	109.74 ± 5.18
Substrate Area #4	2.66 ± 0.11	104.85 ± 8.09	2.67 ± 0.04	104.34 ± 5.78

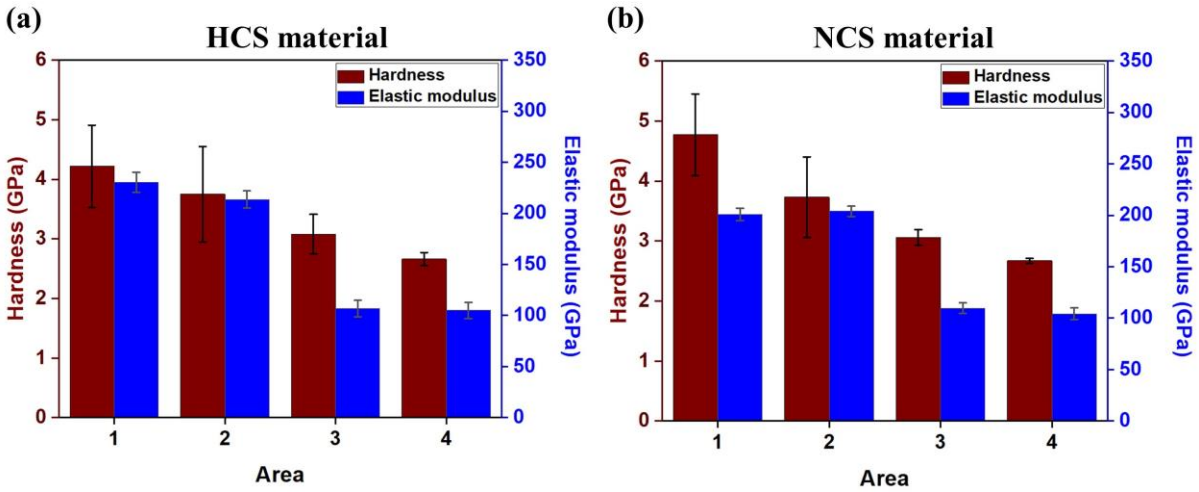

Figure 7-5. Hardness and elastic modulus of the different values in the polished cross-sections of (a) HCS material and (b) NCS material.

For the coating area in HCS material, the hardness and elastic modulus of Area #2 are ~89% and ~93% of that in Area #1 (middle of the coating), respectively. The substrate areas have overall lower hardness and elastic modulus than the Cr coating. Note that, similar to the CS Cr-coated materials in Chapter 6, the cold spray manufacturing process also causes hardening of the substrate close to the interface region, as the HCS material also has a higher hardness value (~16%) in Area #3 when compared to Area #4.

As for the NCS material, the hardness of Area #2 are ~78% of that in Area #1. For the substrate region, the hardness and elastic modulus in Area #3 are ~15% and ~5% higher than that in Area #4, respectively.

Note that, for the area in the middle of Cr coating, the hardness of HCS materials is ~11.5% lower than that of NCS materials; and the elastic modulus of HCS materials is ~14.7% higher than that of NCS materials. These imply the different manufacturing parameters of these two types of coating could affect their local properties, which consequently affect the residual stresses in the coatings and their mechanical behaviour at both testing temperatures, as will be

presented in Section 7.3 and Section 7.4, respectively. For both types of the materials, the hardness and elastic modulus values of substrate away from interface (Area #4) are found similar, as they use the same type of substrate, zircaloy-4. The potential influences of local properties on the interfacial toughness of these two types of materials will be discussed in Section. 7.7.

7.3. Residual stresses in Cr coatings

FIB-DIC experiments were performed on these two types of materials by the method described in Section 3.3.4.2, for measuring the residual stresses in the Cr coatings. Three ring-cores were milled on both types of coatings, with representative examples presented in Fig. 7.6. For the thin coating layer, the residual stresses are widely reported in the tangential direction [355]. Therefore, in current study, only the residual stresses in the Y direction (tangential direction) are investigated. The elastic modulus values measured in the middle of these two Cr coatings (by nanoindentation method) are applied for the calculation of residual stresses: 230.32 GPa for HCS material, and 203.81 GPa for the NCS material.

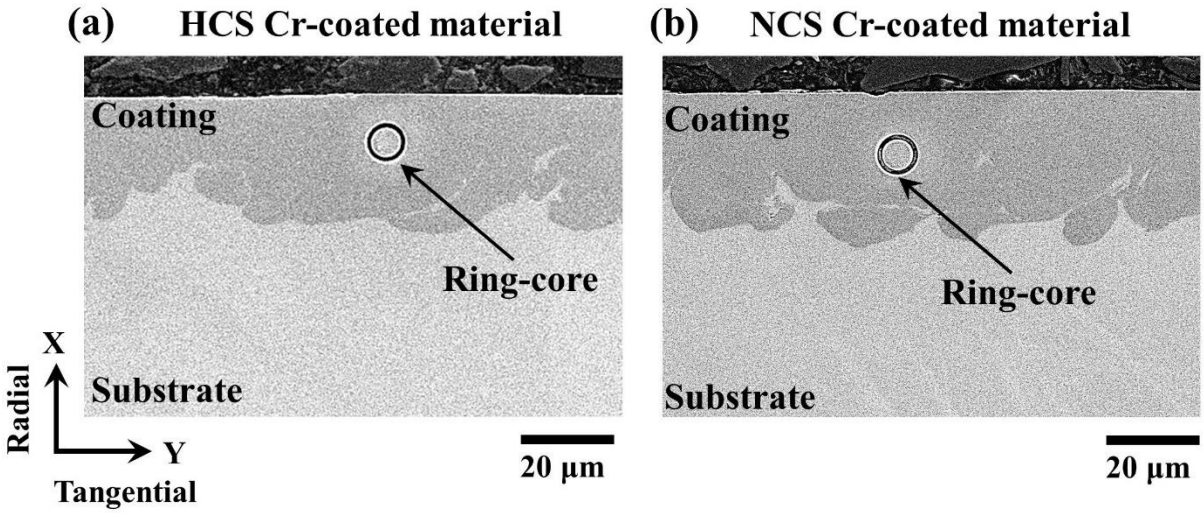

Figure 7-6. SEM images (in BSE mode) of the polished cross-sections of the as-received Cr-coated Zircaloy cladding materials showing the FIB-DIC areas where ring-cores were milled: (a) HCS Cr-coated materials and (b) NCS Cr-coated materials.

Before conducting the milling step, as presented in Section 3.3.4.2, random dot speckle patterns were firstly deposited on the coating by, with example presented in Fig. 3.11. These images are used as reference images for DIC analysis. Before the DIC calculation, a DIC sensitivity study was conducted for each type of the coating by the following steps: (i) one SEM image (image 1) was collected after the deposition of dot speckle patterns, and was selected as reference image; (ii) then, another SEM image (image 2) was taken at the same location as image 1; (iii) these two images were then registered, and imported into the open-source

MATLAB-based 2D DIC programme NCORR [326] to calculate the displacement, strain and stress. As no milling process was performed, therefore, zero displacement, zero strain and zero stress are expected for the results of the DIC sensitivity study.

Results of the DIC sensitivity study are presented in Fig. 7.7. For both HCS and NCS materials, the calculated displacement value and strain value in the Y direction (tangential direction) are very close to zero. Specially, for HCS material, the displacement and stain are 2.36×10^{-6} μm and 7.85×10^{-6}, respectively. For NCS material, the displacement and stain are 1.19×10^{-6} μm and 2.34×10^{-6}, respectively. These results indicate the accurate calculation of the DIC method in current project.

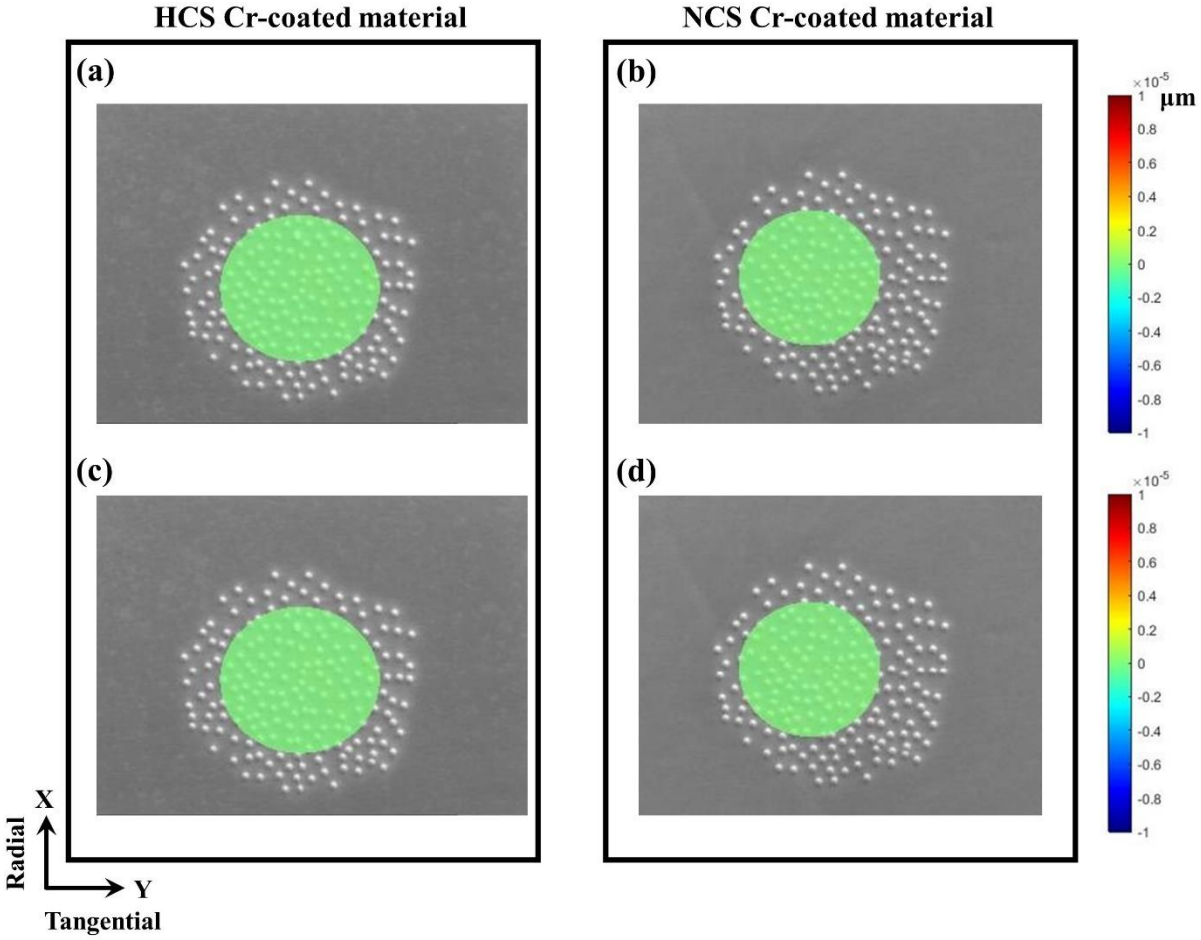

Figure 7-7. Results of the DIC sensitivity study of both the HCS and NCS Cr-coated Zircaloy materials, including the displacement and strain in the Y direction (tangential direction), with (a) and (c) for the displacement and strain of the HCS material, respectively; and (b) and (d) for the displacement and strain of the NCS material, respectively.

Fig. 7.8a and Fig. 7.8b display the relief of tangential stain and tangential stress with corresponding increasing milling depth of the HCS Cr coating, respectively. The relaxation of tensile strain and stress indicates the HCS Cr coating is in compressive residual stress [355]. The relaxation of tangential stain firstly increases with the milling depth until ~15 μm; after

that, a plateau is reached where complete strain relief is achieved, in a value of 0.15%, Fig. 7.8a. This strain is subsequently used to calculate the residual stress, and ~250 MPa compressive stress is measured in the HCS Cr coating.

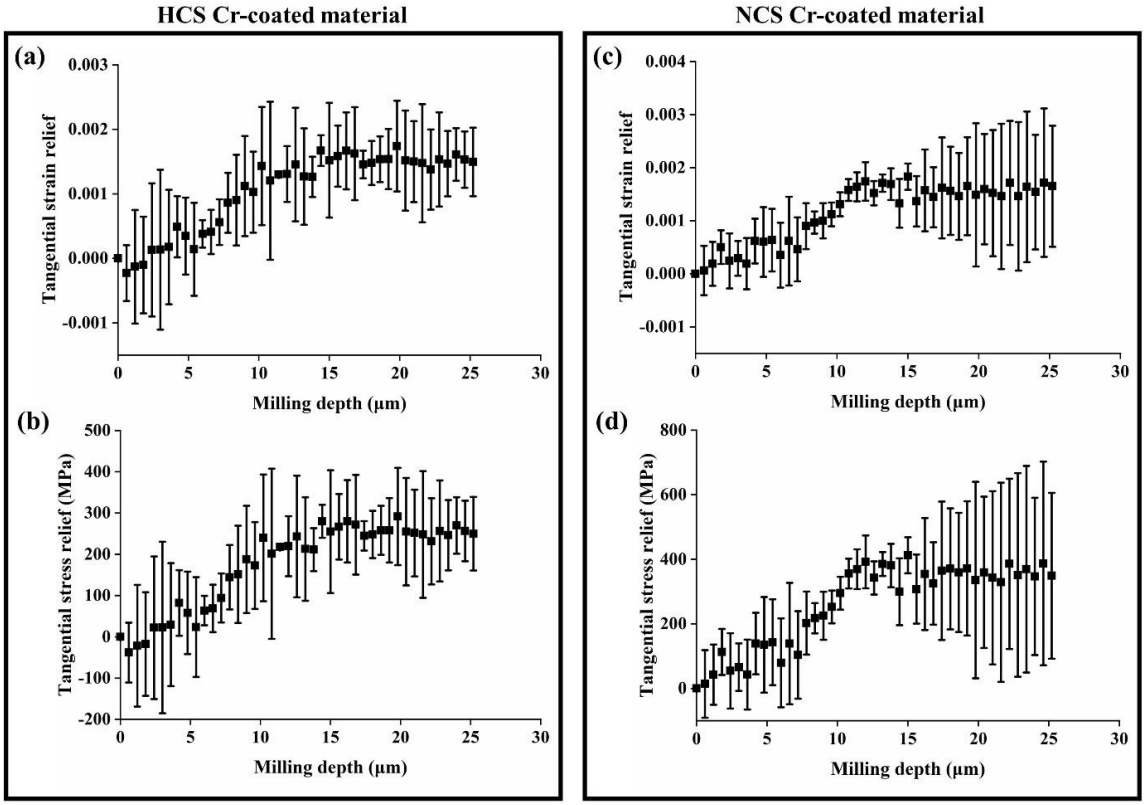

Figure 7-8. (a) and (b) are curves for the tangential strain relief with the corresponding milling depth and tangential stress relief with the corresponding milling depth of HCS materials, respectively; (c) and (d) are curves for the tangential strain relief with the corresponding milling depth and tangential stress relief with the corresponding milling depth of NCS materials, respectively.

For NCS Cr coating, before reaching the milling depth of ~14 μm, the relief of tangential strain increases with the depth. After that, a plateau is reached with the strain of 0.16%, Fig. 7.8c. And ~360 MPa compressive stress is estimated in the NCS Cr coating, Fig. 7.8d. Note that, the compressive residual stress in NCS Cr coating is 36% higher than that in the HCS Cr coating. The variation of residual stress in the Cr coatings could potentially affect the strength of first coating cracks occurred and coating crack patterns, as will be discussed in Section. 7.7.

7.4. Hoop strength at RT and 345°C

For both HCS and NCS materials, two samples were tested at each temperature, and their mechanical behaviour was found similar. Therefore, for the same type of materials, one load–displacement curve for each testing temperature is presented in Fig. 7.9. And Table A.7 summarized the detailed C-ring testing sequence for all the tested samples.

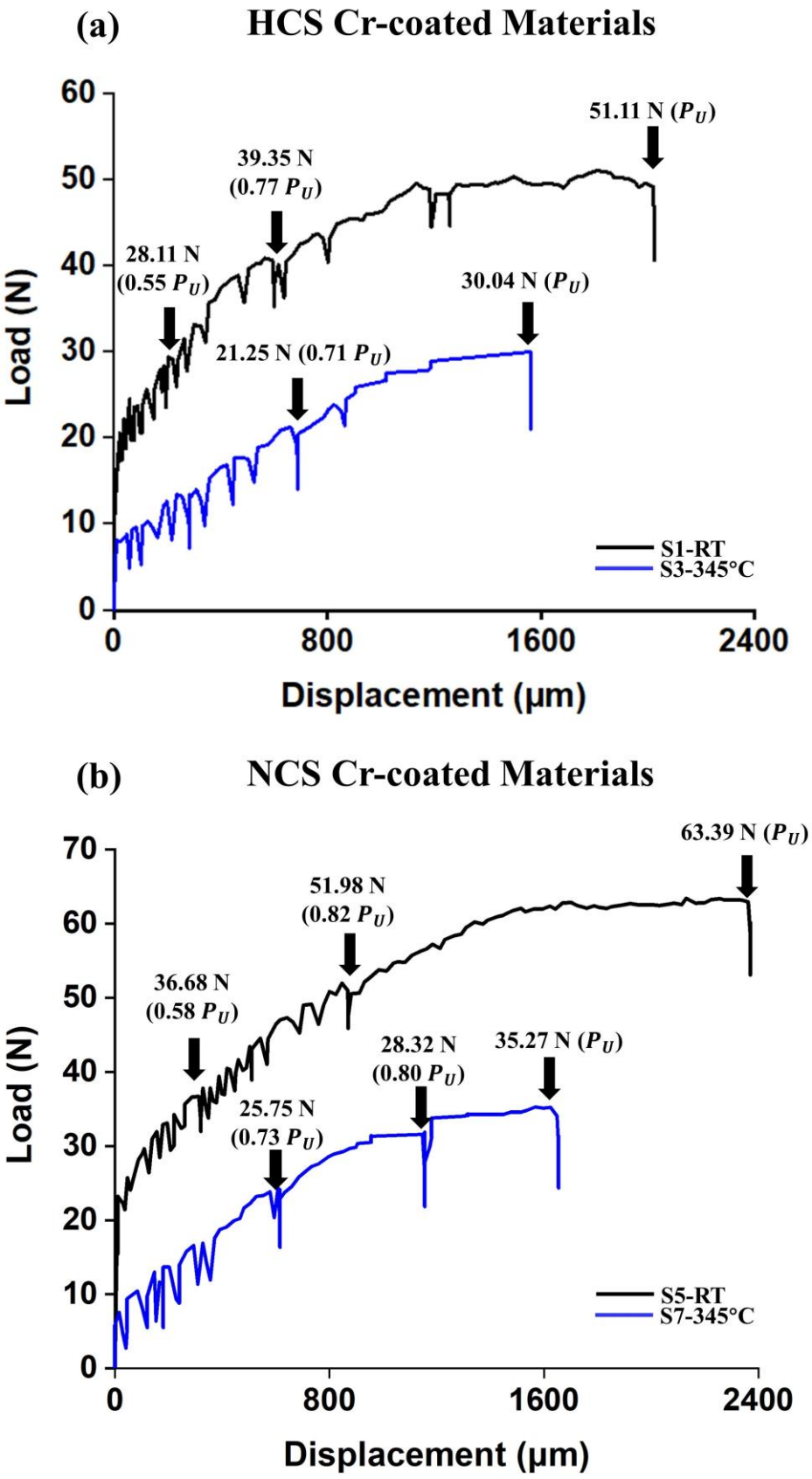

Figure 7-9. Representative load–displacement curves of the C-ring compression experiments of two types of Cr-coated materials tested at both RT and 345°C: (a) curves for the HCS materials including: sample S1 tested at RT and sample S3 tested at 345°C; (b) NCS materials including sample S5 tested at RT and sample S7 tested at 345°C. The black arrows indicate locations collected for the μXCT scans.

Similar to the CS and PVD materials investigated in Chapter 6, for HCS and NCS materials, load relaxations were observed at both temperatures, Fig. 7.9. As discussed in Section 6.3, the comprehensive investigation of such load relaxation is beyond the research scope of current PhD project; and the load relaxation values, as well as their correlation to the applied load are tabulated in Table A.8.

It is worth noting again, the sample's deformation in current Chapter is much higher than the validity criteria cited in ASTM Standard C1323-16 [246]. Therefore, the strength values in current Chapter could be overestimated values. Similar as the CS and PVD in Chapter 6, the RT maximum hoop strengths of both HCS and NCS materials are found to be higher than that at 345°C. For the HCS materials, the RT maximum hoop strength is ~59% higher than that as 345°C. As for NCS materials, the RT maximum hoop strength is ~84% higher than that at 345°C. These values are tabulated in Table 7.2. Moreover, the hoop strain at the onset of coating cracks and at peak load was calculated using the corresponding hoop stress and the measured elastic modulus of both HCS and NCS materials. Results are summarized in Table 7.2. As described in Section 6.3, the calculated hoop strain at peak load could differ from the actual values. And the calculated strain values at 345°C could be lower than the actual values.

Table 7-2. The width of specimens, loads and corresponding hoop stresses and strains where coating cracks were first observed, peak loads and calculated maximum hoop stresses for HCS Cr-coated and NCS Cr-coated cladding materials tested at both RT and 345°C.

Specimen	Sample width (mm)	Load and corresponding hoop stress[a] and strain where coating cracks were first observed	Peak load (N)	Maximum hoop stress[a] (MPa) and strain
HCS-S1-RT	2.28	28.11 N/714.97 MPa/0.31%	51.11	1299.94/0.56%
HCS-S2-RT	2.44	32.04 N/765.26 MPa/0.33%	56.49	1342.56/0.58%
HCS-S3-345°C	2.21	21.25 N/583.30 MPa/0.25%	30.04	788.24/0.34%
HCS-S4-345°C	2.37	25.74 N/629.93 MPa/0.27%	34.79	851.25/0.37%
NCS-S5-RT	2.19	36.68 N/1007.21 MPa/0.50%	63.39	1736.57/0.86%
NCS-S6-RT	2.51	42.94 N/1028.78 MPa/0.51%	75.51	1804.87/0.89%
NCS-S7-345°C	2.27	25.75 N/680.48 MPa/0.33%	35.27	932.17/0.46%
NCS-S8-345°C	2.39	28.50 N/715.36 MPa/0.35%	39.58	993.56/0.49%

[a] calculated using Eq. 3.1, ASTM C1323-16 [246].

As described in Section 3.3, for each sample under loading, the *in-situ* radiography projections are utilized to detect coating cracks. Eq. 3.1 is also used to calculate the hoop stresses of all the samples when the initiation of coating cracks being detected by these *in-situ* radiography

projections, as well as confirmed by real-time μXCT images. For both the HCS and NCS materials tested at both temperatures, loads, as well as the corresponding hoop stresses for the initiation of coating cracks are also summarized in Table 7.2. It is found that, for the stresses of the initiation of coating cracks at both RT and 345°C, NCS materials are 38% and 15% higher than that of the HCS materials, respectively. And the hoop strain at the initiation of coating cracks at both RT and 345°C, NCS materials are 56% and 31% higher than that of the HCS materials, respectively.

7.5. Failure processes and crack toughening mechanisms at RT and 345°C

This section investigates the progressive failure processes (by real-time μXCT images) and coating crack toughening mechanisms (by SEM images collected from post-tested materials) of HCS and NCS materials tested at RT and 345°C. Additionally, FIB-SEM tomography was used to investigate the crack pathways in the coating, and along the coating/substrate interface. For both HCS and NCS materials tested at each temperature, one specimen is selected as representative example. Note that, for each sample, the 2D μXCT slices and corresponding 3D reconstructed μXCT images presented in current section are collected from the same location in the sample.

7.5.1. HCS Cr-coated materials

For the HCS materials tested at RT, the sample S1 is selected as representative example. It can be found that, with the continuous increasing of load, no obvious coating cracks were observed at 0.30 P_U (estimated hoop stress: 389.98 MPa, hoop strain: 0.17%) from the *in-situ* radiography projection and the μXCT image, Fig. 7.10a. With the load reaching to 0.55 P_U (714.97 MPa, 0.31%), multiple coating cracks were observed from the radiography projection, and one μXCT scan was collected at this loading stage. Four coating cracks formed simultaneously, Fig. 7.10b. These cracks were found exhibited similar behaviours. Consequently, three of these cracks (identified as Crack#1 to Crack #3 in the magnified μXCT image in Fig. 7.10b) were used to illustrate the failure process. Fig. 7.10e displays the 3D visualization of part of coating cracks (Crack#1 to Crack #3) of ~290 μm in length (~13% of the sample's width: ~2.28 mm).

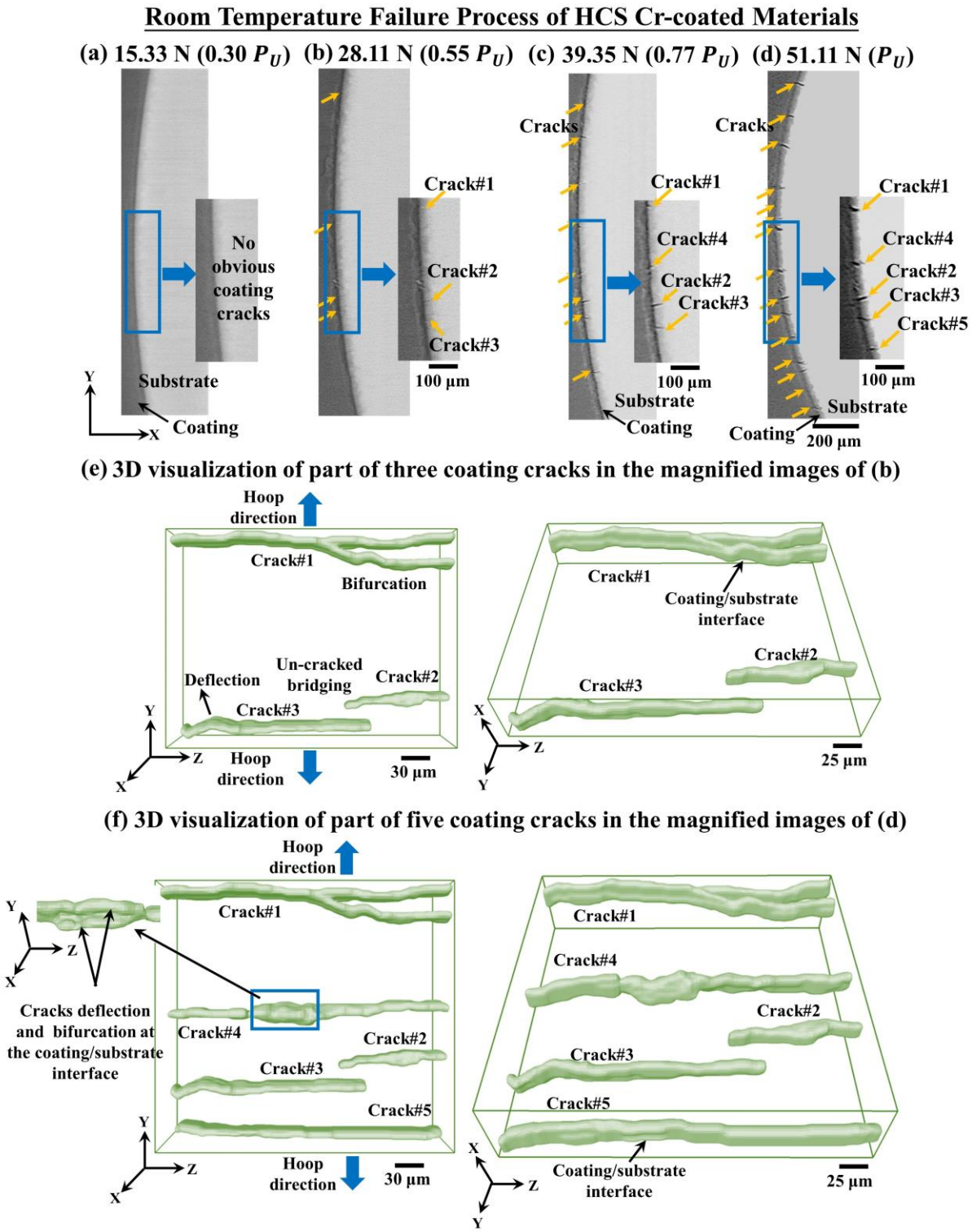

Figure 7-10. (a) to (d) are real-time μXCT slices (X-Y plane) of sample S1 to show the initiation and propagation of the cracks in the HCS materials at RT; magnified images are also included in (a) to (d), which collected from the same location in the sample: (a) scan at 15.33 N (0.30 P_U), (b) scan at 28.11 N (0.55 P_U), (c) scan at 39.35 N (0.77 P_U), and (d) scan collected at peak load 51.11 N (P_U). (e) and (f) are respectively 3D visualization of part of the coating cracks in the magnified images in (b) and (d), respectively.

All coating cracks were observed do not propagate in underlying substrate and arrested at the interface, Fig. 7.10e. These coating cracks were all nearly 90° against the hoop direction, Fig. 7.10e. Once formed, the Crack#1 propagated through the sample' width. and Crack#2 and Crack#3 did not propagate through the sample' width, and un-cracked bridging can be seen at their tips, Fig. 7.10e. Other crack toughening mechanisms, including bifurcation (observed in Crack#1) and deflection (observed in Crack#3) were also observed.

At 0.55 P_U, the average distance between the coating cracks is 343.31 ± 191.40 μm. For another RT sample S2, the simultaneous initiation of these coating cracks was also observed at 0.55 P_U.

From the μXCT at 0.77 P_U (1000.95 MPa, 0.43%) prior to P_U, coating cracks' number were found increased, the formation of Crack#4 was observed in the magnified image in Fig. 7.10c. And the distance between cracks at this loading stage is 102.34 ± 29.33 μm. At P_U (51.11 N; 1299.94 MPa, 0.56%), the distance between these coating cracks further decreased to 74.67 ± 20.19 μm. In the selected range, coating Crack#5 formed, Fig. 7.10d. 3D visualization of these coating cracks revealed, Crack#4 and Crack#5 also propagated through the sample's width, as well as arrested at the coating/substrate interface, Fig. 7.10f.

Fig. 7.11 presented the SEM images, which displays the RT coating crack patterns of HCS materials (using sample S1). These results are consistent with μXCT imaging (Fig. 7.10), coating cracks were found all nearly 90° against the hoop direction, Fig. 7.11a. P-FIB milling was conducted on these cracks to investigate their pathways in the coating, with the FIB-SEM tomography area presented in Fig. 7.11a. The pathways of coating cracks in HCS material were found similar, with one representative example presented in Fig. 7.11b. It can be found coating cracks did not travel to the substrate (arrest at the interface), with some deflection along such interface, Fig. 7.11b. Some un-crack bridging of the cracks in the Cr coating was found, as marked in Fig. 7.11b. Additionally, in the coating, some finer cracks (in a width less than 1 μm) were observed branched out from the main coating crack (Fig. 7.11b).

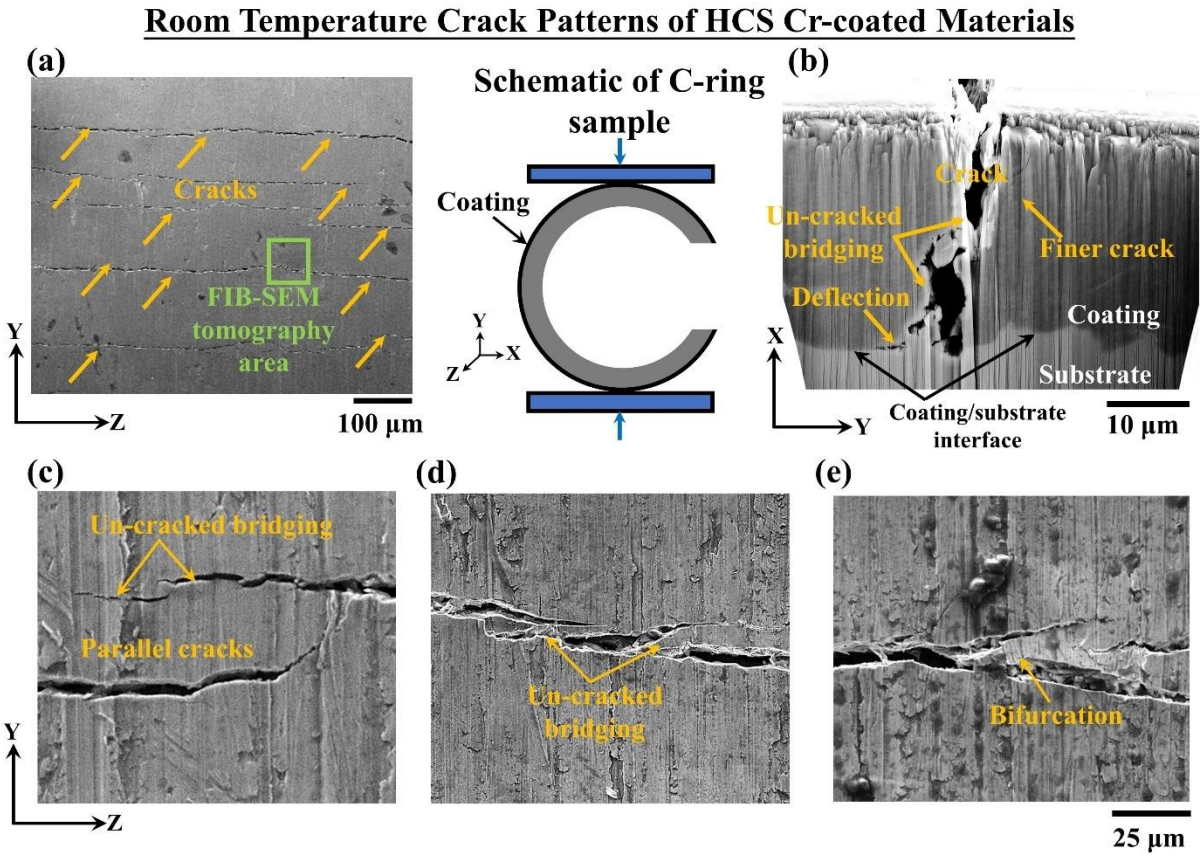

Figure 7-11. SEM images (SE2 mode) showing coating crack patterns of post-tested HCS sample S1 tested at RT: (a) low magnification view of the outer surface of the sample (Y-Z plane); (b) FIB-SEM tomography showing the crack pathways in the Cr coating; (c) to (e) are high magnification views of the outer surface of the sample (Y-Z plane) showing several crack toughening mechanisms. One schematic of C-ring sample with loading is also included.

The width of these finer cracks is lower than the resolution of neither µXCT imaging nor radiography projection and therefore not being observed by these two techniques. Several crack toughening mechanisms were found for these cracks in the coating surface (Y-Z plane), including parallel coating cracks, see Fig. 7.11c, uncracked bridging of the coating cracks, see Figs. 7.11c and 7.11d, and bifurcation of the coating cracks, see Fig. 7.11e. The width of these coating cracks is 1-4 µm. These observations also apply to another HCS sample S2 tested at room temperature.

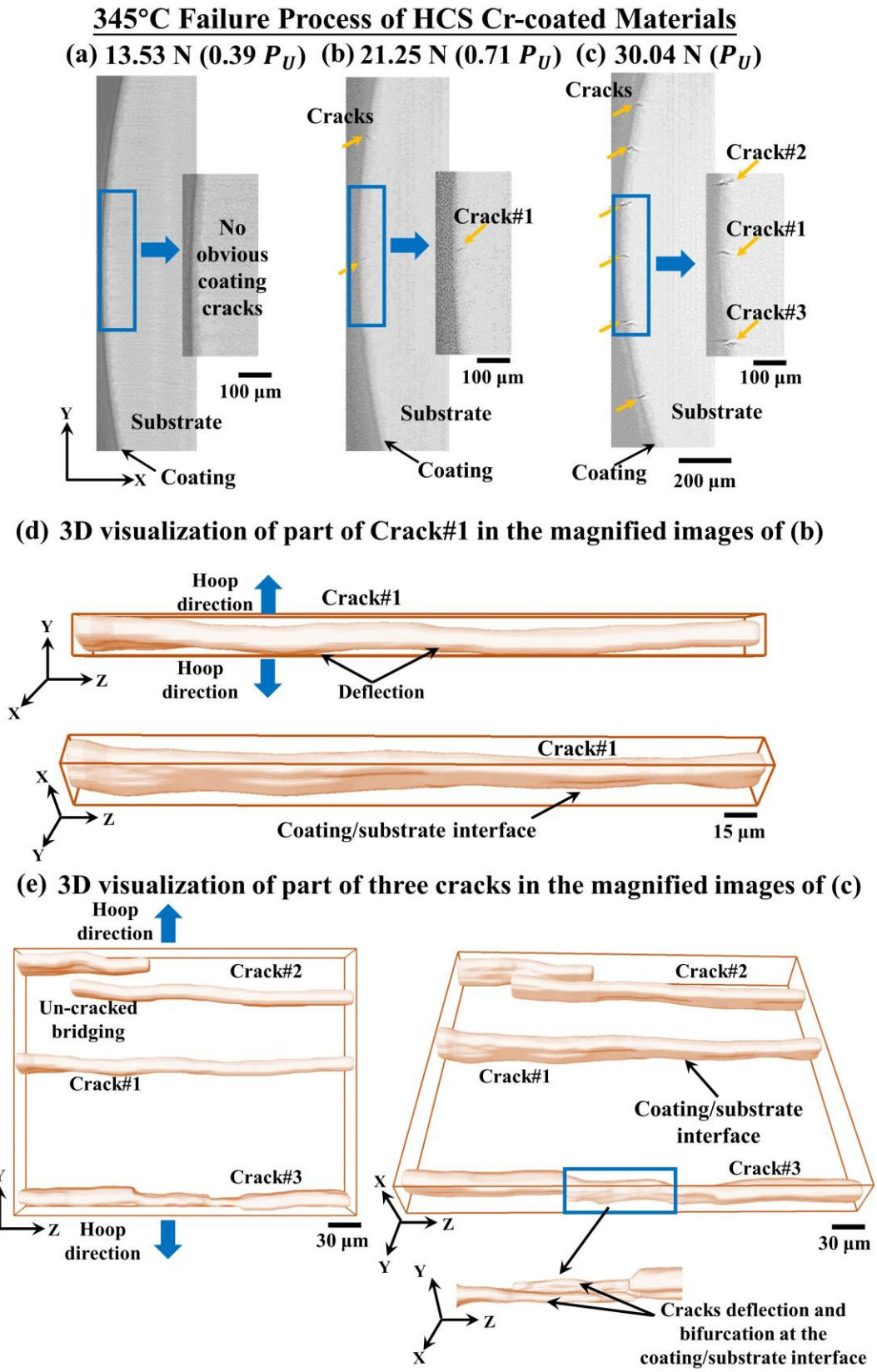

Figure 7-12. (a) to (c) are real-time µXCT slices (X-Y plane) of sample S3 to show the initiation and propagation of the cracks in the HCS Cr-coated materials at 345°C; magnified images are also included in (a) to (c), which collected from the same location in the sample: (a) scan at 13.53 N (0.39 P_U), (b) scan at 21.25 N (0.71 P_U), (c) µXCT scan collected at peak load 30.04 N (P_U). (d) and (e) are respectively 3D visualization of part of the coating cracks in the magnified images in (b) and (c).

For HCS materials tested at 345°C, sample S3 is selected as representative example. No obvious coating cracks were observed from the µXCT scan collected at 0.39 P_U (307.41 MPa, 0.13%), Fig. 7.12a. With the load reaching to 0.71 P_U (583.30 MPa, 0.25%), two coating cracks were observed occurred simultaneously, Fig. 7.12b. Similar behaviours were observed for them, and Crack#1 was chosen as representative example. Fig. 7.12d displays the 3D visualization of part of Crack#1in a length of ~275 µm. Similar to the RT crack behaviour of HCS materials, once formed, Crack#1 travelled across the entire sample's width, and it was also nearly 90° against the hoop direction, Fig. 7.12d. Crack#1 was also found arrested at the interface. The average distance between the coating cracks is 466.81 µm. For another 345°C HCS sample S4, the simultaneous formation of two cracks in the Cr coating was observed at similar loading step: 0.74 P_U.

At P_U (788.24 MPa, 0.34%), coating cracks' number increased (Fig. 7.12c), and the distance between cracks reduced from 466.81 µm to 197.31 ± 61.90 µm. In Fig. 7.12c, the formation of Crack#2 and Crack#3 were observed in the magnified µXCT image. And 3D visualization of them revealed that, un-cracked bridging was found at the tips of Crack#2, and for Crack#3, bifurcation and deflection of the crack along the interface was observed, see Fig. 7.12e. These newly formed cracks were nearly 90° against the hoop direction and arrested at the interface, Fig. 7.12.

Post-tested coating crack patterns of HCS materials tested at 345°C are investigated via SEM imaging, as presented in Fig. 7.13. In the coating surface, cracks were nearly 90° against the hoop direction (Fig. 7.13a). Fig. 7.13b displays the crack pathways in the Cr coating, and cracks were found arrested at the interface, which is consistent with the observations from real-time µXCT slices. Cracks were observed deflected along the boundaries of the boundary between Cr splats, Fig. 7.13b. Similar to the RT crack patterns, finer cracks in Cr coating were found, with examples displayed in Fig. 7.13b. Several crack toughening mechanisms were observed for the cracks in the Cr coating, including parallel cracks (Fig. 7.13c) and uncracked bridging at the tips of cracks (Fig. 7.13d). The width of these coating cracks is ranging from 1-8 µm, which is higher than that at RT (1-4 µm). Note that, some finer tortuous cracks were found at the tips of these large cracks, such coating cracks patterns were only found for 345°C materials.

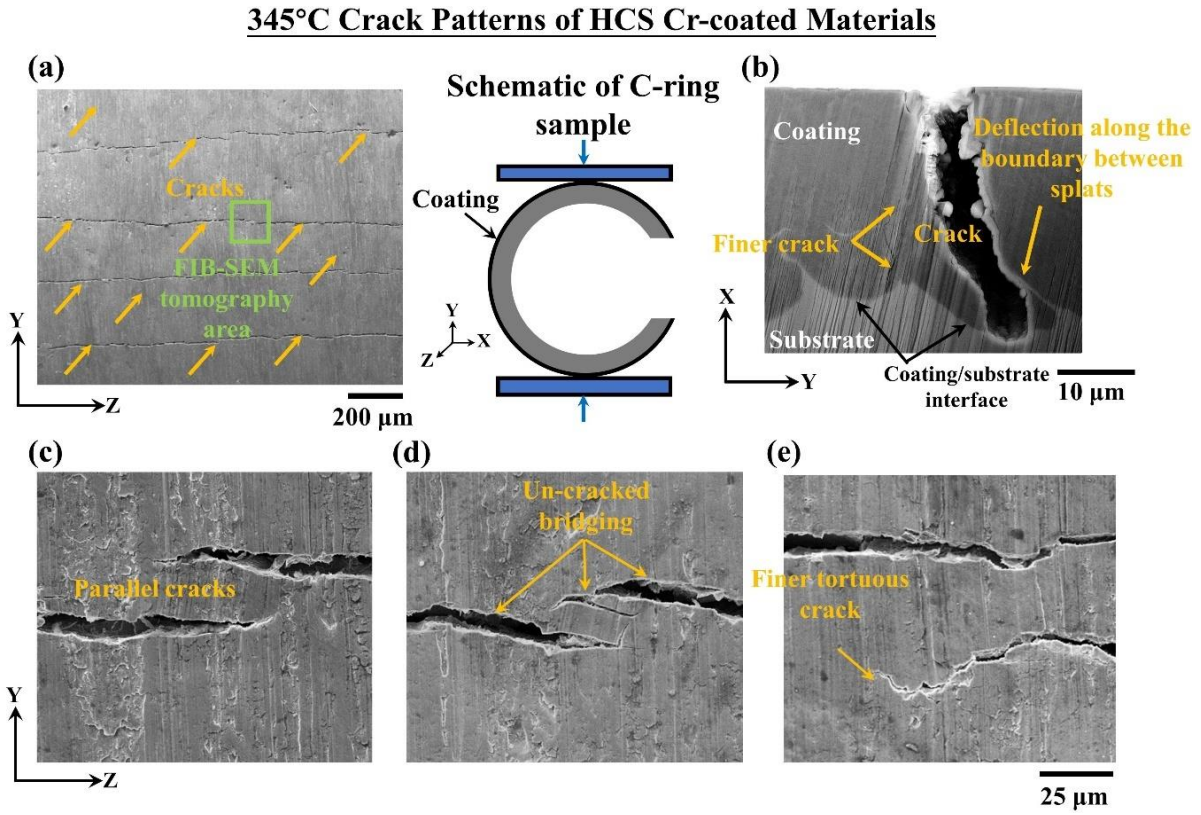

Figure 7-13. SEM images (SE2 mode) showing coating crack patterns of post-tested HCS sample S3 tested at 345°C: (a) low magnification view of the outer surface of the sample (Y-Z plane); (b) FIB-SEM tomography showing the crack pathways in the Cr coating, (c) to (e) are high magnification views of the outer surface of the sample (Y-Z plane) showing several crack toughening mechanisms. One schematic of C-ring sample with loading is also included.

To be summarized, for HCS materials tested at both temperatures, multiple coating cracks were found occur concurrently. At RT, these cracks formed at 0.55 P_U to 0.57 P_U; however, at 345°C, multiple coating cracks were found occur at 0.71 P_U to 0.74 P_U. At both temperatures, once formed, most of the cracks in the Cr coating travelled through the sample's width, coating cracks' number increased with the increasing of the loading; and the coating cracks' number at 345°C are much smaller than at RT. At both temperatures, cracks all arrested along the coating/substrate interface, and crack deflection along such interface was found. In the surface of the C-ring sample, these cracks are nearly 90° against the hoop direction at both temperatures, and the width of these cracks were 1–4 µm at RT, and 1–8 µm at 345°C. Note that, the finer tortuous cracks at tip of primary cracks were only observed at 345°C. Lastly, no spallation of the coating was observed at either room temperature or 345°C.

7.5.2. NCS Cr-coated materials

For NCS materials tested at room temperature, sample S5 is used as representative example to illustrate the failure process of the NCS cladding materials. No obvious coating cracks were observed at 0.28 P_U (486.24 MPa, 0.24%), Fig. 7.14a. With further increasing of load to 0.58

P_U (1007.21 MPa, 0.50%), the simultaneously formation of three coating cracks were observed, Fig. 7.14b. Similar behaviour was found for them, and two cracks (Crack#1 and Crack#2) in the magnified image were segmented out and part of them (a selected length of ~310 μm, ~14% of the C-ring sample's width: ~2.19 mm) were visualized in 3D, as displayed in Fig. 7.14e. It can be found that, Crack#1 stopped in the Cr coating; while Crack#2 propagated across the sample's width. These cracks in the Cr coating arrested at the interface, Fig. 7.14e. At this loading step, the distance between these cracks was 215.49 ± 120.31 μm. For another room temperature NCS sample S6, the simultaneous initiation of multiple cracks in the Cr coating was also observed at 0.57 P_U.

With further loading, from the μXCT scan at 0.82 P_U (1423.99 MPa, 0.70%), one new crack (Crack#3) was found in the magnified μXCT image, Fig. 7.14c. The average distance between the coating cracks reduced to 111.75 ± 28.89 μm. At P_U (1736.57 MPa, 0.86%), number of cracks in the Cr coating further increased, with another newly formed crack Crack#4 being found in the magnified μXCT image, as presented in Fig. 7.14d. 3D visualization of these coating cracks revealed they arrested at the interface; un-cracked bridging occurred at the tips of Crack#3, Crack#4 travelled through the C-ring sample's width, Fig. 7.14f. Additionally, for the coating Crack#4, bifurcation and deflection of such crack along the interface is observed, as presented in Fig. 7.14f. The distance cracks reduced to 48.13 ± 22.31 μm.

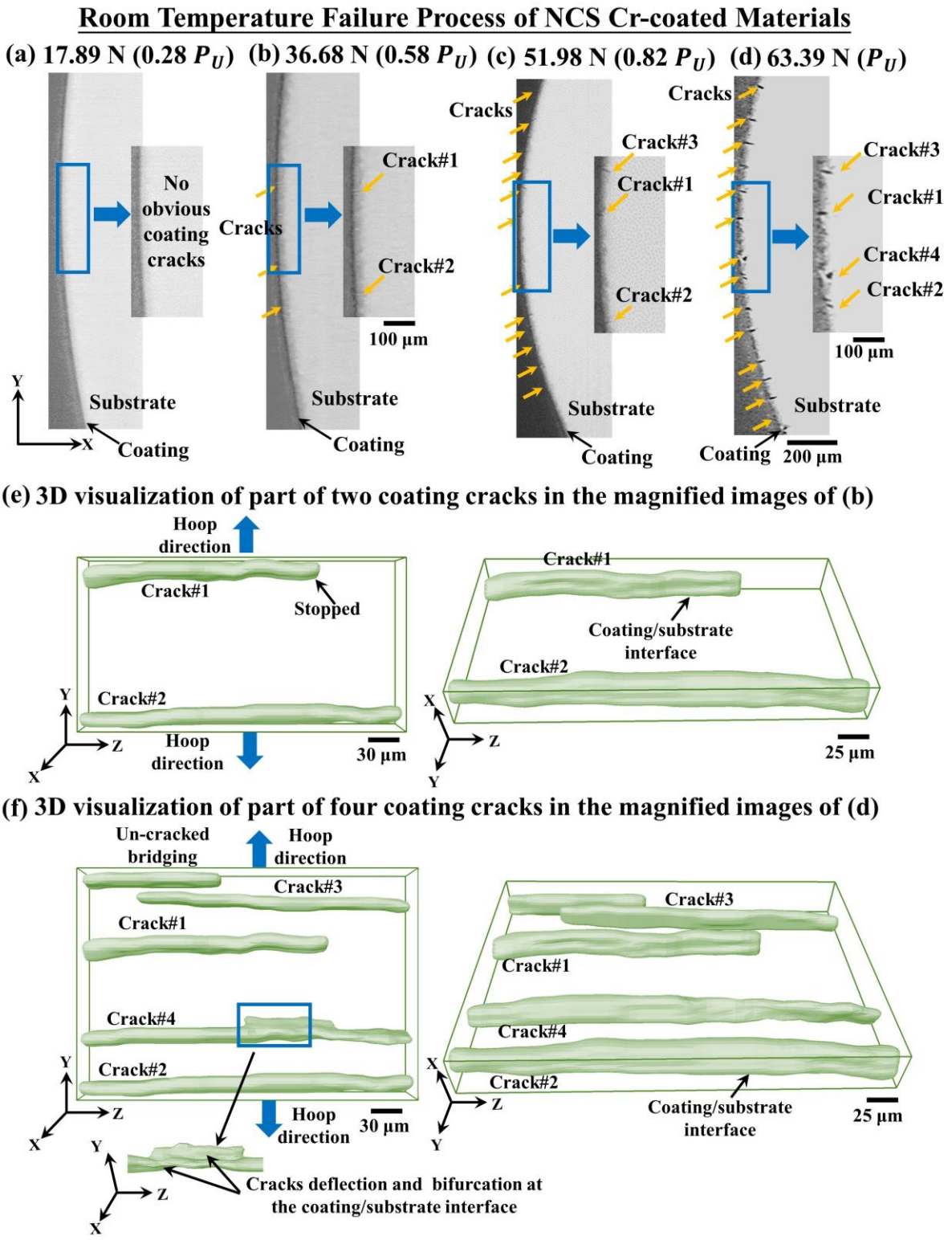

Figure 7-14. (a) to (d) are real-time µXCT slices (X-Y plane) of sample S5 to show the initiation and propagation of the cracks in the NCS Cr-coated materials at RT; magnified images are also included in (a) to (d), which collected from the same location in the sample: (a) scan at 17.89 N (0.28 P_U), (b) scan at 36.68 N (0.58 P_U), (c) µXCT scan collected at 51.98 N (0.82 P_U), and (d) µXCT scan collected at peak load 63.39 N (P_U). (e) and (f) are respectively 3D visualization of part of the coating cracks in the magnified images in (b) and (d).

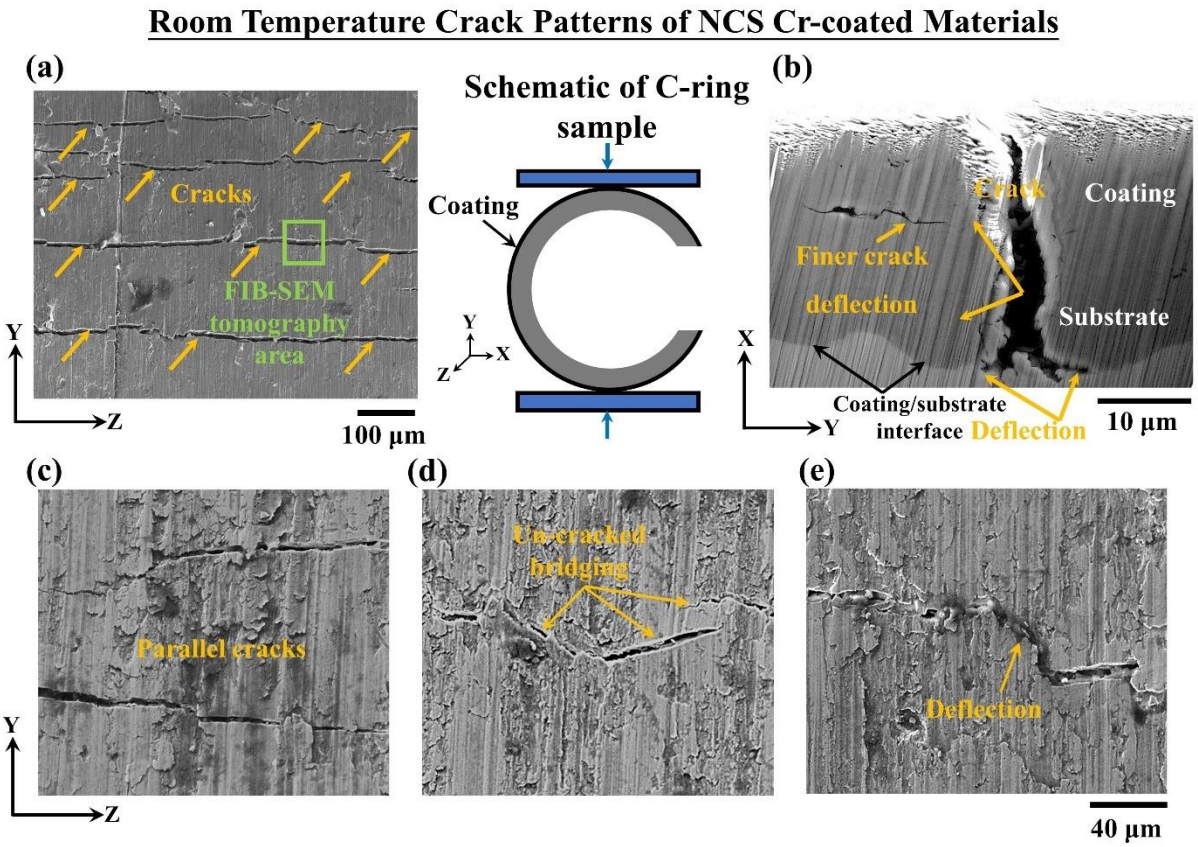

Figure 7-15. SEM images (SE2 mode) showing coating crack patterns of post-tested NCS sample S5 tested at RT: (a) low magnification view of the outer surface of the sample (Y-Z plane); (b) FIB-SEM tomography showing the crack pathways in the Cr coating; (c) to (e) are high magnification views of the outer surface of the sample (Y-Z plane) showing several crack toughening mechanisms. One schematic of C-ring sample with loading is also included.

NCS sample S5 is used as representative example to present the coating crack patterns of NCS materials tested at RT, with the results presented in Fig. 7.15. On the surface of the C-ring sample, cracks were found almost perpendicular to the hoop direction, see Fig. 7.15a, which is in consistency with the observations by imaging (Fig. 7.14). The pathways of cracks in NCS coating can be seen in Fig. 7.15b, where cracks arrested at the interface, some crack deflection along such interface being observed. Similar to the HCS cladding materials at RT, finer cracks (in a width around 1 μm) were also found in the NCS coating, with deflection in the coating, Fig. 7.15b. For cracks in the C-ring sample's surface, some cracking toughening mechanisms can be seen, which include: parallel cracks, as presented in Fig. 7.15c, uncracked bridging, as presented in Fig. 7.15d and deflection, as presented in Fig. 7.15e. Similar to the patterns of coating cracks in RT HCS claddings, the width of coating cracks of NCS materials was also in the range of 1-4 μm. Consistent observations were also found for the room temperature sample S6 of the NCS cladding materials.

For the NCS materials tested at 345°C, the sample S7 is served as representative example. The µXCT scan collected at 0.48 P_U (476.91 MPa, 0.22%) showed no obvious cracks in the coating, Fig. 7.16a. With further loading, the scan collected at 0.73 P_U (680.48 MPa, 0.33%) revealed the simultaneously formation of two coating cracks, Fig. 7.16b. These two cracks were found have similar behaviour, and one of them (Crack#1) was segmented out and visualized in 3D (around 290 µm of the selected length), as presented in Fig. 7.16e. This Crack#1 was found travelled across the sample's width, and arrested at interface. Additionally, crack deflection in coating Crack#1 was also observed, Fig. 7.16e. The distance between these two cracks was 454.92 µm. For another 345°C NCS sample S8, the concurrent formation of two cracks in the coating was also found at similar loading step: 0.73 P_U.

Further increasing of load led to the initiation and formation of more cracks in the coating, with one new crack (Crack#2) occurred in the magnified image, see the µXCT scan collected at 0.80 P_U (794.85 MPa, 0.37%), Fig. 7.16c. The distance between cracks in the coating was 215.14 ± 56.99 µm. The last µXCT scan was collected at P_U (993.56 MPa, 0.46%), another newly formed crack (Crack#3) occur in the magnified image, Fig. 7.16d. 3D visualization of Crack#1 to Crack#3 in the magnified image revealed Crack#2 did not travel across C-ring sample's width, as can be seen in Fig. 7.16f. Crack#3 was found travelled across C-ring sample's width, with bifurcation and deflection along interface being observed, Fig. 7.16f. The distance between cracks in the coating reduced to 169.81 ± 54.47 µm.

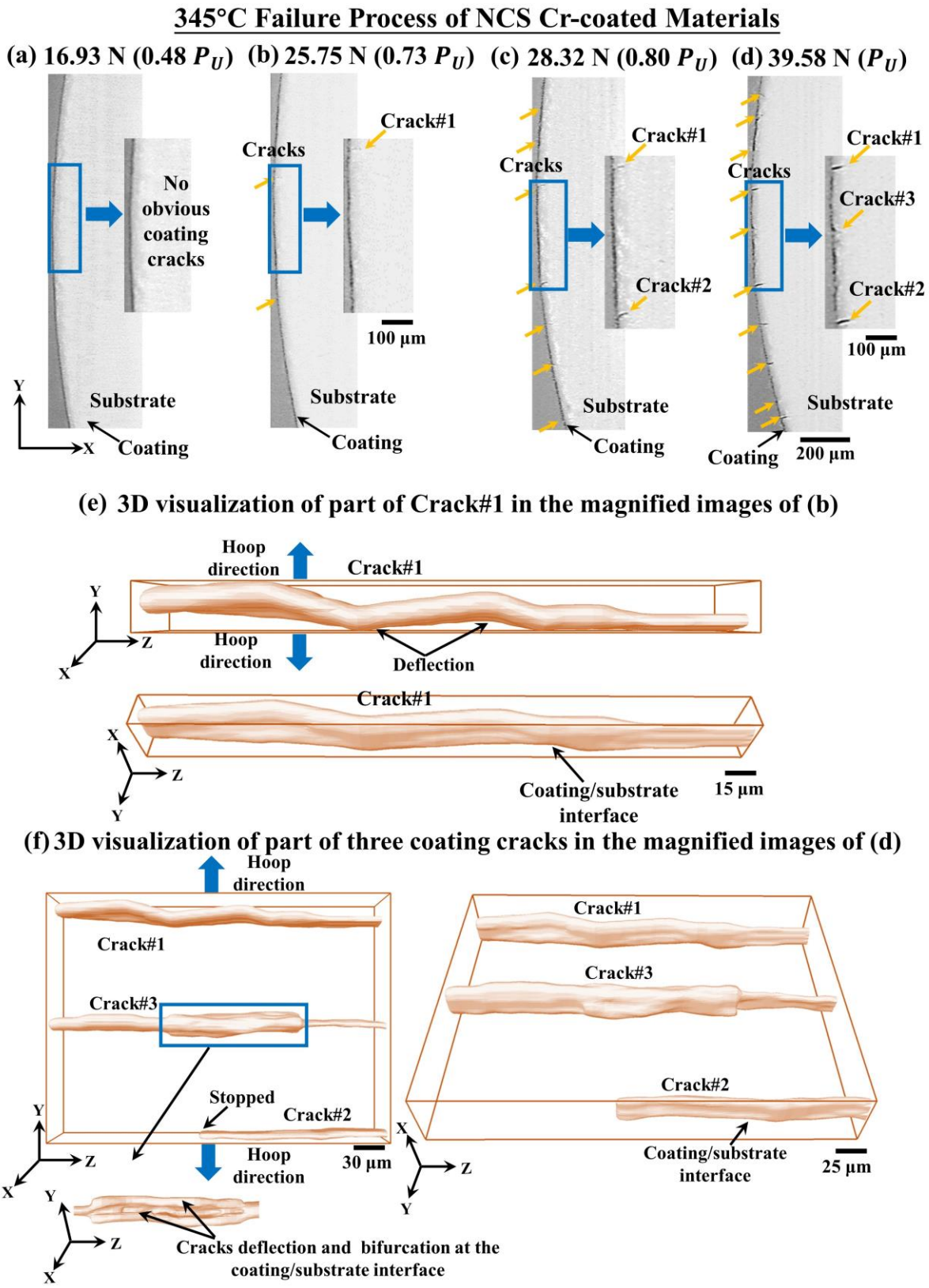

Figure 7-16. (a) to (d) are real-time µXCT slices (X-Y plane) of sample S7 to show the initiation and propagation of the cracks in the NCS materials at 345°C; magnified images are also included in (a) to (d), which collected from the same location in the sample: (a) scan at 0.48 P_U, (b) scan at 0.73 P_U, (c) µXCT scan collected at 0.80 P_U, and (d) µXCT scan collected at peak load. (e) and (f) are respectively 3D visualization of part of the coating cracks in the magnified images in (b) and (d).

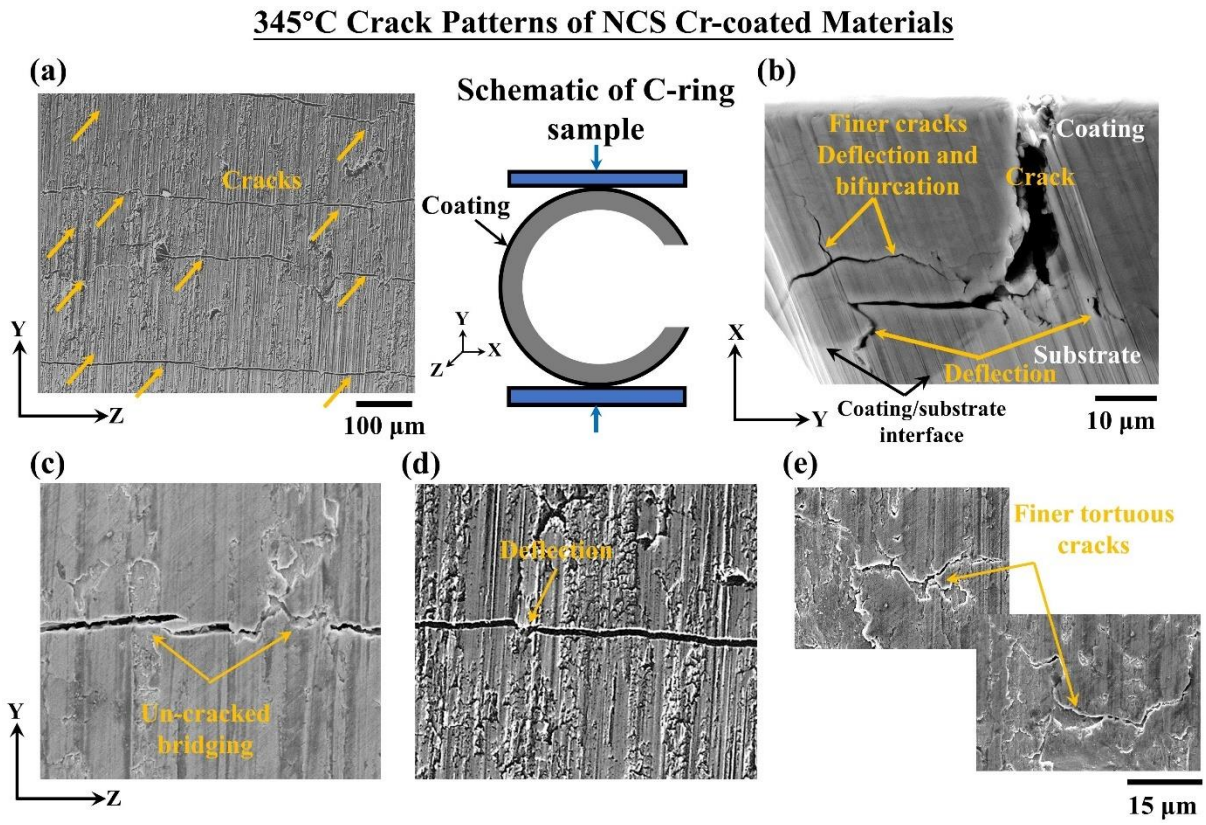

Figure 7-17. SEM images (SE2 mode) showing coating crack patterns of post-tested NCS sample S7 tested at 345°C: (a) low magnification view of the outer surface of the sample (Y-Z plane; (b) FIB-SEM tomography showing the crack pathways in the Cr coating; (c) to (e) are high magnification views of the outer surface of the sample (Y-Z plane) showing several crack toughening mechanisms. One schematic of C-ring sample with loading is also included.

Fig. 7.17 presents the patterns of coating cracks of NCS claddings at 345°C. Similar as patterns of RT coating cracks of NCS claddings, the coating cracks formed at 345°C has also been observed nearly 90° against the hoop direction, as presented in Fig. 7.17a. These cracks were observed arrested at interface, with some deflection along such interface, Fig. 7.17b. Finer cracks (in a width of 1 µm to 2 µm) in the coating were also observed, with deflection and bifurcation in the coating, Fig. 7.17b. Several crack toughening mechanisms were found, which include uncracked bridging (Fig. 7.17c) and deflection (Fig. 7.17d). The width of cracks in the coating was 1-4 µm (similar to RT tests). Similar to HCS claddings at 345°C, some finer tortuous cracks at crack tips of the primary cracks were observed, Fig. 7.17e.

In summary, for NCS cladding materials tested at both RT and 345°C, multiple cracks in the Cr coatings were observed formed concurrently. At RT, these cracks formed at ~57% of the peak load; however, at higher testing temperature (345°C), cracks in the Cr coatings formed at a higher percentage of the peak load (72% to 73%). At both temperatures, number of cracks in the coating increased with increasing loading, with less cracks found at 345°C. At both temperatures, cracks in the Cr coating were all found arrested at the interface, and propagated

nearly 90° against the hoop direction; with some finer tortuous cracks at crack tips only observed at 345°C. No coating spallation was found at either RT or 345°C.

7.6. Interfacial toughness and interfacial failure modes of HCS and NCS materials

In current Chapter, for both HCS and NCS materials tested at both temperatures, cracks in the Cr coatings were all found arrested at the coating/substrate interface, with some single-side deflection (Fig. 7.11b) and double-side deflection (Fig. 7.15b) being observed along such interface. As described in Section 6.5.3, He and Hutchinson method based on first Dundurs' parameter (α) [344], [345] can be used for estimating interfacial toughness or strain (G_{ic}, including single-side deflection of crack and double-side deflection crack) of both HCS and NCS materials tested at RT. The measured elastic modulus and hardness in Area#2 and Area#3 of HCS and NCS are used to determine the first Dundurs' parameter (α). By using Eq. 6.1, the α for HCS and NCS materials are estimated to be -0.31 and -0.28, respectively. As described in Section 6.5.3, the mode I stress-intensity factor (K_{Ic}) at RT: 101.1 MPa/m^2 [346] is inputting in Eq. 6.3 to calculate the critical strain energy release rate (G_{Ic}) of both HCS and NCS materials. Finally, the upper-bound of interfacial toughness (G_{ic}) were estimated, with detailed data points presented in Table 7.3.

Table 7-3. Calculated first Dundurs' parameter (α), critical strain energy release rate (G_{Ic}) and upper bound of the interfacial toughness (G_{ic}) for the situations of singly and doubly deflected interfacial cracks of both HCS and NCS Cr-coated materials tested at RT.

Deflection types	**HCS material**			**NCS material**		
	α	G_{Ic} (J/m^2)	G_{ic} (J/m^2)	α	G_{Ic} (J/m^2)	G_{ic} (J/m^2)
Singly deflected cracks	-0.31	95.71	22.11	-0.28	93.14	21.52
Doubly deflected cracks			10.91			11.46

For NCS cladding materials at RT, compared with the HCS materials, a 2.7% lower G_{ic} for singly deflected cracks (21.52 J/m^2), as well as a 5.0% higher G_{ic} for singly deflected cracks (11.46 J/m^2) are measured.

7.7. Discussion

7.7.1. Local properties and residual stresses of HCS and NCS materials

As described in Section 7.2, different local properties were measured for the HCS and NCS Cr-coated materials. Specifically, in Area #1 (middle of the coating), compared with the H (~4.77 GPa) and E (~200.82 GPa) of NCS materials, the HCS materials have a 11.5% lower H (~4.22 GPa) and a 14.7% higher E (~230.32 GPa). Additionally, compared with the H (~4.49 GPa) and E (~266.06 GPa) of Area #1 of CS materials in Chapter 6, HCS materials have 6.0% lower H and 13.4% lower E. And NCS materials have 6.2% higher H and 24.5% lower E. These were caused by the differences CS manufacturing parameters of these materials [356].

It has been reported that, the variation of CS manufacturing parameters (*e.g.*, gas pressure and temperature, stand-off-distance) could affect the impacting velocity of the particles [93], [94], which consequently affects the bonding strength of the particles in the Cr coating. The poorly bonded particles in the CS Cr coating could result in higher porosity level in the coating, and consequently leads to lower hardness and elastic modulus [357]. Additionally, the impacting velocity of the particles could show influence on the level of plastic deformation of these particles; and a higher plastic deformation commonly results in a increasing in hardness [358]. Moreover, the increasing of the impacting velocity of the particles could enhance the shot peening effect (particles rebounding off the surface and impacted with following particles), and consequently results in a more dense coating with enhanced hardness [359]–[361]. Therefore, in order to acquire specific local properties of the CS Cr coatings, the application of specific manufacturing parameters is imperative.

Compared with the RT interfacial toughness of CS materials in Chapter 6, different values were estimated for HCS and NCS materials in current Chapter. Specially, for HCS materials, the interfacial toughness for singly (22.11 J/m^2) and doubly (10.91 J/m^2) deflected cracks are 1.3% and 2.6% lower than the CS materials, respectively. And for NCS materials, the interfacial toughness for singly (21.52 J/m^2) and doubly (11.46 J/m^2) deflected cracks are 3.9% lower and 2.3% higher than the CS materials, respectively. These are also caused by the variation of CS manufacturing parameters of these CS materials, which affect the bonding strength between particles and underlying substrate [78], and consequently affect the interfacial toughness.

For both HCS and NCS materials, compressive residual stresses were measured in the Cr: ~250 MPa and ~360 MPa, respectively. This is consistent with the open literatures, as compressive residual stresses are widely reported in various types of CS coatings due to the peening effect

[362]–[364]. The variations of residual stress in the coating could also be affected by the variations of CS manufacturing parameters, including: gas pressure, gas temperature, particle velocity, powder feed rate and spray angle [97]. Additionally, as described in Section 7.3, NCS Cr coating has a 36% higher compressive residual stress than the HCS Cr coating. Such variation could potentially affect the coating failure strengths, strains, and coating crack patterns of the HCS and NCS materials, as will be discussed in the following section.

7.7.2. Hoop strength and strain of initiation of coating cracks

As described in Section 7.4, the estimated maximum hoop strengths of HCS and NCS materials at both temperatures could be overestimated, due to the large deformation of C-ring samples. Therefore, a more prudent approach would involve the comparison of hoop strengths observed during the initial occurrence of coating cracks in both HCS and NCS materials.

Compared with such strength and strain of first formation of cracks in the Cr coatings of CS materials in Chapter 6, HCS materials have 27.5% lower strength and 15.8% strain at RT; 3.9% higher strength and 18.2% higher strain at 345°C. For NCS materials, in comparison of CS materials (in Chapter 6), they have similar strength and 31.6% higher strain at RT; 19.5% higher strength and 54.5% higher strain at 345°C. Such variations could be caused by the variations of CS manufacturing parameters for these materials [93], [94], which subsequently affect the microstructures, local properties, residual stresses and bonding strengths of the Cr coatings, and consequently affect the hoop strengths of the coatings. Such variation could also affect the failure processes and coating crack patterns of these materials, as will be discussed in Section 7.7.3. Moreover, as discussed in Section 6.5.3, the variation in surface roughness of these materials could potentially affect the initiation of coating cracks. Therefore, future work will be conducted on the investigation of surface roughness of these materials.

As discussed in Section 6.5.6, during handling the HCS and NCS Cr-coated materials, as well as fixed them by the grid assembly in the reactors, stresses could be introduced to them is various directions. Based on the observations in current Chapter, for preventing the initiation and formation of cracks in the Cr coating during such processes, the strain in the hoop direction for HCS materials should be less than 0.32% and 0.26% at RT and 345°C, respectively. And such strain should be less than 0.50% and 0.34% at RT and 345°C for NCS materials, respectively.

7.7.3. Failure processes and coating crack patterns at RT and 345°C

For HCS and NCS materials tested at RT and 345°C, the distance between coating cracks, crack density (number of cracks per area), and corresponding hoop strain are summarized in Table 7.4.

Table 7-4. Distance between the coating cracks, crack density and corresponding hoop strain at different loading steps of HCS and NCS materials tested at RT and 345°C.

Materials	Temperature	Loading stage	Distance between coating cracks (μm)	Crack density (#/μm^2)	Hoop strain
HCS	RT	0.55 P_U	343.31 ± 191.40	0.002	0.31%
		0.77 P_U	102.34 ± 29.33	0.007	0.43%
		P_U	74.67 ± 20.19	0.009	0.56%
	345°C	0.71 P_U	466.81	0.001	0.25%
		P_U	197.31 ± 61.90	0.005	0.34%
NCS	RT	0.58 P_U	215.49 ± 120.31	0.005	0.50%
		0.82 P_U	111.75 ± 28.89	0.007	0.70%
		P_U	48.13 ± 22.31	0.012	0.86%
	345°C	0.73 P_U	454.92	0.001	0.33%
		0.80 P_U	215.14 ± 56.99	0.005	0.37%
		P_U	169.81 ± 54.47	0.006	0.46%

For HCS and NCS materials at room temperature, similar failure processes were found, as can be divided into three steps: (i) the initial deformation stage without formation and initiation of cracks in the Cr coatings; (ii) multiple cracks formed at 55% to 58% of the peak load, and these cracks propagated nearly 90° to the hoop direction; (iii) with increasing of load, number of the cracks in the Cr coatings increased; and distances between them at peak load reached to ~22% of that at the stage of the first formation of cracks in the Cr coating. However, as discussed in Section 7.7.2, the hoop strength and strain at the initiation of coating cracks of NCS materials are higher than the HCS material.

Furthermore, when comparing the distances between coating cracks in HCS materials at the initiation stage of coating cracks and at peak load, NCS materials exhibited approximately a 37.2% decrease and a 35.5% decrease, respectively. This could be attributed to the higher magnitude of compressive residual stress in NCS Cr coating (360 MPa) compared to HCS Cr coating (250 MPa). As suggested by Liu *et al.* [180], the increasing of compressive residual

stress in the SiC layers in TRISO particles could increase their failure strains. Therefore, the higher compressive residual stress in NCS Cr coating could potentially enhance its resistance for the initiation and development of cracks in the Cr coating, subsequently increases its strength at the first formation of cracks in the Cr coating, and increase the coating cracks number to prevent the emergence of large fatal coating cracks.

Furthermore, the RT failure processes of HCS and NCS materials were different from the CS materials in Chapter 6, as the formation of cracks in the Cr coatings occurred at 0.90 P_U and 0.41% hoop strain. Additionally, once formed, the distance between cracks in the Cr coatings of CS materials is 98.89 ± 34.71 μm (0.007/ μm^2 of crack density), which is 28.8% and 45.9% of that of HCS (343.31 ± 191.40 μm; 0.002/ μm^2) and NCS materials (215.49 ± 120.31 μm; 0.005/ μm^2), respectively. Such variations could also be attributed to the different CS manufacturing parameters of these materials, which lead to the variation of microstructures, porosity and particle bonding strengths of the Cr coatings, and consequently result in different failure processes [8].

The failure processes for the HCS and NCS materials tested at 345°C were similar, as can be divided into three steps: (i) the initial deformation stage with no observation of the coating cracks' formation; (ii) two cracks in the Cr coatings formed at 0.71 P_U to 0.74 P_U, with nearly 90° to the hoop direction; (iii) with increasing of loading, the distances between cracks in the Cr coating at P_U reached to ~40% of that at the stage of the first formation of cracks in the Cr coatings. Such observations are different from the CS materials tested at 345°C in Chapter 6: the first formation of finer tortuous cracks, and the subsequent formation of two or three primary coating cracks. These finer tortuous cracks were only observed at some cracks' tips of the HCS and NCS materials tested at 345°C, Figs. 7.12 and 7.16.

As discussed in Section 6.5.5.1, such finer tortuous cracks could be caused by the thermal expansion mismatch of coating and substrate, which creates a multi-dimensional stress-state in the Cr coating at elevated temperatures [53]. However, due to the different manufacturing parameters, the microstructures, local properties and bonding strengths of HCS and NCS Cr coatings are from that of CS Cr coating iin Chapter 6. Such variation could lead to quite different thermal expansion coefficients of HCS, NCS and CS (Chapter 6) Cr coatings (as that of Cr ranging from 4.9 to 8.2 × 10^{-6}/°C [347], [348]). Therefore, the generated multi-dimensional stresses in HCS and NCS Cr coatings at 345°C could be quite smaller than that in CS Cr coatings in Chapter 6, as well as much smaller when compared with the hoop tensile

stress in the HCS and NCS Cr coatings during the C-ring compression loading. Therefore, for the HCS and NCS materials tested at 345°C in current Chapter, the thermal expansion mismatch of Cr and substrate showed less influences on the failure of the coatings when compared to the dominant tensile hoop stresses.

These findings imply that variations in the manufacturing parameters of the process can yield diverse properties and failure processes of Cr coatings, even when subjected to identical testing temperatures. Therefore, it is not right to assume the identical failure processes observed in a specific material will also be applied to all others. Moreover, the observations in current Chapter are significant important for accurately modelling of the mechanical performances and failure processes of such CS Cr-coated zircaloy claddings.

7.8. Conclusion

The differences in the manufacturing parameters of HCS and NCS Cr-coated materials in current Chapter result in their different local properties: in the middle of Cr coating, HCS material exhibit a 11.5% lower hardness and 14.7% higher elastic modulus. Such variations also result in the differences in interfacial toughness of these materials, with 2.7% lower and 5.0% higher interfacial toughness measured for NCS materials for singly deflected and doubly deflected cracks, respectively.

Compressive residual stresses were measured in both HCS and NCS Cr coatings, with NCS materials has a 36% higher stress. Such higher residual stress in NCS Cr coatings could be attributed to the higher strength at the first formation of cracks in the Cr coating and lower coating crack number at both temperatures, as well as enhancing the resistance of the initiation and formation of large cracks in the Cr coating.

For HCS and NCS cladding materials, the hoop strength at the first formation of cracks in the Cr coating at 345°C were 18% and 31% lower than at RT. Additionally, at the same testing temperatures, a higher hoop strength at the first formation of cracks in the Cr coating was found in the NCS cladding materials, with respectively 38% (RT) and 15% (345°C) higher than that of the HCS materials.

The failure processes and crack patterns of both HCS and NCS cladding materials were studied. At the same testing temperatures, similar failure processes were observed for HCS and NCS materials. At room temperature, multiple cracks in the Cr coating formed at 0.55 P_U to 0.58 P_U, and coating crack number increased with increasing of load; at 345°C, two cracks in the Cr coating formed at 0.71 P_U to 0.74 P_U, and the distance between cracks in the Cr coatings

decreased with further loading. At the same testing temperatures, NCS materials have a smaller crack density. Note that, these failure processes are all different with that of CS materials investigated in Chapter 6.

For both HCS and NCS materials at RT and 345°C, cracks in the Cr coating arrested at the coating/substrate interface without propagation into the underlying substrate. At both temperatures, all the cracks in the Cr coatings of HCS and NCS materials formed nearly 90° to the hoop direction; with some finer tortuous cracks at cracks' tips only observed at 345°C. The patterns of coating cracks of HCS and NCS materials at 345°C were significant different with that of CS materials in Chapter 6. Which could be caused by the variation of stress-states in the coating of these materials, caused by the differences in the manufacturing parameters of these materials.

In summary, the different manufacturing parameters of HCS and NCS materials result in differences in local properties, interfacial toughness, residual stresses, as well as mechanical performances and coating crack patterns under C-ring compression loading. Additionally, the properties mentioned above are all different with that of CS materials investigated in Chapter 6 under same testing conditions; and a detailed comparison of these data points tabulated in Table 7.5.

Table 7-5. Summary of the different properties of HCS and NCS Cr-coated materials (in current Chapter), as well as CS Cr-coated materials (in Chapter 6) tested at both RT and 345°C.

Properties		**HCS materials**	**NCS materials**	**CS materials**
Area of Cr grain in the coating	-	0.16 ± 0.31 μm^2	0.18± 0.36 μm^2	0.16 ± 0.42 μm^2
Local properties of as-received materials (GPa)	Area#1	4.22 of H; 230.32 of E	4.77 of H; 200.82 of E	4.49 of H; 266.06 of E
	Area#2	3.75 of H; 213.59 of E	3.73 of H; 203.81 of E	3.79 of H; 249.47 of E
	Area#3	3.08 of H; 106.79 of E	3.06 of H; 109.74 of E	3.02 of H; 109.53 of E
	Area#4	2.66 of H; 104.85 of E	2.67 of H; 104.34 of E	2.62 of H; 105.61 of E
Compressive residual stress (MPa)	-	~250	~360	-
First Dundurs' parameter (α)	Singly deflected cracks Doubly deflected cracks	-0.31	-0.28	-0.37
Interfacial toughness G_{ic} (J/m^2)	Singly deflected cracks	22.11	21.52	22.39
	Doubly deflected cracks	10.91	11.46	11.20
Hoop strength and strain at the initiation of coating cracks	RT	~740 MPa/0.32%	~1018 MPa/0.50%	~1020 MPa/0.41%
	345°C	~607 MPa/0.26%	~698 MPa/0.34%	~584 MPa/0.22%
Maximum hoop stresses and strain	RT	~1322 MPa/0.57%	~1771 MPa/0.87%	~1168 MPa/0.45%
	345°C	~820 MPa/0.35%	~963 MPa/0.47%	~649 MPa/0.25%
Distance between coating cracks at the first initiation of coating cracks (μm)	RT	343.31 ± 191.40	215.49 ± 120.31	98.89 ± 34.71
	345°C	466.81	454.92	334.67 ± 154.31
Distance between coating cracks at peak load (μm)	RT	74.67 ± 20.19	48.13 ± 22.13	58.38 ± 17.21
	345°C	197.31 ± 61.90	169.81 ± 54.47	314.89 ± 141.77

8. Conclusions

This PhD project was motivated by the two distinct sets of research problems outlined in the literature review Chapter. The conclusions from current Chapter have been published in Materials & Design during the PhD project. The current Chapter contains minor additions and modifications compared to the published article by Yuan *et al.* [14]. Guanjie Yuan: Investigation, Formal analysis, Data curation, Writing – original draft, Writing – review & editing; J. Paul Forna-Kreutzer: Experiments; Peng Xu: Resources; Sean Gonderman: Resources, Review & editing; Christian Deck: Resources, Review & editing; Luke Olson: Resources, Review & editing; Edward Lahoda: Resources, Review & editing; Robert O. Ritchie: Resources, Funding acquisition, Supervision, Writing – review & editing; Dong Liu: Conceptualization, Resources, Methodology, Funding acquisition, Supervision, Writing – review & editing. The current Chapter also contains minor additions and modifications compared to the published article by Yuan *et al.* [1]. Guanjie Yuan: Investigation, Formal analysis, Data curation, Writing – original draft, Writing – review & editing; J. Paul Forna-Kreutzer: Experiments; Jon Ell: Experiments; Harold Barnard: Resources, Review & editing; Benjamin R. Maier: Resources, Review & editing; Edward Lahoda: Resources, Review & editing; Jorie Walters: Resources, Review & editing; Robert O. Ritchie: Resources, Funding acquisition, Supervision, Writing – review & editing; Dong Liu: Conceptualization, Resources, Methodology, Funding acquisition, Supervision, Writing – review & editing.

The first question was primarily focused on establishing a thorough comprehension of the relationship between the microstructures, local properties, residual stress distributions, and the mechanical properties and failure processes at both RT and 1200°C of the nuclear-grade SiC_f-SiC_m cladding materials. By using the high-temperature C-ring compression tests combined with real-time μXCT, two types of materials were investigated.

The second set of the research question was aimed at understanding the relationship between manufacturing methods, microstructures, local properties, residual stress in the coating, and the mechanical behaviours, failure processes and coating crack patterns of nuclear-grade Cr-coated zircaloy-4 cladding materials with temperatures. By using the high-temperature C-ring compression tests with *in-situ* μXCT, four types of materials were investigated.

For the as-received SiC_f-SiC_m cladding material with single-layer outer/inner SiC coatings, the hardness and elastic modulus of the SiC fibre are lower than the other individual components (SiC coatings, SiC matrix) in the materials. This is caused by the presence of residual carbon

phase in the SiC fibre. Compared to the materials tested at RT, enhanced maximum hoop strength of the entire composite materials and increased failure strain in the outer SiC coating were estimated at 1200°C. These suggest room temperature tests can be potentially used as a conservative estimate of the high temperature performance for the SiC_f-SiC_m cladding materials. Residual stress mapping using Raman spectroscopy revealed a relatively tensile residual stress in the outer SiC coating at room temperature. The relaxation of such tensile stress at 1200°C may potentially contribute to the observed higher failure strain of the outer coating at 1200°C. Distinct failure processes were observed at RT and 1200°C. At both testing temperatures, the initiation of crack was observed in the outer SiC coating, which leads to a subsequent load drop. As the cracks propagated into the underlying composite with further loading, diverse toughening mechanisms such as crack bridging, crack deflection, bifurcation, parallel cracks, and tortuous crack pathways activate simultaneously at both room temperature and 1200°C to resist the damage. Note that, crack deflection in the SiC coating was only observed at 1200°C. However, in the C-ring compression configuration, no evident fiber pull-out or breakage is observed at either temperature. The failure processes of the SiC_f-SiC_m cladding materials tested at both temperatures, were different from the conventional understanding of the presumed three-stage failure processes of such SiC_f-SiC_m cladding materials.

For the SiC_f-SiC_m cladding material with multi-layers outer SiC coating, the CVI process employed for the SiC matrix effectively yielded a relatively low porosity in the material. However, the resultant matrix exhibited diminished crystallinity, leading to a decrease in its elastic modulus, which in turn could potentially compromise the cladding material's resistance to irradiation. Furthermore, variations in the CVI parameters might influence the distribution of residual stress within the SiC fibre. Similar mechanical behavior was observed at both room RT and 1200°C for samples with initial damage induced during the sample preparation process under loading. This indicates that the materials exhibit good damage tolerance under the current level of initial damage. Various crack toughening mechanisms simultaneously activated to resist damage, including crack deflection, un-cracked ligament bridging, tortuous crack paths, and parallel cracks. With further loading towards peak levels, fiber pull-out was observed. Two specific areas in the materials exhibited unexpected detrimental effects on structural integrity and hermeticity at both temperatures. These areas included regions with a scarcity or absence of fibre bundles and locations where macropores existed on the inner surface. Potential

solutions might involve changing of the braiding angles of fiber bundles and employing a protective inner SiC coating to address these issues.

Distinct manufacturing processes of CS and PVD methods yielded diverse microstructures and local properties of the Cr coatings. In CS materials, the high-speed spraying process induced substrate hardening near the interface, while smaller Cr grains proximate to the interface in PVD materials contributed to heightened coating hardness. Regarding hoop strengths measured at 345°C for both CS and PVD materials, they exhibited approximately 50% of their strengths at RT. However, in comparison to PVD materials, CS materials displayed around a higher strength and strain for the formation of initial coating cracks at the same temperatures. This disparity might be ascribed to the augmented interfacial roughness and splatted Cr grains present within CS Cr coatings. Notably, for both types of material tested at both temperatures, all coating cracks arrested at the coating/substrate interface without penetrating the substrate, and crack could deflect along such interface. Utilizing Dundurs' parameter based on locally measured properties from the current study and fracture toughness values from the literature, the estimated interfacial toughness of CS materials surpassed that of PVD materials at RT. This observation is deemed credible due to the CS coating-substrate system possessing a more tortuous interlocking interface. Investigations of failure processes of both coating types revealed distinctive characteristics. CS coatings exhibited considerably larger overall crack density at both temperatures compared to PVD coatings. Noteworthy was the discovery of tortuous fine cracks exclusively in CS coatings at 345°C during the initial loading stage. Following the formation of primary cracks at 345°C due to heightened tensile hoop stress, these cracks did not increase in number but instead widened as the load increased to peak load. In contrast, PVD coatings displayed a decreasing trend in average crack distances at both temperatures, eventually reaching 50–60% of the crack distance observed at their initial formation upon reaching peak load. Moreover, at 345°C, the PVD coatings demonstrated an increase in the number of cracks along with widened cracks as the load increased, indicating a more ductile behavior. Additionally, crack orientations in the PVD coatings displayed larger deviations from the perpendicular direction of the tensile hoop stress. In both CS and PVD coatings, primary cracks (except for the tortuous fine cracks in CS at 345°C) emerged simultaneously at around 80–90% of the peak load, a pattern that remained consistent across the temperatures. No coating spallation was observed for both types of materials at both testing temperatures.

Distinct manufacturing parameters of HCS and NCS materials resulted in different local properties and interfacial toughness. Compressive residual stresses were estimated in both HCS and NCS Cr coatings, with NCS materials displaying 36% higher stress. This heightened residual stress in NCS Cr coatings potentially accounts for their higher hoop strength and strain during the initial formation of coating cracks, reduced crack density, and an enhanced resistance against the development of critical coating cracks at both temperatures. At 345°C, both HCS and NCS materials showed a reduction in hoop strength and strain at the onset of coating crack formation compared to that at RT. Moreover, at same testing temperatures, NCS materials exhibited higher hoop strength and strain during initial coating crack formation when compared to HCS materials. Exploration into the failure processes and crack patterns of both material types revealed similar behavior at same testing temperatures. For both HCS and NCS materials at both temperatures, all coating cracks arrested at the coating/substrate interface without propagation into the underlying substrate. For both types of materials tested at both temperatures, cracks were observed deflection along such interface. Moreover, these cracks typically formed nearly perpendicular to the hoop direction, with finer tortuous cracks observed only at the tips of cracks at 345°C. The width of coating cracks for HCS materials increased at 345°C compared to RT, whereas for NCS materials, the width remained consistent across both temperatures. The distinctive crack patterns observed in HCS and NCS materials at 345°C differed significantly from those in CS materials, potentially attributed to variations in stress-states within their coatings arising from disparate manufacturing parameters. No coating spallation was observed for both types of materials at both testing temperatures.

In summary, experimental observations in current PhD project present novel and direct insights into the mechanical behaviour and failure processes of nuclear-grade SiC_f-SiC_m cladding materials and Cr-coated zircaloy-4 cladding materials with temperatures. These observations are also critical for improving the design of these materials for future industrial application.

9. Future work

(i) High temperature mechanical tests on the SiC_f-SiC_m cladding and Cr-coated zircaloy cladding materials. The current PhD project only focuses on the hoop strengths of these two types of materials. As discussed in Section 6.5, the cladding materials are ~4 m in length. Due to their self-weight, strain and stress in the axial direction will occur when handling these claddings. Therefore, future work will be conducted aiming at investigating the mechanical properties and failure processes of these materials at elevated temperatures under bending test. Moreover, in current project limited materials tested at only two temperatures: RT and 1200°C for SiC_f-SiC_m cladding and RT and 345°C for Cr-coated zircaloy cladding. To have a more comprehensive understanding of the correlation between microstructures, mechanical properties and failure processes at elevated temperatures, more mechanical testing will be conducted at more temperatures.

(ii) High temperature Raman measurements on the SiC_f-SiC_m cladding materials. As discussed in Section 4, the relaxation of tensile residual stress in the single-layer outer SiC coating of the SiC_f-SiC_m cladding materials at 1200°C could potentially increase the failure strength and strain of the coating. Therefore, further experiments will be conducted by the high temperature Raman spectroscopy in CDTR group in UOB. Such technique allows the quantitatively analysis of the magnitude of residual stress in the outer SiC coating with elevated temperatures, as well as their influences on the mechanical performances of the entire composite materials.

(iii) Investigation of the properties of irradiated SiC_f-SiC_m cladding and Cr-coated zircaloy cladding materials. Under servicing in LWRs, the cladding materials undergo irradiation, which will consequently change the properties of the cladding materials, including: dimensions, local properties, residual stress distribution, microstructures and mechanical properties. Therefore, future study will focus on this research area.

(iv) Investigation of the brittle to ductile transition temperatures of Cr coatings. As discussed in Section 6.5.5.2, the various manufacturing processes of the Cr coatings could result in the variation in their brittle to ductile transition temperatures [53]. Which subsequently affect the failure strengths, failure processes and crack patterns of the coatings, and consequently affect the mechanical performances of the entire coated cladding system. Subsequent investigations should consider conducting additional experiments with finer temperature increments to explore and ascertain the brittle to ductile transition temperature of these Cr-coated cladding

materials. Moreover, outer surface roughness could also potentially affect the crack initiation in such Cr-coated materials. Therefore, future work will be focused on this field.

(v) High temperature mechanical testing of SiC_f-SiC_m cladding and Cr-coated zircaloy cladding materials in steam environments. The purpose of application Cr coatings on zircaloy cladding is to enhance its oxidation resistance under extreme conditions (*e.g.*, LOCA). The current PhD Chapter investigates the mechanical behaviour of these materials in Ar environment. Therefore, fur the future industrial application of these Cr-coated zircaloy materials, further experiments will be conducted in steam air environments at elevated temperatures to investigate the mechanical properties and oxidation resistance. Additionally, un-coated zircaloy claddings will be selected as reference materials, and be tested in the same conditions as the Cr-coated materials.

(vi) Synchrotron X-Ray diffraction (XRD) experiments on SiC_f-SiC_m cladding and Cr-coated zircaloy cladding materials. The microfocus XRD results will provide key insights into the lattice strain distribution in these cladding materials. This will enable the analysis of residual stresses to be accurately quantified and provide a more comprehensive understanding of the locked-in forces that arise as the result of fabrication processes of these materials. In particular, it will serve to validate and refine the existing models of residual stress generation. These results will be combined with the research on local properties (by nanoindentation) and microstructural characterization (by EBSD), to provide a complete understanding of the impact of production processes on these systems. These insights are essential in refining the production processes and thermal treatment steps, in order to maximize the performance and efficiency of these promising classes of cladding materials.

A. Appendices

Table A-1. Finite-element calculation of stress distribution for different C-ring sample geometries by Embree *et al.*[247] (σ_y and σ_z represent for hoop and axial stress, respectively).

r_i/r_o	b/t	σ_y/σ_z
0.75	3	33.58
0.95	3	-1290.75
0.75	4	14.22
0.95	4	856.86
0.75	5	9.24
0.95	5	154.67

Table A-2. Detailed C-ring compression/μXCT testing sequence for all specimens of SiC_f-SiC_m materials with single-layer outer SiC coating.

Specimen	Testing Sequence
S1-1 RT	**(1)** Preload Scan; **(2)** Scan at: 11.35N (0.37 P_U); **(3)** Scan at 20.89 N (0.62 P_U); **(4)** Scan at 17.58 N (0.52 P_U);**(5)** Scan at 20.64 N (0.61 P_U); **(6)** Scan at 28.81 N (0.85 P_U); **(7)** Peak load at 33.71 N (P_U); **(8)** Scan after peak load at 28.43 N (0.84 P_U); **(9)** Scan after peak load at 15.54 N (0.46 P_U)
S1-2 RT	**(1)** Preload Scan; **(2)** Scan at: 5.69 N (0.17 P_U); **(3)** Scan at 14.47 N (0.42 P_U); **(4)** Scan at 16.83 N (0.49 P_U); **(5)** Scan at 21.59 N (0.63 P_U); **(6)** Scan at 25.41 N (0.74 P_U); **(7)** Peak load at 34.13 N (P_U); **(8)** Scan after peak load at 10.02 N (0.29 P_U)
S1-3 1200°C	**(1)** Preload Scan; **(2)** Scan at: 19.75 N (0.51 P_U); **(3)** Scan at 30.57 N (0.79 P_U); **(4)** peak load at 38.65 N (P_U); **(5)** Scan after peak load at 25.21 N (0.65 P_U); **(6)** Scan after peak load at 13.78 N (0.36 P_U)
S1-4 1200°C	**(1)** Preload Scans; **(2)** Scan at 11.23 N (0.28 P_U); **(3)** Scan at 17.91 N (0.44 P_U); **(4)** Scan at 26.03 N (0.64 P_U); **(5)** Scan at 33.98 N (0.84 P_U); **(6)** peak load at 40.57 N (P_U); **(7)** Scan after peak load at 8.51 N (0.21 P_U)

Table A-3. Magnitude of the load relaxation in SiC_f-SiC_m materials with single-layer outer SiC coating samples, with S1-3 and S1-4 tested at 1200°C at increasing loading steps.

Specimen	Load before XCT scan (N)	Load after XCT scan (N)	Load relaxation (N)	Percentage of load relaxation (%)
S1-3	19.75 (0.51 P_U)	16.49 (0.43 P_U)	3.26	16.51
	30.57 (0.79 P_U)	28.25 (0.73 P_U)	2.32	7.59
	25.88 (0.67 P_U)	23.93 (0.62 P_U)	1.95	7.53
S1-4	11.23 (0.28 P_U)	9.27 (0.23 P_U)	1.96	17.45
	17.91 (0.44 P_U)	15.84 (0.39 P_U)	2.07	11.56
	26.03 (0.64 P_U)	24.67 (0.61 P_U)	1.36	5.22
	33.98 (0.84 P_U)	31.56 (0.78 P_U)	2.42	7.12

Table A-4. Detailed C-ring compression/μXCT testing sequence for all specimens of SiC_f-SiC_m materials with multi-layer outer SiC coating.

Specimen	Testing Sequence
S2-1 RT	**(1)** Preload Scan; **(2)** Scan at 5.14 N (0.12 P_U); **(3)** Scan at: 12.36 N (0.29 P_U); **(4)** Scan at 24.21 N (0.56 P_U); **(5)** Scan at 27.53 N (0.64 P_U); **(6)** Scan at 38.58 N (0.90 P_U); **(7)** Peak load at 42.87 N (P_U); **(8)** Scan after peak load at 18.71 N (0.44 P_U);
S2-2 RT	**(1)** Preload Scan; **(2)** Scan at: 10.07 N (0.21 P_U); **(3)** Scan at 19.20 N (0.41 P_U); **(4)** Scan at 30.67 N (0.65 P_U); **(5)** Scan at 38.69 N (0.82 P_U); **(6)** Peak load at 46.97 N (P_U); **(7)** Scan after peak load at 27.66 N (0.59 P_U); **(8)** Scan after peak load at 8.67 N (0.18 P_U);
S2-3 1200°C	**(1)** Preload Scan; **(2)** Scan at: 19.43 N (0.46 P_U); **(4)** Scan at 24.76 N (0.58 P_U); **(5)** Scan at 32.54 N (0.77 P_U); **(6)** Peak load at 42.33 N (P_U); **(7)** Scan after peak load at 35.22 N (0.83 P_U); **(8)** Scan after peak load at 13.41 N (0.32 P_U);
S2-4 1200°C	**(1)** Preload Scan; **(2)** Scan at 10.30 N (0.26 P_U); **(3)** Scan at 16.78 N (0.42 P_U); **(4)** Scan at 23.85 N (0.59 P_U); **(5)** Scan at 28.08 N (0.70 P_U); **(6)** peak load at 40.38 N (P_U); **(7)** Scan after peak load at 36.85 N (0.91 P_U);

Table A-5. Magnitude of the load relaxation in SiC_f-SiC_m materials with multi-layer outer SiC coating samples, with S2-3 and S2-4 tested at 1200°C at increasing loading steps.

Specimen	Load before XCT scan (N)	Load after XCT scan (N)	Load relaxation (N)	Percentage of load relaxation (%)
S2-3	19.53 (0.46 P_U)	15.87 (0.43 P_U)	3.66	18.74%
	25.21 (0.60 P_U)	21.71 (0.51 P_U)	3.50	13.88%
	32.68 (0.77 P_U)	26.95 (0.64 P_U)	5.73	17.53%
	40.69 (0.67 P_U) after peak load	35.12 (0.62 P_U) after peak load	5.57	13.69%
	36.09 (0.85 P_U) after peak load	29.90 (0.71 P_U) after peak load	6.19	17.15%
S2-4	10.63 (0.26 P_U)	7.87 (0.19 P_U)	2.76	25.96%
	17.05 (0.42 P_U)	13.24 (0.33 P_U)	3.81	22.34%
	24.94 (0.62 P_U)	20.72 (0.51 P_U)	4.22	16.92%
	28.42 (0.84 P_U)	24.96 (0.78 P_U)	3.46	12.17%
	38.34 (0.95 P_U)	32.77 (0.81 P_U)	5.57	14.53%

Table A-6. Detailed C-ring compression/μXCT testing sequence for all specimens of CS and PVD Cr-coated materials.

Specimen	Testing Sequence
CS S1-RT	**(1)** Preload Scan; **(2)** Scan at: 31.36 N (0.64 P_U); **(3)** Scan at 44.52 N (0.91 P_U); **(4)** Scan at 47.20 N (0.97 P_U); **(5)** Peak load at 48.72 N (P_U); **(6)** Scan at peak load at 48.72 N (P_U);
CS S2-RT	**(1)** Preload Scan; **(2)** Scan at: 30.67 N (0.77 P_U); **(3)** Scan at 37.32 N (0.88 P_U); **(4)** Peak load at 39.81 N (P_U); **(5)** Scan at peak load at 42.42 N (P_U);
CS S3-345°C	**(1)** Preload Scan; **(2)** Scan at: 17.87 N (0.78 P_U); **(3)** Scan at: 20.85 N (0.90 P_U); **(4)** Peak load at 23.04 N (P_U); **(5)** Scan at peak load at 23.04 N (P_U);
CS S4-345°C	**(1)** Preload Scan; **(2)** Scan at: 18.52 N (0.64 P_U); **(3)** Scan at: 25.95 N (0.90 P_U); **(4)** Peak load at 28.83 N (P_U); **(5)** Scan at peak load at 28.83 N (P_U);
PVD S5-RT	**(1)** Preload Scan; **(2)** Scan at: 2.81 N (0.05 P_U); **(3)** Scan at 30.87 N (0.60 P_U); **(4)** Scan at 40.95 N (0.80 P_U); **(5)** Scan at 46.06 N (0.89 P_U); **(6)** Peak load at 51.67 N (P_U); **(7)** Scan at peak load at 51.67 N (P_U);
PVD S6-RT	**(1)** Preload Scan; **(2)** Scan at: 28.71 N (0.57 P_U); **(3)** Scan at 38.66 N (0.76 P_U); **(4)** Scan at 46.52 N (0.92 P_U); **(5)** Peak load at 50.73 N (P_U); **(6)** Scan at peak load at 50.73 N (P_U);
PVD S7-345°C	**(1)** Preload Scan; **(2)** Scan at: 19.07 N (0.70 P_U); **(3)** Scan at: 21.27 N (0.78 P_U); **(4)** Peak load at 27.21 N (P_U); **(5)** Scan at peak load at 27.21 N (P_U);
PVD S8-345°C	**(1)** Preload Scan; **(2)** Scan at: 11.52 N (0.50 P_U); **(3)** Scan at: 18.66 N (0.81 P_U); **(4)** Peak load at 23.04 N (P_U); **(5)** Scan at peak load at 23.04 N (P_U);

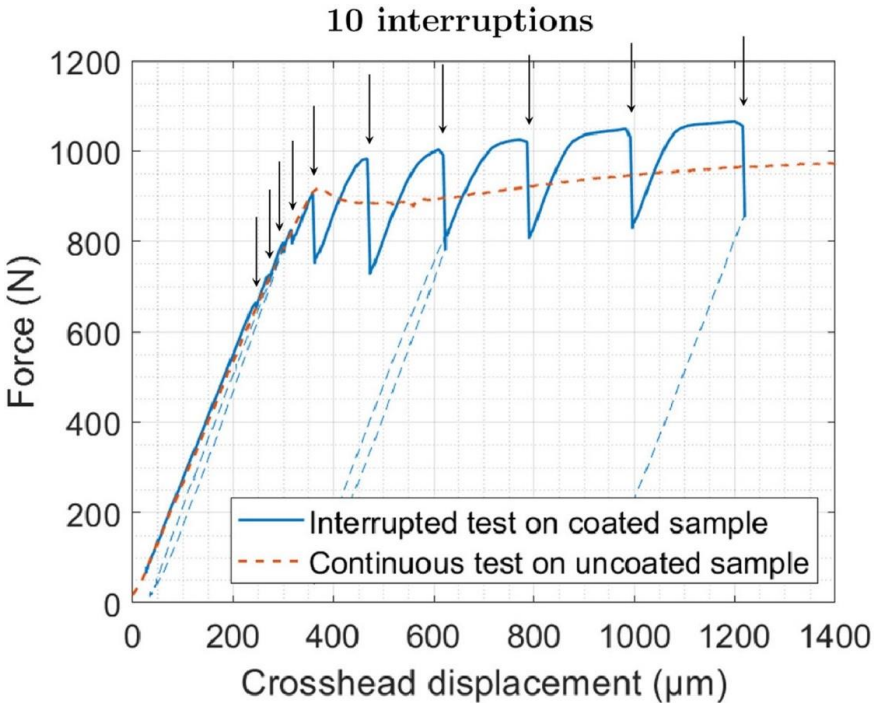

Figure A-1. Load-displacement curve for PVD Cr-coated zircaloy cladding materials under tensile test at RT (with load relaxation marked by arrows). Figure is reproduced from ref. [112].

Table A-7. Magnitude of the load relaxation in CS and PVD Cr-coated materials tested at both RT and 345°C.

Specimen	Load before XCT scan (N)	Load after XCT scan (N)	Load relaxation (N)	Percentage of load relaxation (%)
CS-S1-RT	31.36 (0.64 P_U)	28.45 (0.58 P_U)	2.91	9.28
	44.52 (0.91 P_U)	39.63 (0.81 P_U)	4.89	10.98
	47.20 (0.97 P_U)	44.95 (0.92 P_U)	2.25	4.77
CS-S2-RT	30.67 (0.77 P_U)	28.02 (0.70 P_U)	2.65	8.64
	37.32 (0.88 P_U)	33.10 (0.78 P_U)	5.22	11.31
CS-S3-345°C	17.87 (0.78 P_U)	15.47 (0.67 P_U)	2.40	13.43
	20.85 (0.90 P_U)	14.39 (0.62 P_U)	6.46	30.98
CS-S4-345°C	18.52 (0.64 P_U)	15.75 (0.55 P_U)	2.77	14.96
	25.95 (0.90 P_U)	20.32 (0.70 P_U)	5.67	21.85
PVD-S5-RT	30.87 (0.60 P_U)	28.89 (0.56 P_U)	1.98	6.41
	40.95 (0.80 P_U)	35.87 (0.69 P_U)	5.08	12.41
	46.06 (0.89 P_U)	40.31 (0.78 P_U)	5.75	12.48
PVD-S6-RT	28.71 (0.57 P_U)	25.02 (0.49 P_U)	3.69	12.85
	38.66 (0.76 P_U)	34.53 (0.68 P_U)	4.13	10.68
	46.52 (0.92 P_U)	41.50 (0.82 P_U)	5.02	10.79
PVD-S7-345°C	19.07 (0.70 P_U)	15.09 (0.55 P_U)	3.98	20.87
	21.27 (0.78 P_U)	14.73 (0.54 P_U)	6.54	24.04
PVD-S8-345°C	11.52 (0.50 P_U)	9.59 (0.42 P_U)	1.93	16.75
	18.66 (0.81 P_U)	14.85 (0.64 P_U)	3.81	20.42

Table A-8. Detailed C-ring compression/μXCT testing sequence for all specimens of HCS and NCS Cr-coated materials.

Specimen	Testing Sequence
HCS S1 RT	**(1)** Preload Scan; **(2)** Scan at: 15.33 N (0.30 P_U); **(3)** Scan at 28.11 N (0.55 P_U); **(4)** Scan at 39.35 N (0.77 P_U); **(5)** Scan at Peak load at 51.11 N (P_U);
HCS S2 RT	**(1)** Preload Scan; **(2)** Scan at: 17.32 N (0.31 P_U); **(3)** Scan at 32.04 N (0.57 P_U); **(4)** Scan at 41.68 N (0.74 P_U); **(5)** Scan at Peak load at 56.49 N (P_U);
HCS S3 345°C	**(1)** Preload Scan; **(2)** Scan at: 13.53 N (0.39 P_U); **(3)** Scan at 21.25 N (0.71 P_U); **(4)** Scan at Peak load at 30.04 N (P_U);
HCS S4 345°C	**(1)** Preload Scan; **(2)** Scan at: 11.92 N (0.34 P_U); **(3)** Scan at 25.74 N (0.74 P_U); **(4)** Scan at Peak load at 34.79 N (P_U);
NCS S5 RT	**(1)** Preload Scan; **(2)** Scan at: 17.89 N (0.28 P_U); **(3)** Scan at 36.68 N (0.58 P_U); **(4)** Scan at 51.98 N (0.82 P_U); **(5)** Scan at Peak load at 63.39 N (P_U);
NCS S6 RT	**(1)** Preload Scan; **(2)** Scan at: 21.78 N (0.29 P_U); **(3)** Scan at 42.94 N (0.57 P_U); **(4)** Scan at 58.01 N (0.77 P_U); **(5)** Scan at Peak load at 75.51 N (P_U);
NCS S7 345°C	**(1)** Preload Scan; **(2)** Scan at: 16.93 N (0.48 P_U); **(3)** Scan at 25.75 N (0.73 P_U); **(4)** Scan at 28.32 N (0.80 P_U); **(5)** Scan at Peak load at 35.27 N (P_U);
NCS S8 345°C	**(1)** Preload Scan; **(2)** Scan at: 17.42 N (0.44 P_U); **(3)** Scan at 28.50 N (0.72 P_U); **(4)** Scan at Peak load at 39.58 N (P_U);

Table A-9. Magnitude of the load relaxation in HCS Cr-coated and NCS Cr-coated materials tested at both RT and 345°C.

Specimen	**Load before XCT scan (N)**	**Load after XCT scan (N)**	**Load relaxation (N)**	**Percentage of load relaxation (%)**
HCS-S1-RT	15.33 (0.30 P_U)	13.21 (0.26 P_U)	2.12	13.83
	28.11 (0.55 P_U)	23.34 (0.46 P_U)	4.77	16.97
	39.35 (0.77 P_U)	34.34 (0.67 P_U)	5.01	12.73
	51.11 (P_U)	44.56 (0.87 P_U)	6.55	12.81
HCS-S2-RT	17.32 (0.31 P_U)	14.61 (0.26 P_U)	2.71	15.65
	32.04 (0.57 P_U)	27.62 (0.49 P_U)	4.42	13.80
	41.68 (0.74 P_U)	36.37 (0.64 P_U)	5.31	12.76
	56.49 (P_U)	49.60 (0.88 P_U)	6.89	12.19
HCS-S3-345°C	13.53 (0.39 P_U)	9.54 (0.32 P_U)	3.99	29.49
	21.25 (0.71 P_U)	14.11 (0.47 P_U)	7.14	33.60
	30.04 (P_U)	21.93 (0.73 P_U)	8.11	27.00
HCS-S4-345°C	11.92 (0.34 P_U)	7.74 (0.22 P_U)	4.18	35.07
	25.74 (0.74 P_U)	17.93 (0.52 P_U)	7.81	30.34
	34.79 (P_U)	25.13 (0.72 P_U)	9.66	27.77
NCS-S5-RT	17.89 (0.28 P_U)	15.01 (0.24 P_U)	2.88	13.83
	36.68 (0.58 P_U)	30.66 (0.48 P_U)	6.02	16.41
	51.98 (0.82 P_U)	45.25 (0.71 P_U)	6.73	12.95
	63.39 (P_U)	55.38 (0.87 P_U)	8.01	12.64
NCS-S6-RT	21.78 (0.29 P_U)	17.66 (0.23 P_U)	4.12	18.92
	42.94 (0.57 P_U)	35.28 (0.47 P_U)	7.66	17.84
	58.01 (0.77 P_U)	49.59 (0.66 P_U)	8.42	14.51
	75.51 (P_U)	64.73 (0.86 P_U)	10.78	14.28
NCS-S7-345°C	16.93 (0.48 P_U)	11.37 (0.32 P_U)	5.56	32.84
	25.75 (0.73 P_U)	18.26 (0.52 P_U)	7.49	29.09
	28.32 (0.80 P_U)	20.23 (0.57 P_U)	8.09	28.57
	35.27 (P_U)	26.14 (0.74 P_U)	9.13	25.87
NCS-S8-345°C	17.42 (0.44 P_U)	10.82 (0.27 P_U)	6.60	37.89
	28.50 (0.72 P_U)	19.41 (0.49 P_U)	9.09	31.89
	39.58 (P_U)	26.27 (0.66 P_U)	13.31	33.63

B. References

[1] Yuan G, Forna-Kreutzer J P, Ell J, et al. In situ X-ray computed micro-tomography imaging of failure processes in Cr-coated Zircaloy nuclear fuel cladding materials[J]. Materials & Design, 2023, 234: 112373.

[2] Sitton S B. Development of advanced accident-tolerant fuels for commercial LWRs[J]. Nucl News, 2014: 83.

[3] Umretiya, R. V., Elward, B., Lee, D., Anderson, M., Rebak, R. B., & Rojas, J. V. (2020). Mechanical and chemical properties of PVD and cold spray Cr-coatings on Zircaloy-4. *Journal of Nuclear Materials*, *541*, 152420.

[4] Maier B, Yeom H, Johnson G, et al. Development of cold spray chromium coatings for improved accident tolerant zirconium-alloy cladding[J]. Journal of Nuclear Materials, 2019, 519: 247-254.

[5] Quillin K, Yeom H, Dabney T, et al. Microstructural and nanomechanical studies of PVD Cr coatings on SiC for LWR fuel cladding applications[J]. Surface and Coatings Technology, 2022, 441: 128577.

[6] Ševeček M, Gurgen A, Seshadri A, et al. Development of Cr cold spray–coated fuel cladding with enhanced accident tolerance[J]. Nuclear Engineering and Technology, 2018, 50(2): 229-236.

[7] Holzwarth U, Stamm H. Mechanical and thermomechanical properties of commercially pure chromium and chromium alloys[J]. Journal of Nuclear Materials, 2002, 300(2-3): 161-177.

[8] Yin S, Meyer M, Li W, et al. Gas flow, particle acceleration, and heat transfer in cold spray: a review[J]. Journal of Thermal Spray Technology, 2016, 25: 874-896.

[9] Nozawa T, Kim S, Ozawa K, et al. Stress envelope of silicon carbide composites at elevated temperatures[J]. Fusion Engineering and Design, 2014, 89(7-8): 1723-1727.

[10] Koyanagi T, Katoh Y, Nozawa T. Design and strategy for next-generation silicon carbide composites for nuclear energy[J]. Journal of Nuclear Materials, 2020, 540: 152375.

[11] Hasegawa A, Kohyama A, Jones R H, et al. Critical issues and current status of SiC/SiC composites for fusion[J]. Journal of Nuclear Materials, 2000, 283: 128-137.

[12] Shimoda K, Hinoki T, Kishimoto H, et al. Enchanced high-temperature performances of SiC/SiC composites by high densification and crystalline structure[J]. Composites Science and Technology, 2011, 71(3): 326-332.

[13] Koyanagi T, Katoh Y. Mechanical properties of SiC composites neutron irradiated under light water reactor relevant temperature and dose conditions[J]. Journal of Nuclear Materials, 2017, 494: 46-54.

[14] Yuan G, Forna-Kreutzer J P, Xu P, et al. In situ high-temperature 3D imaging of the damage evolution in a SiC nuclear fuel cladding material[J]. Materials & Design, 2023, 227: 111784.

[15] Gu Z. History review of nuclear reactor safety[J]. Annals of Nuclear Energy, 2018, 120: 682-690.

[16] Li G, Wang X, Liang B, et al. Modeling and control of nuclear reactor cores for electricity generation: A review of advanced technologies[J]. Renewable and

Sustainable Energy Reviews, 2016, 60: 116-128.

[17] Rebak R B. Current materials in light water reactors. Why do we need a materials renewal[J]. Accident-Tolerant Materials for Light Water Reactor Fuels; Elsevier: Amsterdam, The Netherlands, 2020: 15-41.

[18] Zinkle S J, Terrani K A, Gehin J C, et al. Accident tolerant fuels for LWRs: A perspective[J]. Journal of Nuclear Materials, 2014, 448(1-3): 374-379.

[19] "http://www.reddit.com/r/nuclear/comments/juh39n/"

[20] Zinkle S J, Was G S. Materials challenges in nuclear energy[J]. Acta Materialia, 2013, 61(3): 735-758.

[21] Karoutas Z, Brown J, Atwood A, et al. The maturing of nuclear fuel: Past to Accident Tolerant Fuel[J]. Progress in Nuclear Energy, 2018, 102: 68-78.

[22] Chen S L, He X J, Yuan C X. Recent studies on potential accident-tolerant fuel-cladding systems in light water reactors[J]. Nuclear Science and Techniques, 2020, 31(3): 32.

[23] McClenny L D, Butt M I, Abdoelatef M G, et al. Experimentally validated multiphysics modeling of fracture induced by thermal shocks in sintered UO2 pellets[J]. Journal of Nuclear Materials, 2022, 565: 153719.

[24] Hallstadius L, Johnson S, Lahoda E. Cladding for high performance fuel[J]. Progress in Nuclear Energy, 2012, 57: 71-76.

[25] Chen H, Wang X, Zhang R. Application and development progress of Cr-based surface coatings in nuclear fuel element: I. selection, preparation, and characteristics of coating materials[J]. Coatings, 2020, 10(9): 808.

[26] Franklin D G. Zircaloy-4 cladding deformation during power reactor irradiation[M]//Zirconium in the Nuclear Industry. ASTM International, 1982.

[27] Kido T, Kanasugi K, Sugano M, et al. PWR Zircaloy cladding corrosion behavior: quantitative analyses[J]. Journal of nuclear materials, 1997, 248: 281-287.

[28] Roberts J T A, Gelhaus F E. Zircaloy performance in light-water reactors[J]. Zirconium in the Nuclear Industry, 1979.

[29] Terrani K A. Accident tolerant fuel cladding development: Promise, status, and challenges[J]. Journal of Nuclear Materials, 2018, 501: 13-30.

[30] Cheng B, Gilmore P M, Klepfer H H. PWR Zircaloy fuel cladding corrosion performance, mechanisms, and modeling[C]//Zirconium in the Nuclear Industry: Eleventh International Symposium. ASTM International, 1996.

[31] Hagen S, Hofmann P. Physical and Chemical Behavior of LWR Fuel Elements up to very high Temperatures[M]. Kernforschungszentrum Karlsruhe, 1987.

[32] Whitmarsh C L. Review of Zircaloy-2 and Zircaloy-4 properties relevant to NS Savannah reactor design[M]. Oak Ridge National Laboratory for the US Atomic Energy Commission, 1962.

[33] Garzarolli F, Stehle H, Steinberg E. Behavior and properties of zircaloys in power reactors: A short review of pertinent aspects in LWR fuel[C]//Zirconium in the Nuclear Industry: Eleventh International Symposium. ASTM International, 1996.

[34] Franklin D G, Adamson R B. Implications of Zircaloy creep and growth to light water reactor performance[J]. Journal of Nuclear Materials, 1988, 159: 12-21.

[35] Erbacher F J, Leistikow S. Zircaloy fuel cladding behavior in a loss-of-coolant accident:

a review[J]. Zirconium in the Nuclear Industry, 1987.

[36] Abolhassani S, Graber T, Gavillet D, et al. Recent observations on the evolution of secondary-phase particles in zircaloy-2 under irradiation in a BWR to high burn-up[J]. 2000.

[37] Kroll W J. A contribution to the history of ductile titanium and zirconium[J]. Journal of the less common metals, 1965, 8(6): 361-367.

[38] Rickover H G, Geiger L D, Lustman B. History of the development of zirconium alloys for use in nuclear reactors[R]. Energy Research and Development Administration, Washington, DC (USA). Div. of Naval Reactors, 1975.

[39] Suman S, Khan M K, Pathak M, et al. Hydrogen in Zircaloy: Mechanism and its impacts[J]. International Journal of Hydrogen Energy, 2015, 40(17): 5976-5994.

[40] Whitmarsh C L. Review of Zircaloy-2 and Zircaloy-4 properties relevant to NS Savannah reactor design[M]. Oak Ridge National Laboratory for the US Atomic Energy Commission, 1962.

[41] Duan Z, Yang H, Satoh Y, et al. Current status of materials development of nuclear fuel cladding tubes for light water reactors[J]. Nuclear Engineering and Design, 2017, 316: 131-150.

[42] Novikov V, Markelov V, Gusev A, et al. Some results on the properties investigations of zirconium alloys for VVER-1000 fuel cladding[J]. 2011.

[43] Shebaldov P V, Peregud M M, Nikulina A V, et al. E110 alloy cladding tube properties and their interrelation with alloy structure-phase condition and impurity content[C]//Zirconium in the Nuclear Industry: Twelfth International Symposium. ASTM International, 2000.

[44] Sabol G P, Kilp G R, Balfour M G, et al. Development of a cladding alloy for high burnup[C]//Zirconium in the Nuclear Industry: Eighth International Symposium. ASTM International, 1989.

[45] Sabol G P. ZIRLO™—an alloy development success, J[J]. ASTM Int, 2005, 2(2): 3-24.

[46] Foster J P, Yueh H K, Comstock R J. ZirloTM cladding improvement[M]. ASTM International, 2008.

[47] Yueh H K, Colburn D J, Comstock R J, et al. Improved ZIRLOTM cladding performance through chemistry and process modifications[M]. West Conshohocken, PA, USA: ASTM International, 2005.

[48] Doriot S, Gilbon D, Béchade J L, et al. Microstructural stability of M5TM alloy irradiated up to high neutron fluences[M]. ASTM International, 2005.

[49] Mardon J P, Charquet D, Senevat J. Influence of composition and fabrication process on out-of-pile and in-pile properties of M5 alloy[C]//Zirconium in the Nuclear Industry: Twelfth International Symposium. ASTM International, 2000.

[50] Garat V, Deuble D, Dunn B, et al. Quantification of the margins provided by M5® cladding in accidental conditions[C]//LWR Fuel Performance Meeting (TopFuel), Manchester, United Kingdom. 2012.

[51] Garde A M, Comstock R J, Pan G, et al. Advanced zirconium alloy for PWR application[M]. ASTM International, 2010.

[52] Alam T, Khan M K, Pathak M, et al. A review on the clad failure studies[J]. Nuclear Engineering and Design, 2011, 241(9): 3658-3677.

[53] Jiang J, Zhai H, Du M, et al. Temperature-dependent deformation and cracking behavior in Cr coating for accident tolerant fuel cladding: An in situ SEM study[J]. Surface and Coatings Technology, 2021, 427: 127815.

[54] Kashkarov E, Afornu B, Sidelev D, et al. Recent advances in protective coatings for accident tolerant Zr-based fuel claddings[J]. Coatings, 2021, 11(5): 557.

[55] Charit I. Accident tolerant nuclear fuels and cladding materials[J]. Jom, 2018, 70(2): 173-175.

[56] Yanez J, Kuznetsov M, Souto-Iglesias A. An analysis of the hydrogen explosion in the Fukushima-Daiichi accident[J]. International Journal of Hydrogen Energy, 2015, 40(25): 8261-8280.

[57] Labib A, Harris M J. Learning how to learn from failures: The Fukushima nuclear disaster[J]. Engineering Failure Analysis, 2015, 47: 117-128.

[58] Krejčí J, Kabátová J, Manoch F, et al. Development and testing of multicomponent fuel cladding with enhanced accidental performance[J]. Nuclear Engineering and Technology, 2020, 52(3): 597-609.

[59] Rebak R B. Worldwide development of accident tolerant fuels, areas of study, claddings, and fuels[J]. Accid. Toler. Mater. Light Water React. Fuels, Elsevier, 2020: 43-62.

[60] Fazi A, Sattari M, Stiller K, et al. Development and Performance Evaluation of Accident Tolerant Coated Fuel Claddings for Light Water Reactors[M]. Chalmers University of Technology, 2023.

[61] Tang C, Stueber M, Seifert H J, et al. Protective coatings on zirconium-based alloys as accident-tolerant fuel (ATF) claddings[J]. Corrosion reviews, 2017, 35(3): 141-165.

[62] Kam D H, Lee J H, Lee T, et al. Critical heat flux for SiC-and Cr-coated plates under atmospheric condition[J]. Annals of Nuclear Energy, 2015, 76: 335-342.

[63] Fazi A, Stiller K, Andrén H O, et al. Cold sprayed Cr-coating on Optimized ZIRLO™ claddings: the Cr/Zr interface and its microstructural and chemical evolution after autoclave corrosion testing[J]. Journal of Nuclear Materials, 2022, 560: 153505.

[64] Kim H G, Kim I H, Jung Y I, et al. Progress of surface modified Zr cladding development for ATF at KAERI[C]//Proceedings of the 2017 Water Reactor Fuel Performance Meeting, Ramada Plaza Jeju, Jeju Island, Korea. 2017: 10-14.

[65] Kuprin A S, Belous V A, Voyevodin V N, et al. Vacuum-arc chromium-based coatings for protection of zirconium alloys from the high-temperature oxidation in air[J]. Journal of Nuclear Materials, 2015, 465: 400-406.

[66] Bao W, Xue J, Liu J X, et al. Coating SiC on Zircaloy-4 by magnetron sputtering at room temperature[J]. Journal of Alloys and Compounds, 2018, 730: 81-87.

[67] Park D J, Kim H G, Jung Y I, et al. Behavior of an improved Zr fuel cladding with oxidation resistant coating under loss-of-coolant accident conditions[J]. Journal of nuclear materials, 2016, 482: 75-82.

[68] Alat E, Motta A T, Comstock R J, et al. Ceramic coating for corrosion (c3) resistance of nuclear fuel cladding[J]. Surface and coatings technology, 2015, 281: 133-143.

[69] Van Nieuwenhove R, Andersson V, Balak J, et al. In-Pile testing of CrN, TiAlN, and AlCrN coatings on zircaloy cladding in the Halden reactor[C]//18th International Symposium on Zirconium in the Nuclear Industry. ASTM International, 2018: 965-982.

[70] Yeom H, Lockhart C, Mariani R, et al. Evaluation of steam corrosion and water

quenching behavior of zirconium-silicide coated LWR fuel claddings[J]. Journal of Nuclear Materials, 2018, 499: 256-267.

[71] Barsoum M W. The MN+ 1AXN phases: A new class of solids: Thermodynamically stable nanolaminates[J]. Progress in solid state chemistry, 2000, 28(1-4): 201-281.

[72] Park D J, Kim H G, Park J Y, et al. A study of the oxidation of FeCrAl alloy in pressurized water and high-temperature steam environment[J]. Corrosion Science, 2015, 94: 459-465.

[73] Burns J R, Brown N R. Neutron cross section sensitivity and uncertainty analysis of candidate accident tolerant fuel concepts[J]. Annals of Nuclear Energy, 2017, 110: 1249-1255.

[74] Maier B, Yeom H, Johnson G, et al. Development of cold spray coatings for accident-tolerant fuel cladding in light water reactors[J]. Jom, 2018, 70: 198-202.

[75] Maier B R, Yeom H, Johnson G, et al. In situ TEM investigation of irradiation-induced defect formation in cold spray Cr coatings for accident tolerant fuel applications[J]. Journal of Nuclear Materials, 2018, 512: 320-323.

[76] Ševeček M, Krejčí J, Shahin M H, et al. Fatigue behavior of cold spray-coated accident tolerant cladding[J]. Topfuel Prague, Czech Republic, 2018.

[77] Ševeček M, Shirvan K, Ballinger R G. Study of thermal creep of coated cladding materials[J]. 2018.

[78] Yeom H, Dabney T, Johnson G, et al. Improving deposition efficiency in cold spraying chromium coatings by powder annealing[J]. The International Journal of Advanced Manufacturing Technology, 2019, 100: 1373-1382.

[79] Brachet J C, Idarraga-Trujillo I, Le Flem M, et al. Early studies on Cr-Coated Zircaloy-4 as enhanced accident tolerant nuclear fuel claddings for light water reactors[J]. Journal of Nuclear Materials, 2019, 517: 268-285.

[80] J Bischoff J, Delafoy C, Vauglin C, et al. AREVA NP's enhanced accident-tolerant fuel developments: Focus on Cr-coated M5 cladding[J]. Nuclear Engineering and Technology, 2018, 50(2): 223-228.

[81] Wei T, Zhang R, Yang H, et al. Microstructure, corrosion resistance and oxidation behavior of Cr-coatings on Zircaloy-4 prepared by vacuum arc plasma deposition[J]. Corrosion Science, 2019, 158: 108077.

[82] Park J H, Kim H G, Park J, et al. High temperature steam-oxidation behavior of arc ion plated Cr coatings for accident tolerant fuel claddings[J]. Surface and Coatings Technology, 2015, 280: 256-259.

[83] Kuprin A S, Belous V A, Voyevodin V N, et al. Irradiation resistance of vacuum arc chromium coatings for zirconium alloy fuel claddings[J]. Journal of Nuclear Materials, 2018, 510: 163-167.

[84] Bourdon G, Ševecek M, Krejčí J, et al. High-temperature steam and air oxidation of chromium-coated optimized ZIRLO™[J]. 2019.

[85] Chalupová A, Krejčí J, Cvrček L, et al. Coated cladding behavior during high-temperature transients[J]. 2019.

[86] Kim H G, Yang J H, Kim W J, et al. Development status of accident-tolerant fuel for light water reactors in Korea[J]. Nuclear Engineering and Technology, 2016, 48(1): 1-15.

[87] Kim H G, Kim I H, Jung Y I, et al. Adhesion property and high-temperature oxidation behavior of Cr-coated Zircaloy-4 cladding tube prepared by 3D laser coating[J]. Journal of Nuclear Materials, 2015, 465: 531-539.

[88] Kim H G, Kim I H, Jung Y I, et al. Out-of-pile performance of surface-modified Zr cladding for accident tolerant fuel in LWRs[J]. Journal of Nuclear Materials, 2018, 510: 93-99.

[89] Papyrin A. The development of the cold spray process[M]//The cold spray materials deposition process. Woodhead Publishing, 2007: 11-42.

[90] Gärtner F, Stoltenhoff T, Schmidt T, et al. The cold spray process and its potential for industrial applications[J]. Journal of Thermal Spray Technology, 2006, 15: 223-232.

[91] Yin S, Cavaliere P, Aldwell B, et al. Cold spray additive manufacturing and repair: Fundamentals and applications[J]. Additive manufacturing, 2018, 21: 628-650.

[92] Adaan-Nyiak M A, Tiamiyu A A. Recent advances on bonding mechanism in cold spray process: A review of single-particle impact methods[J]. Journal of Materials Research, 2023, 38(1): 69-95.

[93] Tan A W Y, Sun W, Phang Y P, et al. Effects of traverse scanning speed of spray nozzle on the microstructure and mechanical properties of cold-sprayed Ti6Al4V coatings[J]. Journal of Thermal Spray Technology, 2017, 26: 1484-1497.

[94] Moridi A, Gangaraj S M H, Vezzu S, et al. Number of passes and thickness effect on mechanical characteristics of cold spray coating[J]. Procedia Engineering, 2014, 74: 449-459.

[95] Deng S, Liang H, Cai Z, et al. Kinematic optimization of robot trajectories for thermal spray coating application[J]. Journal of thermal spray technology, 2014, 23: 1382-1389.

[96] Singh N K, Uddin K Z, Muthulingam J, et al. Analyzing the effects of particle diameter in cold spraying of thermoplastic polymers[J]. Journal of Thermal Spray Technology, 2021, 30(5): 1226-1238.

[97] Cold spray in the realm of additive manufacturing[M]. Berlin/Heidelberg, Germany: Springer, 2020.

[98] Tiamiyu A A, Sun Y, Nelson K A, et al. Site-specific study of jetting, bonding, and local deformation during high-velocity metallic microparticle impact[J]. Acta Materialia, 2021, 202: 159-169.

[99] Tiamiyu A A, Schuh C A. Particle flattening during cold spray: Mechanistic regimes revealed by single particle impact tests[J]. Surface and Coatings Technology, 2020, 403: 126386.

[100] Fazi A, Aboulfadl H, Iyer A H S, et al. Characterization of as-deposited cold sprayed Cr-coating on Optimized ZIRLO™ claddings[J]. Journal of Nuclear Materials, 2021, 549: 152892.

[101] Calla E, McCartney D G, Shipway P H. Effect of deposition conditions on the properties and annealing behavior of cold-sprayed copper[J]. Journal of thermal spray technology, 2006, 15: 255-262.

[102] Zou Y, Qin W, Irissou E, et al. Dynamic recrystallization in the particle/particle interfacial region of cold-sprayed nickel coating: Electron backscatter diffraction characterization[J]. Scripta Materialia, 2009, 61(9): 899-902.

[103] Shah H, Romero J, Xu P, et al. Development of surface coatings for enhanced accident

tolerant fuel[J]. Water React. Fuel Perform. Meet., Jeju Island, Korea, 2017.

[104] Roache D C, Jarama A, Bumgardner C H, et al. Unveiling damage mechanisms of chromium-coated zirconium-based fuel claddings by coupling digital image correlation and acoustic emission[J]. Materials Science and Engineering: A, 2020, 774: 138850.

[105] Roache D C, Bumgardner C H, Harrell T M, et al. Unveiling damage mechanisms of chromium-coated zirconium-based fuel claddings at LWR operating temperature by in-situ digital image correlation[J]. Surface and Coatings Technology, 2022, 429: 127909.

[106] Burden D E, Harrell T M, Bumgardner C H, et al. Unveiling fracture mechanics of a curved coating/substrate system by combined digital image correlation and numerical finite element analyses[J]. Engineering Fracture Mechanics, 2024, 296: 109827.

[107] Greene J E. Tracing the recorded history of thin-film sputter deposition: From the 1800s to 2017[J]. Journal of Vacuum Science & Technology A, 2017, 35(5).

[108] Baptista A, Silva F, Porteiro J, et al. Sputtering physical vapour deposition (PVD) coatings: A critical review on process improvement and market trend demands[J]. Coatings, 2018, 8(11): 402.

[109] Pinto G, Silva F J G, Porteiro J, et al. A critical review on the numerical simulation related to physical vapour deposition[J]. Procedia Manufacturing, 2018, 17: 860-869.

[110] Anders A. A review comparing cathodic arcs and high power impulse magnetron sputtering (HiPIMS)[J]. Surface and Coatings Technology, 2014, 257: 308-325.

[111] Kubart T, Gudmundsson J T, Lundin D. Reactive high power impulse magnetron sputtering[M]//High Power Impulse Magnetron Sputtering. Elsevier, 2020: 223-263.

[112] Nguyen D V, Le Saux M, Gélébart L, et al. Mechanical behavior of a chromium coating on a zirconium alloy substrate at room temperature[J]. Journal of Nuclear Materials, 2022, 558: 153332.

[113] Kim J, Joung S H, Lee Y. Effect of Cr coating on the mechanical integrity of Accident Tolerant Fuel cladding under ring compression test[J]. Journal of Nuclear Materials, 2023, 585: 154603.

[114] Katoh Y, Snead L L, Henager Jr C H, et al. Current status and recent research achievements in SiC/SiC composites[J]. Journal of Nuclear Materials, 2014, 455(1-3): 387-397.

[115] Rebak R B. Alloy selection for accident tolerant fuel cladding in commercial light water reactors[J]. Metallurgical and Materials Transactions E, 2015, 2: 197-207.

[116] Singh G, Gorton J, Schappel D, et al. Deformation analysis of SiC-SiC channel box for BWR applications[J]. Journal of Nuclear Materials, 2019, 513: 71-85.

[117] Snead L L, Nozawa T, Katoh Y, et al. Handbook of SiC properties for fuel performance modeling[J]. Journal of nuclear materials, 2007, 371(1-3): 329-377.

[118] Carpenter D M. An assessment of silicon carbide as a cladding material for light water reactors[D]. Massachusetts Institute of Technology, 2010.

[119] Deck C P, Jacobsen G M, Sheeder J, et al. Characterization of SiC–SiC composites for accident tolerant fuel cladding[J]. Journal of Nuclear Materials, 2015, 466: 667-681.

[120] Yajima S, Hayashi J, Omori M, et al. Development of a silicon carbide fibre with high tensile strength[J]. Nature, 1976, 261(5562): 683-685.

[121] Yajima S, Hayashi J, Omori M. Continuous silicon carbide fiber of high tensile strength[J]. Chemistry Letters, 1975, 4(9): 931-934.

[122] Yajima S, Hasegawa Y, Hayashi J, et al. Synthesis of continuous silicon carbide fibre with high tensile strength and high Young's modulus: Part 1 Synthesis of polycarbosilane as precursor[J]. Journal of Materials Science, 1978, 13: 2569-2576.

[123] Katoh Y, Snead L L. Silicon carbide and its composites for nuclear applications–Historical overview[J]. Journal of Nuclear Materials, 2019, 526: 151849.

[124] Snead L L, Katoh Y, Kohyama A, et al. Evaluation of neutron irradiated near-stoichiometric silicon carbide fiber composites[J]. Journal of Nuclear Materials, 2000, 283: 551-555.

[125] Hegeman J B J, Van der Laan J G, Van Kranenburg M, et al. Mechanical and thermal properties of SiCf/SiC composites irradiated with neutrons at high temperatures[J]. Fusion engineering and design, 2005, 75: 789-793.

[126] Ozawa K, Nozawa T, Katoh Y, et al. Mechanical properties of advanced SiC/SiC composites after neutron irradiation[J]. Journal of nuclear materials, 2007, 367: 713-718.

[127] Le Flem M, Michaux A, Sauder C, et al. Evaluation of potential alternative nuclear fuel cladding materials for LWRs applications with increased margins in LOCA and beyond LOCA conditions at CEA. Evaluation of Potential Alternative Nuclear Fuel Cladding Materials for LWRs-CEA Studies[R]. 2013.

[128] Rohmer E, Martin E, Lorrette C. Mechanical properties of SiC/SiC braided tubes for fuel cladding[J]. Journal of Nuclear Materials, 2014, 453(1-3): 16-21.

[129] Shapovalov K, Jacobsen G M, Alva L, et al. Strength of SiCf-SiCm composite tube under uniaxial and multiaxial loading[J]. Journal of Nuclear Materials, 2018, 500: 280-294.

[130] Shapovalov K, Jacobsen G M, Shih C, et al. C-ring testing of nuclear grade silicon carbide composites at temperatures up to 1900 C[J]. Journal of Nuclear Materials, 2019, 522: 184-191.

[131] Jacobsen G M, Stone J D, Khalifa H E, et al. Investigation of the C-ring test for measuring hoop tensile strength of nuclear grade ceramic composites[J]. Journal of Nuclear Materials, 2014, 452(1-3): 125-132.

[132] Saucedo-Mora L, Lowe T, Zhao S, et al. In situ observation of mechanical damage within a SiC-SiC ceramic matrix composite[J]. Journal of Nuclear Materials, 2016, 481: 13-23.

[133] Zhang Q. Fabrication of SiCf/SiC composites by polymer infiltration pyrolysis method[J]. 2022.

[134] Wang P, Liu F, Wang H, et al. A review of third generation SiC fibers and SiCf/SiC composites[J]. Journal of Materials Science & Technology, 2019, 35(12): 2743-2750.

[135] Bunsell A R, Piant A. A review of the development of three generations of small diameter silicon carbide fibres[J]. Journal of Materials Science, 2006, 41: 823-839.

[136] Koyanagi T, Katoh Y, Nozawa T, et al. Recent progress in the development of SiC composites for nuclear fusion applications[J]. Journal of Nuclear Materials, 2018, 511: 544-555.

[137] YANG D, SONG Y, YU Y, et al. Fabrication of SiC fibres from yttrium-containing polycarbosilane[J]. Transactions of Nonferrous Metals Society of China, 2012, 22(4): 879-886.

[138] Katoh Y, Ozawa K, Shih C, et al. Continuous SiC fiber, CVI SiC matrix composites for nuclear applications: Properties and irradiation effects[J]. Journal of Nuclear Materials, 2014, 448(1-3): 448-476.

[139] Dong S M, Chollon G, Labrugere C, et al. Characterization of nearly stoichiometric SiC ceramic fibres[J]. Journal of Materials Science, 2001, 36: 2371-2381.

[140] Yao R, Feng Z, Chen L, et al. Oxidation behavior of Hi-Nicalon SiC monofilament fibres in air and O2–H2O–Ar atmospheres[J]. Corrosion Science, 2012, 57: 182-191.

[141] Ichikawa H. Recent advances in Nicalon ceramic fibres including Hi-Nicalon type S[C]//Annales de Chimie Science des Matériaux. No longer published by Elsevier, 2000, 25(7): 523-528.

[142] Naslain R. Design, preparation and properties of non-oxide CMCs for application in engines and nuclear reactors: an overview[J]. Composites Science and Technology, 2004, 64(2): 155-170.

[143] Ishikawa T, Kohtoku Y, Kumagawa K, et al. High-strength alkali-resistant sintered SiC fibre stable to 2,200 C[J]. Nature, 1998, 391(6669): 773-775.

[144] Sacks M D. Effect of composition and heat treatment conditions on the tensile strength and creep resistance of SiC-based fibers[J]. Journal of the European Ceramic Society, 1999, 19(13-14): 2305-2315.

[145] Snead M A, Katoh Y, Koyanagi T, et al. SiC/SiC Cladding Materials Properties Handbook[R]. Oak Ridge National Laboratory (ORNL), Oak Ridge, TN (United States), 2017.

[146] Igawa N, Taguchi T, Nozawa T, et al. Fabrication of SiC fiber reinforced SiC composite by chemical vapor infiltration for excellent mechanical properties[J]. Journal of Physics and Chemistry of Solids, 2005, 66(2-4): 551-554.

[147] Chen Y, Gélébart L, Chateau C, et al. Crack initiation and propagation in braided SiC/SiC composite tubes: Effect of braiding angle[J]. Journal of the European Ceramic Society, 2020, 40(13): 4403-4418.

[148] Sauder C. Ceramic matrix composites: nuclear applications[J]. Ceramic matrix composites: materials, modeling and technology, 2014: 609-646.

[149] Zhao S, Zhou X, Yu J, et al. Fabrication and characterization of 2.5 D and 3D SiCf/SiC composites[J]. Fusion Engineering and Design, 2013, 88(9-10): 2453-2456.

[150] Hou Z, Luo R, Yang W, et al. Effect of interface type on the static and dynamic mechanical properties of 3D braided SiCf/SiC composites[J]. Materials Science and Engineering: A, 2016, 669: 66-74.

[151] Amsc N, CMPS A A. Composite materials handbook[J]. Polymer matrix composites materials usage, design, and analysis, 2002.

[152] Wang Y, Ma Y, Zheng R, et al. Microstructure of PyC dominates interfacial shear failure in SiCf/SiC composites: From localized sliding to uniform plasticity[J]. Composites Part A: Applied Science and Manufacturing, 2023, 174: 107742.

[153] Fitzgerald K, Shepherd D. Review of SiCf/SiCm corrosion, erosion and erosion-corrosion in high temperature helium relevant to GFR conditions[J]. Journal of Nuclear Materials, 2018, 498: 476-494.

[154] Katoh Y, Nozawa T, Snead L L. Mechanical Properties of Thin Pyrolitic Carbon Interphase SiC–Matrix Composites Reinforced with Near-Stoichiometric SiC Fibers[J].

Journal of the American Ceramic Society, 2005, 88(11): 3088-3095.

[155] Shimoda K, Park J S, Hinoki T, et al. Influence of pyrolytic carbon interface thickness on microstructure and mechanical properties of SiC/SiC composites by NITE process[J]. Composites Science and Technology, 2008, 68(1): 98-105.

[156] Lamon J. Properties and characteristics of CVD SiC and SiC/SiC composites[J]. Comprehensive nuclear materials, 2012, 2: 323-338.

[157] Fitzer E, Fritz W, Schoch G. The chemical vapour impregnation of porous solids. modelling of the cvi-process[J]. Le Journal de Physique IV, 1991, 2(C2): C2-143-C2-150.

[158] Chen Y, Gélébart L, Chateau C, et al. Analysis of the damage initiation in a SiC/SiC composite tube from a direct comparison between large-scale numerical simulation and synchrotron X-ray micro-computed tomography[J]. International Journal of Solids and Structures, 2019, 161: 111-126.

[159] Deck C P, Khalifa H E, Sammuli B, et al. Fabrication of SiC–SiC composites for fuel cladding in advanced reactor designs[J]. Progress in Nuclear Energy, 2012, 57: 38-45.

[160] Singh G, Gonczy S, Deck C, et al. Interlaboratory round robin study on axial tensile properties of SiC-SiC CMC tubular test specimens[J]. International Journal of Applied Ceramic Technology, 2018, 15(6): 1334-1349.

[161] Bernachy-Barbe F, Gélébart L, Bornert M, et al. Anisotropic damage behavior of SiC/SiC composite tubes: Multiaxial testing and damage characterization[J]. Composites Part A: Applied Science and Manufacturing, 2015, 76: 281-288.

[162] Kim D, Lee H G, Park J Y, et al. Fabrication and measurement of hoop strength of SiC triplex tube for nuclear fuel cladding applications[J]. Journal of Nuclear Materials, 2015, 458: 29-36.

[163] Nance J, Subhash G, Sankar B, et al. Measurement of residual stress in silicon carbide fibers of tubular composites using Raman spectroscopy[J]. Acta Materialia, 2021, 217: 117164.

[164] Katoh Y, Dong S M, Kohyama A. Thermo-mechanical properties and microstructure of silicon carbide composites fabricated by nano-infiltrated transient eutectoid process[J]. Fusion Engineering and Design, 2002, 61: 723-731.

[165] Katoh Y, Snead L L, Henager Jr C H, et al. Current status and critical issues for development of SiC composites for fusion applications[J]. Journal of Nuclear Materials, 2007, 367: 659-671.

[166] Kohyama A. “Inspire” Project for R&D of Sic/Sic Fuel Cladding by Nite Method[J]. Ceramics for Environmental and Energy Applications II: Ceramic Transactions, Volume 246, 2014: 99-107.

[167] Yonathan P, Lee J H, Yoon D H, et al. Improvement of SiCf/SiC density by slurry infiltration and tape stacking[J]. Materials Research Bulletin, 2009, 44(11): 2116-2122.

[168] Snead L L, Nozawa T, Ferraris M, et al. Silicon carbide composites as fusion power reactor structural materials[J]. Journal of Nuclear Materials, 2011, 417(1-3): 330-339.

[169] Koyanagi T, Kondo S, Hinoki T. The influence of sintering additives on the irradiation resistance of NITE SiC[J]. Journal of nuclear materials, 2011, 417(1-3): 435-439.

[170] Shimoo T, TSUKADA I, NARISAWA M, et al. Change in properties of polycarbosilane-derived SiC fibers at high temperatures[J]. Journal of the Ceramic

Society of Japan, 1997, 105(1223): 559-563.

[171] Zhang J, Khalifa H E, Deck C, et al. Thermal diffusivity measurement of curved samples using the flash method[C]//Ceramic Materials for Energy Applications V: A Collection of Papers Presented at the 39th International Conference on Advanced Ceramics and Composites. Hoboken, NJ, USA: John Wiley & Sons, Inc., 2015: 43-56.

[172] Shimoda K, Hinoki T. Effects of fiber volume fraction on the densification and mechanical properties of unidirectional SiCf/SiC-matrix composites[J]. Journal of the European Ceramic Society, 2021, 41(2): 1163-1170.

[173] Hironaka K, Nozawa T, Hinoki T, et al. High-temperature tensile strength of near-stoichiometric SiC/SiC composites[J]. Journal of nuclear materials, 2002, 307: 1093-1097.

[174] Hayasaka D, Park J S, Kishimoto H, et al. Gas leak tightness of SiC/SiC composites at elevated temperature[J]. Fusion Engineering and Design, 2016, 109: 1498-1501.

[175] Ceder J. Characterization of uranium oxide powders and sinterability[J]. 2021.

[176] Deck C P, Khalifa H, Jacobsen G, et al. Demonstration of engineered multi-layered SiC-SiC cladding with enhanced accident tolerance[C]//2018 Water Reactor Fuel Performance Meeting, Prague, Czech Republic, September. 2018.

[177] Chen Y, Gélébart L, Chateau C, et al. 3D detection and quantitative characterization of cracks in a ceramic matrix composite tube using X-ray computed tomography[J]. Experimental Mechanics, 2020, 60: 409-424.

[178] Croom B P, Xu P, Lahoda E J, et al. Quantifying the three-dimensional damage and stress redistribution mechanisms of braided SiC/SiC composites by in situ volumetric digital image correlation[J]. Scripta Materialia, 2017, 130: 238-241.

[179] Shang J K, Ritchie R O. Crack bridging by uncracked ligaments during fatigue-crack growth in SiC-reinforced aluminum-alloy composites[J]. Metallurgical Transactions A, 1989, 20: 897-908.

[180] Liu D, Knol S, Ell J, et al. X-ray tomography study on the crushing strength and irradiation behaviour of dedicated tristructural isotropic nuclear fuel particles at 1000 C[J]. Materials & Design, 2020, 187: 108382.

[181] Cnudde V, Boone M N. High-resolution X-ray computed tomography in geosciences: A review of the current technology and applications[J]. Earth-Science Reviews, 2013, 123: 1-17.

[182] Landis E N, Keane D T. X-ray microtomography[J]. Materials characterization, 2010, 61(12): 1305-1316.

[183] Withers P J, Bouman C, Carmignato S, et al. X-ray computed tomography[J]. Nature Reviews Methods Primers, 2021, 1(1): 18.

[184] Stock S R. Recent advances in X-ray microtomography applied to materials[J]. International materials reviews, 2008, 53(3): 129-181.

[185] Salvo L, Suéry M, Marmottant A, et al. 3D imaging in material science: Application of X-ray tomography[J]. Comptes Rendus Physique, 2010, 11(9-10): 641-649.

[186] Stock S R. X-ray microtomography of materials[J]. International materials reviews, 1999, 44(4): 141-164.

[187] Hanke R, Fuchs T, Salamon M, et al. X-ray microtomography for materials characterization[M]//Materials characterization using Nondestructive Evaluation (NDE)

methods. Woodhead Publishing, 2016: 45-79.

[188] Maire E, Withers P J. Quantitative X-ray tomography[J]. International materials reviews, 2014, 59(1): 1-43.

[189] Sun W, Brown S B, Leach R K. An overview of industrial X-ray computed tomography[J]. 2012.

[190] Naresh K, Khan K A, Umer R, et al. The use of X-ray computed tomography for design and process modeling of aerospace composites: A review[J]. Materials & Design, 2020, 190: 108553.

[191] Grodzins L. Optimum energies for x-ray transmission tomography of small samples: Applications of synchrotron radiation to computerized tomography I[J]. Nuclear Instruments and Methods in Physics Research, 1983, 206(3): 541-545.

[192] Flannery B P, Deckman H W, Roberge W G, et al. Three-dimensional X-ray microtomography[J]. Science, 1987, 237(4821): 1439-1444.

[193] Sun W, Symes D R, Brenner C M, et al. Review of high energy x-ray computed tomography for non-destructive dimensional metrology of large metallic advanced manufactured components[J]. Reports on Progress in Physics, 2022, 85(1): 016102.

[194] Dann R, Turner M, Close M, et al. Multi-scale characterisation of coastal sand aquifer media for contaminant transport using X-ray computed tomography[J]. Environmental Earth Sciences, 2011, 63: 1125-1137.

[195] Weitkamp T, Diaz A, Nohammer B, et al. Hard x-ray phase imaging and tomography with a grating interferometer[C]//Developments in X-ray Tomography IV. SPIE, 2004, 5535: 137-142.

[196] Donoghue P C J, Bengtson S, Dong X, et al. Synchrotron X-ray tomographic microscopy of fossil embryos[J]. Nature, 2006, 442(7103): 680-683.

[197] Nabeyama A, Kurita A, Asano K, et al. xCT deficiency accelerates chemically induced tumorigenesis[J]. Proceedings of the National Academy of Sciences, 2010, 107(14): 6436-6441.

[198] Gall A, Fröhler B, Maurer J, et al. Cross-virtuality analysis of rich X-ray computed tomography data for materials science applications[J]. Nondestructive Testing and Evaluation, 2022, 37(5): 566-581.

[199] Toda H, Toda H. Fundamentals of X-Ray Imaging[J]. X-Ray CT: Hardware and Software Techniques, 2021: 17-49.

[200] Martz H E, Logan C M, Schneberk D J, et al. X-ray Imaging: fundamentals, industrial techniques and applications[M]. CRC Press, 2016.

[201] Handbook of X-ray imaging: physics and technology[M]. CRC press, 2017.

[202] DENISON* C, Carlson W D, Ketcham R A. Three-dimensional quantitative textural analysis of metamorphic rocks using high-resolution computed X-ray tomography: Part I. Methods and techniques[J]. Journal of Metamorphic Geology, 1997, 15(1): 29-44.

[203] Feldkamp L A, Davis L C, Kress J W. Practical cone-beam algorithm[J]. Josa a, 1984, 1(6): 612-619.

[204] Turbell H. Cone-beam reconstruction using filtered backprojection[M]. Linkopings Universitet (Sweden), 2001.

[205] Mayo S, Miller P, Wilkins S W, et al. Laboratory-based x-ray micro-tomography with submicron resolution[C]//Developments in X-ray Tomography V. SPIE, 2006, 6318:

439-446.

[206] Zwanenburg E A, Williams M A, Warnett J M. Review of high-speed imaging with lab-based x-ray computed tomography[J]. Measurement Science and Technology, 2021, 33(1): 012003.

[207] Hanna R D, Ketcham R A. X-ray computed tomography of planetary materials: A primer and review of recent studies[J]. Geochemistry, 2017, 77(4): 547-572.

[208] Kastner J, Harrer B, Requena G, et al. A comparative study of high resolution cone beam X-ray tomography and synchrotron tomography applied to Fe-and Al-alloys[J]. Ndt & E International, 2010, 43(7): 599-605.

[209] Cakmak E, Bingham P, Cunningham R W, et al. Non-destructive characterization of additively manufactured components with x-ray computed tomography for part qualification: A study with laboratory and synchrotron x-rays[J]. Materials Characterization, 2021, 173: 110894.

[210] An N, Shuai S, Hu T, et al. Application of synchrotron X-ray imaging and diffraction in additive manufacturing: a review[J]. Acta Metallurgica Sinica (English Letters), 2022: 1-24.

[211] Wu S C, Xiao T Q, Withers P J. The imaging of failure in structural materials by synchrotron radiation X-ray microtomography[J]. Engineering Fracture Mechanics, 2017, 182: 127-156.

[212] Gao Y, Hu W, Xin S, et al. A review of applications of CT imaging on fiber reinforced composites[J]. Journal of Composite Materials, 2022, 56(1): 133-164.

[213] Ferreira T R, Pires L F, Reichardt K. 4D X-ray computed tomography in soil science: An overview and future perspectives at Mogno/Sirius[J]. Brazilian Journal of Physics, 2022, 52(2): 33.

[214] von der Heyden B P. Shedding light on ore deposits: A review of synchrotron X-ray radiation use in ore geology research[J]. Ore Geology Reviews, 2020, 117: 103328.

[215] Thompson A, Maskery I, Leach R K. X-ray computed tomography for additive manufacturing: a review[J]. Measurement Science and Technology, 2016, 27(7): 072001.

[216] Guignot N, King A, Boulard E. Synchrotron x-ray computed microtomography for high pressure science[J]. Journal of Applied Physics, 2020, 127(24).

[217] Mertens J C E, Williams J J, Chawla N. Note: Design and construction of a multi-scale, high-resolution, tube-generated X-Ray computed-tomography system for three-dimensional (3D) imaging[J]. Review of Scientific Instruments, 2014, 85(1).

[218] Stock S R. Microcomputed tomography: methodology and applications[M]. CRC press, 2019.

[219] Micro-computed Tomography (micro-CT) in Medicine and Engineering[R]. Berlin/Heidelberg, Germany: Springer, 2020.

[220] Industrial X-ray computed tomography[M]. Cham, Switzerland: Springer International Publishing, 2018.

[221] Morales-Rodriguez A, Reynaud P, Fantozzi G, et al. Porosity analysis of long-fiber-reinforced ceramic matrix composites using X-ray tomography[J]. Scripta Materialia, 2009, 60(6): 388-390.

[222] Gélébart L, Chateau C, Bornert M, et al. X-Ray Tomographic Characterization of the

Macroscopic Porosity of Chemical Vapor Infiltration SIC/SIC Composites: Effects on the Elastic Behavior[J]. International Journal Of Applied Ceramic Technology, 2010, 7(3): 348-360.

[223] Liu D, Gludovatz B, Barnard H S, et al. Damage tolerance of nuclear graphite at elevated temperatures[J]. Nature communications, 2017, 8(1): 1-9.

[224] Jiang M, El-Turke A, Lolov G, et al. Multiple length-scale microstructural characterisation of four grades of fine-grained graphite[J]. Journal of Nuclear Materials, 2021, 550: 152876.

[225] Pei R, McDonald S A, Shen L, et al. Crack healing behaviour of Cr2AlC MAX phase studied by X-ray tomography[J]. Journal of the European Ceramic Society, 2017, 37(2): 441-450.

[226] Fey T, Stumpf M, Chmielarz A, et al. Microstructure, thermal conductivity and simulation of elastic modulus of MAX-phase (Ti2AlC) gel-cast foams[J]. Journal of the European Ceramic Society, 2018, 38(10): 3424-3432.

[227] Sloof W G, Pei R, McDonald S A, et al. Repeated crack healing in MAX-phase ceramics revealed by 4D in situ synchrotron X-ray tomographic microscopy[J]. Scientific reports, 2016, 6(1): 23040.

[228] Lowe T, Bradley R S, Yue S, et al. Microstructural analysis of TRISO particles using multi-scale X-ray computed tomography[J]. Journal of Nuclear Materials, 2015, 461: 29-36.

[229] Forna-Kreutzer J P, Ell J, Barnard H, et al. Full-field characterisation of oxide-oxide ceramic-matrix composites using X-ray computed micro-tomography and digital volume correlation under load at high temperatures[J]. Materials & Design, 2021, 208: 109899.

[230] Ning Z, Li G, Melvin D L R, et al. Dendrite initiation and propagation in lithium metal solid-state batteries[J]. Nature, 2023, 618(7964): 287-293.

[231] Pérez-Ramos A, Figueirido B. Toward an “ancient” virtual world: improvement methods on X-ray CT data processing and virtual reconstruction of fossil skulls[J]. Frontiers in Earth Science, 2020, 8: 345.

[232] Tammas-Williams S. XCT analysis of the defect distribution and its effect on the static and dynamic mechanical properties in Ti-6Al-4V components manufactured by electron beam additive manufacture[M]. The University of Manchester (United Kingdom), 2016.

[233] Buljac A, Jailin C, Mendoza A, et al. Digital volume correlation: progress and challenges[C]//Advancements in Optical Methods & Digital Image Correlation in Experimental Mechanics, Volume 3: Proceedings of the 2019 Annual Conference on Experimental and Applied Mechanics. Springer International Publishing, 2020: 113-115.

[234] Roberts B C, Perilli E, Reynolds K J. Application of the digital volume correlation technique for the measurement of displacement and strain fields in bone: a literature review[J]. Journal of biomechanics, 2014, 47(5): 923-934.

[235] Bay B K. Methods and applications of digital volume correlation[J]. The Journal of Strain Analysis for Engineering Design, 2008, 43(8): 745-760.

[236] Yue Z, Song Y, Li P, et al. Applications of digital image correlation (DIC) and the strain gage method for measuring dynamic mode I fracture parameters of the white marble specimen[J]. Rock Mechanics and Rock Engineering, 2019, 52: 4203-4216.

[237] Bale H, Blacklock M, Begley M R, et al. Characterizing three-dimensional textile ceramic composites using synchrotron X-ray micro-computed-tomography[J]. Journal of the American Ceramic Society, 2012, 95(1): 392-402.

[238] Madi K, Tozzi G, Zhang Q H, et al. Computation of full-field displacements in a scaffold implant using digital volume correlation and finite element analysis[J]. Medical engineering & physics, 2013, 35(9): 1298-1312.

[239] Tozzi G, Dall'Ara E, Palanca M, et al. Strain uncertainties from two digital volume correlation approaches in prophylactically augmented vertebrae: Local analysis on bone and cement-bone microstructures[J]. Journal of the mechanical behavior of biomedical materials, 2017, 67: 117-126.

[240] Palanca M, Tozzi G, Cristofolini L, et al. Three-dimensional local measurements of bone strain and displacement: comparison of three digital volume correlation approaches[J]. Journal of biomechanical engineering, 2015, 137(7): 071006.

[241] Oliver W C, Pharr G M. An improved technique for determining hardness and elastic modulus using load and displacement sensing indentation experiments[J]. Journal of materials research, 1992, 7(6): 1564-1583.

[242] Katoh Y, Ozawa K, Hinoki T, et al. Mechanical properties of advanced SiC fiber composites irradiated at very high temperatures[J]. Journal of nuclear materials, 2011, 417(1-3): 416-420.

[243] Karakoc O, Koyanagi T, Nozawa T, et al. Fiber/matrix debonding evaluation of SiCf/SiC composites using micropillar compression technique[J]. Composites Part B: Engineering, 2021, 224: 109189.

[244] Haboub A, Bale H A, Nasiatka J R, et al. Tensile testing of materials at high temperatures above 1700 C with in situ synchrotron X-ray micro-tomography[J]. Review of Scientific Instruments, 2014, 85(8).

[245] Bale H A, Haboub A, MacDowell A A, et al. Real-time quantitative imaging of failure events in materials under load at temperatures above 1,600 C[J]. Nature materials, 2013, 12(1): 40-46.

[246] ASTM Standard C1323-26, Standard Test Method for Ultimate Strength of Advanced Ceramics with Diametrally Compressed C-Ring Specimens at Ambient Temperature, ASTM International, West Conshohocken, PA, 2016, doi: 10.1520/C1323-16.2.

[247] Embree T L, Segall A E. Evaluation of the uniaxiality of the stress state in C-ring fracture strength specimens[J]. Journal of Testing and Evaluation, 2004, 32(2): 153-160.

[248] Yakovlev M A, Vanselow D J, Ngu M S, et al. A wide-field micro-computed tomography detector: micron resolution at half-centimetre scale[J]. Journal of synchrotron radiation, 2022, 29(2): 505-514.

[249] Gürsoy D, De Carlo F, Xiao X, et al. TomoPy: a framework for the analysis of synchrotron tomographic data[J]. Journal of synchrotron radiation, 2014, 21(5): 1188-1193.

[250] Ferreira. T and Rasband. W, "User Guide User Guide ImageJ.

[251] Thermo ScienticTM AvizoTM Software 9, User's Guide, 2018.

[252] Zaefferer S. A critical review of orientation microscopy in SEM and TEM[J]. Crystal Research and Technology, 2011, 46(6): 607-628.

[253] Goldstein J I, Newbury D E, Michael J R, et al. Scanning electron microscopy and X-

ray microanalysis[M]. springer, 2017.

[254] Lawes G. Scanning electron microscopy and X-ray microanalysis[J]. 1987.

[255] Ishitani T, Tsuboi H. Objective comparison of scanning ion and scanning electron microscope images[J]. Scanning, 1997, 19(7): 489-497.

[256] Instrument_Ref, Cold mounting systems for all materialographic applications, Struers, 2020, https://www.struers.com/en/Library#brochures.

[257] Jäpel T. Feasibility study on local elastic strain measurements with an ebsd pattern cross correlation method in elastic-plastically deforming materials: applications on high manganese TWIP steels[D]. Dissertation, Aachen, Techn. Hochsch., 2014, 2015.

[258] He S, Horton E, Moore S, et al. A correlative approach to evaluating the links between local microstructural parameters and creep initiated cavities[J]. Materials & Design, 2024, 241: 112905.

[259] Wilkinson A J, Britton T B. Strains, planes, and EBSD in materials science[J]. Materials today, 2012, 15(9): 366-376.

[260] Carneiro Í, Simões S. Recent advances in EBSD characterization of metals[J]. Metals, 2020, 10(8): 1097.

[261] Wilkinson A J, Britton T B, Jiang J, et al. A review of advances and challenges in EBSD strain mapping[C]//IOP Conference Series: Materials Science and Engineering. IOP Publishing, 2014, 55(1): 012020.

[262] Nowell M M, Witt R A, True B W. EBSD sample preparation: techniques, tips, and tricks[J]. Microscopy Today, 2005, 13(4): 44-49.

[263] Humphreys F J. Review grain and subgrain characterisation by electron backscatter diffraction[J]. Journal of materials science, 2001, 36: 3833-3854.

[264] Illingworth J, Kittler J. The adaptive Hough transform[J]. IEEE Transactions on Pattern Analysis and Machine Intelligence, 1987 (5): 690-698.

[265] Vander Voort G, Van Geertruyden W, Dillon S, et al. Metallographic preparation for electron backscattered diffraction[J]. Microscopy and Microanalysis, 2006, 12(S02): 1610-1611.

[266] Ajantiwalay T, Trowbridge T, Winston A, et al. Best practices for preparing radioactive specimens for EBSD analysis[J]. Micron, 2019, 118: 1-8.

[267] Liu Y, King H E, Van Huis M A, et al. Nano-tomography of porous geological materials using focused ion beam-scanning electron microscopy[J]. Minerals, 2016, 6(4): 104.

[268] Focused ion beam systems: basics and applications[M]. Cambridge University Press, 2007.

[269] Arregui-Mena J D, Edmondson P D, Campbell A A, et al. Site specific, high-resolution characterisation of porosity in graphite using FIB-SEM tomography[J]. Journal of Nuclear Materials, 2018, 511: 164-173.

[270] Focused ion beam systems: basics and applications[M]. Cambridge University Press, 2007.

[271] Nan N, Wang J. FIB-SEM three-dimensional tomography for characterization of carbon-based materials[J]. Advances in Materials Science and Engineering, 2019, 2019(1): 8680715.

[272] Introduction to focused ion beams: instrumentation, theory, techniques and practice[M].

Springer Science & Business Media, 2004.

[273] Phaneuf M W. Applications of focused ion beam microscopy to materials science specimens[J]. Micron, 1999, 30(3): 277-288.

[274] Leide A. Reaction-bonded silicon carbide for nuclear fusion blanket applications[D]. University of Oxford, 2019.

[275] Volkert C A, Minor A M. Focused ion beam microscopy and micromachining[J]. MRS bulletin, 2007, 32(5): 389-399.

[276] Maňák J, Vokoun D. Microbending experiments on pure magnesium with nonbasal slip orientation[J]. Materials, 2018, 11(8): 1434.

[277] Shahbeyk S, Voyiadjis G Z, Habibi V, et al. Review of size effects during micropillar compression test: Experiments and atomistic simulations[J]. Crystals, 2019, 9(11): 591.

[278] Munroe P R, Rubanov S. Artefacts in germanium transmission electron microscope specimens prepared by focused ion beam milling[M]//Microscopy of Semiconducting Materials 2003. CRC Press, 2018: 621-624.

[279] Tsurusawa H, Nakanishi N, Kawano K, et al. Robotic fabrication of high-quality lamellae for aberration-corrected transmission electron microscopy[J]. Scientific Reports, 2021, 11(1): 21599.

[280] Tabor D. Mohs's hardness scale-a physical interpretation[J]. Proceedings of the Physical Society. Section B, 1954, 67(3): 249.

[281] Duan P. Modelling and experimental characterization of nanoindentation responses of various biocomposite materials[D]. Newcastle University, 2018.

[282] Kushch V I, Dub S N, Litvin P M. Determination of the young modulus from elastic section of the Berkovich indenter loading curve[J]. Journal of Superhard Materials, 2007, 29: 228-234.

[283] Sharma H K, Sharma R K, Saxena R S, et al. A review of nanoindentation and related cathodoluminescence studies on semiconductor materials[J]. Journal of Materials Science: Materials in Electronics, 2022, 33(27): 21223-21245.

[284] Hainsworth S V, Page T F. Nanoindentation studies of chemomechanical effects in thin film coated systems[J]. Surface and Coatings Technology, 1994, 68: 571-575.

[285] Burnett P J, Rickerby D S. The mechanical properties of wear-resistant coatings: II: Experimental studies and interpretation of hardness[J]. Thin solid films, 1987, 148(1): 51-65.

[286] Page T F, Hainsworth S V. Using nanoindentation techniques for the characterization of coated systems: a critique[J]. Surface and Coatings Technology, 1993, 61(1-3): 201-208.

[287] Doerner M F, Nix W D. A method for interpreting the data from Depth-sensing Indentation[J]. J. Mater. Res, 1986, 1: 4.

[288] Sneddon I N. The relation between load and penetration in the axisymmetric Boussinesq problem for a punch of arbitrary profile[J]. International journal of engineering science, 1965, 3(1): 47-57.

[289] Chai P, Li S, Li Y, et al. Mechanical behavior investigation of 4H-SiC single crystal at the micro–nano scale[J]. Micromachines, 2020, 11(1): 102.

[290] Suman S, Khan M K, Pathak M, et al. Investigation of elevated-temperature mechanical properties of δ-hydride precipitate in Zircaloy-4 fuel cladding tubes using

nanoindentation[J]. Journal of Alloys and Compounds, 2017, 726: 107-113.

[291] Orlando A, Franceschini F, Muscas C, et al. A comprehensive review on Raman spectroscopy applications[J]. Chemosensors, 2021, 9(9): 262.

[292] Porter M D, Lipert R J, Siperko L M, et al. SERS as a bioassay platform: fundamentals, design, and applications[J]. Chemical Society Reviews, 2008, 37(5): 1001-1011.

[293] Sharma B, Frontiera R R, Henry A I, et al. SERS: Materials, applications, and the future[J]. Materials today, 2012, 15(1-2): 16-25.

[294] Wang K, Huang M, Chen J, et al. A “drop-wipe-test” SERS method for rapid detection of pesticide residues in fruits[J]. Journal of Raman Spectroscopy, 2018, 49(3): 493-498.

[295] Chen K, Leona M, Vo-Dinh T. Surface-enhanced Raman scattering for identification of organic pigments and dyes in works of art and cultural heritage material[J]. Sensor Review, 2007, 27(2): 109-120.

[296] Harris D C, Bertolucci M D. Symmetry and spectroscopy: an introduction to vibrational and electronic spectroscopy[M]. Courier Corporation, 1989.

[297] Smekal A. Zur Quantentheorie der Streuung und Dispersion[J]. Zeitschrift für Physik, 1925, 32(1): 241-244.

[298] Raman C V, Krishnan K S. A new type of secondary radiation[J]. Nature, 1928, 121(3048): 501-502.

[299] Das R S, Agrawal Y K. Raman spectroscopy: Recent advancements, techniques and applications[J]. Vibrational spectroscopy, 2011, 57(2): 163-176.

[300] Mercier B, Castelain T, Jondeau E, et al. Density fluctuations measurement by rayleigh scattering using a single photomultiplier[J]. AIAA Journal, 2018, 56(4): 1310-1316.

[301] Xu Z, He Z, Song Y, et al. Topic review: application of Raman spectroscopy characterization in micro/nano-machining[J]. Micromachines, 2018, 9(7): 361.

[302] Wan F, Du L, Chen W, et al. A novel method to directly analyze dissolved acetic acid in transformer oil without extraction using Raman spectroscopy[J]. Energies, 2017, 10(7): 967.

[303] High pressure surface science and engineering[M]. CRC Press, 2019.

[304] Krishna R, Jones A N, Edge R, et al. Residual stress measurements in polycrystalline graphite with micro-Raman spectroscopy[J]. Radiation Physics and Chemistry, 2015, 111: 14-23.

[305] Krajewska Z M, Gudowski W. Raman Spectroscopy Studies of TRISO-Particle Fuel[C]//Journal of Physics: Conference Series. IOP Publishing, 2021, 2048(1): 012007.

[306] DiGregorio J F, Furtak T E, Petrovic J J. A technique for measuring residual stress in SiC whiskers within an alumina matrix through Raman spectroscopy[J]. Journal of applied physics, 1992, 71(7): 3524-3531.

[307] Gouadec G, Karlin S, Colomban P. Raman extensometry study of NLM202® and Hi-Nicalon® SiC fibres[J]. Composites Part B: Engineering, 1998, 29(3): 251-261.

[308] Sebastiani M, Bemporad E, Carassiti F, et al. Residual stress measurement at the micrometer scale: Focused ion beam (FIB) milling and nanoindentation testing[J]. Philosophical Magazine, 2011, 91(7-9): 1121-1136.

[309] Sebastiani M, Bemporad E, Melone G, et al. A New Methodology For In-Situ Residual Stress Measurement In MEMS Structures[C]//AIP Conference Proceedings. American

Institute of Physics, 2010, 1300(1): 120-126.

[310] Korsunsky A M, Bemporad E, Sebastiani M, et al. On the measurement and interpretation of residual stress at the micro-scale[J]. International Journal of Modern Physics B, 2010, 24(01n02): 1-9.

[311] Sebastiani M, Bolelli G, Lusvarghi L, et al. High resolution residual stress measurement on amorphous and crystalline plasma-sprayed single-splats[J]. Surface and Coatings Technology, 2012, 206(23): 4872-4880.

[312] Winiarski B, Withers P J. Micron-scale residual stress measurement by micro-hole drilling and digital image correlation[J]. Experimental mechanics, 2012, 52: 417-428.

[313] Winiarski B, Gholinia A, Tian J, et al. Submicron-scale depth profiling of residual stress in amorphous materials by incremental focused ion beam slotting[J]. Acta materialia, 2012, 60(5): 2337-2349.

[314] Salvati E, Korsunsky A M. An analysis of macro-and micro-scale residual stresses of Type I, II and III using FIB-DIC micro-ring-core milling and crystal plasticity FE modelling[J]. International Journal of Plasticity, 2017, 98: 123-138.

[315] Lunt A J G, Baimpas N, Salvati E, et al. A state-of-the-art review of micron-scale spatially resolved residual stress analysis by FIB-DIC ring-core milling and other techniques[J]. The Journal of Strain Analysis for Engineering Design, 2015, 50(7): 426-444.

[316] Lord J, Cox D, Ratzke A, et al. A good practice guide for measuring residual stresses using FIB-DIC[J]. 2018.

[317] Winiarski B, Langford R M, Tian J, et al. Mapping residual stress distributions at the micron scale in amorphous materials[J]. Metallurgical and Materials transactions A, 2010, 41: 1743-1751.

[318] Sebastiani M, Eberl C, Bemporad E, et al. Focused ion beam four-slot milling for Poisson's ratio and residual stress evaluation at the micron scale[J]. Surface and Coatings Technology, 2014, 251: 151-161.

[319] Moazam M A, Honarpisheh M. Experimental and Numerical Study on the Accuracy Residual Stress Measurement by Incremental Ring-Core Method[J]. AUT Journal of Mechanical Engineering, 2018, 2(2): 137-148.

[320] Salvati E, Sui T, Ying S, et al. On the accuracy of residual stress evaluation from focused ion beam DIC (FIB-DIC) ring-core milling experiments[C]//5th International Conference on Nanotechnology: Fundamentals and Applications (ICNFA), 2014. 2014: 265.

[321] Bemporad E, Brisotto M, Depero L E, et al. A critical comparison between XRD and FIB residual stress measurement techniques in thin films[J]. Thin Solid Films, 2014, 572: 224-231.

[322] Sabaté N, Vogel D, Gollhardt A, et al. Residual stress measurement on a MEMS structure with high-spatial resolution[J]. Journal of microelectromechanical systems, 2007, 16(2): 365-372.

[323] Korsunsky A M, Constantinescu A. The influence of indenter bluntness on the apparent contact stiffness of thin coatings[J]. Thin Solid Films, 2009, 517(17): 4835-4844.

[324] Hoffmann M, Birringer R. Quantitative measurements of Young's modulus using the miniaturized disk-bend test[J]. Materials Science and Engineering: A, 1995, 202(1-2): 18-25.

[325] Tomioka Y, Yuki N. Bend stiffness of copper and copper alloy foils[J]. Journal of materials processing technology, 2004, 146(2): 228-233.

[326] Blaber J, Adair B, Antoniou A. Ncorr: open-source 2D digital image correlation matlab software[J]. Experimental Mechanics, 2015, 55(6): 1105-1122.

[327] Nogami S, Hasegawa A, Snead L L, et al. Effect of He pre-implantation and neutron irradiation on mechanical properties of SiC/SiC composite[J]. Journal of nuclear materials, 2004, 329: 577-581.

[328] Frazer D, Abad M D, Krumwiede D, et al. Localized mechanical property assessment of SiC/SiC composite materials[J]. Composites Part A: Applied Science and Manufacturing, 2015, 70: 93-101.

[329] Xiao Z, Yang Y, Jin N, et al. Microstructure and thermal residual stress analysis of SiC fiber through Raman spectroscopy[J]. Journal of Raman Spectroscopy, 2013, 44(9): 1306-1311.

[330] Niu X, Zhang H, Pei Z, et al. Measurement of interfacial residual stress in SiC fiber reinforced Ni-Cr-Al alloy composites by Raman spectroscopy[J]. Journal of Materials Science & Technology, 2019, 35(1): 88-93.

[331] Hironaka K, Nozawa T, Hinoki T, et al. High-temperature tensile strength of near-stoichiometric SiC/SiC composites[J]. Journal of nuclear materials, 2002, 307: 1093-1097.

[332] Gulden T D. Mechanical Properties of Polycrystalline β-SiC[J]. Journal of the American Ceramic Society, 1969, 52(11): 585-590.

[333] Brauner C, Frerich T, Herrmann A S. Cure-dependent thermomechanical modelling of the stress relaxation behaviour of composite materials during manufacturing[J]. Journal of Composite Materials, 2017, 51(7): 877-898.

[334] Zhu S, Mizuno M, Kagawa Y, et al. Monotonic tension, fatigue and creep behavior of SiC-fiber-reinforced SiC-matrix composites: a review[J]. Composites Science and Technology, 1999, 59(6): 833-851.

[335] Ritchie R O, Liu D. Introduction to fracture mechanics[M]. Elsevier, 2021.

[336] Evans A G. Perspective on the development of high-toughness ceramics[J]. Journal of the American Ceramic society, 1990, 73(2): 187-206.

[337] Zhou W, Long Y. Mechanical properties of CVD-SiC coatings with Si impurity[J]. Ceramics International, 2018, 44(17): 21730-21733.

[338] Koyanagi T, Katoh Y, Lance M J. Raman spectroscopy of neutron irradiated silicon carbide: C orrelation among R aman spectra, swelling, and irradiation temperature[J]. Journal of Raman Spectroscopy, 2018, 49(10): 1686-1692.

[339] Guan K, Zeng Q, Liu Y, et al. A multiscale model for CVD growth of silicon carbide[J]. Computational Materials Science, 2021, 196: 110512.

[340] Huang J J, Militzer C, Xu J, et al. Growth of silicon carbide multilayers with varying preferred growth orientation[J]. Surface and Coatings Technology, 2022, 447: 128853.

[341] Chateau C, Gélébart L, Bornert M, et al. Micromechanical modeling of the elastic behavior of unidirectional CVI SiC/SiC composites[J]. International Journal of Solids and Structures, 2015, 58: 322-334.

[342] Reiley T C, Nix W D. The structure and mechanical properties of physically vapor deposited chromium[J]. Metallurgical Transactions A, 1976, 7: 1695-1701.

[343] Graening T, Massey C P, Linton K, et al. Microstructure investigation and mechanical properties of coated zircaloy cladding[R]. Oak Ridge National Laboratory (ORNL), Oak Ridge, TN (United States), 2021.

[344] Ming-Yuan H, Hutchinson J W. Crack deflection at an interface between dissimilar elastic materials[J]. International journal of solids and structures, 1989, 25(9): 1053-1067.

[345] Liu D, Fabes S, Li B S, et al. Characterization of the interfacial toughness in a novel “GaN-on-diamond” material for high-power RF devices[J]. ACS Applied Electronic Materials, 2019, 1(3): 354-369.

[346] Ren Y. Fracture toughness behavior of Zircaloy-4 in the form of fuel cladding tubing in nuclear reactors[M]. 2004.

[347] Perry J H. Chemical engineers' handbook: prepared by a staff of specialists[M]//Chemical engineers' handbook: prepared by a staff of specialists. 1950: 1042-1042.

[348] CRC handbook of chemistry and physics[M]. CRC press, 2004.

[349] de Menibus A H, Guilbert T, Auzoux Q, et al. Hydrogen contribution to the thermal expansion of hydrided Zircaloy-4 cladding tubes[J]. Journal of Nuclear Materials, 2013, 440(1-3): 169-177.

[350] Zanellato O, Preuss M, Buffiere J Y, et al. Synchrotron diffraction study of dissolution and precipitation kinetics of hydrides in Zircaloy-4[J]. Journal of Nuclear Materials, 2012, 420(1-3): 537-547.

[351] Wehling H J, Warnemünde R. Vibration monitoring of light water reactors with advanced methods and the new microprocessor-based SÜS-86 system[J]. Progress in Nuclear Energy, 1988, 21: 79-88.

[352] Kitano K, Ozawa M. Analysis of stress applied to a ruptured cladding tube under horizontal vibration[J]. Journal of Nuclear Science and Technology, 2020, 57(9): 1051-1061.

[353] Yagnik S, Garde A. Zirconium alloys for LWR fuel cladding and core internals[J]. Structural Alloys for Nuclear Energy Applications, 2019: 247-291.

[354] Christon M A, Lu R, Bakosi J, et al. Large-eddy simulation, fuel rod vibration and grid-to-rod fretting in pressurized water reactors[J]. Journal of Computational Physics, 2016, 322: 142-161.

[355] Leide A J, Haynes T A, Tzelepi N, et al. Measurement of residual stresses in surrogate coated nuclear fuel particles using ring-core focussed ion beam digital image correlation[J]. Nuclear Materials and Energy, 2023, 36: 101470.

[356] Żórawski W, Molak R, Mądry J, et al. Experimental and numerical investigations of titanium deposition for cold spray additive manufacturing as a function of standoff distance[J]. Materials, 2021, 14(19): 5492.

[357] Birt A M, Champagne V K, Sisson R D, et al. Microstructural analysis of cold-sprayed Ti-6Al-4V at the micro-and nano-scale[J]. Journal of thermal spray technology, 2015, 24: 1277-1288.

[358] Rokni M R, Widener C A, Crawford G A, et al. An investigation into microstructure and mechanical properties of cold sprayed 7075 Al deposition[J]. Materials Science and Engineering: A, 2015, 625: 19-27.

[359] Li W Y, Zhang C, Guo X P, et al. Effect of standoff distance on coating deposition characteristics in cold spraying[J]. Materials & design, 2008, 29(2): 297-304.

[360] Li C J, Li W Y. Deposition characteristics of titanium coating in cold spraying[J]. Surface and Coatings Technology, 2003, 167(2-3): 278-283.

[361] Marrocco T, McCartney D G, Shipway P H, et al. Production of titanium deposits by cold-gas dynamic spray: numerical modeling and experimental characterization[J]. Journal of Thermal Spray Technology, 2006, 15: 263-272.

[362] Marzbanrad B, Toyserkani E, Jahed H. Customization of residual stress induced in cold spray printing[J]. Journal of Materials Processing Technology, 2021, 289: 116928.

[363] Suhonen T, Varis T, Dosta S, et al. Residual stress development in cold sprayed Al, Cu and Ti coatings[J]. Acta Materialia, 2013, 61(17): 6329-6337.

[364] Valarezo A, Sampath S. An integrated assessment of process-microstructure-property relationships for thermal-sprayed NiCr coatings[J]. Journal of thermal spray technology, 2011, 20: 1244-1258.